DEPARTAMENT DE FÍSICA ATÒMICA
MOLECULAR I NUCLEAR

VNIVERSITAT DE VALÈNCIA

(ESTUDI GENERAL)

Study of the event reconstruction and expected performances for point-like sources of the future ANTARES neutrino telescope

PhD THESIS

EMILIANO CARMONA FLORES

September 2003

D. JUAN JOSÉ HERNÁNDEZ REY, Investigador Científico del C.S.I.C.,

CERTIFICA :

Que la presente memoria, **Study of the event reconstruction and expected performances for point-like sources of the future ANTARES neutrino telescope**, ha sido realizada bajo su dirección en el Departamento de Física Atómica, Molecular y Nuclear de la Universitat de València por D. Emiliano Carmona Flores y constituye su Tesis Doctoral, que presenta para optar al grado de Doctor en Física.

Y para que conste, en cumplimiento de la legislación vigente, firmo el presente Certificado en Paterna a 30 de Septiembre de 2003.

Fdo.: Juan José Hernández Rey

Visto bueno del Director del Depto.: D. Ramón Cases Ruiz

SS
A S:·)
SS

Agradecimientos

Deseo dar las gracias en primer lugar a mi director de tesis, Juan José Hernández Rey, por la oportunidad de integrarme en el grupo ANTARES Valencia cuando estaba en sus comienzos, y por su ayuda durante todo el desarrollo de este trabajo. Sinceramente quiero agradecerle el apoyo y la confianza que me ha prestado durante estos años, sin los cuales no me habría sido posible finalizar esta tesis.

También quiero dar las gracias a Juan Zúñiga por su ayuda y sus comentarios. Las discusiones con él a lo largo de este trabajo han sido decisivas para su conclusión exitosa.

Gracias a Jurgen Brunner por su ayuda en muchos aspectos relacionados con el Monte Carlo y la reconstrucción en ANTARES. Gracias también a Teresa Montaruli por su ayuda y sus valiosos comentarios relacionados con el estudio de las fuentes puntuales de neutrinos.

Mi agradecimiento también para todo el personal del IFIC, en especial para Asun, por estar siempre dispuesta a ayudar antes incluso de que se lo pidan, y para Rosario, Amparo y Javier por su cercanía y por toda la ayuda prestada.

Agradezco al proyecto GRID de Valencia el habernos permitido utilizar su granja antes de estar abierta a todo el mundo, lo que facilitó enormemente este trabajo.

Gracias a Sergio por haber hecho que Marsella fuera un lugar mucho más divertido y agradable.

Gracias al resto de los miembros del grupo ANTARES de Valencia, a Juande por su ayuda y por ser tan buen compañero de despacho y a Juanan, Víctor y Diego, por su ayuda y por crear un ambiente de trabajo tan agradable.

Gracias también a Santi, Paco, María José, Pablo y Arantza por todos los buenos momentos compartidos dentro y fuera del IFIC.

Y gracias a mis padres y mis hermanos por toda la motivación y el apoyo que me han dado, sin el cual probablemente este trabajo no hubiera llegado a realizarse.

Finalmente, gracias a Mari Carmen por haber estado siempre conmigo, ayudándome y apoyándome tanto.

Durante todo el tiempo transcurrido hasta completar este trabajo han sido muchas más las personas que en un momento u otro me han ayudado y a quienes tengo que darles las gracias. Mi agradecimiento también para todos ellos aunque todos los nombres no puedan caber en esta página.

Contents

Estudio de la reconstrucción de sucesos y las prestaciones esperadas para fuentes puntuales en el telescopio de neutrinos ANTARES

Introducción

Astronomía de neutrinos

La astronomía de neutrinos es una disciplina de aparición relativamente reciente que ofrece un considerable potencial para el estudio de las regiones más lejanas del Cosmos.

La astronomía tradicional basada en fotones ha permitido explorar ampliamente el Universo utilizando todas las longitudes de onda del espectro electromagnético, desde las ondas de radio de $\lambda \sim 10^4$ cm hasta los rayos gamma del orden del TeV. Estos últimos han permitido realizar importantes descubrimientos en la región de más alta energía, como las fuentes de rayos gamma. Sin embargo, el poder de exploración de los fotones de alta energía se ve limitado por su atenuación al interaccionar con la radiación de fondo (efecto GZK). Asimismo, debido a su interacción con la materia, los fotones no permiten explorar regiones densas. En su estudio han de utilizarse partículas que interaccionen débilmente.

Al igual que los fotones, los neutrinos son también partículas neutras y estables, capaces de transportar información astronómica, pero a diferencia de los fotones no sufren apenas absorción al atravesar el espacio, lo cual los convierte en los candidatos idóneos para la exploración de las regiones más densas y lejanas del Universo, inaccesibles para la astronomía tradicional.

Hasta la fecha los únicos neutrinos de fuentes extraterrestres detectados han sido los neutrinos solares, originados en las reacciones nucleares en el núcleo del Sol [1] y los provenientes de la supernova SN1987A [2–4], de energías del orden de algunas decenas de MeV. Sin embargo, el interés principal de la astronomía de neutrinos corresponde precisamente a la región de más alta energía (E_ν por encima de GeV-TeV). Ello es debido por una parte a que la sección eficaz de los neutrinos, así como al alcance y la resolución angular de los muones, que aumentan con la energía, lo cual favorece su detección. Por otra parte, los neutrinos de alta energía ofrecen la posibilidad de utilizar como blanco enormes medios naturales (agua, hielo o la atmósfera). Asimismo, la astronomía de neutrinos de alta energía puede explorar algunas cuestiones cosmológicas candentes, como la naturaleza de la materia oscura, el origen de los rayos cósmicos o la física de los objetos más brillantes del Universo.

Fuentes de neutrinos de alta energía

En el Universo existen diversos procesos susceptibles de producir neutrinos de alta energía (por encima de 100 MeV). Algunos de tales fenómenos se consideran fuentes garantizadas de neutrinos, porque existen fuertes evidencias de su existencia, y los flujos resultantes pueden ser predichos con precisión, pues no dependen de modelos específicos. Es el caso de los rayos cósmicos, que producen neutrinos al interaccionar con la atmósfera terrestre, con la atmósfera solar o con el medio interestelar. En el primer caso se habla de neutrinos atmosféricos, un fondo irreducible para los telescopios de neutrinos, cuyo flujo ha sido medido ampliamente por diversos experimentos y cuyo estudio ha proporcionado la primera evidencia indiscutible de la masa del neutrino (oscilaciones).

Por otra parte existen diversos modelos teóricos que predicen la producción de neutrinos de alta energía en muchos objetos astrofísicos. Tales fuentes no están garantizadas por la evidencia experimental, si bien la existencia de algunas de ellas es altamente probable, y los flujos predichos dependen del modelo teórico correspondiente. El estudio de estas fuentes constituye precisamente uno de los objetivos fundamentales de cualquier telescopio de neutrinos.

Es posible efectuar una clasificación de las fuentes probables en función de si los neutrinos tienen o no un origen acelerado:

- Cualquier escenario que prediga la aceleración de partículas cargadas a muy alta energía conlleva la producción de neutrinos cuando tales partículas interaccionan con un blanco de materia o radiación. Entre los principales candidatos que pueden producir señales detectables por un telescopio de neutrinos en este tipo de procesos se cuentan los sistemas binarios de rayos X, los restos de jóvenes supernovas cercanas, los núcleos galácticos activos (AGNs) y Blazars, la dispersión de los rayos cósmicos de alta energía con la radiación de fondo de microondas y los llamados *Gamma Ray Bursts* (GRBs), violentas explosiones capaces de emitir enormes cantidades de energía. Es posible, asimismo, que existan fuentes aún desconocidas de neutrinos de alta energía susceptibles de ser descubiertas por los nuevos telescopios.

- La detección de neutrinos de alta energía puede también señalar la existencia de nuevos fenómenos ajenos a los aceleradores cósmicos. Es el caso de la materia oscura no bariónica. Si existiera alguno de los candidatos propuestos para resolver este problema, conocidos genéricamente como WIMPs (*Weakly Interactive*

Massive Particles), con gran probabilidad daría lugar al desintegrarse a neutrinos detectables. Una de los candidatos a materia oscura es la partícula supersimétrica más ligera (LSP), que corresponde en muchos modelos al neutralino más ligero. De existir estas partículas y representar una fracción importante de la masa del halo galáctico, se acumularían en el centro de cuerpos masivos, como el Sol o la Tierra, donde se desintegrarían produciendo neutrinos, de modo que cabría esperar fuentes puntuales en el centro de estos cuerpos. Otras posibilidades involucran monopolos GUT, monopolos relativistas, SUSY Q-balls, cuerdas cósmicas, etc. Algunas de estas partículas, con masas por encima de 10^{14} eV están más allá de las energías alcanzables en cualquier acelerador terrestre. La detección de neutrinos provenientes de la desintegración de cualquiera de ellas sería una prueba de su existencia.

Telescopios de neutrinos

El principio de operación de los telescopios de neutrinos se basa en la detección de la radiación de Cherenkov producida por muones [5]. Los neutrinos muónicos de alta energía provenientes de fuentes cósmicas interaccionan eventualmente con nucleones presentes en la Tierra o en el medio detector, produciendo muones capaces de atravesar grandes distancias sin detenerse. Tales muones emiten luz de Cherenkov visible cuando atraviesan las grandes masas de agua o hielo utilizadas como blanco a una velocidad superior a la de la luz en el medio. Cuanto mayor es la energía del neutrino original, tanto mejor es la correlación entre las direcciones del neutrino y el muon resultante, de modo que la reconstrucción de la dirección del muon permite identificar asimismo la dirección original del neutrino.

Las dificultades técnicas a las que se enfrenta la astronomía de neutrinos son importantes. Por una parte, la baja sección eficaz de los neutrinos requiere la utilización de enormes blancos para conseguir una tasa de sucesos adecuada. Las estimaciones existentes de los flujos de neutrinos indican la necesidad de telescopios de áreas efectivas de km^2 para detectar fuentes puntuales. Por otra parte es necesario eliminar el fondo debido a muones de otros orígenes, cuyo flujo supera al de la señal en varios órdenes de magnitud. El empleo de medios naturales como volumen de detección plantea problemas específicos para cada experimento, en función de su emplazamiento particular.

Hoy en día la astronomía de neutrinos es un campo en rápido desarrollo, con una generación de nuevos telescopios de grandes áreas efectivas en construcción o en avanzado estado de diseño. La mayoría de ellos utilizan medios transparentes naturales en los cuales se sitúan sensores ópticos para detectar la luz de Cherenkov, aunque en los últimos años han aparecido nuevas iniciativas basadas en la detección por medio de microondas, ondas de radio y de sonido.

El experimento ANTARES

El experimento ANTARES (*Astronomy with a Neutrino Telescope and Abyss environmental RESearch*) pertenece a esta generación de nuevos telescopio de neutrinos. El detector se ubicará cerca de la costa sur de Francia, a unos 40 km de Tolón, y a una profundidad de 2400 m. El proyecto comporta una colaboración interdisciplinar que incluye a físicos, ingenieros, oceanólogos y astrónomos de Francia, Reino Unido, Alemania, España, Holanda, Italia y Rusia.

El detector ANTARES consiste en una serie de 12 líneas idénticas, cada una de las cuales soporta 75 fotomultiplicadores, junto con la electrónica asociada y los sistemas de posicionamiento. Cada línea está anclada al fondo marino y es mantenida en posición vertical por una boya unida a su extremo superior. La longitud instrumentada comienza a 100 m sobre el fondo y cubre unos 350 m. Las líneas estarán separadas entre sí por una distancia de unos 60 m. Todas ellas estarán conectadas a un único armario de conexiones (*junction box*) por el cual pasan todos los datos captados antes de ser transmitidos a la estación de tierra a través de un cable electro-óptico submarino de unos 40 km de longitud.

En la primera fase del proyecto se estudiaron los parámetros ambientales relevantes del lugar de emplazamiento del detector y se realizaron pruebas sobre diversos componentes mecánicos y electrónicos del detector. Asimismo, también se estudiaron y perfeccionaron las operaciones de despliegue y recuperación de las líneas. En la actualidad ANTARES se encuentra en fase de construcción del detector. Algunos elementos definitivos (*junction box*, cable principal) han sido ya instalados y se encuentran en operación. Se espera que la primera línea completa sea instalada en 2004 y que la construcción del detector finalice, y éste se encuentre operativo en el año 2006.

Objetivos

El objetivo principal de este trabajo es el estudio detallado de las prestaciones del detector ANTARES en cuanto a la búsqueda de fuentes puntuales.

En primer lugar se introduce una nueva estrategia de reconstrucción de sucesos que a pesar de haber sido definida originalmente para el caso de fuentes puntuales, se demuestra superior a la estrategia estándar en circunstancias más generales, especialmente en el rango de más alta energía.

Con este punto de partida se estudian las prestaciones esperadas del detector y se analizan las técnicas de búsqueda destinadas a detectar fuentes puntuales.

Algoritmos de reconstrucción

La reconstrucción de la traza de los muones en ANTARES se basa en el tiempo de llegada a los fotomultiplicadores de los fotones de Cherenkov directos. Estos son los primeros fotones que llegan procedentes de la traza del muon, y son los únicos que pueden relacionarse mediante una expresión sencilla con los parámetros de la traza.

Los fotones indirectos, retrasados por la dispersión en el agua o producidos por las cascadas hadrónicas o electromagnéticas, pueden alcanzar más tarde los módulos ópticos, conteniendo una información menos precisa sobre la traza. Al mismo tiempo pueden llegar a los fotomultiplicadores fotones correspondientes al fondo de ^{40}K, que carecen de correlación alguna con la traza y deben ser rechazados por los algoritmos de reconstrucción.

La diferencia entre el tiempo de llegada de un fotón de Cherenkov directo a un fotomultiplicador y el tiempo real de un *hit* (señal producida en un fotomultiplicador) depende de numerosos parámetros (los parámetros de la traza, la orientación del módulo óptico, las propiedades ópticas del agua, etc.). Utilizando la simulación de Monte Carlo se puede estimar la distribución de tales diferencias de tiempo para cualquier traza.

En ANTARES la estrategia de reconstrucción estándar comienza con un *pre-fit*, basado en coincidencias locales entre señales, que proporciona una primera estimación, habitualmente razonable, de los parámetros de la traza. A continuación se asigna a cada *hit* una probabilidad de provenir de dicha traza, a partir de las distribuciones de diferencias de tiempo calculadas con el Monte Carlo. De este modo se puede construir una función de verosimilitud $\mathcal{L}$ (*likelihood*). El programa de reconstrucción estándar busca el conjunto de parámetros de la traza que maximiza la verosimilitud.

En este trabajo proponemos una alternativa al *pre-fit* estándar diseñada para mejorar la eficiencia de la reconstrucción en el caso en que la dirección de procedencia del neutrino es conocida (fuentes puntuales) y por tanto también lo es, aproximadamente, la del muon. El algoritmo propuesto hace uso de las relaciones geométricas entre la traza y los *hits* de los fotones de Cherenkov, gracias al ángulo fijo ($\theta_C = 42.2°$) entre la dirección de los fotones y la del muon.

Más aún, la nueva estrategia puede ser ampliada para ser aplicable a un caso más general, sin información a priori sobre la dirección original del neutrino. Esto da lugar a una estrategia iterativa que constituye una alternativa ventajosa al *pre-fit* estándar.

El capítulo 3 de esta tesis describe detalladamente el *pre-fit* con tres parámetros y la estrategia iterativa, y muestra las ventajas de estas estrategias con respecto al *pre-fit* estándar, a partir de la comparación de los resultados obtenidos en cada caso.

Estudio de las prestaciones del detector

Independientemente de la estrategia utilizada para la reconstrucción, es necesario aplicar una serie de criterios de selección ("cortes") a los resultados a fin de eliminar los sucesos mal reconstruidos. Los cortes a aplicar dependen de la estrategia particular.

Para completar la nueva técnica de reconstrucción introducida por la estrategia iterativa, hemos explorado diversos conjuntos de parámetros a fin de elegir los cortes que garanticen una mejor eliminación del fondo atmosférico (muones descendentes) manteniendo el máximo número posible de sucesos de señal.

Una vez determinado el conjunto de cortes a utilizar, es posible comparar resultados obtenidos utilizando la nueva estrategia de reconstrucción con los de la reconstrucción estándar. En particular es posible comparar las prestaciones del detector relativas a la reconstrucción utilizando cada una de las estrategias. Tales prestaciones se expresan fundamentalmente en términos de dos parámetros:

- área efectiva, el área efectiva para neutrinos (muones) mide la eficiencia del detector y representa la extensión que tendría una superficie plana de eficiencia 100% que observase el mismo número de neutrinos (muones) atravesándola. Esta cantidad, independiente del flujo incidente, es función de la energía y de la dirección del neutrino.

- resolución angular, la resolución angular para neutrinos (muones) es la mediana de la distribución del ángulo entre las direcciones de la traza reconstruida y la traza del neutrino (muon). La resolución angular para muones es la que realmente describe el comportamiento del detector, puesto que la resolución para neutrinos incluye el inevitable ángulo entre el neutrino y el muon que produce.

Ambas cantidades han sido calculadas, tanto para neutrinos como para muones, utilizando tanto la estrategia de reconstrucción estándar como la nueva. El estudio de los resultados permite una comparación de ambas reconstrucciones independiente del flujo.

Las prestaciones reales del detector, es decir, el número esperado de sucesos detectados y la resolución angular para los mismos, se obtienen convolucionando las magnitudes anteriores con el flujo de neutrinos. Para el cálculo de estas cantidades se ha utilizado por una parte el flujo predicho de neutrinos atmosféricos, por tratarse de la fuente de sucesos más segura en un telescopio de neutrinos, y por otra un flujo isótropo difuso de distribución en energía E^{-2}, como correspondería a una fuente astronómica.

Para completar el análisis de la nueva estrategia iterativa para la reconstrucción, se ha estudiado el efecto que tiene sobre las prestaciones del detector la variación de algunos parámetros ambientales, en concreto la dispersión de los fotones en el agua en función de su diferente longitud de onda y la difusión. Esto nos proporciona una mejor comprensión de la dependencia que la estrategia de reconstrucción presenta respecto a estos parámetros, para los cuales el Monte Carlo asume implícitamente modelos o valores que podrían diferir de los reales.

El capítulo 4 de la tesis describe detalladamente los criterios de selección utilizados para cada estrategia, así como la comparación de las prestaciones esperables en cada caso.

Fuentes puntuales

Uno de los objetivos principales de cualquier telescopio de neutrinos es el estudio de las posibles fuentes puntuales de neutrinos de alta energía. Por una parte, el análisis de los objetos astronómicos que se consideran candidatos a fuentes puntuales de neutrinos puede permitir discriminar entre los modelos teóricos que predicen para ellos flujos diversos. Por otra parte, es preciso analizar la sensibilidad del detector a fuentes puntuales insospechadas.

Los sucesos provenientes de una fuente puntual serán indistinguibles de otros sucesos ascendentes presentes en el detector (neutrinos atmosféricos, flujos difusos, sucesos mal reconstruidos), que actúan como fondo físico irreducible para esta búsqueda. El análisis de los datos para distinguir los sucesos de interés ha de basarse por tanto en la distribución de los mismos.

La detección de una fuente vendrá determinada por la acumulación inesperada de sucesos en una región del cielo. Asimismo, en caso de no obtenerse ninguna señal procedente de estas fuentes, el detector podrá establecer límites sobre los flujos correspondientes.

En este trabajo se han empleado dos métodos de *binning*, es decir, división del cielo visible en bines que se estudian individualmente para detectar la presencia de una fuente. La ventaja de tales métodos es que se basan únicamente en el análisis estadístico de los datos y, a diferencia de otras técnicas de búsqueda, no precisan un conocimiento exhaustivo del fondo o del comportamiento del detector, y no dependen de las incertidumbres en parámetros físicos (como flujos o secciones eficaces). Además estas técnicas aprovechan la distribución uniforme en ascensión recta de los sucesos del fondo.

Las técnicas de *binning* son técnicas robustas que se basan en agrupar los sucesos detectados de manera que una fuente puntual suficientemente intensa aparecerá como un *bin* que contiene un exceso significativo de sucesos. La significancia del exceso se determina a partir de un análisis estadístico de los datos empleando la distribución (aleatoria) de los sucesos de fondo. Por ello, son los propios datos los que indican si existe o no una fuente puntual, independientemente de modelos e hipótesis sobre el fondo o la señal.

Se ha llevado a cabo un cuidadoso estudio encaminado a optimizar las técnicas anteriores para la detección de fuentes puntuales en ANTARES, mediante una adecuada elección del tamaño y la forma de los bines. Para este análisis se ha hecho uso de datos del Monte Carlo, al igual que para el estudio del potencial de descubrimiento de una fuente puntual.

Los capítulos 5 y 6 de la tesis presentan los métodos analizados para la búsqueda de fuentes puntuales, y los análisis realizados para optimizar estas técnicas. Asimismo se presentan los resultados obtenidos en cuanto a sensibilidad del detector y los límites (en ausencia de señal) que mediante estas técnicas podría establecer sobre los flujos el detector ANTARES tras diferentes periodos de toma de datos.

Discusión de los resultados

Nueva estrategia de reconstrucción

La traza del muon queda determinada por cinco parámetros: las coordenadas (x, y) en que la traza corta a un plano de referencia perpendicular (que se escoge arbitrariamente como aquel que pasa por el centro del detector), el instante de tiempo en que el muon atraviesa dicho plano, y los ángulos (θ, ϕ) que determinan su dirección.

Si la dirección es conocida, el problema se puede reducir a uno en dos dimensiones proyectando los *hits* sobre el plano de referencia. La determinación espacial de la traza se reduce entonces a la del punto $(x,\, y)$.

Dado un par de *hits* se define la cantidad Δr_{ij} como la diferencia entre las distancias, medidas sobre el plano de referencia, entre dichos *hits* y la traza. El punto $(x,\, y)$ se encuentra sobre una hipérbola determinada por Δr_{ij} y que tiene por focos a las proyecciones de ambos puntos. Combinando tres *hits* se encuentra una segunda hipérbola y es posible determinar los puntos de corte entre ambas. Finalmente, utilizando diferentes combinaciones de tres *hits* se construye un histograma que permite determinar el punto $(x,\, y)$ con considerable precisión.

A partir de los valores de $(x,\, y)$ es posible calcular un valor del quinto parámetro t_0 para cada *hit* individual. Con los valores calculados se construye un histograma que muestra un pico muy estrecho, lo cual permite no solo calcular el valor de t_0, sino también realizar una selección de los *hits* antes de aplicar el ajuste completo.

Los resultados demuestran que el nuevo *pre-fit* permite reconstruir con gran precisión la dirección de la traza en la mayoría de los casos. También en el caso en que la dirección conocida no es la del muon, sino la del neutrino original (como ocurriría en el caso de conocer la dirección de un conjunto de fuentes puntuales) la reconstrucción es mucho mejor que la obtenida con el *pre-fit* estándar.

Al aumentar el número de *hits*, la cantidad de combinaciones a realizar para el *pre-fit* anterior, y con ella el coste computacional del método, se dispara. Por esta razón hemos desarrollado una estrategia (*hit cleaning*) para descartar el máximo número de *hits* que no provienen de fotones de Cherenkov directos. Aplicando esta técnica antes del *pre-fit* se consigue reducir en aproximadamente una tercera parte el tiempo de computación, sin degradar los resultados del *pre-fit*. Al contrario, en la mayoría de los casos, el *pre-fit* obtiene un mayor porcentaje de sucesos reconstruidos, gracias a la mejor calidad de los *hits* utilizados.

Para ampliar el ámbito de utilización de esta técnica a sucesos cuya dirección no es conocida a priori, se utiliza una estrategia iterativa. Para ello, se realiza un barrido del espacio de parámetros $(\theta,\, \phi)$ alrededor de unos valores iniciales seleccionados por el *pre-fit* estándar y se escoge aquella dirección para la cual el *pre-fit* selecciona un mayor número de *hits*. A continuación se inicia un proceso iterativo en el cual se alternan dos fases:

- en la primera se calculan los parámetros $(x,\, y,\, t_0)$ aplicando el *pre-fit* anterior con la dirección seleccionada;
- en la segunda se realiza un ajuste estándar, pero manteniendo constantes los valores de $(x,\, y,\, t_0)$, lo cual proporciona los valores de $(\theta,\, \phi)$.

El proceso finaliza cuando los valores θ, ϕ convergen. El conjunto definitivo de parámetros que se utiliza como entrada para la rutina de reconstrucción completa se obtiene finalmente aplicando una última iteración en la que se varían los cinco parámetros, y que utiliza los *hits* seleccionados por la estrategia de *pre-fit*.

El análisis de los resultados muestra que la nueva estrategia de reconstrucción (que hemos llamado *estrategia iterativa*) obtiene una mejor aproximación a los valores verdaderos de los parámetros de la traza en un porcentaje más alto de los sucesos reconstruidos que el *pre-fit* estándar. Sin embargo, se observa también que, cualquiera que sea el *pre-fit* empleado, no todos los sucesos pueden ser reconstruidos correctamente y siempre existe una fracción de sucesos mal reconstruidos que es deseable descartar.

Para ello, es necesario definir cuidadosamente los criterios de selección a aplicar tras la reconstrucción, a fin de eliminar los sucesos mal reconstruidos. Los cortes a aplicar dependen de la estrategia utilizada para la reconstrucción.

Prestaciones esperadas del detector

Si se comparan los resultados para la resolución angular de muones, es decir el ángulo entre la traza real y la reconstruida obtenidos mediante la estrategia iterativa y la estándar antes de aplicar ningún criterio de selección posterior, se observa que la resolución angular es mejor en el caso de la estrategia iterativa. Sin embargo, esta técnica también reconstruye un mayor número de eventos incorrectos a 2 θ_C, el doble del ángulo de Cherenkov[1].

Para poder comparar en pie de igualdad las prestaciones obtenibles utilizando ambas técnicas es necesario aplicar en cada caso los cortes adecuados para seleccionar los sucesos reconstruidos de calidad aceptable.

Los criterios de selección escogidos para la estrategia iterativa están basados en los criterios de selección estándar, que consiguen una buena resolución angular pero fallan al rechazar los sucesos de fondo atmosférico. Por esta razón, en el caso de la estrategia iterativa se han optimizado algunos de los cortes estándar y se ha añadido un nuevo parámetro a fin de distinguir los sucesos falsamente reconstruidos como ascendentes. El conjunto de cortes final, escogido tras estudiar diversas posibilidades, consigue rechazar prácticamente todo el fondo de sucesos atmosféricos mientras preserva la mayoría de los sucesos bien reconstruidos. Asimismo se ha comprobado que el conjunto de cortes utilizado no introduce ningún sesgo apreciable en los resultados.

Aplicando ambas estrategias de reconstrucción a las muestras disponibles de muones atmosféricos se comprueba que los cortes de la estrategia estándar no son suficientes para eliminar los sucesos de fondo reconstruidos erróneamente como ascendentes y evitar que dominen por encima de cualquier otra fuente de sucesos ascendentes. Este resultado demuestra la necesidad de restringir los cortes de selección estándar para eliminar el fondo atmosférico. Por otra parte, la estrategia iterativa, optimizada para reconstruir sucesos ascendentes, ofrece una natural protección contra este tipo de fondo, pero a cambio no es apta para estudiar flujos descendentes.

Los resultados de la comparación de las áreas efectivas muestran que la nueva estrategia de reconstrucción proporciona un aumento considerable de las prestaciones.

[1] Algunos sucesos tienden a ser reconstruidos a 2 θ_C de la traza verdadera por ser esta una solución matemáticamente válida desde el punto de vista de la distribución temporal.

Tanto el área efectiva para neutrinos como para muones presentan un incremento notable al utilizar la nueva estrategia de reconstrucción, especialmente a altas energías ($E_\nu > 100$ TeV) donde el aumento es en general superior al **100%**.

La comparación de los resultados obtenidos para la resolución angular con ambas estrategias demuestra que para energías por debajo del TeV las dos técnicas producen resultados muy similares para neutrinos, mientras que para muones la estrategia iterativa es ligeramente mejor. La diferencia es mucho más significativa para altas energías. Así, para la estrategia estándar la mejor resolución angular que se obtiene para muones es $0.4°$, correspondiendo a una energía de ~ 0.6 PeV. Para la estrategia iterativa, en cambio, los mejores resultados se obtienen cuanto mayor es la energía de las trazas, siendo mejor que $< 0.15°$ para $E_\nu > 10$ PeV.

La convolución de los resultados anteriores con el flujo previsto para neutrinos atmosféricos y para fuentes astronómicas permite estimar las prestaciones reales del detector con la señal que esperamos detectar. Los resultados obtenidos, que demuestran que la estrategia iterativa reconstruye mayor número de sucesos y logra una mejor resolución angular, se resumen en la siguiente tabla:

	flujo atmosférico		**flujo** $E^{-2.0}$	
estrategia	$N_{sucesos}$/año	res. angular	$N_{sucesos}$/año	res. angular
estándar	760.4	0.7°	6.8	0.5°
iterativa	1832.6	0.5°	14.5	0.3°

La tabla anterior recoge los resultados tanto para el flujo de neutrinos atmosféricos (una fuente garantizada de neutrinos) como para un flujo de neutrinos con un índice espectral de 2.0 y una normalización correspondiente al límite superior de Waxman y Bahcall [6].

Aunque generalmente los programas de Monte Carlo simulan la propagación de los fotones en la materia utilizando su velocidad de fase, un tratamiento correcto debe usar la velocidad de grupo. Para estudiar en qué medida afecta este parámetro a la reconstrucción se han comparado los resultados obtenidos considerando o no la velocidad de grupo en el Monte Carlo y en la reconstrucción. Se observa un sensible empeoramiento en número de sucesos reconstruidos y resolución angular cuando la reconstrucción no tiene en cuenta el valor correcto de la velocidad de los fotones. Sin embargo, aún en este peor caso, la reconstrucción iterativa supera a la estándar y se ve menos afectada por las variaciones en la velocidad de los fotones.

Para completar el estudio de la reconstrucción se ha estudiado su comportamiento cuando se utilizan en la simulación distintos modelos de dispersión de la luz en el agua, lo cual da idea de la sensibilidad del método a posibles indeterminaciones en los parámetros. Los resultados muestran que cuanto más dispersivo sea el medio, tanto peor son los resultados obtenidos tras la reconstrucción. Aún así, para todos los modelos de dispersión estudiados se cumple que los resultados de la estrategia iterativa son superiores a los resultados obtenidos con la estrategia estándar con el modelo de dispersión de referencia, tanto en términos de áreas efectivas como, sobre todo, en términos de resolución angular.

Búsqueda de fuentes puntuales

Para la búsqueda de fuentes puntuales hemos utilizado dos técnicas de *binning*:

- Con el método de **grid** (cuadrícula) el cielo se divide en una cuadrícula en coordenadas de declinación y ascensión recta, de manera que se cuenta el número de sucesos contenido dentro de cada recuadro de esa cuadrícula.

- Con el método de **cluster** (acumulación) se construye un cono de un cierto radio alrededor de cada uno de los sucesos de la muestra a estudiar y se cuenta el número de sucesos contenidos dentro de cada cono.

La significancia de cada bin o cono (probabilidad de que el fondo haya producido aleatoriamente el número observado de sucesos) se calcula de forma ligeramente diferente en cada caso. En el caso del *grid*, teniendo en cuenta que el fondo está uniformemente repartido en ascensión recta, se calcula la probabilidad de que el fondo produzca el reparto de sucesos observado entre todos los bines que hay en una misma banda de declinación. En el caso de los conos, se calcula la probabilidad de que el fondo produzca aleatoriamente el número observado de sucesos en cada cono.

A partir de las significancias (logaritmos de los niveles de confianza) calculadas para cada bin o cono, se definen unos criterios que permiten separar las acumulaciones fortuitas de sucesos de las acumulaciones producidas verdaderamente por una fuente puntual. El criterio que hemos utilizado habitualmente para decidir la detectabilidad de una fuente exige que el número de sucesos seleccionados que han sido emitidos por la fuente garantice una probabilidad de al menos el 50% de ver en un bin o en un cono un exceso cuya probabilidad de ser producido por el fondo sea menor de 3σ. Sin embargo, también se han calculado otras combinaciones como, por ejemplo, probabilidades del 90% de ver la fuente o probabilidades de que el fondo produzca un exceso de 2σ ó 5σ.

Ambas técnicas han sido aplicadas a una muestra generada por Monte Carlo y correspondiente a los sucesos garantizados en un año de toma de datos. La contribución principal a la muestra, por tanto, es la de neutrinos y antineutrinos atmosféricos, si bien habrá también contribuciones de otro origen, como muones atmosféricos mal reconstruidos o sucesos debidos al flujo difuso de neutrinos, aunque en mucha menor medida. La muestra utilizada para optimizar los métodos de *binning* está compuesta exclusivamente por fondo. Para estudiar las prestaciones en cuanto a búsqueda, sin embargo, se le añaden sucesos de señal correspondientes a fuentes puntuales. Los sucesos correspondientes a tal fuente tendrán una cierta distribución en energía dependiente del índice espectral. Las técnicas se han optimizado para un índice espectral $\gamma = 2.0$, puesto que para un índice espectral mayor el flujo de neutrinos de alta energía cae rápidamente y el potencial de detección es mucho menor, aunque el número de sucesos en la muestra requerido para una detección no depende apenas de γ.

Para optimizar las técnicas de búsqueda se ha estudiado el porcentaje de éxito en la detección de la fuente puntual simulada por el Monte Carlo para diferentes elecciones del único parámetro libre del *grid* o el *cluster*. Se considera que el método tiene éxito en la detección si el bin que resulta con mayor significancia identifica correctamente la posición de la fuente simulada. Hemos encontrado así los mejores parámetros para construir tanto el *grid* como los conos que permitan detectar la fuente con el menor número posible de sucesos de señal, y se ha determinado cuál es este número mínimo de sucesos que la fuente debe emitir para ser detectada. Sin embargo no existe una misma cuadrícula o un mismo conjunto de conos óptimo para todas las declinaciones simultáneamente. Por ello, hemos escogido un *grid* y un conjunto de conos que en conjunto proporcionan los resultados óptimos para ambas técnicas, puesto que las diferencias debidas a pequeñas variaciones de los parámetros no son importantes, siempre que la elección esté próxima a los valores óptimos.

El número medio de sucesos necesario en una muestra de un año para alcanzar el criterio del 50%-3σ con las distintas técnicas aparece recogido en la siguiente tabla:

$\delta(°)$	***Grid***	***Cluster***
$-73.4°$	8.4	8.7
$-28.9°$	7.3	7.0
$+39.8°$	5.7	5.6

Esta tabla muestra que los resultados obtenidos por ambas técnicas son casi idénticos, lo que demuestra la correcta optimización de ambas, y asegura que se alcanzan las mejores prestaciones, independientemente de la técnica de análisis empleada.

El número medio de sucesos/año requerido para un descubrimiento puede reducirse si se incrementa el tiempo de observación. Si se pasa de uno a tres años de observación el número de sucesos/año necesario se reduce en un factor ~ 2.3. Si se pasa de uno a cinco años de observación, entonces el factor de reducción es ~ 3.4.

Los resultados anteriores indican que solo fuentes muy potentes podrán ser detectadas por ANTARES. Sin embargo, aun cuando el flujo individual de cada fuente sea tan pequeño que no es posible detectarlas individualmente, es posible utilizar el efecto combinado de varias de ellas para detectar un exceso significativo. Este análisis se lleva a cabo utilizando el método de *cluster*. En efecto, existen determinados objetos astronómicos que se consideran posibles fuentes de neutrinos de alta energía. Es posible utilizar una lista de tales fuentes candidatas para buscar cuál es el número total de sucesos en los conos dibujados a su alrededor, y determinar la probabilidad de que tal número venga producido por el fondo, así como el número mínimo de sucesos necesarios para producir un exceso suficientemente significativo. El estudio se ha realizado sobre la lista de 49 fuentes candidatas (emisores conocidos de rayos gamma) visibles desde ANTARES y sobre un subconjunto de las mismas formado por las 13 fuentes que han demostrado experimentalmente ser emisoras de rayos gamma de energía superior al TeV (consideradas fuentes más probables de neutrinos de alta energía). Se observa que cuanto mayor es el número de fuentes empleadas menor es el número de sucesos/fuente necesario, sin embargo también es mayor el fondo y, globalmente, el número total de sucesos requerido es mayor.

Límites a los flujos

Cuando no se encuentra una fuente puntual es posible dar un límite máximo al flujo que no se ha podido detectar, sea en una región del cielo cubierta por un bin de la cuadrícula para el método de *grid* o en un cono alrededor de una fuente candidata. Dicho límite se calcula usando el valor medio de las áreas efectivas en el rango de sensibilidad del detector, la visibilidad de la fuente (porcentaje de tiempo que la fuente se encuentra bajo el horizonte) y la eficiencia de recolección de la señal en el bin o cono.

En el caso de los áreas efectivas para neutrinos, para obtener un área efectiva promedio es necesario convolucionar el espectro de neutrinos (isótropo y caracterizado por un índice espectral entre 2 y 3) con el área efectiva para neutrinos. En el caso de los muones, es necesario utilizar el flujo de muones en el detector. Sin embargo, esta cantidad no es conocida de antemano y es necesario primero deducirla a partir del número de sucesos detectados y del área efectiva para muones. Cada flujo de neutrinos produce un flujo distinto de muones en el detector y cada flujo de muones es convolucionado con el área para muones para proporcionar un valor promedio para el flujo de muones correspondiente. Todos estos cálculos son realizados utilizando histogramas en tres dimensiones (θ, ϕ, E) tanto de los flujos, como de las áreas efectivas. Los resultados muestran que, independientemente del índice espectral, cuanto mayor es la declinación, menor es el área efectiva, salvo por un incremento en el rango entre $\delta = -45°$ y $\delta = -10°$.

Por su parte, la visibilidad de una región del cielo se calcula utilizando funciones astronómicas que nos permiten convertir de coordenadas ecuatoriales (δ, AR) a coordenadas locales (θ, ϕ) en el detector. La visibilidad sólo depende de la declinación de la fuente y de la latitud del detector. En el caso de ANTARES todas las fuentes con declinaciones menores de $-42°$ son visibles el 100% del tiempo, disminuyendo la visibilidad al aumentar la declinación hasta llegar a cero en $\delta = +48°$.

Por último, es necesario conocer las eficiencias de bines y conos recogiendo los neutrinos procedentes de fuentes situadas en la región del cielo que cubren. Este parámetro viene dado tanto por el ángulo físico irreducible entre el neutrino y el muon como por el error introducido en la reconstrucción de la traza del muon. También se puede hablar sólo de eficiencia para muones y en tal caso sólo se tiene en cuenta el ángulo debido a la reconstrucción. Tanto para neutrinos como para muones, las eficiencias aumentan al aumentar la declinación debido sobre todo al tamaño distinto de los bines y conos en función de la declinación. En conjunto, el efecto de la visibilidad de la fuente y del área efectiva se cancela, al menos parcialmente, con el efecto de la eficiencia.

Al igual que en las búsquedas, antes de calcular los límites es necesario encontrar la mejor cuadrícula y los mejores conos para hacerlo. En este caso el criterio de elección se basa en la razón señal/fondo (S/F), dada por el cociente entre la eficiencia de los bines o conos y el límite superior que se calcula con el número observado de sucesos y el fondo promedio. Este límite se calcula utilizando el método de Feldman y Cousins [7] a un nivel de confianza del 90%. Dicho valor proporciona un límite superior a la señal estadísticamente aceptable cuando se observan N_0 sucesos y se esperan N_{bf} sucesos de fondo. La optimización se ha realizado para un índice espectral $\gamma = 2.0$. Sin embargo, tanto la cuadrícula óptima como los conos óptimos no son muy diferentes si γ varía, por lo que se pueden utilizar los mismos en el rango $\gamma = 2.0 - 3.0$. Sin embargo, el valor óptimo de la razón S/F sí disminuye cuando γ aumenta.

El *grid* óptimo determinado se aplica a la muestra de Monte Carlo para establecer un límite sobre el flujo en todo el cielo visible. El método no precisa ningún conocimiento previo sobre la distribución del fondo, puesto que el número de sucesos esperado en un bin se calcula directamente a partir de los datos, aprovechando el hecho de que la distribución del fondo es uniforme en ascensión recta. Para cada bin de la cuadrícula se determina un límite superior para el flujo. Esta cantidad es un límite sobre el flujo integral en el rango de energías estudiado, y representa la máxima señal admisible de acuerdo con la señal observada, que puede emitir una fuente desconocida localizada en ese bin. Se observa que los límites alcanzables son peores para los bines de mayor declinación. La comparación de los límites calculados con los resultados de AMANDA indican que ANTARES podrá estudiar un rango mayor de declinaciones con una sensibilidad que es mucho mayor que la de AMANDA-B10 (aunque obviamente en el caso de ANTARES se trata de una simulación y en el caso de AMANDA-B10 son datos reales) y que es comparable o mejor, dependiendo de la declinación, que la del detector AMANDA-II.

Por otro lado, cuando se conoce la posición de una posible fuente de neutrinos de alta energía, se puede utilizar el método de *cluster* para establecer un límite superior sobre el flujo emitido por dicha fuente. La sensibilidad de este tipo de límite es superior a la de los límites sobre todo el cielo, gracias al conocimiento de la posición de la fuente. Se ha estudiado el resultado obtenido mediante la aplicación del método de *cluster* a cada una de las 49 posibles fuentes antes mencionadas. Cada límite obtenido es únicamente aplicable a una dirección o posible fuente. Los valores calculados se han comparado con los límites establecidos por otros experimentos. Así, se encuentra que los límites alcanzables por ANTARES son mejores que los establecidos por los otros detectores, en el rango en que sus regiones de visibilidad se solapan. Sin embargo, hay que señalar de nuevo que los resultados obtenidos para ANTARES corresponden solamente a la simulación Monte Carlo, y no a datos reales.

Tanto en el caso de los límites para todo el cielo como en el caso de los límites para fuentes puntuales, al incrementar el tiempo de observación se incrementa su sensibilidad. Sin embargo, este aumento no es equivalente al incremento de tiempo y así se tiene que los límites son un factor ~ 2.5 mejores tras tres años de toma de datos y un factor ~ 3.9 tras cinco años de toma de datos.

Se ha calculado también el flujo mínimo (en términos de neutrinos y muones) que debe emitir una fuente puntual para ser descubierta por ANTARES. El estudio se ha realizado mediante el método de *grid* y el de *cluster*, y se han encontrado para ambos métodos resultados muy similares. Ello es consecuencia de que el número mínimo de sucesos necesario, como se vio anteriormente, es casi el mismo. Se han comparado los resultados utilizando diversos criterios para decidir si se trata de una fuente real o de una fluctuación estadística, y se observa que, con independencia de los criterios fijados, el comportamiento en función de la declinación es similar. Por otra parte, con independencia de la declinación, es menos exigente incrementar de 3σ a 5σ la significancia necesaria para considerar que se trata de un descubrimiento que incrementar la probabilidad de descubrimiento del 50% al 90%.

Finalmente, por comparación con los límites para fuentes puntuales y para tener una idea mejor de la magnitud de los límites, hemos calculado el límite para flujos difusos de neutrinos de altas energías. En este caso, la estrategia es muy diferente porque los sucesos de señal no pueden ser distinguidos del fondo por su distribución angular ya que llegan isótropamente de todo el cielo visible. Para separar señal del fondo se utiliza la energía de los sucesos. Los sucesos de fondo provienen principalmente de los neutrinos atmosféricos que presentan una caída muy rápida de su flujo con la energía. Mientras, la señal viene dada por un flujo isótropo de neutrinos con un espectro en energía caracterizado por un índice espectral que típicamente se asume que es 2.0 ($\Phi_\nu \propto E^{-2}$). Por tanto, existirá una energía por encima de la cual la señal domina sobre el fondo.

En este caso, para calcular los límites hemos empleado una técnica utilizada en la colaboración AMANDA que permite calcular un valor medio del límite al flujo. Ese sería el valor medio que se obtendría si se repitiera el experimento muchas veces. Para ello se necesita conocer el fondo medio y la señal.

Es necesario, como de costumbre, encontrar un corte que nos proporcione un número óptimo de sucesos de señal y de fondo, de manera que el límite sea el mejor posible. Utilizando la energía reconstruida como parámetro, se puede hacer un corte adicional en los sucesos seleccionados tras la reconstrucción. De esta manera podemos seleccionar sucesos con una energía reconstruida mayor o igual que la de corte.

Utilizando el Monte Carlo, hemos calculado un límite al flujo de neutrinos difusos empleando el número de sucesos de fondo y de señal que pasan cada corte empleado. Así, hemos podido determinar que el valor óptimo de corte en la energía reconstruida es 10^5 GeV, que coincide con la energía en la que los sucesos de señal empiezan a ser más importantes que el fondo de neutrinos atmosféricos. El mejor límite al flujo que se obtiene es $E^2\,\bar{\Phi}^{limit}_{90\%}(E) = 8.8 \times 10^{-8} cm^{-2}s^{-1}sr^{-1}GeV$, tras un año de toma de datos. Este resultado es sensiblemente mejor que el de AMANDA B-10, que era de $10^{-6}cm^{-2}s^{-1}sr^{-1}GeV$ para 130.1 días de toma de datos [8], y comparable al resultado de AMANDA-II de $\sim 2 \times 10^{-7}cm^{-2}s^{-1}sr^{-1}GeV$ tras 197 días de datos [9,10]. Si bien, hay que recordar una vez más que en el caso de ANTARES no se trata de datos reales sino de simulaciones Monte Carlo.

Conclusiones

Tras completarse con éxito la fase de I+D, el telescopio de neutrinos ANTARES se encuentra ya en fase de construcción. En los próximos años se completará la instalación del telescopio. Ese será el momento de aplicar las técnicas desarrolladas en el presente trabajo a los datos reales tomados por el detector. Por el momento, sin embargo, se ha procurado desarrollar técnicas robustas que no dependan excesivamente del conocimiento detallado que se tenga del detector ni de ninguna hipótesis o modelo adicional.

El diseño final del detector, optimizado para neutrinos astronómicos de alta energía, permitirá asimismo llevar a cabo estudios sobre oscilaciones de neutrinos, candidatos a materia oscura y flujo de neutrinos atmosféricos. Para todos estos análisis es crucial la eficiencia y precisión de la reconstrucción de sucesos en el detector. En este trabajo hemos desarrollado una nueva estrategia de reconstrucción que mejora las prestaciones de la reconstrucción respecto a las obtenidas utilizando la estrategia estándar.

Esta reconstrucción también se ha aplicado a la búsqueda de fuentes puntuales de neutrinos astronómicos en combinación con dos técnicas de *binning* que nos permiten tanto realizar búsquedas como establecer límites a los flujos en caso de no detectar fuentes.

Una nueva estrategia de reconstrucción

Utilizando las relaciones geométricas entre la traza y los fotones Cherenkov, hemos desarrollado una técnica que permite relacionar entre sí los parámetros de la traza. Conocida la dirección del muon y utilizando la información de los *hits* producidos, esta técnica permite obtener los otros 3 parámetros que definen la traza. Sobre la base de este resultado hemos creado una nueva estrategia de reconstrucción que permite obtener los 5 parámetros de la traza utilizando un método iterativo que recurre a dichas relaciones geométricas.

Junto con la nueva estrategia de reconstrucción se han desarrollado unos nuevos criterios de selección cuyo objetivo es rechazar aquellas trazas que no han sido bien reconstruidas. En la práctica, los cortes de selección han sido elegidos de manera que eliminen la mayor cantidad posible de fondo atmosférico (sucesos descendentes) a la vez que se conserva el máximo número de sucesos de señal (ascendentes). Los cortes de selección propuestos no sesgan los datos y permiten eliminar el fondo atmosférico.

Posteriormente, hemos realizado una comparación entre los resultados obtenidos con la nueva estrategia tras aplicar dicha selección y los producidos por la estrategia estándar con su selección correspondiente. Las conclusiones más importantes son las siguientes:

- Tanto el fondo de muones como el de multi-muones atmosféricos pueden ser perfectamente controlados con los cortes de selección definidos para la estrategia estándar. Sin embargo, en el caso de la reconstrucción y selección estándar, el fondo atmosférico es demasiado alto y dominaría sobre los sucesos que sí son realmente ascendentes, por lo que la selección estándar debe ser endurecida.

- Tanto el área efectiva de neutrinos como la de muones experimentan una notable mejora cuando la estrategia aplicada es la iterativa, especialmente para los valores más altos de la energía. El incremento supera el **100%** a energías por encima de 100 TeV.

- La resolución angular obtenida con la nueva estrategia es notablemente mejor que la de la estrategia estándar. El mejor valor obtenido con la estrategia estándar era de **0.4**° y empeoraba al aumentar la energía por encima de 1 PeV. Con la nueva estrategia, en cambio, la resolución angular mejora con la energía y el mejor valor, **0.15**°, se obtiene a la máxima energía simulada.

- Al comparar las prestaciones de las reconstrucciones con un flujo de neutrinos dado, se observa que la nueva estrategia reconstruye un **140%** más de neutrinos atmosféricos y un **100%** de sucesos de un flujo E^{-2} que la estrategia estándar. Respecto a la resolución angular, el promedio para neutrinos atmosféricos es de **0.64**° en la estándar y de **0.48**° en la iterativa. A su vez, para el flujo E^{-2} los valores son **0.49**° y **0.26**° respectivamente.

- También se ha estudiado cómo afecta a la reconstrucción la variación del índice de refracción del agua. Cuando el índice de refracción es distinto en la reconstrucción que en la simulación porque no se tiene en cuenta el efecto de la velocidad de grupo, entonces la estrategia estándar pierde un **30%** de área efectiva frente al **15%** perdido por la nueva estrategia. El efecto sobre la resolución angular es más importante. La mejor resolución angular se alcanza en ambas reconstrucciones entre 10^3 y 10^4 GeV y es de 0.8° para la reconstrucción estándar y de 0.6° para la nueva. Encontramos que, en cualquier caso, la nueva estrategia es superior a la estándar. Si el índice de refracción coincide en la simulación y en la reconstrucción se vuelve a la situación inicial y los resultados solo varían ligeramente al variar el índice espectral.

- Por último, se ha estudiado la variación de las prestaciones de la nueva reconstrucción con distintos modelos de dispersión de la luz. Se observa que cuanto más dispersivo es el medio peores son las prestaciones de la reconstrucción. Sin embargo, las diferencias con respecto al modelo de referencia sólo son importantes en los casos más extremos. Aún en el caso más pesimista, la nueva reconstrucción es superior a la reconstrucción estándar con el modelo de referencia.

Por tanto, la nueva reconstrucción no sólo es una alternativa perfectamente válida a la reconstrucción estándar, sino que permite mejorar considerablemente las prestaciones del detector y a la vez eliminar prácticamente todo el fondo de sucesos atmosféricos.

Búsqueda de fuentes puntuales de neutrinos

En primer lugar hemos realizado una búsqueda *ciega* de fuentes puntuales con dos técnicas de binning, la técnica de *cluster* y la técnica de *grid*. Tanto la cuadrícula de la técnica de grid como el tamaño de los conos en la técnica de cluster han sido optimizados para la detección de una señal con índice espectral de 2.

Con la cuadrícula y conos óptimos, los resultados más importantes obtenidos en las búsquedas son los siguientes

- La probabilidad de detectar una fuente puntual a un cierto nivel de confianza aumenta rápidamente con el número de sucesos emitidos por la fuente. El número mínimo de sucesos en la muestra procedentes de la fuente que son necesarios para un descubrimiento (3σ) se sitúa entre **8.5** ($\delta = -73.4°$) y **5.6** ($\delta = +39.8°$).

- Los resultados obtenidos con las técnicas de cluster y de binning son prácticamente iguales. Una vez optimizados ambos métodos, se alcanza un límite común en las búsquedas que no depende de la técnica particular que se emplee.

- Al aumentar el tiempo de toma de datos se mejora sensiblemente la sensibilidad de ambas técnicas, aunque en un factor menor que el factor de aumento en el tiempo. El incrementar el tiempo de toma de datos de 1 a 3 años representa una mejora en la sensibilidad de un factor **2.3**. Para 5 años de toma de datos el aumento es un factor **3.3**.

- Cuando se busca el efecto combinado de varias fuentes, se encuentra que el número de sucesos por fuente y año necesario para encontrar un exceso significativo es menor, pero no así el número total de sucesos. Al aumentar el número de fuentes candidatas, baja el número de sucesos por fuente necesario, pero aumenta el número total.

Por último, en el caso de que no se encuentre una fuente de neutrinos, las mismas técnicas pueden ser utilizadas para dar un límite a los flujos de neutrinos o muones procedentes de una fuente puntual que no podemos ver. Los resultados más importantes del análisis son:

- Los bines y conos óptimos para calcular límites son mayores que los utilizados en las búsquedas. El grid óptimo para las búsquedas es de anchura inicial de los bines de **1.0**° frente al de **2.5**° de los límites. En el caso de los conos, los diámetros óptimos son **0.5**° y **1.2**° para búsquedas y límites respectivamente.

- Al aumentar el índice espectral los límites empeoran pero el tamaño óptimo para bines y conos se mantiene prácticamente constante. Para $\gamma = 2.5$ el cociente S/B es un ∼**15%** peor y para $\gamma = 3.0$ un ∼**30%** peor.

- El límite para una declinación dada obtenido con la técnica de grid es siempre peor que el límite correspondiente con la técnica de cluster.

- Los límites tanto para neutrinos como para muones empeoran al aumentar la declinación, fundamentalmente debido a la visibilidad de la fuente.

- Los límites a flujos con distintos índices espectrales han sido calculados con ambas técnicas tanto para neutrinos como para muones. Las diferencias entre índices espectrales son más importantes para neutrinos que para muones. Los límites empeoran al aumentar el índice espectral.

- Todos los límites a los flujos mejoran al aumentar el tiempo de observación. El factor de aumento en la sensibilidad es siempre menor que el factor de aumento en el tiempo. Para 3 años de toma de datos la mejora con respecto al límite para un año de toma de datos en un factor $\sim$**2.5**. Para 5 años de toma de datos, la mejora es un factor $\sim$**3.8**.

- Se puede definir un flujo de descubrimiento a partir del número de sucesos necesario para descubrir una fuente puntual. A medida que aumenta la declinación aumenta el flujo necesario para realizar el descubrimiento de una fuente puntual. A una misma declinación, los flujos de descubrimiento son siempre peores (mayores) que los flujos límite.

- Por último, hemos calculado un límite para flujos difusos. El límite es $E^2\,\bar{\Phi}^{limit}_{90\%}(E) = 8.8 \times 10^{-8} cm^{-2} s^{-1} sr^{-1} GeV$. Este límite es un factor ~ 10 mayor (peor) que el correspondiente límite para fuentes puntuales específicas con índice espectral 2.

Preface

Neutrino Astronomy is a relatively recent field which offers a unique potential to explore the furthest and densest regions of the Universe. The study of high energy neutrinos presents a great interest as it offers very good prospects for new discoveries.

Overcoming the technical challenges associated to the development and operation of large neutrino telescopes, there is nowadays a new generation of this kind of experiments, some of them already under construction, devoted to the exploration of such a promising field. Their results could provide new evidences about the physics that rules some astrophysical objects, and may address some fundamental questions of Physics and Cosmology. The astronomy with high energy neutrinos leaves as well an open chance for the discovery of unsuspected astronomical phenomena.

The ANTARES project is carried by an international collaboration aiming to install a neutrino telescope in the Mediterranean Sea.

The main goal of this work is the study of ANTARES performances concerning the discovery of point-like neutrino sources. The existence of such sources is still unproved, although different astronomic objects are considered capable of emitting high energy neutrinos, as predicted by different theoretical models. The discovery of such sources, or even the establishment of limits on their neutrino fluxes, could allow the discrimination among different models, and throw some light on the physics of these yet mysterious objects.

The performance of a neutrino detector strongly relies on the precision of the reconstruction strategy. One of the main contributions of this work is the definition and characterisation of a new reconstruction strategy. This strategy was initially designed for searches of point-like sources, but it is extended to the most general case and shown to perform better than the standard reconstruction technique.

With the defined strategy, a careful study is carried out on the analyses to be applied to the data in order to search for point-like source signals. Such analyses involve blind searches, surveys over a predetermined set of candidate sources, and establishing limits on the fluxes in case that no signal is obtained.

In the first chapter of the this work we review the basic principles of neutrino astronomy, from the limitations of the traditional photon astronomy and the way they are overcome by neutrino Astronomy, to the guaranteed or postulated sources of high energy neutrinos.

In chapter 2, the subject of neutrino telescopes is discussed. Their operation principles are described, and a review of existing neutrino telescopes is presented. Then, we describe in detail the ANTARES detector, the subject of this thesis.

Chapter 3 describes the new reconstruction strategy introduced in this work, whereas chapter 4 presents the detailed comparison of the attainable detector performances with the standard and the new strategy.

In the last part of this work, the proposed analysis of data for point-like sources searches is presented. In chapter 5 we describe in detail two complementary binning methods that can be applied to ANTARES data in order to perform such searches. Both the case of blind searches and the survey of a predetermined set of point-like sources are covered. Finally, in chapter 6 we study the limits that ANTARES would set on neutrino and muon fluxes in case that no observation of a point-like source took place after one or more years of data taking. We have studied the attainable limits on the all–sky fluxes and on particular point-like sources.

Chapter 1

High energy neutrino astronomy

1.1 Introduction

The neutrino is one of the fundamental particles in the Standard Model of Particle Physics. Nowadays, the neutrino is known to play a very important role in Particle Physics, Astrophysics and Cosmology.

1.1.1 A brief history

In 1927, C. Ellis and W. Wooster confirmed experimentally that the energy spectrum of the electron emitted during beta decays:

$$A(Z, N) \rightarrow A(Z+1, N-1) + e^-$$

was continuous, and that the apparently missed energy in the reaction was not due to a loss of energy of the electron during its travel from the nucleus. In 1930, W. Pauli made the hypothesis that the missing energy and angular momentum could be carried away by a neutral particle that escaped undetected. The neutral particle discovered by J. Chadwick in 1932 [11], the neutron, was soon discarded as the candidate for Pauli's proposed particle. In 1934 Fermi proposed an effective theory of the beta decay, including Pauli's hypothetical particle, that he called neutrino, and assuming the existence of the new weak interaction [12]. The first evidence of experimental observation of neutrinos was obtained by F. Reines and C. Cowan in 1953 in a detector close to the Hanford nuclear plant [13]. The experiment used the flux of artificial neutrinos produced in a nuclear reactor ($\sim 10^{12} - 10^{13}$ cm^{-2}s^{-1}), much higher than fluxes from natural sources. In 1956 they confirmed the observation with a detector close to the Savannah River nuclear plant [14].

In 1962, an experiment by L. Lederman, M. Schwartz and J. Steinberger showed that the neutrino associated to the muon was a different particle than the neutrino associated to the electron [15]. When in 1975 the tau particle was discovered by M. Perl at SLAC and was identified as a heavier version of the electron and the muon, the existence of a τ neutrino was also predicted, although its experimental detection took more than 20 years. In 1998, the LEP experiments proved that there are only three families or species of neutrinos with mass below that of the Z boson and coupled to it. Finally, in 2000, the DONUT experiment at Fermilab showed that the neutrino associated to the tau lepton is a different entity to the two other neutrinos [16].

1.1.2 The SM and the neutrino mass

Neutrinos are electrically neutral particles of spin 1/2. There are at least three flavours of light (less than half the mass of the Z boson) left handed neutrinos (ν_e, ν_μ and ν_τ). Each neutrino has an anti-particle which is right handed. In the Standard Model, neutrinos only interact via charged current reactions, which are mediated by $W^\pm$ bosons and via neutral current reactions, mediated by Z bosons.

Electron and muon neutrinos are produced in decay processes such as those of neutron, muon, pion decay and others. Tau neutrinos are produced in $\tau^\pm$ decays.

In the Standard Model, neutrinos are massless particles, but there is strong evidence that neutrinos have mass. Nevertheless, from direct kinematic studies, only mass upper limits have been obtained: 3 eV for electron neutrinos, 0.19 MeV for muon neutrinos and 18.2 MeV for the tau neutrino [17]. The most clear indication of neutrino mass are the observation of neutrino oscillations. In terms of quantum mechanics, neutrino oscillations can be explained assuming that neutrinos have mass and that the mass eigenstates (1, 2, 3) are not the same as the eigenstates of weak interaction (e, μ, τ). Oscillations are described in terms of the difference in mass squared (Δm^2) and the mixing angle between families.

The first evidence of neutrino oscillations appeared with the first measurements of solar neutrinos (see 1.1.3). At present there are evidences of disappearance phenomena in neutrino fluxes from different sources. Super-Kamiokande collaboration [18,19] has shown a deficit of atmospheric neutrinos compared to theoretical predictions. The SNO experiment [20,21] has measured the total and the electron neutrino flux coming from the Sun. The measured electron neutrino flux is deficient by roughly a factor of three, whilst the total flux is consistent with the standard solar model. The Kamland experiment, which detects neutrinos from several power plants has clear indications of electron neutrino disappearance [22]. From these experiments, the oscillation parameters $\sin^2(\theta)$ and Δm^2 are obtained for each mixing. The emerging picture is that $\Delta m_{12}^2 \approx 10^{-4}$ eV and the corresponding mixing is high, but not maximal, whereas $\Delta m_{23}^2 \approx 10^{-3}$ eV and $\sin^2\theta_{23} \approx 0.5$. Non-interacting (sterile) neutrinos are not needed to explain the data.

Finally, neutrinos are believed to be stable particles. They are also very elusive particles, what makes experiments with neutrinos very difficult. The mean free path of a 1 MeV neutrino in lead is about 1 light year. Both properties of neutrinos, stability and penetration power, make them very suitable for astronomy compared to other messengers. The drawback is that very large neutrino detectors and/or very intense neutrino beams are required for neutrino detection.

1.1.3 Cosmic neutrinos

In 1946 B. Pontecorvo proposed the capture in ^{37}Cl as a possible method to detect neutrinos. In 1954, R. Davis made a first experiment using 1000 gallons ($\sim$ 4000 l) of carbon tetrachloride close to the Savannah river nuclear plant. In 1964, R. Davis and J. Bahcall proposed the detection of solar neutrinos with a detector of 100000 gallons ($\sim 400,000$ l) of perchloroethylene, C_2Cl_4 [23, 24]. The detector was located in the Homestake mine, in South Carolina (USA). The experiment detected for the first time neutrinos coming from the Sun, but the signal was approximately one third of the theoretical expectations [25]. This result gave origin to the so-called *solar neutrino problem*. A possible cause for the anomaly was that missing electron neutrinos had converted into another flavour, unobservable for the experiment, but this was thought a less likely explanation than the inaccuracy of the solar model on which the theoretical predictions were based.

The capabilities of the early experiments that began the extra-terrestrial neutrino detection were limited due to the absence of tracking of the detectors. Over the next 25 years, little progress was made in extra-terrestrial neutrino observation compared with other aspects of neutrino physics. Table 1.1 presents the most relevant neutrino experiments carried out from 1965 to present, excluding the neutrino telescopes.

Detector	**Date**	$\mu Area$ (m^2)	**Technique**
KGF, South India	1965-1970	10	LS + FT
CWI, South Africa	1965-1970	110	LS + FT + Fe
Silver king, Utah	1966-1970	30	WC + Ctrs + Fe
KGF, South India	1978-1988	20	ST
Baksan, Caucasus	1980-Present	250	LS tanks
IMB, Ohio	1981-1990	400	WC
HPW, Utah	1982-1985	100	WC
Kamioka, Japan	1982-1995	120	WC
NUSEX, Mt. Blanc	1983-1988	10	St + Fe
Fréjus, France	1985-1988	90	St + Fe
Soudan I, Minn.	1985-1990	10	St + Concrete
Soudan II, Minn.	1990-Present	100	DT + Fe
Macro, Italy	1995-2000	800	LS + ST
LVD, Italy	1996-Present	500	LS tanks + ST
Super-Kamiokande	1996-Present	740	WC
SNO, Canada	1999-Present	300	D_2O WC
Borexino, Italy	2003-2010	<100	LS
KamLAND, Japan	2002-Present	100	LS

Table 1.1: Underground detectors with capability for detecting high energy neutrinos. WC, water Cherenkov; ST, streamer tubes; LS, liquid scintillator ; PS, plastic scintillator; FT, flash tubes.

Meanwhile, the neutrino anomaly was confirmed by almost three decades of data [26]. In 1985, the IMB water detector found a deficit in muon neutrino interactions. This was confirmed by Kamiokande in 1988. The Kamiokande experiment was first designed to detect nucleon decays, but it was refurbished to be able to detect low energy neutrinos (9 MeV threshold for electrons). This so-called Kamiokande II experiment made use of 680 tons of water at 1 km depth. It started operating in 1986 and was able to show a neutrino signal compatible with that of the Sun, but with a deficit of a factor two with respect to theoretical predictions [1]. The experiment also gave the first unmistakable evidence that the neutrino signal was correlated with the Sun's direction in the sky. In that sense, it was the first neutrino *telescope* in history. Kamiokande II and IMB also detected a burst of neutrinos associated to the explosion of the supernova SN1987A in the Large Magellanic Cloud [2–4].

In 1997 Soudan II was the first iron detector to observe the disappearance of neutrinos, corroborating the results from the previous experiments. The Super-Kamiokande detector (50000 tons of water) continued the task of Kamiokande II and gave a clear signal of disappearance of atmospheric muon neutrinos [27].

The age of neutrino telescopes truly begins with a second generation of neutrino detectors dedicated to neutrino astronomy. They are characterised by large areas that allow astronomical observations. The pioneer experiment in the field was the DUMAND project [28, 29] in Hawaii. This project was finally cancelled in 1995 but it developed several techniques that have been used by other projects and represented a great stimulus for the field. Table 1.2 presents a list of the experiments devoted to high energy neutrino astronomy.

At present, the techniques used by the neutrino telescopes are the detection of Cherenkov light in water (ice), the detection of μ-wave radiation and the detection of the acoustic wave produced after the interaction of the neutrino. Among the water Cherenkov telescopes, only Baikal and AMANDA are taking data and have reported observations of neutrino events, most probably from atmospheric origin. Even more, the AMANDA experiment is being upgraded to the ICECUBE experiment with a size of 1 km^2. The remaining water Cherenkov experiments are in their construction stage or in advanced testing and will start working in the following years. More details concerning these experiments and the techniques they use for neutrino detection can be found in chapter 2.

1.2 High energy neutrino astronomy

Photons have been to date the most used and fruitful subject of study for astronomers. Ranging from 10^4 cm radio-waves to TeV gamma rays, they have been the instrument for an extensive study of the Universe. They have provided recent discoveries in the high energy domain as gamma-ray sources or Gamma Ray Bursts, however the exploration power of photons with higher energies is limited by the attenuation of gamma rays due to interactions with low energy photons of the cosmic background

Detector	**Status**	$\mu Area$ (m^2)	**Technique**	**Threshold (GeV)**
DUMAND-2, Hawaii	1992-1995	2×10^4	WC	20
Baikal NT-200, Siberia	1996-Present	3×10^3	WC	10
AMANDA II, South Pole	1996-Present	3×10^4	WC in ice	20
NESTOR, Greece	Construction	10^5	WC	1
SADCO, Greece	Testing	10^6	Acoustic	$> 10^6$
RICE, South Pole	Construction	10^6	μ-wave	$\sim 10^6$
ANTARES, France	Construction	5×10^4	WC	10
NEMO, Italy	Proposed	?	WC	?
RAMAND, USA	Testing	?	μ-wave	10^{11}
ICECUBE, South POLE	Construction	10^6	WC in ice	>100
SALSA	Proposed	10^8 m^3	μ-wave	10^6
GLUE	Existing	10^{11}	μ-wave	$10^{1}0$
ANITA	Construction	1.5×10^{10} m^3	μ-wave	10^9
FORTE	Existing	1.8×10^{12} m^3	μ-wave	$10^{1}3$

Table 1.2: Experiments dedicated to neutrino astronomy. WC stands for water Cherenkov; μ-wave, for microwave detection; Acoustic, for acoustic wave detection.

radiation. This is known as the *GZK effect* [30, 31]. The range of TeV gamma rays is of the order of 100 Mpc, hence observation of the far distant high energy Universe is vetoed for photons. Also, due to their interaction with matter, photons do not allow exploration of dense regions, which will require a weakly interacting emissary.

Protons in hadronic cosmic rays do also carry information on astronomical sources. However, since protons are deviated by magnetic fields as they travel from the source, their arrival direction cannot be associated with that of the source. Nevertheless, at very high energies, above EeV, protons are not bent by the galactic magnetic field and they point back to their source. However, at such energies, absorption by virtue of the GZK effect prevents them from delivering information from far distant sources.

Neutrinos share some physical properties of photons that make them suitable as carriers of astronomical information. Like photons, neutrinos are stable particles. Besides, they have no electric charge so that, unlike protons, they are not deflected by the galactic and extra-galactic magnetic fields and preserve directional information. Moreover neutrinos do nearly not suffer absorption when travelling through the space. Therefore, they constitute an optimal candidate for exploration of dense and far distant regions. Contrary to the case of high energy photons, which may originate from pure electron acceleration, high energy neutrinos would provide with their detection an evidence of proton acceleration.

As mentioned, there are several examples of neutrino telescopes detecting MeV neutrinos from the nuclear reactions in the core of the Sun. These experiments may also detect MeV neutrinos from supernova explosions in our galactic neighbourhood (distance $<$ 10 light years). However the main interest of neutrino astronomy at the moment is focused on high energy neutrinos (E_ν above GeV-TeV) for several reasons:

- Neutrino cross section as well as muon range and angular resolution increase with energy.
- High energy neutrinos offer the opportunity to use large natural target media like water, ice or the atmosphere.
- They offer a great potential for a significant discovery.

Neutrino astronomy experiences at present a rapid development, with a new generation of experiments, characterised by large effective areas, being well under construction or in an advanced design stage. Nevertheless, the instrumental challenges in neutrino astronomy are still considerable.

High-energy neutrino astrophysics can address fundamental questions in Cosmology. Among them, the nature of dark matter, the origin of cosmic rays and the physics of the most luminous objects in the Universe. Finally, high energy neutrino exploration offers the possibility of opening a new window to the Universe, and thus the potential of new discoveries.

1.3 High energy cosmic rays

Long before the existence of the neutrino was suspected, it was known that an extra-terrestrial radiation arrived to the Earth. This radiation was discovered during balloon flights in 1912 by Victor Hess [32] and was called *Cosmic Rays*. We know that cosmic rays consist of an isotropic flux of ionised atomic nuclei (mainly protons and helium), and elementary particles that arrive to the Earth at a rate of $\sim$ 1000 per m^2 per second. It is also accepted that the origin of high energy cosmic rays must be intimately related to the origin of high energy cosmic neutrinos.

Since 1912, the cosmic ray spectrum has been measured up to energies exceeding 10^{20} eV [33], far beyond the reach of any terrestrial accelerator in the foreseeable future. The composition of the cosmic rays at low energies is well established. Between TeV and PeV energies cosmic rays contain protons ($\sim 50\%$), He nuclei ($\sim 25\%$), C, N and O ($\sim 13\%$), Fe ($\sim 13\%$), electrons ($< 1\%$) and photons ($\sim 0.1\%$). Above $\sim$ 100 TeV, it is very difficult to determine their composition. Some experiments report an increasingly heavy composition [34, 35], however this is not clear, since other experiments report a transition to lighter components above 4×10^{15} eV [36].

The spectrum of primary cosmic rays follows a power law over 12 orders of magnitude in energy, see figure 1.1 [37, 38]. Below 100 MeV kinetic energy, the observed proton flux is exclusively due to the Sun, because protons coming from outside the solar system are shielded by the solar wind. The observed value of γ is $\approx \mathbf{2.7}$ for energies between 10^{10} eV and 10^{15} eV. At $\sim 4 \times 10^{15}$ eV the cosmic ray spectrum presents a change in slope, known as the *Knee*. This point is believed to be the division between cosmic rays from galactic and extragalactic origin. Between 10^{15} eV and 10^{18} eV the spectral index is ≈ 3.0. Then, at $\sim 5 \times 10^{18}$ eV, there is a new change in the slope of the spectrum, known as the *Ankle*. Above 10^{19} eV the spectral index is again ≈ 2.7.

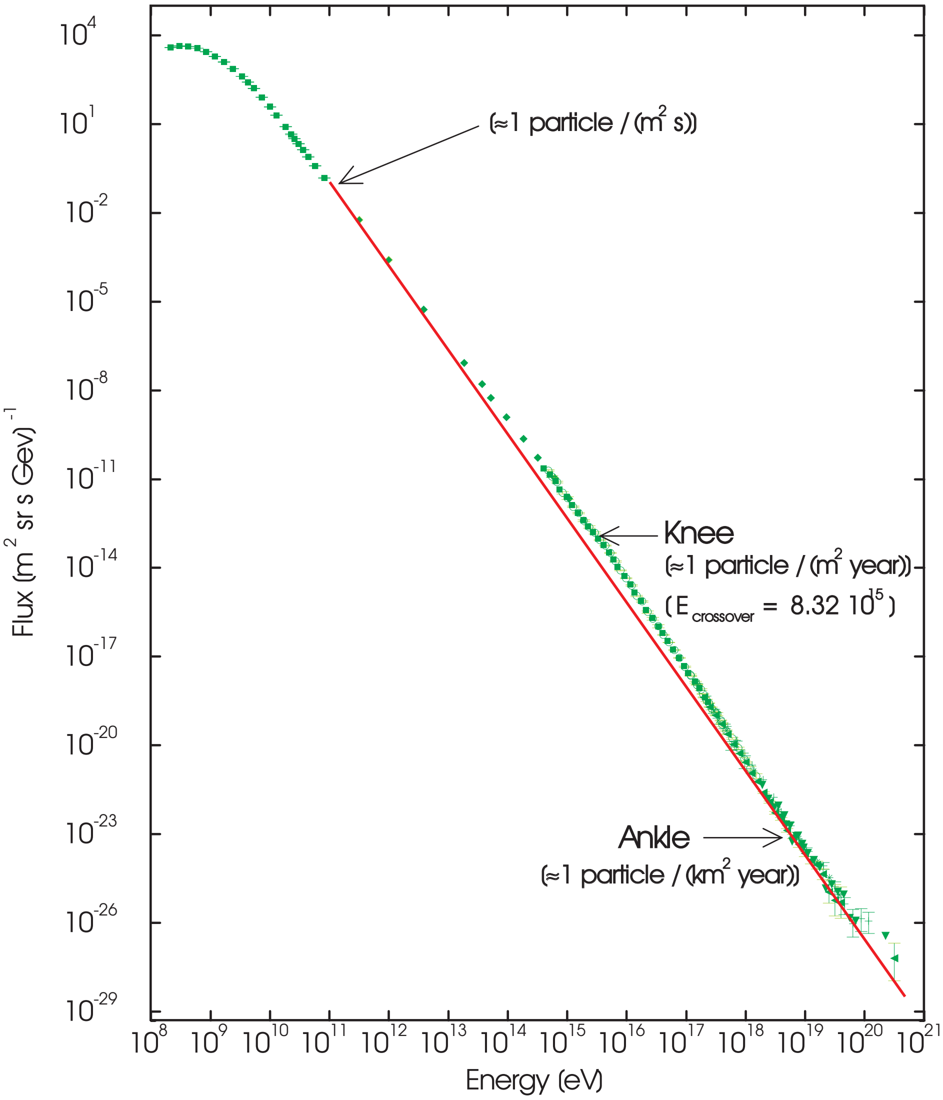

Figure 1.1: cosmic ray spectrum measured by various experiments. All data have been fitted with a single power-law fit that shows significant breaks at the "*Knee*" and the "*Ankle*".

When cosmic rays arrive to Earth, they interact with the nuclei in the upper atmosphere and produce a particle cascade with pions that finally decay to muons. These down-going muons can travel a distance of several kilometres before decaying or being halted. They represent a significant background for any detector willing to detect muons from astrophysical neutrinos. High energy atmospheric neutrinos are also produced in the atmospheric cosmic rays cascades. These neutrinos are produced when some of the atmospheric pions and muons decay in flight within the atmosphere. Due to the high penetration power of neutrinos, this flux arrives from all directions, and constitutes the most important background in a neutrino telescope.

Up to now, the origin of the ultra-energetic cosmic rays and the mechanisms that accelerate them are unknown. However, the most powerful (and least known) phenomena in the Universe are suspected to be their origin. The proposed mechanisms to explain the production of high energy cosmic rays are usually classified into two main categories: accelerated and not accelerated. In the following sub-sections we briefly present the main characteristics of each type of mechanism.

1.3.1 Accelerated origin of the cosmic rays. Bottom-up scenarios

The standard model for the cosmic ray acceleration is known as *first order Fermi mechanism* [39] and it consists in the acceleration by shockwaves in the interstellar medium. This mechanism produces a spectrum with the form:

$$\frac{dN}{dE} = N_0 E^{-\gamma} \tag{1.1}$$

with $\gamma = 2 + \epsilon$ and ϵ a small number.

The observed spectral index is larger because of the escape time of the cosmic rays in the Galaxy. The cosmic rays are believed to be confined in the Galaxy by magnetic fields. The probability for them to escape from the Galaxy depends on its energy. From the observed proportions of some nuclei (i.e. carbon and oxygen) in the primary cosmic rays, it has been determined that the escape time is $\tau(E) \propto E^{-\kappa}$ with $\kappa \approx 0.6$, below 10^{14} eV,

$$dN(E) \sim E^{-(2+\epsilon+\kappa)} dE \tag{1.2}$$

which is consistent with the hypothesis that the cosmic accelerator has an injection spectral index $\gamma = 2.1 - 2.4$.

Many astrophysical objects are believed to produce highly efficient particle acceleration. In the first order Fermi mechanism, the acceleration occurs at the expense of the kinetic energy of the shocked bulk flow. The charged particles are accelerated when they cross back and forward the shockwave. An acceleration cycle takes the sum of the time that the particle is above and below the wavefront.

The acceleration rate is given by:

$$\frac{dE}{dt} \approx \frac{3ZeBc}{\xi} \left(\frac{v}{c}\right)^2 \tag{1.3}$$

being v the speed of the shockwave, Ze the particle charge, B the magnetic field and ξ a constant that depends on the diffusion details in the shockwave.

The spectrum of the accelerated particles follows a power law with $\gamma = 2 + \frac{4}{M^2}$ where $M^2 = v/c_*$ is the square of the Mach number and c_* is the sound speed of the plasma. For strong non relativistic shocks with $M \to \infty$, the asymptotic limit is 2.

The Fermi acceleration ceases to operate when the energy-loss time scale becomes shorter than the acceleration timescale, when the scattering length becomes larger than the shock radius, when the sideways diffusion timescale becomes shorter than the acceleration timescale and when the shock decays. The lifetime of the shock and its radius also limit the maximum energy that can be gained.

Section 1.5.2 describes some of the objects that can produce particle acceleration in the context of neutrino production.

1.3.2 Cosmic rays from decay of heavy particles. Top-down scenarios

The Fermi acceleration mechanism explains the shape of the cosmic ray spectrum. However, the existence of the ultra-high energy cosmic rays above 10^{11} GeV is a serious challenge for the acceleration mechanism. $E_{max} \lesssim 10^{11}$ GeV can barely be achieved in the most powerful astrophysical objects for reasonable values of R and B in these objects.

Instead, it has been proposed that the ultra high energy component of cosmic rays can have a completely different origin, in the sense that they may be produced by the decay of certain massive particles (generally, "X") with mass $m_X > 10^{11}$ GeV. This "X" particle typically decays to quarks and leptons, and the quarks hadronise producing light mesons (pions) and baryons. Finally, the pions decay producing photons, neutrinos and electrons with energies up to $\sim m_X$, without any acceleration mechanism.

1.4 Gamma ray astronomy

The success of the [40]*Energetic Gamma-ray Experiment Telescope* (EGRET) on board of the *Compton Gamma Ray Observatory* (CGRO) and several imaging air Cherenkov telescopes such as Whipple and HEGRA [41–43] has allowed a considerable progress in photon astronomy at high energies. Nowadays, Gamma Ray astronomy is a mature field, but most of its rapid development started in the 1990s.

Gamma ray astronomy is somewhere between cosmic ray astronomy and neutrino astronomy. Gamma ray photons share with neutrinos the absence of charge and their stability, properties that make them very suitable for astronomy. Both types of particles travel along straight lines from the source to the observer. However, gamma rays have a limited range because they interact more easily with matter and radiation. This disadvantage is turned into an advantage because it makes detection simpler than in the case of neutrinos.

The mechanism for particle acceleration is only valid for charged particles. In the case of photons, there are two mechanisms for the production of non-thermal gamma rays up to the energies where electron acceleration is quenched by radiation losses. Gamma rays from astrophysical sources can be produced either by accelerated electrons through synchroton radiation, bremstrahlung and inverse Compton scattering, or by accelerated protons or ions through the beam dump processes. In the first case, gamma rays are produced in electromagnetic processes where production of neutrinos is not expected. In the second case, however, the processes involved are hadronic and a neutrino flux is expected with the gamma ray flux. Above 100 TeV, photons can only be produced by the hadronic mechanism.

At energies between 30 MeV and 30 GeV, EGRET has detected more than 270 point-like sources of gamma rays [44]. Figure 1.2 shows the point-like sources of photons with more than 100 MeV in the Third EGRET Catalogue [45]. Some of these sources are associated to known astronomical objects. However, other sources have not yet been identified. Table 1.3 lists the different kind of sources detected by EGRET. In addition, EGRET also detected 5 gamma ray bursts, the gamma ray binary Cen X-3 and one solar flare.

Source type	**Number**
Blazards	94
Pulsars	6
Unidentified	170
Normal Galaxy	1 (LMC)
Radio Galaxy	1 (Cen A)

Table 1.3: Sources in the Third EGRET Catalogue. 27 of the 94 Blazards have only been marginally identified.

At very high energies ($E_\gamma > 300$ GeV) satellite experiments become impractical because the photon fluxes fall rapidly. At these energies, gamma ray astronomy is done with ground-based instruments by detecting the secondary particles and radiation produced by the interaction of high energy photons in the upper atmosphere. Atmospheric Cherenkov Telescopes are used to image the flashes of Cherenkov light produced as a result of the electromagnetic cascades initiated by a gamma ray. The Whipple collaboration was the first one to confirm the detection of TeV gamma rays from an astrophysical source [46] and it has been followed by several high resolution Atmospheric Cherenkov Telescopes like CAT, Cangaroo, Durham, Hegra, HESS and others. Figure 1.3 shows the skymap of point-like sources detected by ground experiments above 10 GeV. The list of detected objects includes galactic and extragalactic sources.

Six of the high energy sources in the previous figure have been detected by multiple experiments at high significance levels (labelled as *Confirmed* in the figure): Crab, Markarian 401, Markarian 521, PSR 1706-443, H1426-428 and 1ES 1959+650. Other

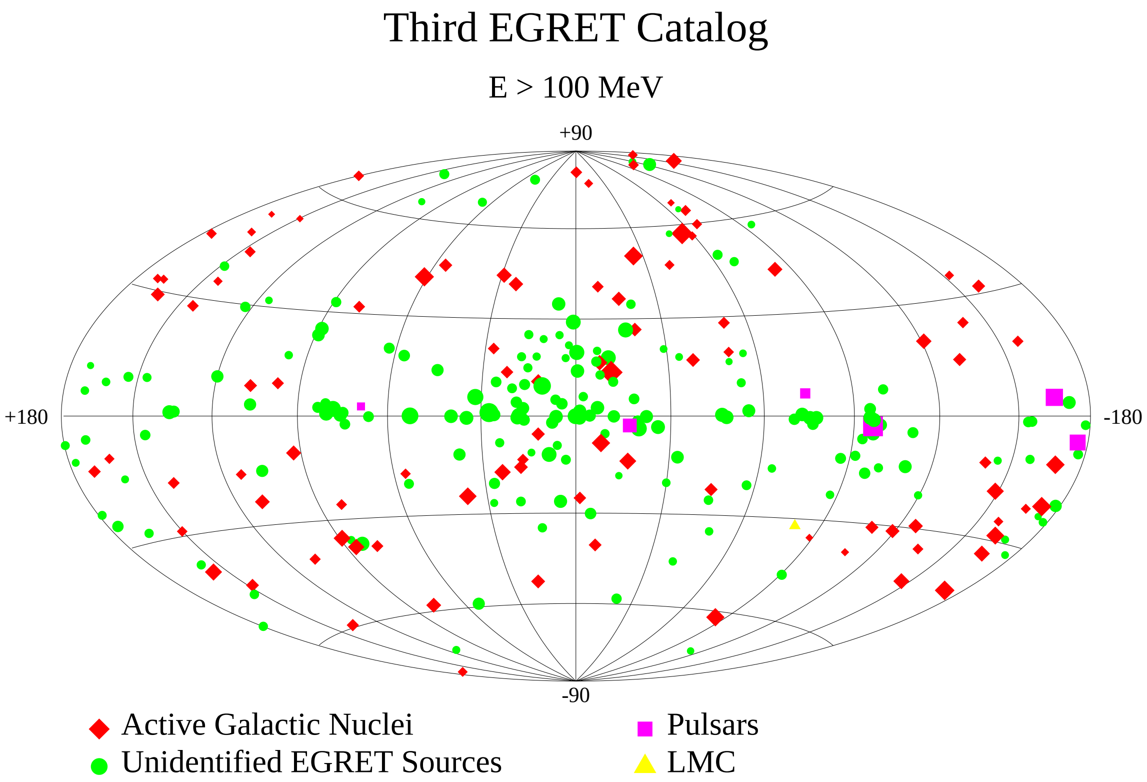

Figure 1.2: Sources of photons with more than 100 MeV in the Third EGRET Catalogue.

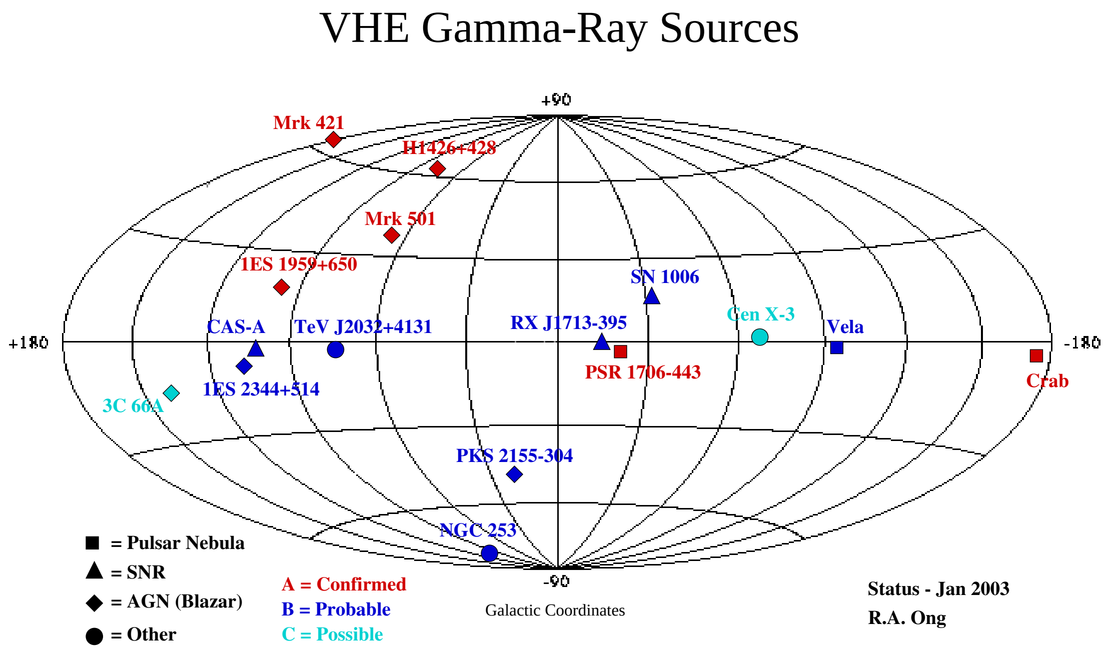

Figure 1.3: Sources of photons with more than 10 GeV detected by atmospheric Cherenkov telescopes.

sources in the figure have been detected at high significances by at least one experiment (they are labelled as *Probable*) and the remaining two have not been confirmed (they are labelled as *Possible*).

At energies above 1 TeV the Crab Nebula was the first extragalactic object to be unambiguously detected. Since then, it has been detected several times by various experiments and it is the standard candle in the 300 GeV to 3 TeV range [47]. Mrk 421 was the first extragalactic source to be detected above 250 GeV. It is located at a redshift of 0.031 and it is the closest BL Lac object (active cores of elliptical galaxies) seen by EGRET. At a redshift of 0.033, Mrk 501 is the second closest X-ray-selected BL Lac known and it was the second blazard discovered at TeV energies by the Whipple collaboration. The comparison of the GeV and TeV skymaps shows that only a handful of the EGRET sources have been detected at TeV energies. The spectral cut-off could be due either to intrinsic absorption at the source or to intergalactic absorption, which occurs when high energy photons (TeV photons preferably) are absorbed by infrared photons (0.5 eV) in the intergalactic medium via pair production ($\gamma\gamma \rightarrow e^{+}e^{-}$).

The infrared extragalactic background light (EBL) is a serious challenge for high energy gamma ray astronomy. It limits the maximum distance at which a source is visible in the range of high energy gamma rays. Nevertheless, it does not represent a problem for the high energy neutrino astronomy, since neutrinos do not interact with the infrared photons. Because of that, some of the sources emitting TeV neutrinos and photons can only be detected using neutrinos because their photons can not arrive to Earth.

1.5 Sources of high energy cosmic neutrinos

Different phenomena in the Universe can produce neutrinos with different energies (see figure 1.4). The least energetic neutrinos are relics from the Big-Bang and they are present since they decoupled from matter after the first 10 seconds. The stars, the supernovae or even the artificial nuclear reactors are additional sources of low energy neutrinos.

High energy neutrinos can be produced by cosmic rays in the Earth's atmosphere (atmospheric neutrinos). In addition, cosmic rays could also produce neutrinos outside the Earth. There are strong evidences of the existence of such events and they are considered as guaranteed. Other high energy neutrinos are those produced in high energy cosmic accelerators or after the decay of some dark matter candidate. However, these neutrinos have only been predicted in theoretical models and they are not guaranteed by any experimental observation. These neutrinos are, however, the most interesting objective for neutrino astronomy.

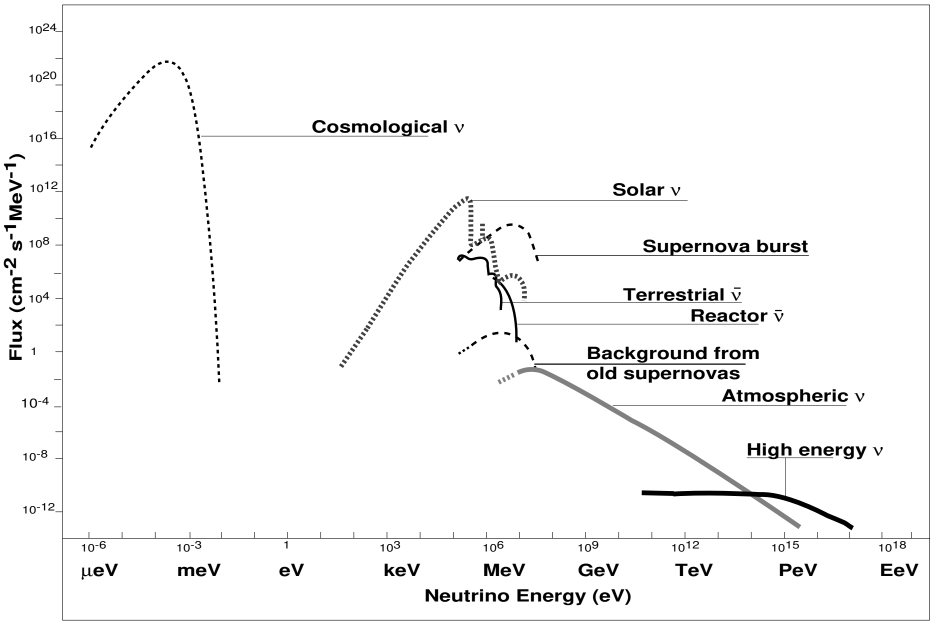

Figure 1.4: Known and predicted sources of neutrinos in the Universe.

1.5.1 Guaranteed high energy neutrino sources

Up to now, there are only two examples of detection of astrophysical neutrinos: the low energy neutrinos from the Sun ($E_\nu \leq 10$ MeV) and the neutrinos from the supernova SN1987a ($E_\nu > 20$ MeV). However, there are other sources of astrophysical neutrinos considered as guaranteed, in the sense that their fluxes can be predicted with higher precision because they do not depend on particular models. The guaranteed sources that produce neutrinos with energies above 100 MeV are described below.

Atmospheric neutrinos

The neutrinos produced in abundance in the Earth's atmosphere by the interaction of primary cosmic rays are known as *atmospheric neutrinos*. Their energies extend from a few MeV to the energies of the most energetic cosmic rays. These neutrinos provide an unavoidable background against neutrinos from extraterrestrial sources. These neutrinos come from pion decays and other mesons in the atmosphere and from the decay of muons produced in beam dump processes:

$$
\begin{array}{rl}
p \longrightarrow \pi^+(+K^+\cdots) \longrightarrow & \mu^+ + \nu_\mu \\
& \downarrow \\
& e^+ + \bar{\nu}_\mu + \nu_e \\
& \\
n \longrightarrow \pi^-(+K^-\cdots) \longrightarrow & \mu^- + \bar{\nu}_\mu \\
& \downarrow \\
& e^- + \nu_\mu + \bar{\nu}_e
\end{array}
\tag{1.4}
$$

Both protons and neutrons can produce mesons with different charge to that of previous expressions. However, the processes with the same charge are slightly favoured.

Below several GeV, the muons (produced mostly after the decay of charged pions) themselves decay. Starting with equal numbers of positive and negative pions yields two muon neutrinos for each electron neutrino. The resulting neutrinos are of nearly equal energy. Independently of the cosmic-ray spectrum, the ratio of muon to electron neutrinos can be calculated with rather good accuracy ($\sim 5\%$). Yet, there is a 20% absolute flux uncertainty for the low-energy atmospheric neutrinos, what limits the progress in untangling the oscillation parameters.

The higher-energy atmospheric muon neutrino differential flux can be approximated by a power law with a spectral index of ~ 3.7 up to 1 PeV and ~ 4.0 above 1 PeV.

In general, the atmospheric muon neutrino ($\nu_\mu + \bar{\nu}_\mu$) flux can be approximated by [48, 49]:

$$
\frac{d^2\Phi_{\nu_\mu}}{dE_{\nu_\mu}d\Omega} \simeq 0.0286 E_\nu^{-2.7}\left(\frac{1}{1+\frac{6.0E_\nu cos\theta^*}{115GeV}} + \frac{0.213}{1+\frac{1.44E_\nu cos\theta^*}{850GeV}}\right) cm^{-2}\cdot s^{-1}\cdot sr^{-1}\cdot GeV^{-1}
\tag{1.5}
$$

The cosmic ray muon ($\mu^- + \mu^+$) flux can be described by a similar expression:

$$
\frac{d^2\Phi_{\mu}}{dE_{\mu}d\Omega} \simeq 0.185 E_\mu^{-\gamma}\left(\frac{1}{1+\frac{1.1E_\mu cos\theta^*}{115GeV}} + \frac{0.054}{1+\frac{1.1E_\mu cos\theta^*}{850GeV}}\right) cm^{-2}\cdot s^{-1}\cdot sr^{-1}\cdot GeV^{-1}
\tag{1.6}
$$

The first term in the sum represents the contribution of neutrinos from the decay of pions, the second term from kaons and other mesons. There, $A_{\pi\nu} = Z_{N\pi}(1-(m_\mu/m_\pi)^2)^\gamma/(1+\gamma)$, $B_{\pi\nu}$ is a constant that depends on the attenuation length of muon and pion. E_π^C and E_K^C are characteristic energies for pion, kaons and other mesons. They represent the competition between absorption and decay processes. If $E_\nu \ll E_i^C$ all parent mesons will decay and the spectrum of neutrinos will be parallel to that of primary cosmic rays. If $E_\nu \gg E_i^C$, the spectrum exponential law increases in a power of E. $E_{\pi^\pm}^C \approx 115$ GeV, $E_{K^\pm}^C \approx 850$ GeV, $E_{D^\pm}^C \approx 4\times 10^7$ GeV are typical values for these energies.

The formulae above are uncertain in magnitude to $\sim 20\%$, although they are good in shape to $\sim 5\%$.

The atmospheric neutrino flux is not isotropic and there is a variation with the zenith angle, more prominent at higher energies. This effect is due to the fact that pions and muons produced nearly tangent to the Earth have longer flight time in less dense atmosphere, so they have more time to decay before interacting. This leads to a peak in the atmospheric neutrino flux near the horizon arrival direction for any location.[1]

Today the atmospheric neutrino flux has been widely measured. Various experiments like Kamiokande, SuperKamiokande, SNO study this flux. Up to now, atmospheric neutrinos have provided the discovery of neutrino oscillations, which is the first convincing evidence for neutrino masses.

Neutrinos from the galactic plane and the Sun

Other guaranteed sources of high energy neutrinos are the Galactic plane and the solar atmosphere. In both cases, neutrinos are produced by the interaction of high energy cosmic rays with matter in a beam-dump process.

In the case of the Sun, neutrinos are created when cosmic rays interact with the solar atmosphere, as in the case of the Earth. Cosmic rays interact in the Sun's atmosphere producing mesons that can decay or further interact producing neutrinos. This depends on their energy and on the density at the point of the first interaction. In the Sun, the fraction of mesons decaying before interaction is larger than in the Earth, because the density of the solar atmosphere is smaller. As a consequence, the resulting neutrino spectra produced in the Sun's atmosphere have a slope similar to that of the original cosmic ray spectrum. In contrast, the neutrino flux produced in the Earth's atmosphere is approximately one power of E steeper than the original cosmic ray flux.

The atmospheric neutrino flux produced in the Sun is high enough to significantly exceed the atmospheric background above 10 TeV in a small angular window. However, the flux is too small to be detected in a 0.1 km^2 detector. The sun can only produce ~ 17 events per year above 100 GeV in a km^2 detector. Despite this, the Sun is still a very interesting object because a higher neutrino flux from the Sun could indicate neutralino annihilation in the inside (see section 1.5.2).

The Galactic plane is another source of guaranteed high energy neutrinos. The Milky Way is an ordinary spiral galaxy that appears as a bright band across the sky when seen in projection. The density of the interstellar medium is $n = 1$ particle/cm^3 and the strength of the magnetic field $3-5\mu$G. Cosmic rays interact with the interstellar medium and produce gamma rays and neutrinos due to hadronic interactions. As in the solar case, the spectra of gamma rays and neutrinos follow the cosmic ray spectrum ($dN/dE \propto E^{-2.7}$).

The neutrino flux in the Galactic plane can be estimated from the observed diffuse gamma ray flux. The disk spectrum is harder than the atmospheric neutrino flux

[1] Below around 400 MeV there are differences due to geomagnetic effects.

(mesons do not interact before decaying) and dominates at high energies. The Galactic centre region stands out against the atmospheric neutrino flux above 250 TeV with a flux of 160 neutrinos/(km^{2}year) coming from a region of 5 square degrees around the Galactic centre [50].

1.5.2 Candidate sources of high energy neutrinos

Different theoretical models predict the production of high energy neutrinos in many astrophysical objects in the Universe. The existence of some of these neutrino sources is more than probable. However, the predicted fluxes depend on the proposed model. This makes these sources *probable* in contrast with the guaranteed neutrino sources. The study of these sources is one of the main objectives for any neutrino telescope.

As in the case of cosmic rays, two scenarios are considered for the production of high energy neutrinos:

- **Bottom-up scenarios**. Neutrinos produced in beam dump processes after the acceleration of charged particles in a cosmic accelerator.
- **Top-down scenarios**. Neutrinos produced after the decay of some massive particle "X".

Neutrinos from accelerated origin

There are various astronomical scenarios where acceleration of charged particles up to very high energy can be attained. After the acceleration, such particles can collide with a target (matter or radiation) producing a cascade of particles that will end decaying and producing neutrinos. These neutrinos will carry a part of the initial energy of the primary particle. It is the same process that produces atmospheric neutrinos, but in this case the source is extra-terrestrial, even extragalactic.

Wherever there is a flux of charged particles interacting with a target of matter or radiation, there is a candidate for the production of high energy neutrinos. We summarise some of the main candidates:

- **Binary X-ray systems**

  Binary systems emitting X radiation are a possible point-like source of high energy neutrinos within our Galaxy. These systems consist of a compact object (a neutron star or a black hole) originating a magnetic field, and a companion star. Matter is transferred from the latter via an accretion disk to the compact object.

  Neutron stars are known to have very strong magnetic fields on their surface (10^{12} G) with rotation periods that may be as short as milliseconds. Particle acceleration can be explained by accretion, and also by dipolar magnetic radiation. The accelerated protons may interact with the disk or the star, and emit neutrinos and photons. Very energetic photons ($> 10^{12}$ eV) were indeed detected from Cygnus-X3 [51, 52] and Hercules-X1.

- **Young Supernovae Remnants**

  Supernovae are important sources of gamma rays and neutrinos at nuclear energies. The energy of such neutrinos is however too small for a neutrino telescope. Thus, in order to detect these neutrinos, the distance to the supernova must be small enough for the flux to be sizeable. Since supernovae are rare phenomena (occurring with an approximate frequency of one every century in our Galaxy) this detection possibility seems unlikely.

  The emission of high energy neutrinos from supernovae has also been shown to be possible [53,54], associated to particle acceleration by the shock waves at early stages.

  After the explosion, supernova remnants (SNRs) can be responsible of the emission of highly energetic neutrinos [55]. Within young SNRs, protons may be accelerated and then interact with the expanding matter of the shell that surrounds the supernova. Such a production mechanism is significant for, at most, ~ 10 years after the explosion. After that, the flux suffers a gradual decrease.

  There exist additional mechanisms associated to young SNs and capable of causing neutrino emission. Frequently, after the SN explosion the star ends up as a pulsar in fast rotation with an intense magnetic field. This may give rise to an important source of high energy neutrinos.

- **Active Galactic Nuclei (AGNs) and *Blazars***

  Active Galactic Nuclei are one of the most promising extragalactic sources of high energy neutrinos. AGNs are among the most energetic objects in the known Universe, with luminosities of $10^{42} - 10^{48}$ erg/s [56]. The only known mechanism that could provide this energy is matter accretion, at a rate of several solar masses per year, by a supermassive black hole in a galaxy centre. Such a process is restricted by the Eddington limit [57].

  Blazars are very bright objects that expel huge amounts of energy. They are thought to be AGNs where one jet is nearly aligned with the direction to the observer.

  The mechanisms of particle acceleration, as well as the composition of relativistic jets emanating from some AGNs, are not yet well known. Certain models favour hadronic mechanisms while others rely on electromagnetic processes. Neutrino production in hadronic models may take place in different places of the AGN, either in the central core or along the jets [58–60]. The different models give rise to diverse predictions concerning the neutrino flux.

  Although there is no direct evidence of neutrino emission from AGNs, the CGRO satellite has in fact observed photons of energies 10^{10} eV from many of such objects. Atmospheric Cherenkov detectors have also detected photons with energies of several tens of TeV [61–63]. The experimental evidences, however, do not allow discrimination among the different models, hence this is a question that neutrino astronomy may address.

- **Scattering on the microwave background**

  Another possibility for neutrino production is the interaction of high-energy cosmic rays with the microwave background radiation [57]. The target, in this case, is the background of remnant photons from the Big Bang, which fills the space with a density of $\sim$400 cm^{-3} and an average energy of 7×10^{-4} eV. The major mechanism of energy loss is photoproduction of resonances for cosmic rays exceeding

  $$E_p \approx \frac{\Delta^2 - m_p^2}{2(1-\cos\theta)} \approx \frac{5 \times 10^{20}}{(1-\cos\theta)} eV \tag{1.7}$$

  where θ is the angle between the proton and the photon directions. The maximum cross-section corresponds to the Δ^+ resonance ($s = 1.52\ GeV^2$). The Δ^+ decays into $p\pi^0$ with probability 2/3 and to $n\pi^+$ with probability 1/3. Neutral pions give rise to very high energy photons, whereas charged pions produce high energy neutrinos by the mechanisms described above.

  Since in each interaction the proton loses around 1/5 of its energy, its attenuation length, Λ_p, turns out to be $\sim$ 10 Mpc.

- **Gamma Ray Bursts (GRBs)**

  GRBs are the most violent known phenomena in the Universe. They are greatly energetic explosions that may last several seconds and that take place at distances in the range of red shifts $z = 0.8 - 3.4$. Data reveal an energy emission of $10^{52\pm1}$ erg only in γ rays, assuming that the emission is isotropic.

  Current models of GRB sources involve dissipation of the kinetic energy of a relativistically expanding fireball [64]. But the nature of the event that releases such an amount of energy in the form of radiation is still under discussion. They could be produced by a black hole formation from a binary system or two neutron stars, or from collapse of a very massive star.

  GRBs and the subsequent shock wave are thought to come from the concentration of one solar mass energy in a region of radius $\sim$ 100 km. The resulting explosion expands ultrarrelativistically with typical Lorentz factors ≥ 300 in the surrounding medium.

  In [65, 66] the emission of neutrinos from GRBs was proposed due to accelerated protons interacting with the fireball. The emitted neutrino flux should be in the energy range $10^{14} - 10^{16}$ eV. There are alternative models, such as that in [67], all of them predicting different neutrino spectra and fluxes.

- **Unknown phenomena**

  The existence of yet unknown or even unsuspected sources of high energy neutrinos is also a possibility. Repeatedly the opening of a new observation window to the Universe has been accompanied with new discoveries. Neutrino astronomy too can provide the opportunity of discovering new phenomena.

Neutrinos from Dark Matter and others

Not all postulated sources of high energy neutrinos correspond to cosmic accelerators. The detection of high energy neutrinos can be a powerful proof of the existence of new exotic phenomena.

There is now astronomical evidence that most of the matter in the Universe is not luminous [68]. This is known as *Dark Matter*. Evidence shows that this dark matter cannot be only baryonic.

A large number of candidates have been put forward to solve the problem of non-baryonic dark matter. In particular, several particles have been proposed with weak cross-sections and masses in the range of GeV-TeV. They are generically known as WIMPs (Weakly Interactive Massive Particles). If WIMPs exist in the halo of our Galaxy, they would occasionally be captured by the Sun or the Earth, and decay or annihilate producing detectable high-energy neutrinos at a rate that depends on the model.

A widely discussed WIMP candidate is the lightest supersymmetric particle (LSP), the lightest neutralino in a number of models. The stable neutralino should be the lightest among the four supersymmetric partners of the two neutral Higgs, the Z and the photon. If neutralinos represent a significant fraction of the Galactic halo mass, they will undergo elastic collisions with matter and accumulate in the centre of massive objects such as the Sun or the Earth. There, they will annihilate and neutrinos will be produced at the end of the possible decay chains. The energy of such neutrinos will depend on the neutralino mass, typically amounting to 1/3 or 1/2 of that mass. Therefore, point-like neutrino sources can be expected from the centre of the Sun and the Earth [69–71]. Also the Galactic centre may be a place to search for such signals [72].

A neutrino telescope that detects such a flux would allow an indirect search of neutralinos over a space region of slightly different parameters than those permitted by direct searches, especially for searches from the Sun and the Galactic centre.

Neutralinos are not the only candidates for dark matter. Other possibilities have been described, such as GUT monopoles, relativistic monopoles, supersymmetric Q-balls, cosmic strings, etc. Some of them, with masses over 10^{14} eV, are far beyond the reach of any terrestrial accelerator. Detection of neutrinos from the decay of any such candidate would be a proof of their existence.

Chapter 2

The ANTARES neutrino telescope

2.1 Detection principles

The extremely low cross-section of neutrino interactions makes them very difficult to be detected. The main considerations when designing high energy neutrino detectors relate to target volume and threshold energy. As the neutrino energy increases, so does their cross section, and thus their detectability.

On the other hand, high energy neutrino astronomy requires sensitivity over a large area. Flux estimates indicate that km^2 effective area telescopes are needed to detect point sources above the GeV region. The cost of covering such areas with detectors that intercept the particles would be prohibitive, so that the experimental method must also detect tracks at some distance from the sensors.

Cherenkov radiation emitted by neutrino induced muons allows such distant detection. In most cases, the need for a large detection volume that compensates the low signal is covered by the use of natural transparent mediums, such as ice and deep lake or sea water. However, other techniques based on the detection of radio waves or sound coming from the neutrino interactions exist, but will not be treated here.

2.1.1 Neutrino interaction

High energy neutrinos are detected by means of their charged current interactions with nucleons, either in the earth or the water. The basic process from the point of view of muon neutrino detection is the production of a charged muon

$$\nu_\mu + N \to \mu^- + X \tag{2.1}$$

where X represents a hadron shower.

The differential cross sections for neutrino deep inelastic charged current interaction in rock and in water are respectively given by [17]

$$\frac{d^2\sigma}{dx\,dy} = \frac{G_F^2 E_\nu M_N}{\pi} \frac{M_W^4}{(Q^2+M_W^2)^2} 2x \left(\frac{T_n+T_p}{2}\right) \tag{2.2}$$

$$\frac{d^2\sigma}{dx\,dy} = \frac{G_F^2 E_\nu M_N}{\pi} \frac{M_W^4}{(Q^2+M_W^2)^2} 2x \left(\frac{8T_n+10T_p}{18}\right) \tag{2.3}$$

where M_N is the mass of the target nucleon, M_W that of the W boson, Q^2 is the squared momentum transfer between the neutrino and the produced muon, and $x = \frac{Q^2}{2E_\nu M_N y}$ and $y = 1 - \frac{E_\ell}{E_\nu}$ are Bjorken scale variables. T_p and T_n correspond to interaction with protons and neutrons, and can be written as

$$T_{n,p} = 2x\left(1 - y - \frac{M_N^2 xy}{2E_\nu M_N}\right) F_{2n,p} + y^2 x F_{1n,p} + \left(y - \frac{y^2}{2}\right) x F_{3n,p} \tag{2.4}$$

$F_{in,p}$, the structure functions for neutron and proton, can be parameterised by parton distribution functions, which depend on x and Q^2.

The asymptotic behaviour of the neutrino cross-section with energy is of the form:

$$\sigma \propto E_\nu \quad \text{for} \quad E_\nu > 10\,\text{TeV} \tag{2.5}$$

$$\sigma \propto E_\nu^{0.4} \quad \text{for} \quad E_\nu > 1\,\text{PeV} \tag{2.6}$$

whereas for lower energies ($E_\nu < 100$ GeV) the cross section remains essentially constant.

The resulting muon can travel a long distance in matter. At the energies of interest for cosmic neutrino detectors, their range in ice or water is 3–20 km. Therefore, the detector can observe muons produced in neutrino interactions that take place well outside the instrumented volume.

The range of such muons increases with energy, so that detection of high energy neutrinos is favoured. The increasing neutrino cross section also enhances detectability of high energy neutrinos. Nevertheless, power law neutrino fluxes fall fast with energy. This competes with the previous effect as it reduces the expected muon fluxes.

The use of high energy muons coming from interactions as described above was proposed by A. M. Markov more than 40 years ago [5]. Although various approaches exist for muon detection [60], the most feasible one relies on the observation of Cherenkov light emitted by the muons at their pass through water or ice.

Directional information of the neutrino can be retrieved from the direction of the produced muon, since the mean relative angle between the neutrino and muon trajectories can be approximated by the expression

$$\langle\theta_{\mu\nu}\rangle = \frac{0.64^o}{(E_\nu/\text{TeV})^{0.56}} \quad E_\nu > 10\ \text{TeV} \tag{2.7}$$

The difference in angle is small and decreases with neutrino energy.

Muons produced by cosmic neutrinos are not the only ones that arrive to the detector. On the contrary, an overwhelmingly higher number of muons come from cosmic ray interactions in the atmosphere. However, whereas neutrinos can pass through Earth without interacting, muons and other known particles are stopped by it. Therefore, an upward going muon uniquely identifies a nearby neutrino interaction, and rejection of down-going muons becomes crucial.

2.1.2 Muon propagation

Muons produced in cosmic neutrino collisions lose energy as they travel from the interaction vertex to the detector. The dominant processes responsible for the energy loss are ionization, pair creation, bremsstrahlung and photo-nuclear interaction.

The joint contribution of these processes can be approximated as:

$$\langle \frac{dE}{dx} \rangle \propto \alpha + \beta E \tag{2.8}$$

The dominant term at low energies (< 1 TeV) comes from ionization. Over 1 TeV the energy loss is dominated by the remaining processes, and turns out to be, in average, proportional to the energy.

2.1.3 Cherenkov radiation

The mechanism used in neutrino telescopes for muon detection is the Cherenkov emission. Charged particles travelling through a medium with a velocity that exceeds the velocity of light propagation in that medium emit an electromagnetic radiation. This is called the Cherenkov effect, and it is known since 1934. The explanation of the phenomenon lies on the ground of classical electrodynamics and it is due to coherent emission along the route of the particle.

In transparent mediums, as water or ice, it appears as a continuum spectrum of visible light that is emitted in a fixed direction with respect to the particle movement. This direction, known as *Cherenkov angle*, is given by

$$\cos\theta_C = \frac{1}{\beta n} \tag{2.9}$$

where n is the refractive index of the medium and $\beta \equiv v/c$ and where v is the particle velocity. The particle will radiate as long as $\beta > 1/n$.

For relativistic particles ($\beta \simeq 1$) the Cherenkov angle does not depend on their energy [73]. Thus particles with relativistic energies will radiate at fixed angle along their path until close to the Cherenkov threshold, which involves only the last few centimetres of range. In particular, for relativistic muons in water ($n = 1.346$) the angle is $\theta_C \approx 42.2^o$.

The spectrum of Cherenkov light is proportional to $1/\lambda^2$. The number of radiated photons per unit length x and wavelength λ is given by the Frank-Tamm formula [74],

$$\frac{d^2N}{dx\ d\lambda} = \frac{2\pi\alpha z^2}{\lambda^2}\left(1 - \frac{1}{\beta^2 n^2}\right) \tag{2.10}$$

where z is the charge of the particle. Although the shortest values of λ are the most favoured by this law, the detectors must also consider the attenuation in the medium and the detector acceptance and optimise detection for the best transmitted wavelengths.

Within the useful wavelength range for water and detectors, it is acceptable to take n as roughly constant. Therefore taking $n = 1.35$ and $\beta = 1$, and integrating over the range 300 nm $< \lambda <$ 600 nm that corresponds to the sensitive range of ANTARES, the number of emitted photons per unit length can be estimated as

$$\frac{dN}{dx} = 345\ \mathrm{cm}^{-1} \tag{2.11}$$

The energy loss due to Cherenkov effect is of the order of 10^{-3} MeV cm^{-1}, negligible with respect to the other mechanisms (for a minimum ionising particle in water, the energy loss is of the order of 2 MeV cm^{-1}).

Nevertheless, the Cherenkov effect constitutes a powerful tool that is at the basis of muon reconstruction in neutrino telescopes. To take advantage of this phenomenon, photomultipliers of large diameter are distributed over a large volume of the transparent medium. They are used to register the arrival times of Cherenkov photons to well-known positions. The muon trajectory is then reconstructed from such measurements. Energy reconstruction is also possible from the measurement of the collected intensity.

2.2 Physical background

Besides the expected signal from cosmic neutrino sources, the detector receives two types of background. One of them is due to the environment and is uncorrelated to the physics of interest. It will be described, in the context of ANTARES site, in section 2.4.1. In this section we discuss the so-called physical background, which is closely related to the physical processes that are under study.

There are two sources of physical background. On one hand, there are muons produced in atmospheric cascades by primary cosmic rays. On the other, there are also atmospheric neutrinos from the same origin, that can produce muons by the same mechanism as the signal neutrinos.

The origin of both types of muons is the interaction of cosmic rays in the atmosphere. When a cosmic proton interacts with an atmospheric nucleus it gives rise to a hadron cascade composed, among others, of π^+ and π^- that can decay giving μ and ν.

Figure 2.1 shows the muon flux induced by atmospheric neutrinos and that of direct atmospheric muons as a function of the zenith angle. The atmospheric muon flux

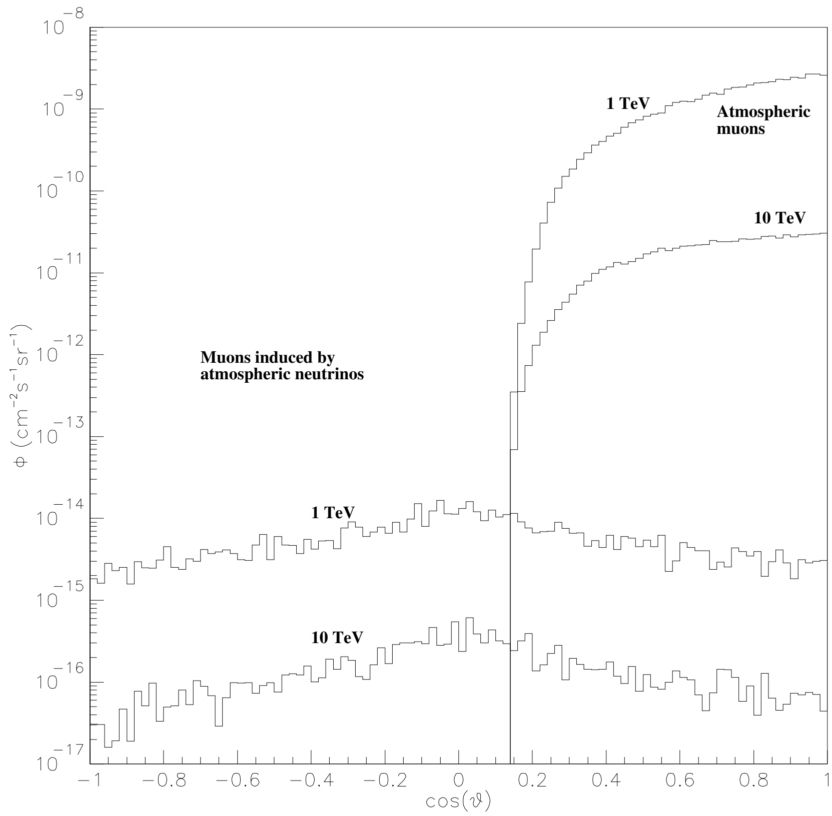

Figure 2.1: Different contributions to muonic background: atmospheric muons and atmospheric neutrino induced muons. Fluxes are shown as a function of the zenith angle for a detector depth of 2300 m.

exceeds that of muons induced by atmospheric neutrinos by six orders of magnitude (see fig. 2.1).

Direct atmospheric muons are absorbed by the Earth. Therefore the expected background is solely constituted of down-going muons and therefore restricts the search for signal exclusively to up-going reconstructed events. Sometimes a group of parallel muons coming from the same atmospheric cascade arrive together to the detector. They are called multi-muons and may induce errors in the reconstruction as they can be wrongly reconstructed as an up-going event. Thus the rejection factor of reconstruction algorithms must be of $1 : 10^6$ in order to distinguish unmistakably a down-going muon or a multi-muon from an up-going muon.

The atmospheric muon background forces the site of the detector to be very deep, in order to have the largest possible shielding. Figure 2.2 shows how the flux of atmospheric muons decreases with depth.

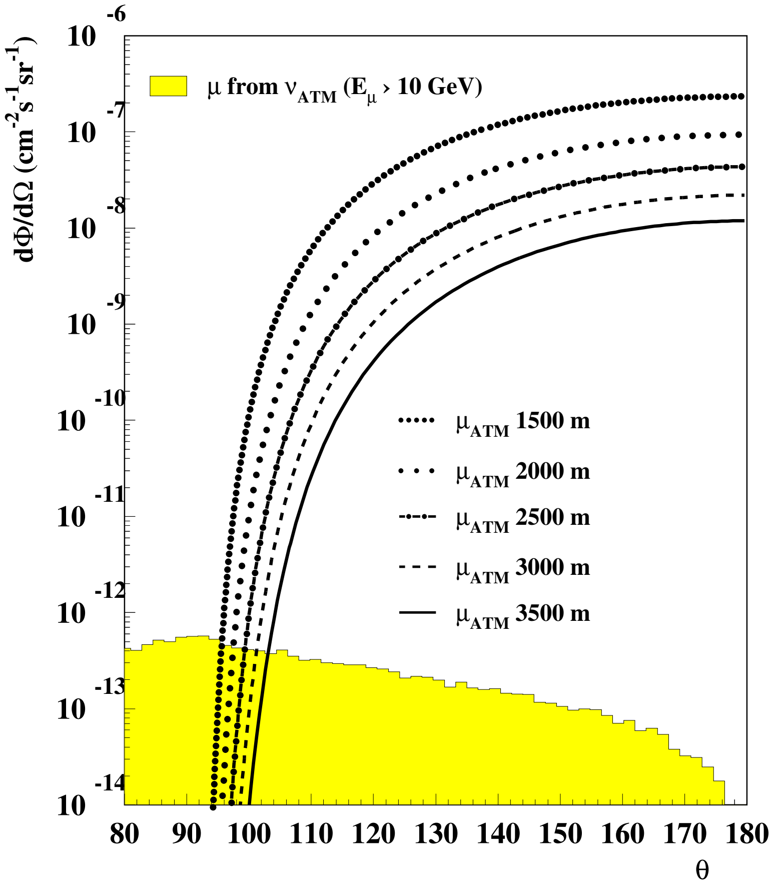

Figure 2.2: Decrease of atmospheric muon background with depth (in meters of water equivalent).

Muons induced by atmospheric neutrinos constitute a much more dangerous irreducible background since such neutrinos cannot be distinguished from cosmic ones. These neutrinos arrive to the detector from all directions, although as seen in fig. 2.1 they show a certain angular dependence. They are not absorbed by the Earth and can give rise to both up-going and down-going muons.

As discussed in chapter 1, their flux can be approximated by an exponential law with an spectral index one unit higher than that of primary cosmic rays. The background decreases faster than the signal from cosmic sources, as this follows the spectrum of cosmic rays. Therefore at high energies cosmic neutrinos are expected to dominate over the atmospheric neutrino background.

2.3 Other neutrino telescopes

In this section we briefly review the characteristics of existing projects for neutrino telescopes (see 1.2). Only those projects based on the Cherenkov light technique are reviewed. See references in [75] for experiments based on other techniques.

2.3.1 DUMAND

The DUMAND project [76], based in Hawaii, was a pioneer experience at the attempt to build a neutrino telescope under water. Although the project was cancelled in 1995, it supposed a big stimulus for the field and many subsequent experiments have benefit from its technical developments.

2.3.2 BAIKAL

The Baikal project [77,78] consists of a neutrino telescope placed at around 1300 m deep in lake Baikal, in Siberia. In winter the surface of the lake freezes, what makes deployment easier than in deep ocean detectors, since it is possible to operate from a solid surface.

The detector consists of 200 PMTs arranged in 8 lines (see fig. 2.3). At present the experiment is already reporting observation. Its performance is, however, limited by the maximum achievable depth and the optical properties of the lake water with absorption lengths about three times shorter than in deep ocean sites, due to the reduced transparency of the lake.

2.3.3 AMANDA and IceCube

The AMANDA project [79,80], started in 1992, is a neutrino telescope located in the South Pole, within the Antarctic ice. Deep ice presents longer absorption length than deep ocean water and therefore collects better Cherenkov light. This allows to cover a larger effective area with the same number of PMTs, since they can be more sparsely distributed. Moreover, the optical background in ice is practically inexistent.

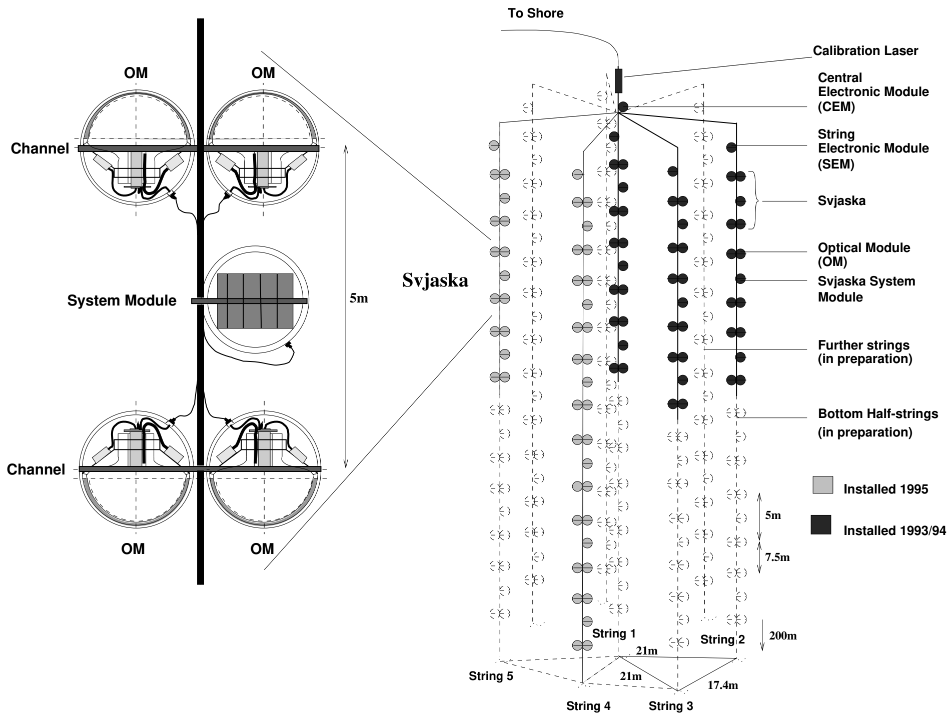

Figure 2.3: Schematic view of the Baikal Neutrino Telescope.

Nevertheless, the scattering length in ice is shorter than in water, and affects negatively the achievable angular resolution.

The first four lines were deployed in 1993–1994 at 1000 m depth (AMANDA-A). The deployment of the detector, AMANDA-B10, started in 1995 and consisted of 10 lines deployed in a cylinder of 120 m diameter, between 1500 and 2000 m. AMANDA-B10, operational since 1997, reported results for measurements on atmospheric neutrinos and searches for astrophysical sources and Dark Matter.

The present version, AMANDA-II, consists of 667 optical modules arranged in 19 lines (see fig. 2.4). The outer nine strings are arranged around a cylinder of 200 m diameter. Its installation started in 1997 and it has been operational since 2000.

Making use of AMANDA's basis on deployment and operation, the IceCube project [81, 82] proposes the installation at the same site of a larger detector with approximately one cubic kilometre. The project consists of 4800 optical modules arranged on 80 lines that should be deployed over the next five years.

Both being located at the South Pole, AMANDA and IceCube are not able to observe the Galactic Centre.

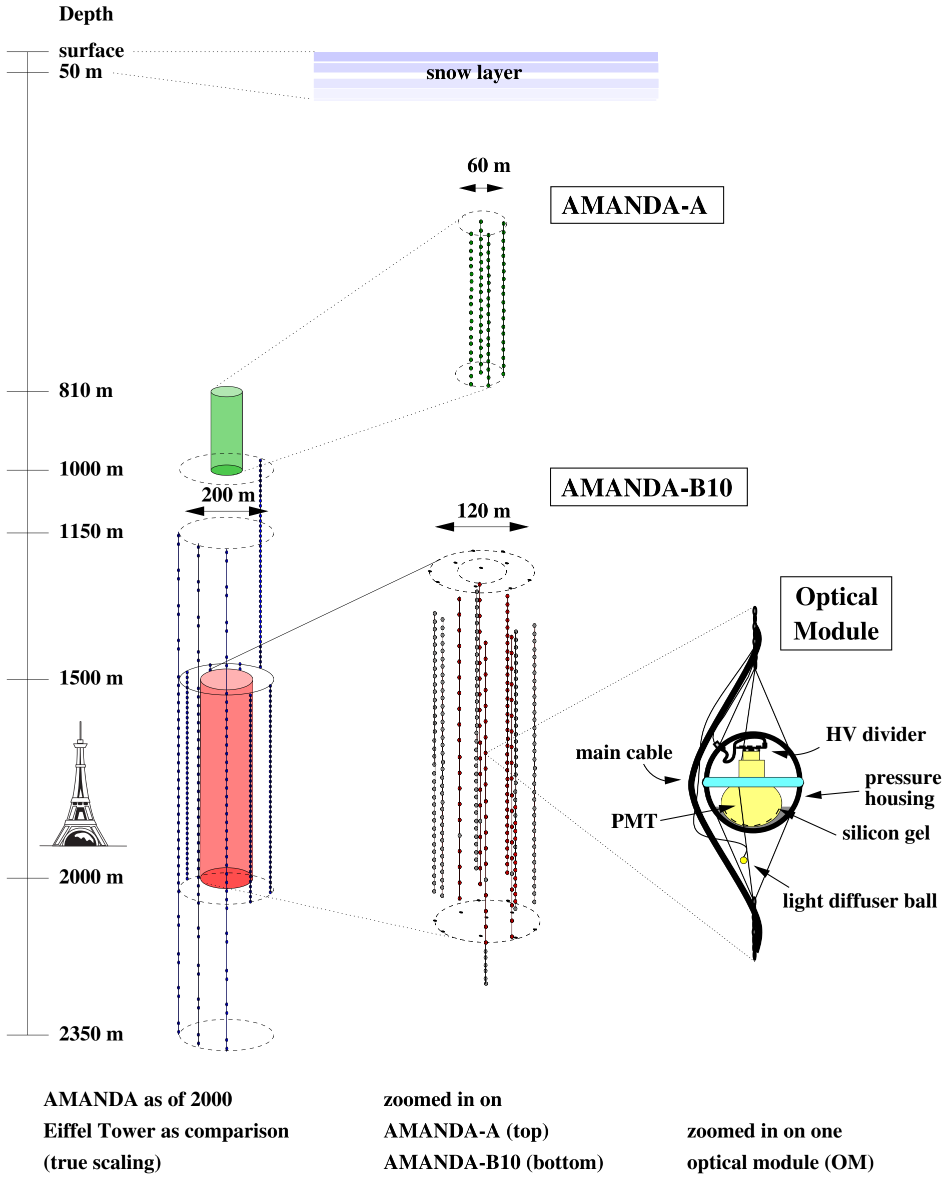

Figure 2.4: Schematic view of the different versions of the AMANDA detector: AMANDA-A (4 lines, 60 m diameter), AMANDA B-10 (10 lines, 120 m diameter) and AMANDA-II (10+9 lines, 200 m diameter).

2.3.4 NEMO

Starting in 1999, the NEMO project [83] proposes the installation of a large area neutrino telescope in the Mediterranean Sea, near the Italian coast of Sicily. At present, the site is still under study. The proposed detector consists of an array of towers with a series of stories, each one supporting four optical sensors.

2.3.5 NESTOR

The NESTOR project [84,85] aims to install a neutrino telescope in the Ionian Sea. The site is located at Pylos, near the Greek coast, at 3800 m depth. NESTOR benefits from the excellent optical properties of the water at such depth, although the same circumstance hinders the deployment.

The proposed detector consists of rigid independent towers formed by 12 hexagonal floors. At each apex and at the centre of each hexagon there are two PMTs, oriented upward and downward. At present the project is in the phase of Research and Development, with one tower deployed.

2.4 The ANTARES experiment

The ANTARES project (Astronomy with a Neutrino Telescope and Abyss environmental RESearch) was born in 1996. At present it is an international collaboration with the interdisciplinary participation of particle physicists, astrophysicists and oceanologists from France, Germany, Italy, The Netherlands, Russia, United Kingdom and Spain. ANTARES facilities are located near the south coast of France, taking advantage of its proximity to the shore and IFREMER[1] installations.

Currently the ANTARES experiment is under construction. After the research and development program covered in the first 5 years of the experiment, today the first components of the detector have been installed and connected to the shore. Moreover, a first prototype string has been installed, connected and recovered between April and July 2003. The aim is to complete the detector up to the 12 proposed strings before the end of 2006.

In this section we describe some of the measurements of environmental parameters relevant for the detector performances. We also present the detector design and a description of the construction stage and future developments.

2.4.1 The ANTARES site

The chosen site is located at a distance of 20 nautical miles from Toulon (see fig. 2.5), at coordinates 42° 50'N, 6° 10'E, and a depth of around 2400 m.

ANTARES must operate within deep sea water, and there is a number of environmental parameters that will affect the detector performance. Among them, water

[1] Institut Français de Recherche pour l'Explotation de la Mer.

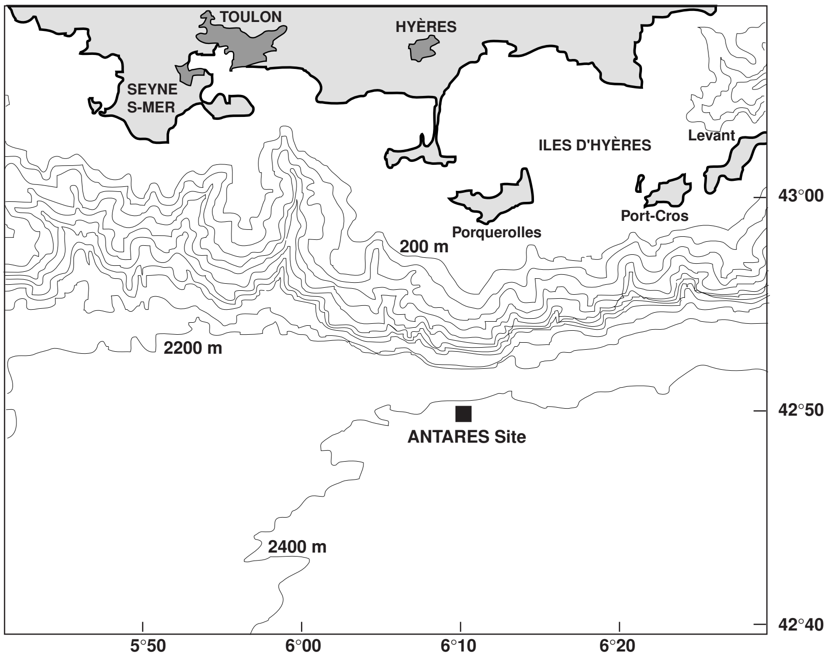

Figure 2.5: Location of the ANTARES site near the south coast of France.

transparency, depth, optical background, undercurrents and sedimentation. Numerous studies and measurements have been taken in order to characterise the main parameters in the finally chosen location.

Optical background

Besides the physical background, described in sect. 2.2, there exists phenomena, not related to the physics under study, which induce a signal in the detector. This optical background has been extensively measured in the ANTARES site [86] in order to determine its time dependence, spatial extension and correlation with currents. The optical background influences the trigger, the electronics and the mechanics of the detector. To perform the measurements, a test line was immersed during variable periods of time during several months. Figure 2.6 shows a typical counting rate obtained for an optical module.

The data stream consists of two components: a continuum base rate of a few tens of kHz, varying slowly on time scales of a few hours, and sharp peaks lasting a few seconds and rising to tens of MHz. The lowest level is relatively stable, and may be partially explained by the bioluminiscence and the radioactive decay of ^{40}K. This element, naturally present in water, decays mainly (BR=89.3%) through β-decay

$$^{40}K \rightarrow {}^{40}Ca + e^{-} + \bar{\nu}_e \tag{2.12}$$

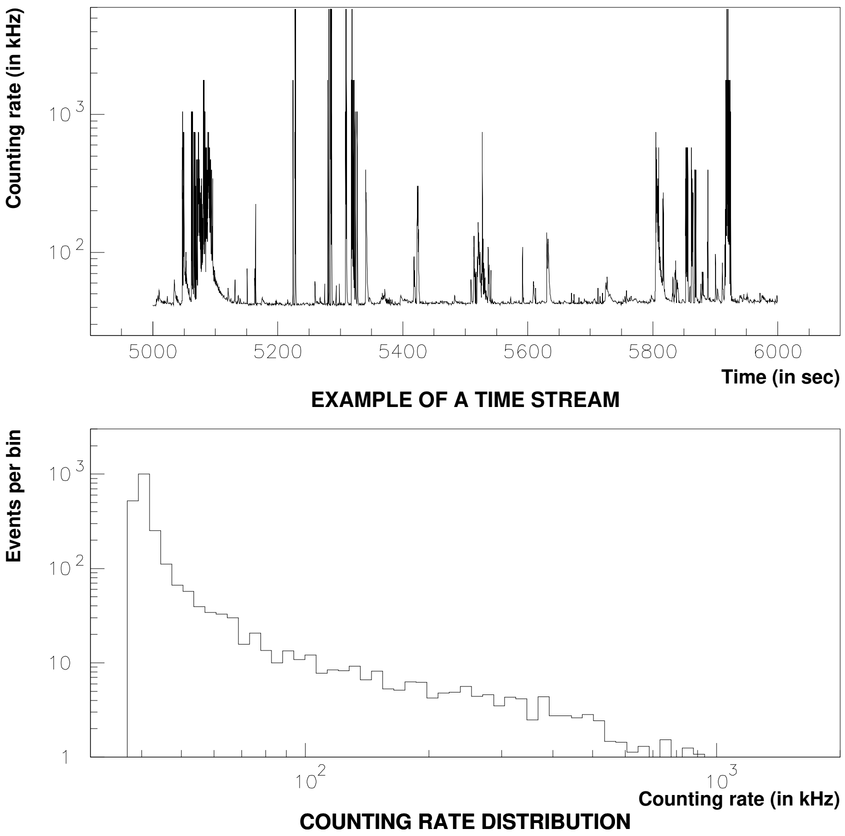

Figure 2.6: Time evolution of the counting rate in an optical module (upper) and probability distribution of the counting rate (lower) [86].

The electron carries a maximum energy of 1.3 MeV, enough to produce emission of Cherenkov photons in water. This produces a continuous random background with a predicted rate of $\sim$ 30 kHz. The remaining are due to bioluminescent activity of bacteria colonies. The amount of this contribution varies depending on the period of data taking. The peaks are also attributed to bioluminiscent emissions. They are correlated to currents and show a limited spatial range.

Over 200 kHz the electronics dead time becomes significant. Using the distribution of fig. 2.6 the estimated dead time of each PMT, i.e. the period during which the rate exceeds 200 kHz, is 5%, randomly distributed over the whole detector.

The influence of this kind of background may be reduced by asking for strict temporal coincidences between at least two modules of each group. The background is more effectively reduced by applying more restrictive cuts on the amplitude of signal at the PMT's. Thus, increasing the threshold from 0.3 to 2 photoelectrons, the counting rate is reduced by a factor $\sim$ 100, with minimum signal loss.

Water optical properties

The water transparency at the detector's site directly affects the muon detection efficiency and the angular resolution. The attenuation length limits the size of the sensitive volume, whereas the scattering of light affects the final angular resolution. These parameters depend on conditions of the water such as salinity or temperature and must be measured in situ.

The effective attenuation length results from the combination of two effects, namely diffusion and absorption, according to the following relation,

$$\frac{1}{\lambda_{att}} = \frac{1}{\lambda_{abs}} + \frac{1}{\lambda_{scatt}} \tag{2.13}$$

The attenuation length was estimated using a PMT and a blue LED, and measuring the required intensity to obtain a constant response of the PMT when the distance between them was varied. The result, for a wavelength of $\lambda = 466$ nm was

$$\lambda_{att} = 41 \pm 1_{stat} \pm 1_{syst}\ m \tag{2.14}$$

In order to distinguish scattering from absorption, another experimental device was used. A pulsed isotropic source was located at 24 or 44 m from a PMT and the delay in the arrival of photons was measured [87]. The observed time distribution of photons is shown in figure 2.7. They allow the estimation of the diffusion length.

Table 2.1 summarises the experimental results for water transparency.

There, $< \cos\theta >$ represents the average diffusion angle. It is possible to define an effective diffusion length as

$$\lambda_{eff.scatt.} = \frac{\lambda_{scatt}}{1 - < \cos\theta >} \tag{2.15}$$

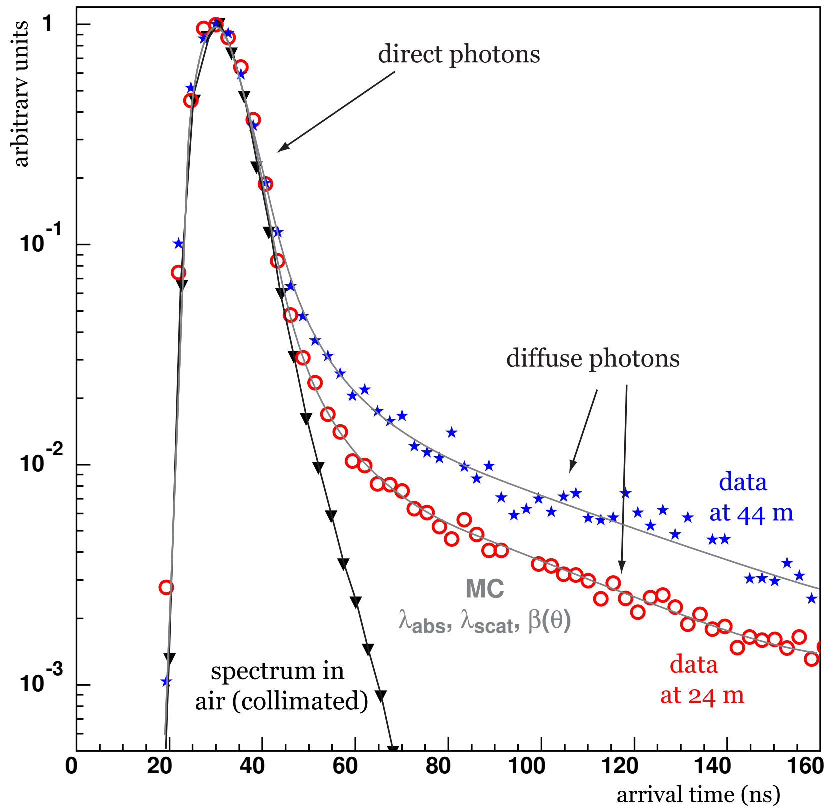

Figure 2.7: Normalised distributions of time of arrival of photons to the photomultiplier for various distances.

Colour	Period	λ_{abs}(m)	λ_{diff} (m)	$< \cos\theta >$
Blue (466 nm)	June 2000	48.4 ± 0.3	79 ± 8	0.74
U.V. (370 nm)	June 2000	28.0 ± 0.1	46 ± 1	0.63

Table 2.1: Measured optical properties of the water.

that may be compared to the absorption length to estimate the relative importance of each effect. The effective diffusion length for blue light is of the order of ~ 300 m, whereas for the U.V. range it is ~ 100 m. In any case, it is larger than the absorption length, so that for ANTARES absorption is the dominant effect.

Sedimentation and biofouling

The detector performance is also affected by two further effects that take place within ocean water, namely biofouling and sedimentation. The former consists in bacterias and micro-organisms growing on the surface of optical modules, whilst the latter is caused by dust settling on the modules. Both effects reduce the transmitted light intensity by gradually reducing the transparency of the glass spheres that host the PMTs.

Sediments affect only the upward facing surface of the optical modules, what excludes the possibility of orienting the PMTs upwards. Bacterias and micro-organisms, on the other hand, grow all over the surface. Films formed by these colonies are almost transparent, but they serve as support for the adherence of sediments.

Whereas proliferation of bacterias decreases with depth, the sedimentation rate strongly depends on the location. Different tests have been performed at the ANTARES site in order to quantify the effect in terms of time and orientation of the optical modules [88].

After one year, the estimated transparency loss is $\sim 2\%$ in the horizontal direction and tends to saturate as shown by fig. 2.8. The occasional recovery of transparency is due to underwater currents, that have the effect of cleaning the modules. Since in the ANTARES detector PMTs are downward oriented, this quantity represents only an upper bound for the actual transparency loss.

The sedimentation rate presents a remarkable seasonal dependence, that can be correlated to variation of meteorological events. The average accumulation rate is 0.04 g/(cm^2 yr).

2.4.2 The ANTARES detector

The ANTARES detector [89] consists of a number of identical independent lines separated by a distance of ~ 60 m. Each line supports 75 optical modules arranged in groups of three, which are equally spaced along the line. Figure 2.9 shows a schematic view of the detector configuration. The finally approved detector will consist of 12 such lines.

An additional instrumentation line will be deployed in addition to the detector ones. Figure 2.10 shows its composition. This line will be equipped with the following electronic devices to perform detailed oceanographic measurements:

- acoustic velocimetres are used to determine the water temperature and the sound velocity;

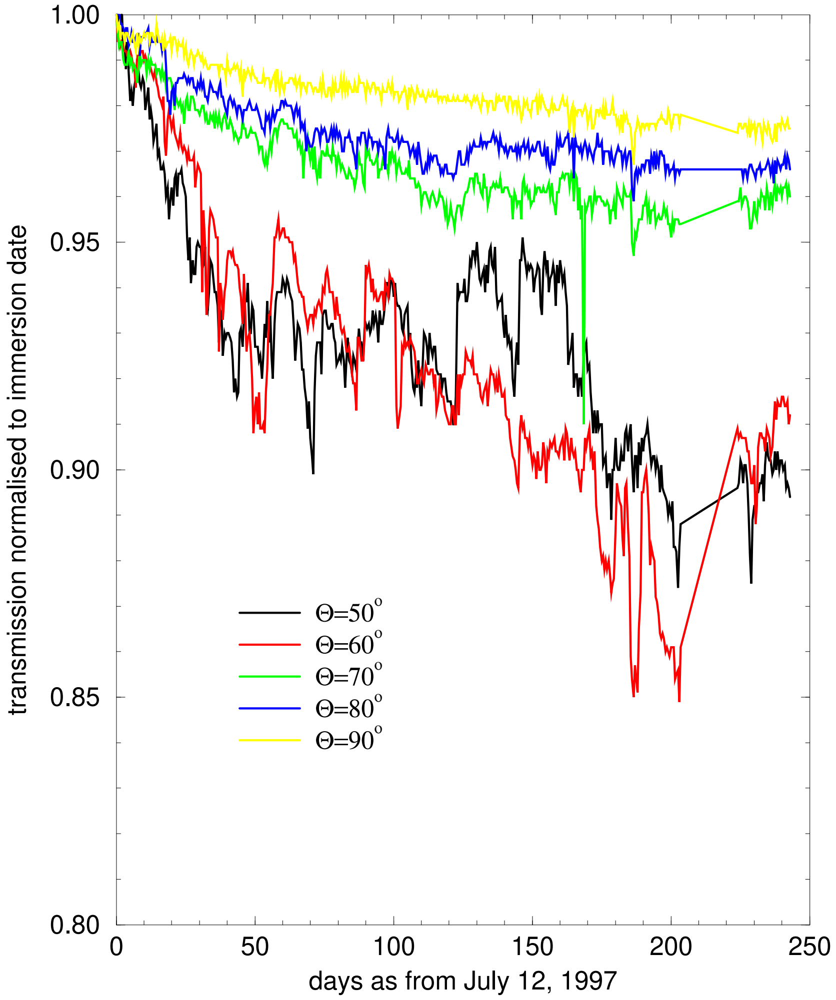

Figure 2.8: Decreasing of transparency of an optical module, at different angles close to the horizontal, over 8 months.

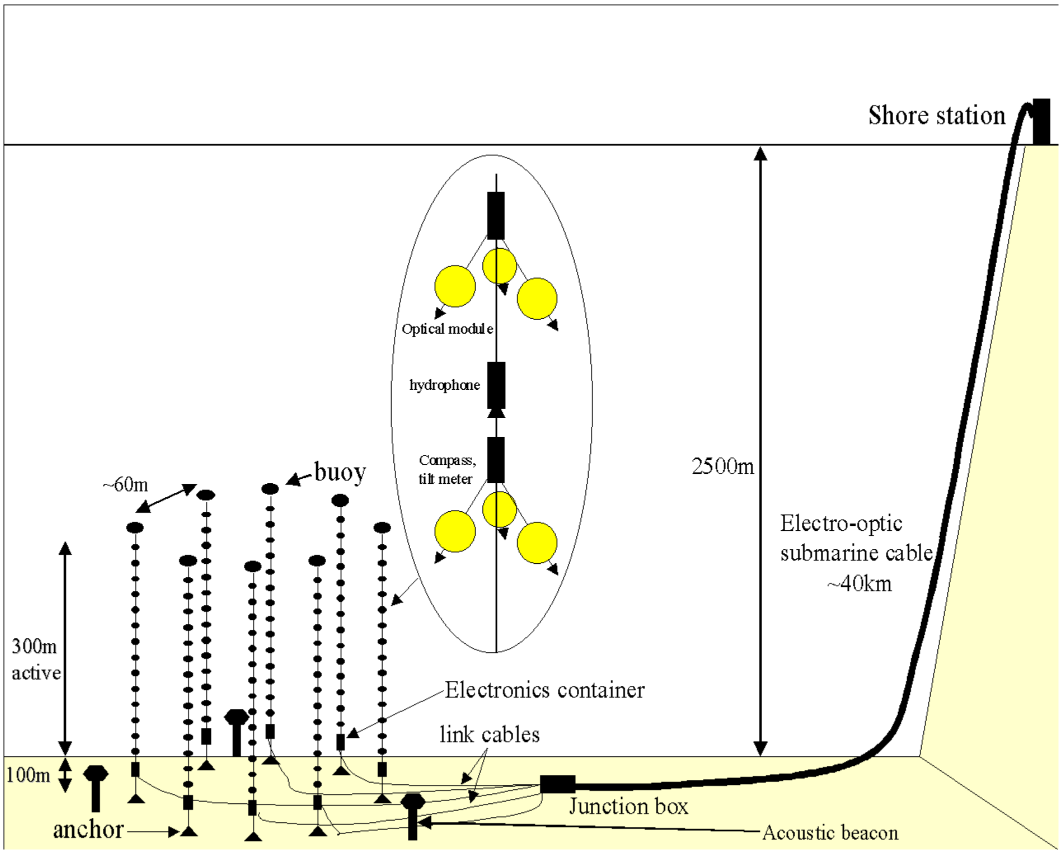

Figure 2.9: Schematic view of the ANTARES detector.

- ADCP (Acoustic Doppler Current Profiler), downward oriented, can trace a profile of underwater currents in ~ 150 m;
- the CTD measures the conductivity, temperature and density with a resolution of 10^{-4} °C, 10^{-4} S/m ;
- the CSTAR transmissometer can measure the variation in the light attenuation coefficient along 25 cm using light of wavelength $\lambda = 470$ nm.

At the bottom of this line a laser beacon emitting very short (FWHM < 1 ns) light pulses of $\lambda = 532$ nm and 1 μJ is used for time calibration, like the LED beacons placed along the instrumentation and detection lines. On the sea bed, at a certain distance from the line, is located a seismometer.

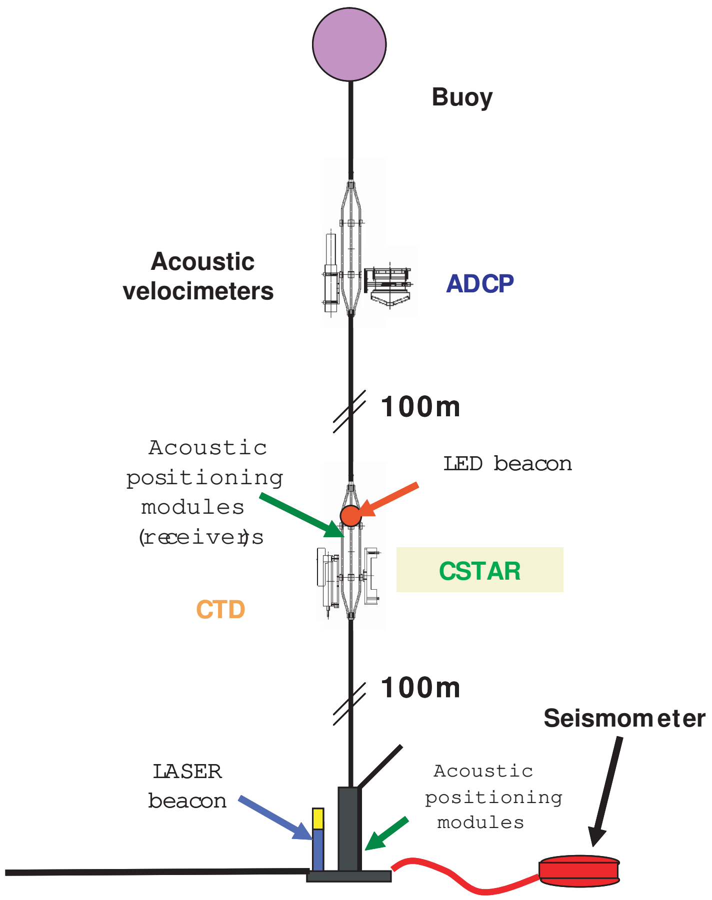

Figure 2.10: Schematic view of the instrumentation line.

All lines are connected to a single junction box which provides power and control signals and which is connected to the shore by a 48 km long electro-optical cable. Connection between cables that link the lines to the junction box is performed by a submarine. All the information collected by the detector passes through the junction box and is transmitted to the detector control room on the shore through this main cable, transformed into light signal.

The Optical Modules

Each PMT is housed in a glass sphere capable to resist the water pressure up to 6 km deep. The sphere, together with the enclosed PMT and accompanying electronics, make up an optical module (OM) [90], the basic component of the ANTARES detector.

Figure 2.11 shows the structure of an optical module. Each glass sphere, of diameter 43 cm, and thickness 1.5 cm, contains a photomultiplier (Hamamatsu R7081-20) with a photocathode diameter of 10 inches. A silicone gel ensures the optical coupling between the photomultiplier and the sphere, also fixing the PMT to the front of the sphere.

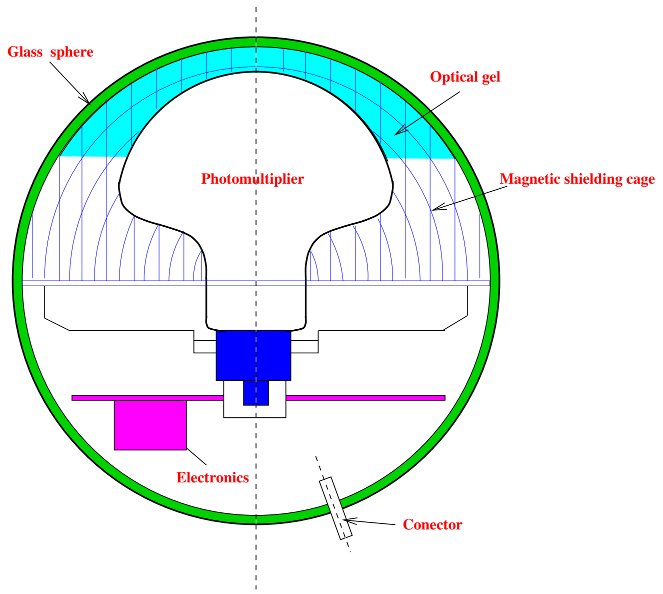

Figure 2.11: Organisation of elements within an optical module.

The inner surface of the back hemisphere is covered with black paint, which absorbs induced photons and reduces the danger of inner reflexion. Finally, each PMT is surrounded by a metal cage in order to shield it from magnetic perturbations. The Earth's magnetic field (of ~ 0.5 G) may indeed deviate the trajectory of low energy electrons inside the photomultiplier, hence degrading the uniformity of the PMT response. The shielding net is made of μ-metal, an iron and nickel alloy of high magnetic permeability.

The detector lines

The optical modules are arranged in triplets, and mechanically attached to the lines. Those OMs within the same group are equally spaced at 120°, and with an orientation of 45° downward from the horizontal direction. Each triplet of optical modules, corresponds to a detector *storey*, that comprises also the accompanying electronics, namely a local control module (LCM), a tiltmeter and a compass located into a common titanium container.

The separation between adjacent storeys in a line is of 14.5 m. Five storeys compose a "sector", the minimal detection unit of the ANTARES telescope.

Every line consists of five sectors, i.e. 25 storeys, covering an active length of 348 m. The total length of the electro-mechanical cable that supports the line and provides connection and energy supply to the storeys is of 450 m. The lowest 100 m are not instrumented, to provide a larger observation volume for the Cherenkov light of upgoing particles.

Along each line, LED beacons will be placed for time calibration. There will be one such LED beacon per sector, consisting of a transparent pressure resistant cylinder that contains 30 blue LEDs (see below). In combination with the acoustic positioning system, this allows the time calibration of PMTs, complementing the function of the laser beacon mentioned above.

Lines are not rigid, but slightly flexible, to reduce the risk of damage due to strains during immersion or to underwater currents. The verticality of the line is maintained by a buoy attached to the upper end of the line.

Each line is fixed to the sea bed by an anchor. At the bottom of the line there is also the electronics for controlling the line, an hydrophone for the acoustic positioning and the system that ensures the connection of the line to the junction box.

Calibration of the OMs

The efficiency of the PMTs is calculated as the product of the quantum efficiency, that measures the probability for a single photon to produce a photoelectron, and the collection efficiency, that represents the probability for a photoelectron in the PMT to reach the first dynode. Fig. 2.12 shows the measured efficiency for normal incidence. The maximum efficiency is found to lie between 320 and 520 nm.

The angular efficiency of the OM was performed using a specific experimental arrangement designed to simulate the immersion conditions. The optical module is placed in a cylinder containing pure water and isolated from outside light. The PMT detects then the Cherenkov light produced by atmospheric muons.

The empirical results show (see fig. 2.13) that the amount of observed light varies as the inverse of the distance from the PMT to the track and that, for a fixed distance, the maximum number of collected photoelectrons occurs at an angle of $\sim 42°$ between the track and the observing direction of the PMT. This can in fact be considered as a measure of the Cherenkov angle in water.

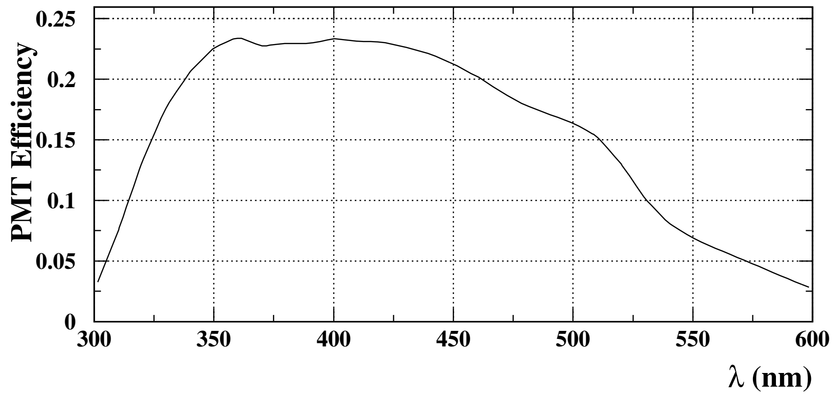

Figure 2.12: Measured efficiency (product of quantum times collection efficiency) of the PMTs.

Signal Digitisation and Time Calibration

All the signals from the PMTs are digitised before being transmitted to the shore by means of an specific integrated circuit called the ARS (Analogue Ring Sampler [91,92]). In every optical module there are two ARS chips in order to reduce the overall dead time.

Only those PMT signals whose amplitude is above a given threshold are digitised. There are two possible modes for digitising signals. If the threshold is reached, the maximum amplitude and time extension determine in which mode an event is processed.

- Most signals ($> 98\%$) correspond to a single photoelectron. These signals present a uniform shape, therefore only their total charge and time are stored and transmitted. The time is given by the moment when the signal overpasses the amplitude threshold. The amplitude is obtained by integrating over a 33 ns window (8 ns before the time of signal and 25 ns afterwards). This processing mode is called SPE (Single Photo-Electron).

- If the amplitude or duration of a signal exceed those of a single photoelectron, then the pulse shape is sampled at a rate $0.3 - 1$ GHz, digitised and transmitted to the shore for a complete analysis. This processing mode is called WF (Wave Form).

The arrival time of a hit must be determined with resolution better than 0.5 ns. The time measurement is based on the general clock of the detector (20 MHz) and the precise determination of time between two clock periods (50 ns) which is granted by the digitised signal of a time-voltage converter (TVC). Figure 2.14 shows this process.

Since the arrival time information is essential for track reconstruction, it is fundamental to control the uncertainties in time measurement. These are mainly due to

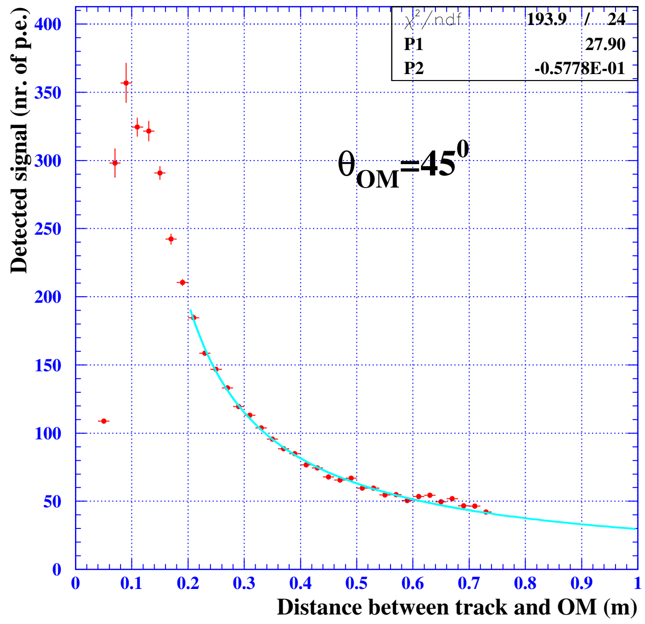

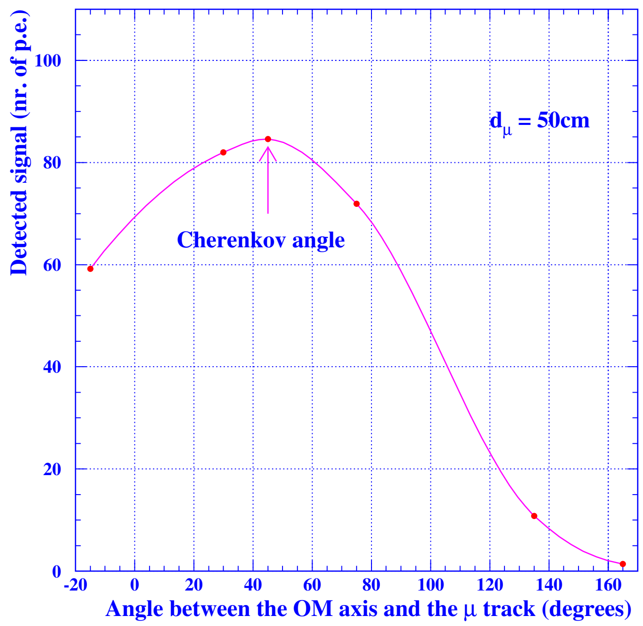

Figure 2.13: Number of collected photoelectrons as a function of the distance to the track (upper) and the angle between the PMT axes and the muon direction (lower).

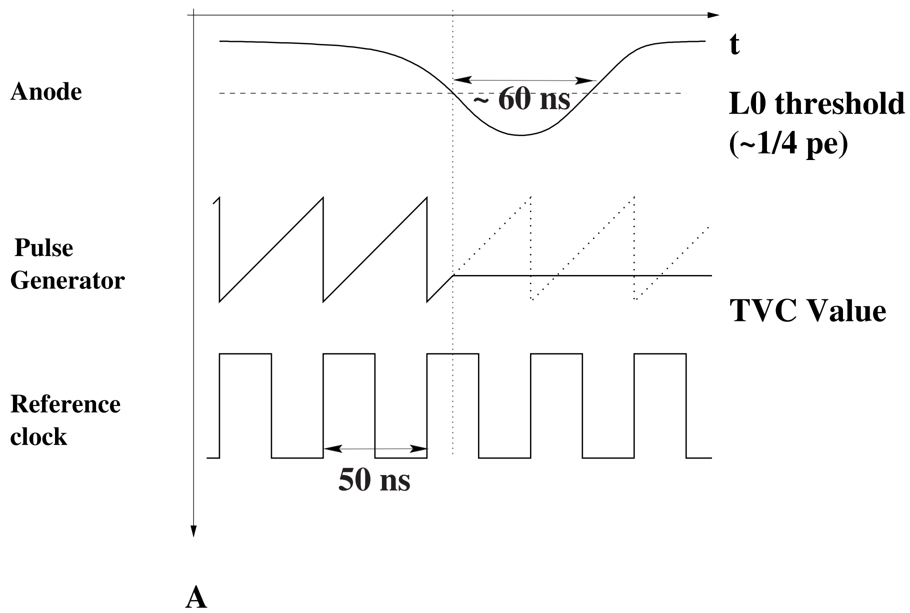

Figure 2.14: Use of the TVC for accurate time determination.

fluctuations in the transit time within PMTs, precision in the electronics ($\sigma < 0.5$ ns) and chromatic dispersion of the group velocity of photons in water ($\sigma \sim 1.5$ ns). Several complementary systems are used for time calibration of the detector [93]. In particular, external light sources (optical beacons) allow to estimate global relative delays. There are two kinds of optical beacons in ANTARES detector.

1. A Laser Beacon is located at the base of the instrumentation line and in the central line. It consists of a Nd-YAG laser, with the associated electronics, enclosed in a titanium container. The laser emits short light pulses (FWHM < 1 ns) at $\lambda = 532$ nm whose high intensity ($\sim 1\ \mu$J) allows most PMTs to be illuminated at once. An internal photo-diode provides precise information on the time of emission.

2. LED Beacons are placed along each detector line and in the instrumentation line. They consist of a pressure resistant cylinder which contains 30 LEDs emitting pulses from 5×10^6 to 8×10^7 photons at $\lambda = 470$ nm. Each LED beacon can illuminate several storeys of the adjacent lines.

All time calibration systems aim to achieve a precision of < 0.5 ns, which allows an angular resolution better than $0.3°$ for the reconstructed tracks of muons with $E > 1$ TeV.

2.4.3 Construction stage

The ANTARES project is currently about to start the construction stage [94]. The first phase of the experiment involved measurements of the most relevant environmental parameters, as well as testing of mechanics, electronics, etc. At the moment, several final devices, such as the junction box and the main cable are already installed.

From November 1999 to June 2000 a demonstrator line with 7 PMTs was deployed at a depth of 1100 m. Its operation allowed testing of the acoustic positioning system, and took measurements which reproduced the atmospheric muon flux.

In October 2001, the main electro-optical cable was installed. The junction box was also installed and connected to the cable by December 2002.

In December 2002, a prototype line (sector line) consisting of a single sector, i.e. 5 storeys to a total of 15 OMs was installed.

In February 2003, a reduced instrumentation line was also deployed for testing. It was more than 200 m long and supported several devices for accurate environmental measurements, a LED beacon and a laser beacon.

Both the sector and the instrumentation line were connected by the Nautile submarine in March 2003 and operated between April and July 2003, being afterwards recovered.

Besides the test of deployment, connection and retrieval operations, the sector and instrumentation line provided a test on the operation of the actual detector components in a real situation. During their operation time, the instrumentation line also performed measurements of the optical background and site parameters.

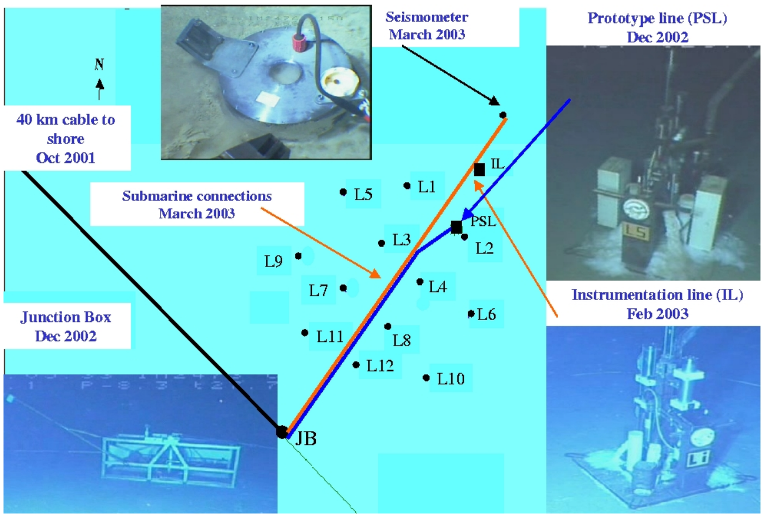

Figure 2.15: Positions of prototype and detector lines [94].

The whole detector, i.e. the 12 detection lines, as shown in fig. 2.15, is expected to be completed by 2006.

2.5 Monte Carlo tools

The ANTARES Collaboration has devoted a great effort in the development of software tools to simulate the expected physical events and the detector response, and for the reconstruction of the events. In this section we present a short description of the ANTARES Monte Carlo tools used in this work.

As discussed above, the experiment is currently under construction and the data acquired up to now are not useful for the kind of analysis under study. Thus our analysis has been performed using only Monte Carlo data. Nevertheless, all the developed techniques and all the results extracted are obtained by treating the Monte Carlo data as if they were real.

In order to fully simulate the physics of the events and of the detection process and the reconstruction of the events, a chain of software tools has been created. The main stages of this generation–simulation–reconstruction procedure are the following:

- **Simulation of the detector geometry**: The program GENDET [95, 96] is used to produce a description of the detector geometry that will be used as input for other Monte Carlo programs.

- **Generation of the events**: Various programs can be used to generate the different types of events in the detector. In particular, the neutrino events from a given neutrino flux and their interaction in the surroundings of the detector can be simulated with GENHEN [97–99] and GEMINI [100]. The interaction points are created in a large cylindrical volume that includes the detector and several kilometres of rock below. The background of atmospheric muons is generated with the program HEMAS [101] which simulates the interactions of cosmic rays at the uppermost layers of the atmosphere.

- **Propagation of the events**: High energy muons can be detected even if they are produced kilometres away from the detector. However, only Cherenkov photons emitted within the detection volume will be capable of producing a signal, and thus there is no point in fully simulating the muon propagation from the generation point. On the contrary, the muon track is propagated from the interaction point up to a can around the instrumented volume, determined by light attenuation length in the sea water, within which the full simulation will be performed. Different codes can be used to perform the propagation of the muon in rock and water, in particular MUSIC [102], PropMu [103] and MUM [104].

- **Simulation of the muon passage through the detector**: The available choices at this stage are the KM3 [105] and GEASIM [106] programs. Both codes simulate the passage of the muon through the simulation can, as well as the associated processes: Cherenkov emission, ionization, pair production, electromagnetic cascade simulation, hadronic cascade production. The simulation of the photons that will produce the signal in the optical modules, which involves their propagation, absorption and scattering, is also performed by these programs. However both programs are not equivalent. GEASIM does not include the scattering of light in water. KM3 does include the scattering, but does not simulate the hadronic cascade which provides a large amount of photons at low energies, while GEASIM does. A detailed comparison between both Monte Carlo codes can be found in [107].

- **Simulation of the detector response**: Both KM3 and GEASIM also perform the simulation of the detector response. After propagating the photons to the optical modules, these programs simulate the photomultiplier response to the arriving light. The programs use a parametrisation of the photomultiplier angular, spectral and time responses to simulate the signal collected by each photomultiplier. They also include a simple simulation of the electronics in the optical module that limits the maximum amount of light collected in the same optical module and the number of hits collected in a short period of time.

- **Reconstruction of the events**: RECO is the main reconstruction program. It contains various reconstruction strategies among which the user can choose according to the kind of study being performed: 3D reconstruction, single string reconstruction and sphere fits. The reconstruction program is described in more detail in chapter 3.

- **Reconstruction of the energy of the events**: RECO program also contains the different strategies developed to reconstruct the energy of the events [108].

The previous list, however, does not cover all the programs available in the ANTARES software scheme, what reflects the large effort devoted within the ANTARES collaboration in this field over the last years. Figure 2.16 shows a scheme with the most important steps involved in the simulation and reconstruction chains.

In the following subsections we present in more detail the generation and simulation steps. Since the improvement of the reconstruction strategy is one of the main goals of this work, the reconstruction step will be discussed separately in chapter 3.

2.5.1 Event generation

The generation stage includes the neutrino interactions that give rise to muons and their propagation up to a detectable distance from the optical modules.

Since Cherenkov photons can travel a significant distance in water, a muon can be detected even if it does not pass through the *instrumented volume* of the detector, i.e. the cylinder containing all the PMTs. Thus a larger cylinder, called *can*, is defined for simulation purposes. A muon passing through this volume may be observed by the detector, thus the full simulation of Cherenkov emission and light propagation is performed within this cylinder. The can boundaries are obtained adding a length $2.5 \times \lambda_{att.eff.}$ to the dimensions of the instrumented volume.

Neutrino interactions are simulated by the generation programs as produced within a larger cylinder, the *generation volume*. Event generation is performed within a given

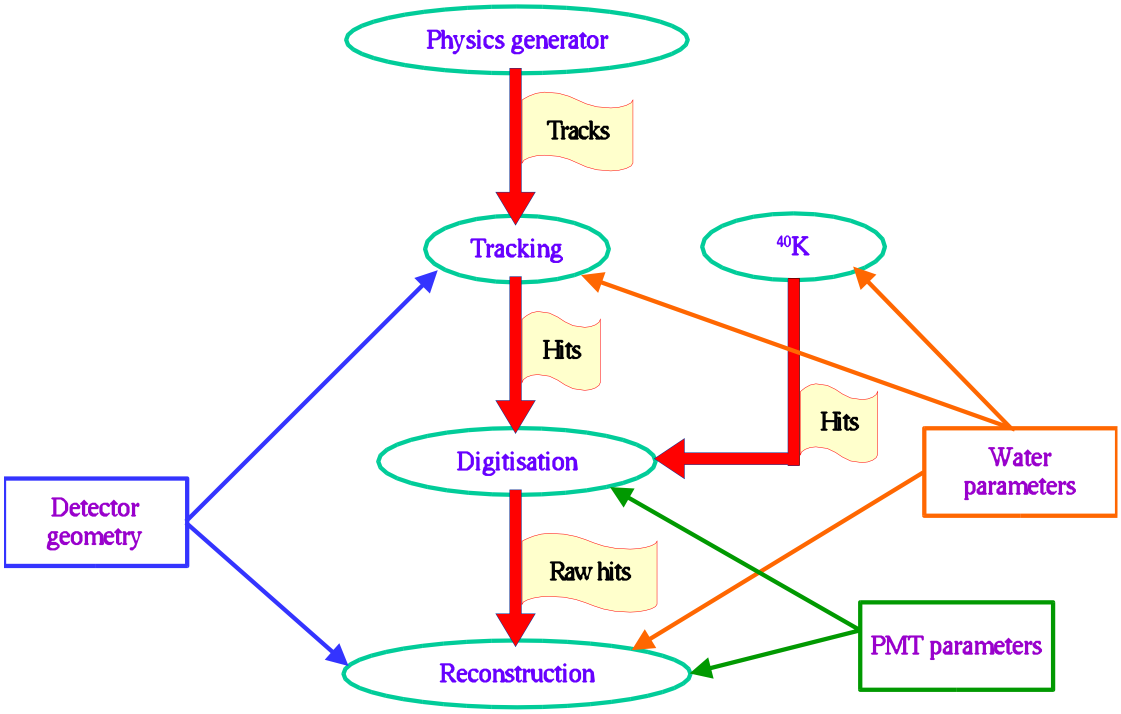

Figure 2.16: Scheme of the ANTARES simulation and reconstruction chain.

range of neutrino energies. For each energy interval the generation volume is determined by the maximum range of a muon carrying the full corresponding neutrino energy.

Within each energy interval, the number of events to be generated depends on the desired total number of events and on the given neutrino flux. Then the neutrino interaction mode is chosen according to the cross-sections of the different process at that energy. The generation can be performed for an isotropical neutrino flux or for a restricted domain in angle, so as to simulate a point-like source.

Once the muon has been generated, its propagation from the interaction point to the can only needs to take into account the muon energy loss, not the full simulation of Cherekov emission. Only those events that reach the can are kept. Then, for each event kept, a generation weight associated to the chosen neutrino flux is recorded as well as a weight corresponding to an atmospheric neutrino model. This allows to use the Monte Carlo simulated events to reproduce a different flux by individually recalculating the weights.

For the atmospheric muon background, the procedure is different. HEMAS program is used to generate the muons from the interactions of cosmic rays in the atmosphere. The shower must be developed and muons must then be propagated until the sea level.

The simulation programs KM3 and GEASIM, propagate the muon as it passes through the can. In KM3, the photon field emitted by a muon of given energy is tabulated from a GEANT3 [109] simulation. For each simulated muon, then, photons are generated. In GEASIM the approach is different, and an analytical function is used to estimate the number of Cherenkov photons arriving to the optical modules. When the muon energy loss, estimated in 1 m intervals, is much larger than that of ionization, an electromagnetic shower may be randomly generated along that track section. In that case, the resulting particles are also propagated.

Both KM3 and GEASIM traditionally used the photons phase velocity for propagation in the water. This, however, was shown not to be correct, and nowadays the simulation programs are able to use the group velocity.

2.5.2 Event simulation

Any signal produced by a photomultiplier in an optical module is called a *hit*. A hit is characterised by the arrival time of the photon to the photomultiplier and the amplitude of the produced signal.

The programs must also simulate hits due to the optical backgrounds at the ANTARES site. These are mainly produced by β decays of ^{40}K and bioluminiscence. As discussed in sect. 2.4.1, the ^{40}K is a source of natural radiactivity giving raise to ionizing electrons that produce light at a rate up to 60 kHz in a 10 inches photomultiplier. The last rate is an extrapolation of the one measured for a an 8 inches PMT. This light randomly arrives to the optical modules, uncorrelated with the muon passage. Another source of optical background is due to the dark noise pulses produced in the photomultiplier itself. However the dark noise pulse rate (around $\sim 2kHz$ for the 10 inches photomultiplier) is small compared with the pulse rate from ^{40}K. Bioluminiscence is another source of uncorrelated hits. Bioluminiscence simulation has not been yet added to the Monte-Carlo chain with a specific program. However, this is not very important since the trigger will kill the bioluminiscence events, which produce a high rate of hits in the same optical modules. If some bioluminiscence hits survive the trigger filters, their number will be small compared with that of ^{40}K hits.

The Monte Carlo simulation of the detector requires both tracking of all produced particles as muons pass through the can and knowledge of the PMTs response as a function of wavelength and angle of the photons.

The simulation of optical modules includes the photomultiplier and the glass sphere. Given a photon flux of wavelength λ, $\Phi_\gamma(\lambda)$, that arrives to the OM with an angle θ_γ with respect to the PMT axis, the number of produced photoelectrons, N_e, is expressed

$$\frac{d\,N_e}{d\,x} = A_{geom}\;\varepsilon\;\alpha\;f(\theta_\gamma)\int \Phi_\gamma(\lambda)\;T(\lambda)\;Q(\lambda)e^{-b/\lambda_{abs}}d\lambda \tag{2.16}$$

where A_{geom} is the photocathode area, ε is the charge collecting efficiency, α represents the effect of the magnetic shielding, $T(\lambda)$ is the transmitivity of the sphere and optical gel, $Q(\lambda)$ the quantum efficiency of the PMT, $f(\theta_\gamma)$ its angular response. Finally, b and λ_{abs} are respectively the total travelled length and the absorption length of the photon, so that the exponential accounts for attenuation.

All intervening parameters have been measured for the actual components of the detector. ε is a normalisation constant.

The Cherenkov photon flux can be calculated from the spectrum of Cherenkov emission ($\propto 1/\lambda^2$) and the expansion of the corresponding wavefront.

$$\Phi_\gamma(\lambda) \propto \frac{1}{\lambda^2 d} \tag{2.17}$$

2.5.3 Analysis tools

The studies carried out in this work need a large amount of data. These data have been produced using the Monte Carlo chain presented above, with the sets of parameters listed in Appendix A). Their analysis requires sophisticated analysis tools capable of handling large volumes of data.

To perform the data analysis, the ROOT analysis tool [110] has been employed. In this context, new specific libraries have been implemented for the ANTARES experiment.

We have created new classes to contain the ANTARES data, taking advantage of the object oriented architecture on which ROOT is based. These new classes describe the physical detector (detector geometry, optical modules) and the events (hits, neutrino tracks, muon tracks, fitted tracks and so on). They have been created to reproduce all the aspects of the detector and the events. Moreover, the structure of the different classes follows that of data in the experiment: each event object contains a neutrino object, various track objects (one being a muon), various hit objects and one fitted track object.

The output from the ANTARES programs is stored in disk as ASCII files. We have written a program to read the ASCII files and write the information into objects using the specifically developed ROOT library. These new data are stored in files using the ROOT binary format. Data on the ROOT files can then be easily accessed and analysed using ROOT tools.

We have also developed some specific functions for some particular applications. These tools have been incorporated to the ROOT analysis package as new libraries, so that they can be used together with the ROOT analysis classes and the new ANTARES data classes. These libraries include functions for coordinate transformations from local coordinates in the detector to astronomical coordinates, and also functions that compute confidence intervals, neutrino fluxes and muon ranges.

Chapter 3

A new reconstruction algorithm

Reconstruction is not a closed issue in ANTARES. A large amount of work is being devoted to optimise muon reconstruction at Monte Carlo level and much more will come when real data will be available. In this chapter, we present a reconstruction algorithm that takes advantage of the geometrical relationships between the hits and the track direction. With this algorithm three of the five track parameters can be obtained provided that the direction of the track (the remaining two parameters) is known. The algorithm can also be extended to obtain an estimation of all the five track parameters.

The chapter begins with an introduction in section 3.1 to the problem of reconstructing events in the three dimensional array of photomultipliers of ANTARES. In particular, we describe the reconstruction procedure followed by the standard reconstruction algorithm. Then, in section 3.2, we introduce a new technique to obtain from the track direction the remaining track parameters, using the information registered in the detector. In section 3.3, we show that not all the hits in the event are needed for the method to work. Instead, a small conveniently selected fraction of the hits provides the same results. A comparison between the standard reconstruction strategy and the new strategy is performed in section 3.4. Section 3.5 introduces an extension of this technique to the general case where the event is reconstructed without any additional information about the track direction. Finally, in section 3.6 the results for this general case are shown.

3.1 Track reconstruction with RECO

The main code for muon track reconstruction in ANTARES is **RECO** ([111–113]). The first version of this program, written in C++, is complemented with additional routines that optimise the reconstruction process. The user can choose among different reconstruction strategies, depending on the type of events he is interested in: down-going atmospheric muon events, very low energy events (single string reconstruction) or multi-string reconstruction.

Within the multi-string reconstruction the user can select any of the three strategies currently available:

- The *Standard strategy*, which is the first reconstruction algorithm written for ANTARES.
- The *Iterative strategy*, described in this chapter, was developed by us [114, 115] and represented the first alternative to the *standard strategy*. It provided a sizeable improvement of the reconstruction performances.
- The *Aart strategy*, developed some time later, also provides an improvement of performances with respect to the *standard strategy*.

These strategies perform what is called a *conical fit*, because they fit the muon track that produces a Cherenkov cone of light. The RECO program also includes routines for fitting an event with a sphere instead, what is called a *spherical fit*. However, events of this kind are produced by other physical situations that are not studied in this work, hence we will not describe them here. In this work we will compare our proposed *Iterative strategy* with the *Standard strategy*. More information about the *Aart strategy* can be found in [116].

3.1.1 The RECO standard strategy

The program **RECO** is an evolution of an older program written in FORTRAN, named POSIDONIA. Many aspects have changed in the code since the earliest version, but the basic concepts on which the reconstruction process is based have remained unchanged. The reconstruction algorithms use the arrival time of light to the photomultipliers, in particular that of the *direct Cherenkov* light emitted by the muons. These are the first photons from the muon to arrive to an optical module. The Cherenkov photons are emitted at a fixed angle from the track direction: $\theta_c = \arccos\left(\frac{1}{n_{water}}\right) \approx 42°$ and follow a straight path. Both features relate the arrival time of the photons to the track parameters, a fact that is used for track reconstruction.

However, *indirect* photons that can arrive to the optical modules are also produced by the passage of the muon. They produce hits, indistinguishable from the direct Cherenkov ones, but whose arrival times are not directly related to the track parameters. The photons produced by the muon electromagnetic and hadronic cascades arrive some time after the direct Cherenkov photons. Scattering is also responsible for the delay of the arrival of the photons to the optical modules. Photons continue their travel after scattering, contrary to what happens in the absorption phenomenon, but their direction is modified. As a result, a scattered photon always arrives later than a direct Cherenkov photon. The hits produced by these delayed photons can be used in the reconstruction, but they contain less precise information about the muon track. Only the direct Cherenkov photons can be directly connected through the track parameters with a simple analytical expression.

Finally, natural sources of optical background are present in the ANTARES site. Background light from ^{40}K decays and bioluminescence can arrive at any time with respect to the direct Cherenkov photons. The hits produced by these photons are uncorrelated with the muon track and should be rejected by the reconstruction.

Figure 3.1 illustrates the different origins of the photons that can arrive to the optical modules.

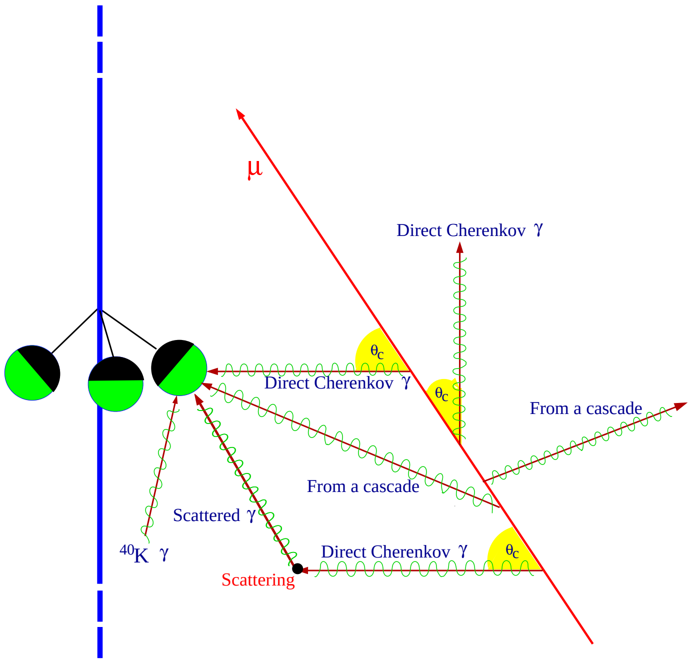

Figure 3.1: Schematic view of the possible origins of the photons that produce signals in an optical module. Direct Cherenkov photons are the first photons from the muon track to arrive to an optical module. Other photons produced by the track arrive some time later. Photons from ^{40}K decays and bioluminescence can arrive at any time since they are not correlated with the passage of the muon.

The muon is assumed to move along a straight line with speed c when crossing the detector, i.e. muon scattering is neglected during reconstruction. The arrival time of the direct Cherenkov photons is related to the track parameters and the optical module position. In particular, the arrival time of a direct Cherenkov photon can be expressed as (see fig. 3.2),

$$\tilde{t}_i = t_0 + \frac{1}{c}(L_i + r_i \tan\theta_c) \tag{3.1}$$

where $\tilde{t}_i$ is the time when the hit is produced, t_0 is the time when the muon was at a certain reference position (x_0, y_0, z_0), L_i is the distance along the track between the reference position and the point of closest approach to the optical module, r_i is the minimum distance between the muon track and the optical module and θ_c is the Cherenkov angle in water ($\theta = \arccos\left(\frac{1}{n_{water}}\right) \approx 42°$).

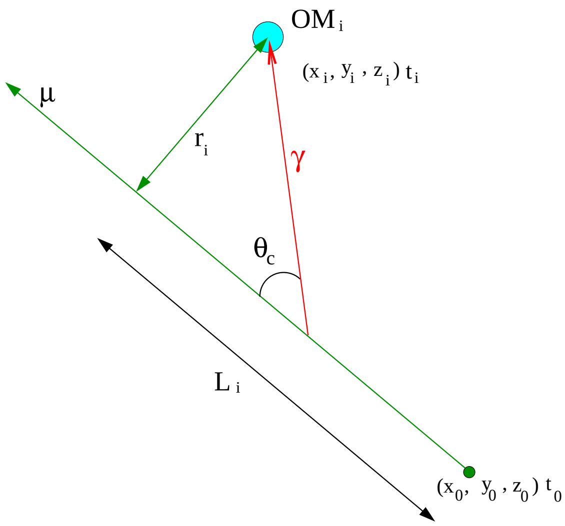

Figure 3.2: Arrival of photons to an optical module.

If the track parameters were known, we could compute the time difference between the actual time (t_i) of the hits in the event, and the expected time for a direct Cherenkov photon coming from the track ($\tilde{t}_i$). The difference between t_i and $\tilde{t}_i$ depends on many variables (track parameters, optical module orientation, water optical properties, etc). However, we can use a Monte Carlo simulation to build a distribution with the time differences in all the optical modules for all the possible tracks crossing the detector. This Monte Carlo estimated distributions can be used as an average probability distribution function (*pdf*) to assign a probability for a hit to come from a track. Since the *pdf* does not change much for different muon energies (see figure 3.3) a common parametrization is used to describe the *pdf* regardless of the muon energy.

For the reconstruction, one of the main routines in **RECO** builds a likelihood function ($\mathcal{L}$) using the Monte Carlo *pdf* and the hit times in each event. The likelihood function is computed by multiplying the probability for each hit to come from a track estimate times the angular factor that takes into account the optical module orientation with respect to the track. The hit probability for a track estimate is obtained from the time difference between the actual hit and the direct Cherenkov photon (equation 3.1) using a parametrization of the Monte Carlo *pdf*. For each track estimate the program re-computes the product of probabilities to obtain a new likelihood.

The muon track is a straight line that can be described with five parameters, namely (see figure 3.4) two for the direction (θ and ϕ), two for the position of a reference point in a plane perpendicular to the track (x and y) that also contains the centre of the detector, and one parameter for the time when the track crossed that plane

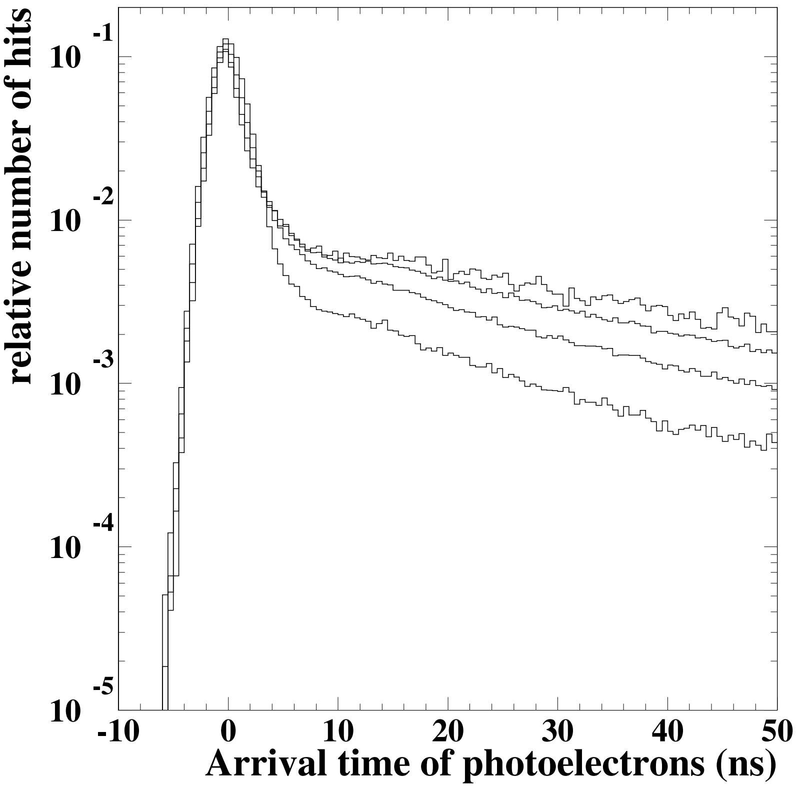

Figure 3.3: Unnormalized probability density function $P(\Delta t)$ for the arrival time of hits originating from muon tracks with respect to the time expected for the corresponding direct Cherenkov photons. The *pdf* is shown for four different energies: 2 TeV, 10 TeV, 50 TeV and 250 TeV, from bottom to top.

(t_0). Following the conventions used in the RECO code, the x direction corresponds to the projection of the z axis in that plane and the y direction is perpendicular to x and to the track direction. In order to find the muon track, we should look for the parameters that provide the maximum likelihood. In practice, the program looks for the five parameters $(\theta, \phi, \mathbf{x}, \mathbf{y}, \mathbf{t_0})$ that minimize the function $-log(\mathcal{L})$.

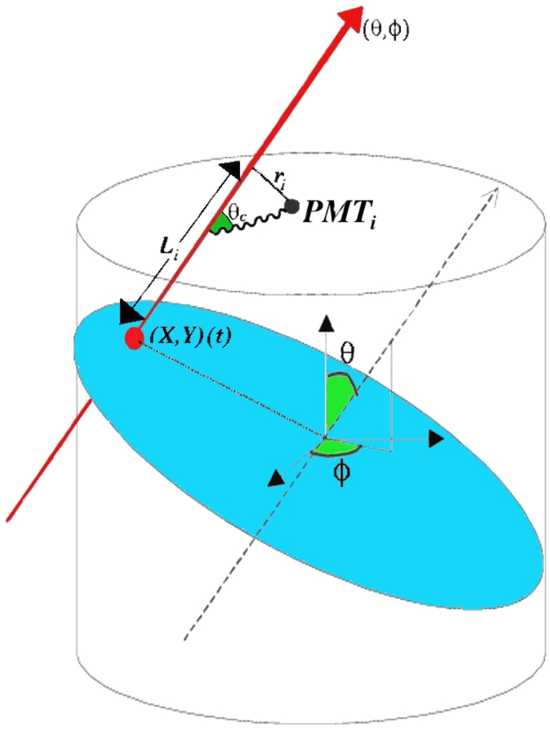

Figure 3.4: Definition of the track parameters for reconstruction.

3.1.2 The track pre-fit

As it is common in a complex minimization process, a first estimate of the parameters is needed in order to guide the minimization algorithm. This first estimate of the track parameters is called the **pre-fit**. The pre-fit is of paramount importance in the reconstruction process because if the starting parameters are far from the correct ones, the minimization process may fail.

The pre-fit used in the *standard strategy* is based on the pre-fit developed by the Dumand collaboration [117]. In a first approximation the track of the muon can be obtained by fitting to a straight line local coincidences in space. A local coincidence is defined as two hits in two optical modules of the same storey whose time difference is smaller than **5 ns** (it is also known as a L_0 *trigger*). The 5 ns time difference is so small that it is very unlikely for ^{40}K decays or bioluminescence to produce such a coincidence.

Using coincidences in the pre-fit prevents the problem of adding background hits that would otherwise spoil it.

With this pre-fit, the hits are considered to lie on the muon track and the muon velocity is treated as a free parameter. This is a good approximation when the track length is longer than the distance from the hits to the track. However, in other cases this approximation is not correct. For instance, for short range muons (low energy) or in the case of tracks that do not cross the detector, this approximation is not valid. In those cases, it wrongly forces the track to go through the optical modules.

In summary, this pre-fit provides in many cases a reasonable first estimate of the track parameters. However, sometimes it is not a good starting point. This may not necessarily mean that the reconstruction will fail, but reduces the chances of success.

3.2 A new pre-fit for 3-Parameter reconstruction

In this section a new approach to performing the pre-fit is explained. This approach is designed for the case when the source direction is known and therefore the muon direction can be assumed to be approximately known. The aim is to increase the reconstruction efficiency by using this knowledge. However, as explained in section 3.5 this new pre-fit can be used more generally in a global 5-parameter pre-fit, i.e. without previous information about the track direction.

In a different context, this technique can be used for the reconstruction of muon tracks produced by point-like sources of neutrinos. In that case, the neutrino direction is fixed and we can assume that the muon direction is very close to the neutrino direction. With this technique we can take advantage of the knowledge of the point-like source location to increase the reconstruction efficiency. Some work is currently being carried out within the ANTARES collaboration in this sense, applied to the detection of GRBs [118]. The GRB position can be detected by an array of detectors located all around the world. This position can be notified a short time after the detection what can be used to increase the reconstruction efficiency if this technique is used.

3.2.1 First step: obtaining the x and y parameters

The new pre-fit is based in the geometrical relationships between the Cherenkov hits and the track that hold as a consequence of the fixed Cherenkov angle. As shown in figure 3.5, for every hit i, a longitudinal distance L_i along the track direction and a transverse distance r_i can be defined. From equation (3.1), r_i can be obtained as a function of the other parameters:

$$r_i = \frac{ct_i - ct_0 - L_i}{\tan\theta_c} \tag{3.2}$$

By combining two hits it is possible to get rid of t_0:

$$\Delta r_{ij} = \frac{c\Delta t_{ij} - \Delta L_{ij}}{\tan\theta_c} \tag{3.3}$$

where $\Delta r_{ij} = r_i - r_j$, $\Delta t_{ij} = t_i - t_j$ and $\Delta L_{ij} = L_i - L_j$. Using expression (3.3), Δr_{ij} can be calculated provided that the track direction (θ, ϕ) is known.

Let us consider a plane perpendicular to the track (following RECO conventions we take in particular the one that contains the centre of the detector, but this is immaterial for the method). For any two hits, i and j, the points in that plane whose difference of distances to the hit projections onto the plane is Δr_{ij} define a hyperbola (dotted line in figure 3.6). In particular, the track projection upon this plane must lie on this hyperbola. The equation of the hyperbola is given by the following expression:

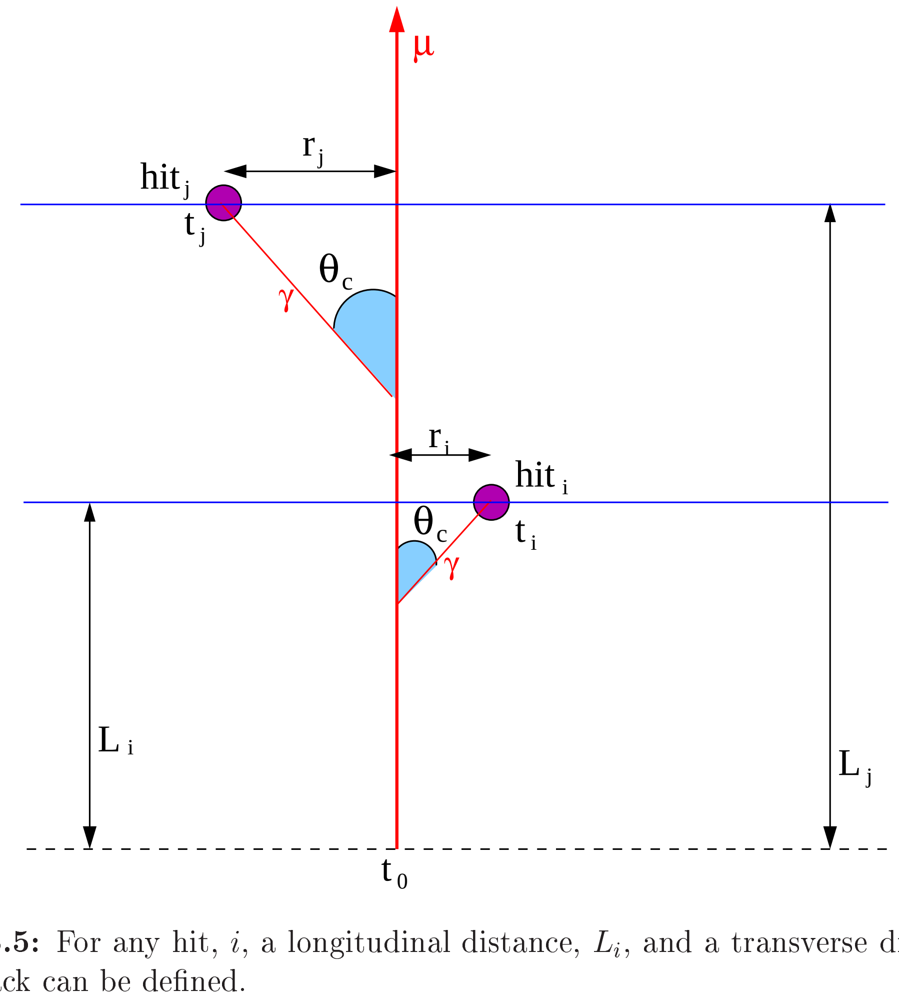

Figure 3.5: For any hit, i, a longitudinal distance, L_i, and a transverse distance, r_i, to the track can be defined.

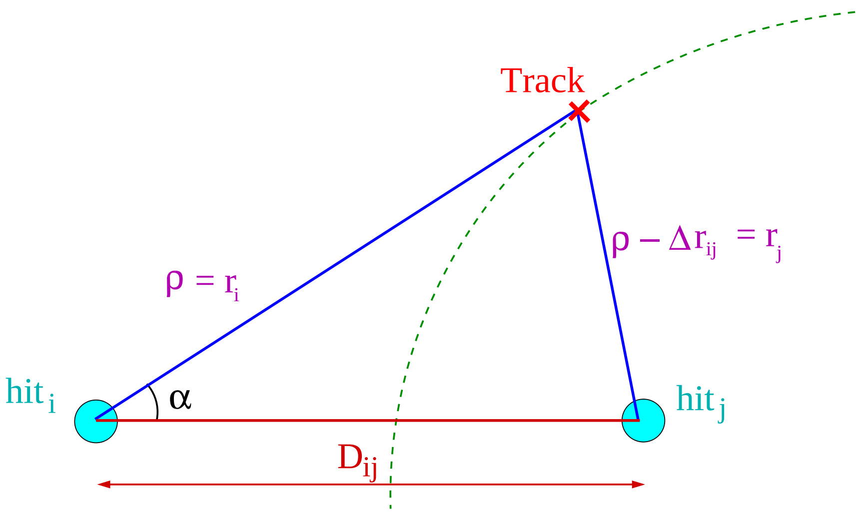

Figure 3.6: The track projection (cross) upon the perpendicular plane should lie on the hyperbola given by equation (3.4).

$$\rho = \frac{1}{2}\frac{D_{ij}^2 - (\Delta r_{ij})^2}{D_{ij}\cos\alpha - \Delta r_{ij}} \tag{3.4}$$

where D_{ij} is the transverse distance between the hit optical modules (see figure 3.6).

With an additional third hit, two hyperbolas can be built and the track projection must be one of their intersection points. In order to find these intersection points, the following equation has to be solved (see figure 3.7 for definitions):

$$\cos\alpha \times (1 - B\cos\psi) - B\sin\psi\sin\alpha = A_{12} - BA_{13} \tag{3.5}$$

where:

$$A_{12} = \frac{\Delta r_{12}}{D_{12}} \tag{3.6}$$

$$A_{13} = \frac{\Delta r_{13}}{D_{13}} \tag{3.7}$$

$$B = \frac{1 - A_{12}^2}{1 - A_{13}^2} \cdot \frac{D_{12}}{D_{13}} \tag{3.8}$$

For any three hits, up to 4 solutions of equation (3.5) can be found. Only one of them corresponds to the track projection in the plane perpendicular to the track. The solutions are given by:

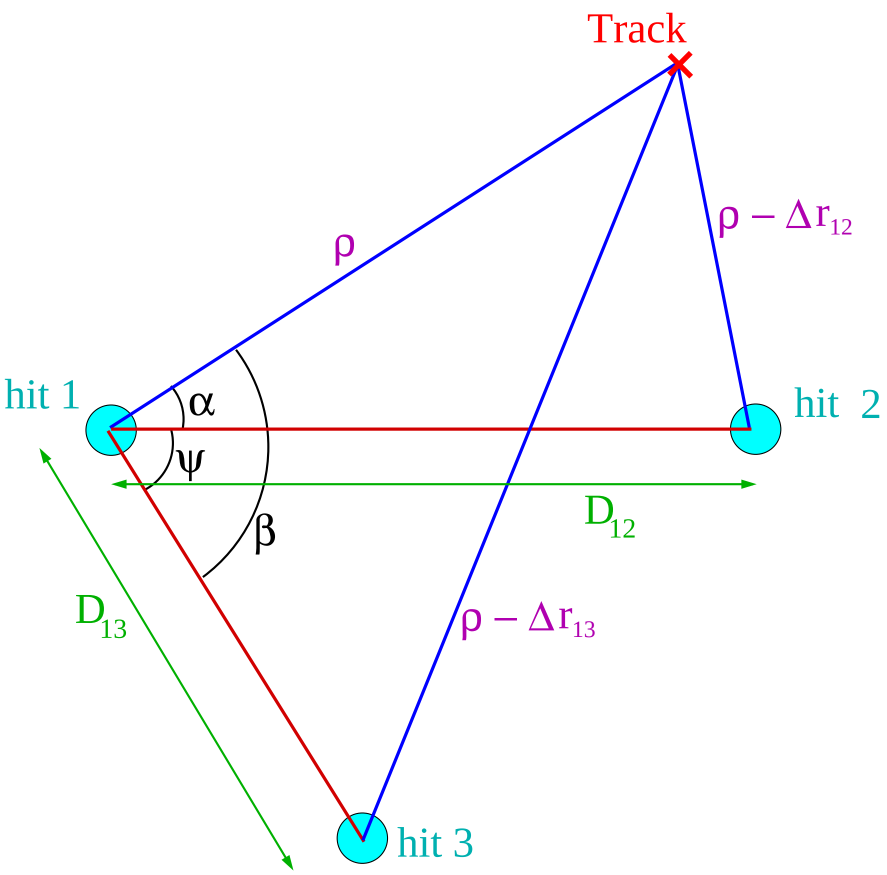

Figure 3.7: Three hits are used to calculate the intersection of two hyperbolas.

$$\cos\alpha = \frac{-CF \pm D\sqrt{C^2 + D^2 - F^2}}{C^2 + D^2} \tag{3.9}$$

where:

$$\begin{aligned} C &= B\cos\psi - 1 & (3.10)\\ D &= B\sin\psi & (3.11)\\ F &= A_{12} - BA_{13} & (3.12) \end{aligned}$$

From α, and using equation 3.4, ρ can be obtained. Each of the four solutions is a candidate x and y of the track projection. Figure 3.8 shows two examples of three hit combinations in the same event.

The solutions of equation (3.5) for different combinations of three Cherenkov hits can be added to the same histogram and used to determine the position of the track projection, since it is the only point where the different hyperbolas always intersect. Figure 3.9 shows a histogram with the solutions for different hit combinations as determined from the solutions of equation (3.5) in two different events.

Sometimes the number of hits in one particular string is much larger than in the other strings, this string dominates the event and the intersection of the hyperbolas tend to lie at both sides of the string projection. Two peaks appear then in the histogram (see figure 3.9) and is difficult to decide which one is the track projection. This ambiguity is a consequence of the fact that one string is not enough to find the track projection.

In Figure 3.10 the projection of the optical modules are shown as squares (black for fired optical modules and grey for quiet optical modules) and that of the track as a triangle. The colours correspond to the distribution of the crossing points of the hyperbolas. As can be seen, the track projection is determined with high accuracy.

3.2.2 Second step: obtaining t_0

Once the x and y coordinates are known, the remaining track parameter, t_0, can be obtained (θ and ϕ are supposed to be known). With the estimated values of x and y, an r_i can be computed for every hit and a corresponding $t_{0,i}$ can be extracted using equation (3.13):

$$t_{0,i} = t_i - \frac{1}{c}(L_i + r_i \tan\theta_c) \tag{3.13}$$

A value $t_{0,i}$ of the reference time is therefore obtained for every hit. For hits that do come from the track, the values of $t_{0,i}$ tend to accumulate in a narrow peak, because they follow the *pdf* distribution. The hits from the background will have a flat time

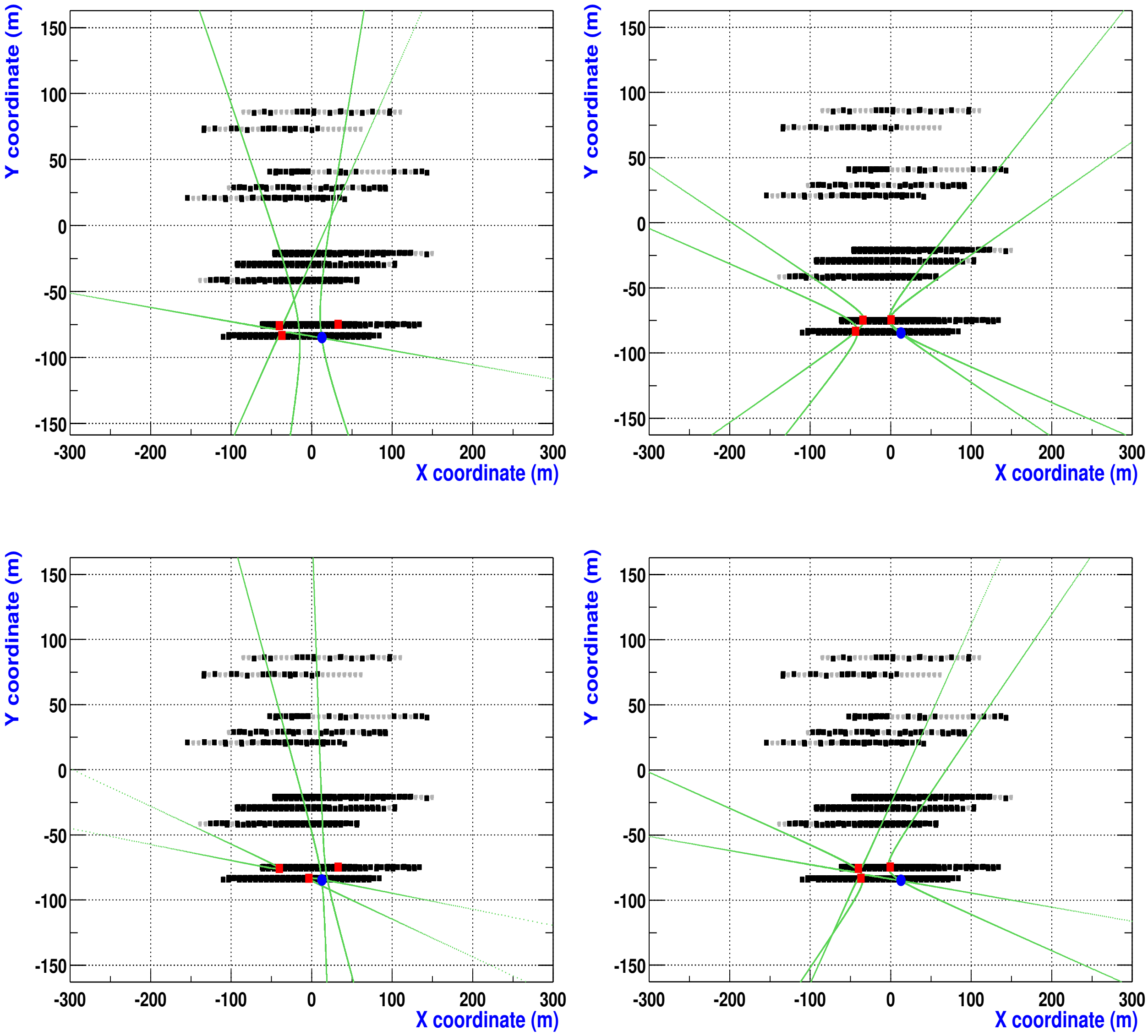

Figure 3.8: Examples of hyperbolas built for different combinations of three hits in the same event. The three highlighted squares correspond to the 3 hits used to build the hyperbolas. The circle is the real track projection and is located in one of the hyperbolas intersections. The optical modules are also represented in light grey color when there is no hit and in black when there is a hit.

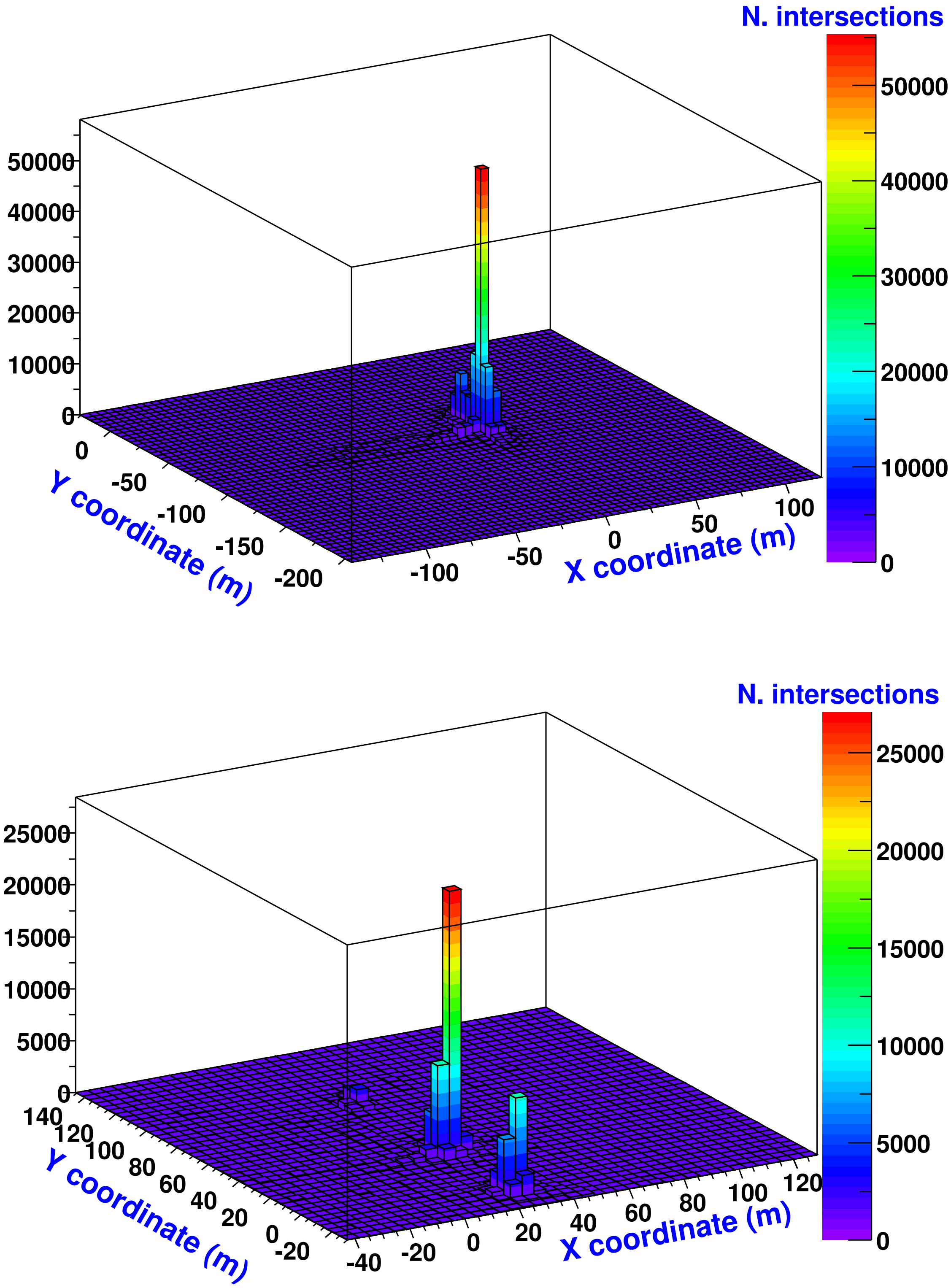

Figure 3.9: Lego plot corresponding to the solutions to equation (3.5) for two different events.

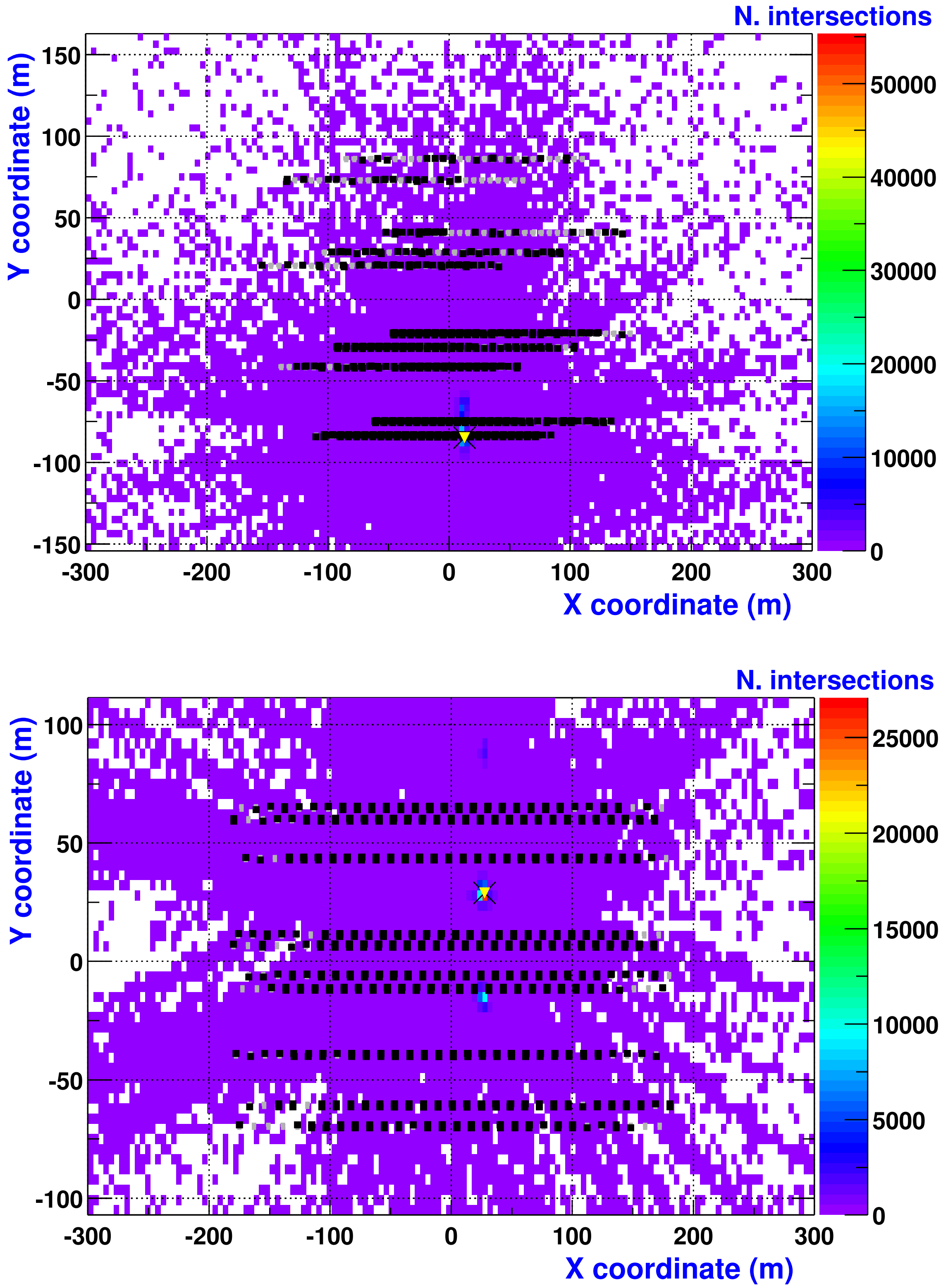

Figure 3.10: Projection of the hits (square points) and the track (triangle) together with the distribution of hyperbolas intersection points in figure 3.9. The position of the track projection obtained from the intersection points is presented as a black X.

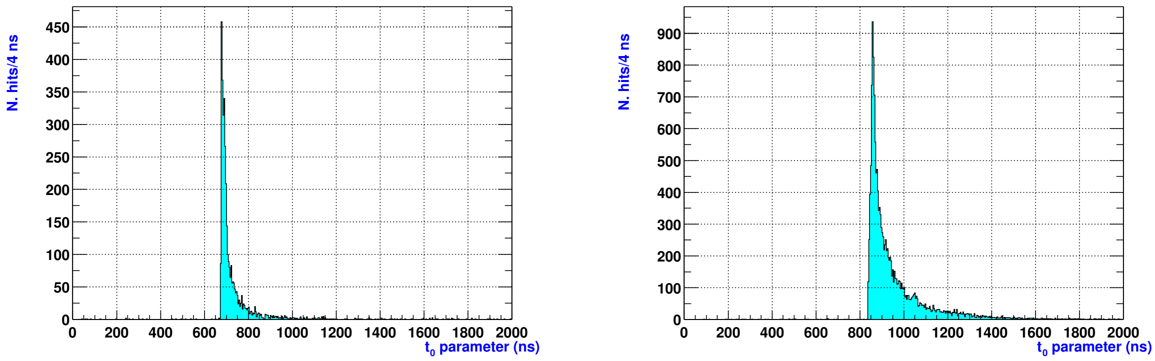

Figure 3.11: Distribution of the track parameter t_0 obtained for the previous two events.

distribution, because they are uncorrelated with the track passage. An example can be seen in figure 3.11 for the two events previously considered.

Since the peaks in the t_0 distribution are in general narrow (∼15 ns), they can be used not only to estimate t_0, but also to make a hit selection. Indeed, a window of ∼20 ns around the peak rejects most of the background hits. Therefore, this method can provide not only the unknown track parameters (x, y and t_0), but also a corresponding hit selection ($\{hit_1, hit_2 ... \ hit_N\}$). The task of the minimization procedure in RECO is therefore reduced to a fine tuning of the track parameters given by the pre-fit and using the hits that the pre-fit has selected.

3.3 Reducing the number of hits: *hit cleaning*

The combination in triplets of all the hits in an event becomes unaffordable as the number of hits increases[1]. In order to reduce the number of combinations a suitable hit filtering is therefore essential. Moreover, as the number of hits increases the fraction of Cherenkov hits (the ones really important for the new pre-fit to work) with respect to the total decreases because the energy lost by the Cherenkov effect is a small fraction of the total energy lost. For that reason, as the total number of hits increases it is more difficult for the new pre-fit to obtain the x, y and t_0 parameters. For the technique to work, only the Cherenkov hits are necessary, so we try to keep these hits and reject the others, especially ^{40}K hits.

The process of keeping only the Cherenkov hits and reject as much as possible of the other hits is called *hit cleaning* and is performed before the hit combination in triplets has started. It consists in removing all the hits in the same optical module, leaving only

[1]Simulated high energy events up to 10^8 GeV can have more than 10^5 hits. This can represent more than $(10^5 \times (10^5 - 1) \times (10^5 - 2))/6$ combinations.

the one that was the first in a coincidence ($\Delta t < 5$ ns) with another hit in the same storey. This hit is assigned an amplitude that is the sum of the amplitudes of all the subsequent hits in the optical module. The idea is to remove the ^{40}K using coincidences. Since the Cherenkov photons are the earliest to arrive, the first coincidence should be produced by a Cherenkov photon or, at least, by the photon with the closest time to the Cherenkov photon.

With the *reduced hits*, we use again local coincidences between optical modules in the same storey (two hits with $\Delta t < 5$ ns). Only hits that are part of such coincidences are taken into account in the following. The strings are then ordered according to their number of coincidences. Finally, the hits in each string are ordered according to their amplitude. This ordering is used to select only the 3 strings with the highest number of coincidences. Among these strings, only the 6 hits with the largest amplitudes are kept. Therefore, independently of the number of hits in an event, a maximum of 18 hits are considered to make the 3-hit combinations. This pre-selection of hits highly reduces the number of combinations to be considered and hence the computation time.

When the number of hits or the number of coincidences in the event are small, we relax the criteria. In those cases, the time interval is increased to consider that a coincidence has occurred from 5 ns to 40 ns. Moreover, we keep up to 10 hits per string in up to 10 strings. Obviously, the quality of these hits is poorer.

The hit reduction process is summarised in Figure 3.12, where elliptical boxes represent the hits remaining after each selection step, while square boxes represent the actions taken.

This technique also implies an important decrease in computing time at the cost of losing a few events. However, for most of the events, the new pre-fit is not degraded by reducing the number of hits. Instead, this situation benefits the new pre-fit because only the Cherenkov hits remain and hence the intersection of the hyperbolas produce a clean histogram where it is easier to identify the position of the track projection.

Figure 3.13 shows the distribution of the intersection points for the events in figure 3.9, now computed with the reduced list of hits (the maximum number of hits being 18).

The results show that, for instance, from 23426 up-going events following a $E^{-1.4}$ distribution between 10 GeV and 10^8 GeV [2], the number of reconstructed events is 4203 when all the hits are used and 5868 when the reduced collection of hits is used. Hence there is an increase of $\sim 40\%$ in the number of reconstructed evens thanks to the hit cleaning process. After the selection cuts (they will be explained in chapter 4) the corresponding numbers are 2541 events selected with all the hits and 3833 events selected with the reduced set of hits, what represents an increase of $\sim 50\%$. Concerning the computation times, the reconstruction with all the hits took 4363 CPU seconds against 3211 CPU seconds with the reduced set of hits. This represents a reduction in CPU time of $\sim 36\%$.

[2] These are the usual parameters used in the Monte Carlo productions we use.

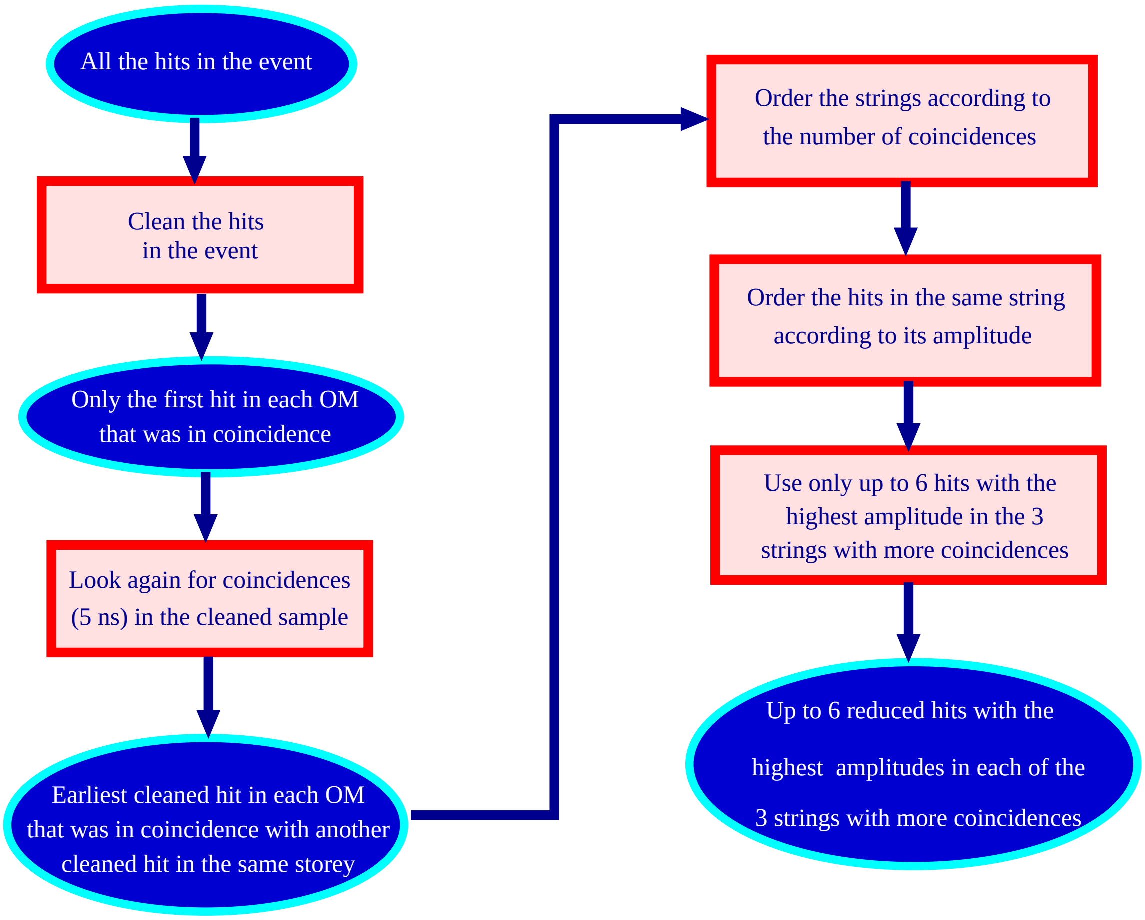

Figure 3.12: Steps taken along the process of hit reduction. Elliptical boxes represent the hits selected after each step. Square boxes represent the steps taken in order to reduce the hits.

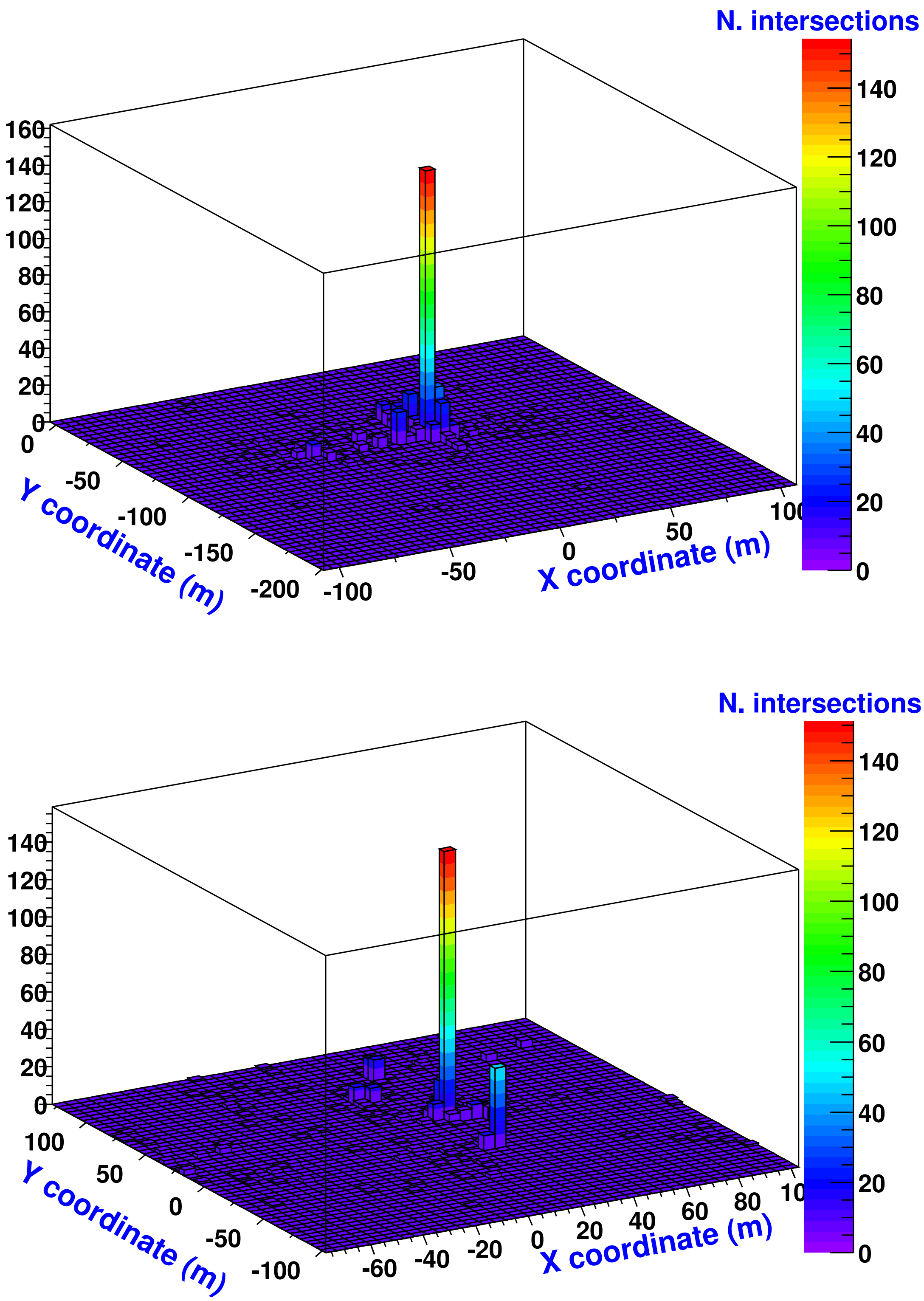

Figure 3.13: Lego plot corresponding to the solutions of equation (3.5) in two different events using only the reduced hit list (up to 18 hits).

3.4 Results with the 3-parameter pre-fit

The new reconstruction method has been tested using events generated with GENNEU (**v5r1**) [97]. A sample of up-going generated neutrinos with 10^{10} primaries, energies between 10 GeV and 10^8 GeV and zenith angles with $0 \leq \cos\theta \leq 1$ were generated in a cylinder surrounding the detector ("the can") with a radius of $\sim$ 250 m. We have applied the pre-fit technique only to those events that meet the trigger condition. The x, y and t_0 track parameters were computed using the direction of the muon in one case and the direction of the neutrino in the other.

The difference between the true track parameter and the value obtained by the new method using the muon direction is shown in figure 3.14.

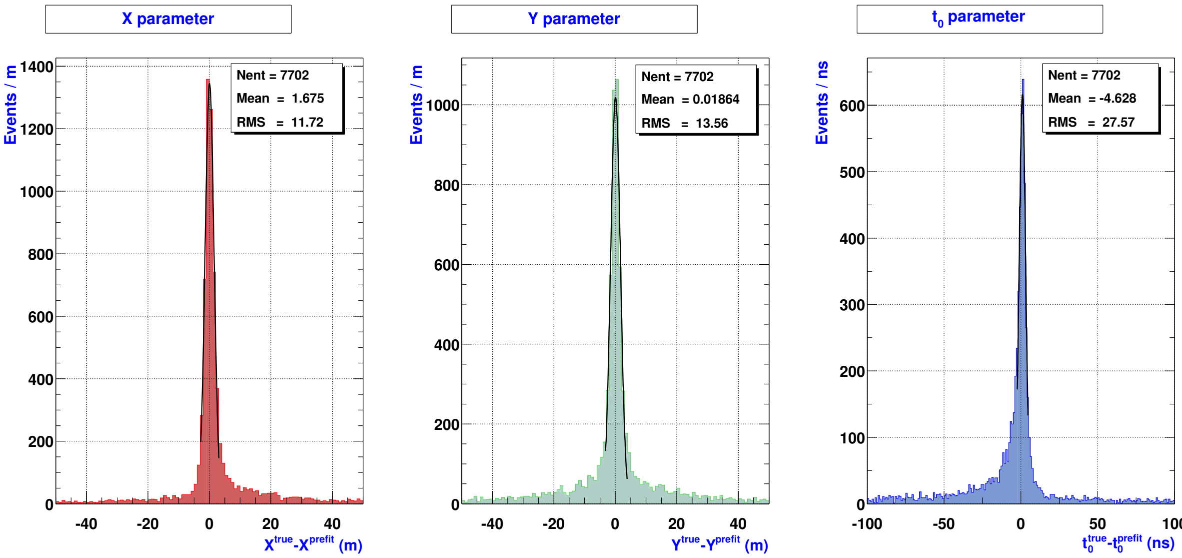

Figure 3.14: Difference between the true track parameter and the value estimated by the new reconstruction method using the muon direction information.

In the sample studied, the pre-fit was used in 6738 triggered events. The results are as follows:

- x **parameter from the pre-fit**: **85%** of the triggered events have $|x_{True} - x_{Pre-fit}| \leq 10\,m$. σ at the peak is 1.4 m.
- y **parameter from the pre-fit**: **75%** of the triggered events have $|y_{True} - y_{Pre-fit}| \leq 10\,m$. σ at the peak is 1.5 m.
- t_0 **parameter from the pre-fit**: **75%** of the triggered events have $|t_{True} - t_{Pre-fit}| \leq 25\,ns$. σ at the peak is 1.9 ns.

As can be seen, the values obtained from the pre-fit are very close to the true track values. The distributions have been fitted to gaussian distributions. These gaussians fit well the peaks, therefore the pre-fit obtains the real parameters of the track with high precision. However, we observe in the distributions that the mean of the difference between the true and the pre-fit value is 1.7 m for x, 1.9 cm (actually, this distribution is very symmetric) for y and -4.6 ns for t_0. This offsets are due to the asymmetric tails of the distributions. The pre-fit can not obtain the proper track parameters for all the events but when it fails, computes a slightly smaller x^{prefit} and y^{prefit} but slightly larger t_0^{prefit} than the real parameters. The importance of this offsets is, however, small because the usual range of the x parameter is between -200 and 200 m, the usual y range is between -150 and 150 m and finally the usual t_0 range is between 700 and 1300 ns. Anyway, the observed offsets are small compared with the typical values of the parameters.

We also observe that the method works better for the x coordinate than for the y coordinate. As can be seen in figure 3.10, the reason is that hits in the same string are projected along the x direction and therefore the spacing among the hits in the x direction is smaller than in the y direction. As a result, the estimate of the x parameter is more accurate than the y parameter estimation.

Up to now, we have used the Monte Carlo known direction of the track. However, if a group of possible neutrino sources are being surveyed, it is not the muon track but the neutrino direction what is actually known. Figure 3.15 shows the difference between the true muon parameters and the parameters obtained by the pre-fit using the neutrino direction information in the same sample.

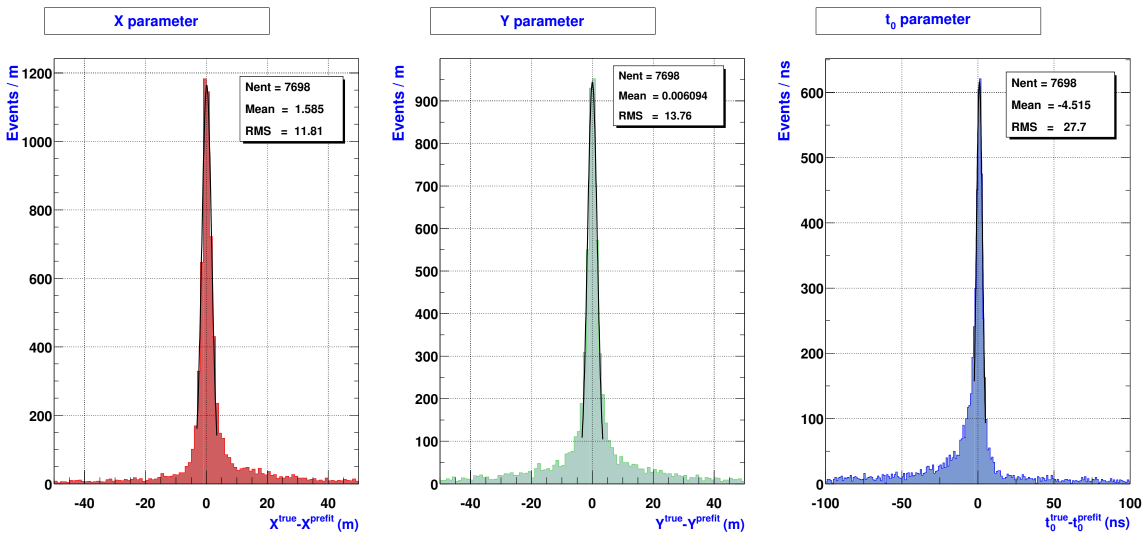

Figure 3.15: Difference between the true track parameter and the value estimated by the new reconstruction method using the neutrino direction.

The results are very similar to those obtained when using the muon direction. In this case, the peaks are slightly broader since the input angles are not those of the muon, but of its parent neutrino. However, since the angular difference is small and decreases with increasing energy, the results are again quite satisfactory:

- x **parameter from the pre-fit**: **85%** of the triggered events have $|x_{True} - x_{Pre-fit}| \leq 10\,m$. σ at the peak is 1.6 m.
- y **paramenter from the pre-fit**: **74%** of the triggered events have $|y_{True} - y_{Pre-fit}| \leq 10\,m$. σ at the peak is 1.6 m.
- t_0 **paramenter from the pre-fit**: **75%** of the triggered events have $|t_{True} - t_{Pre-fit}| \leq 25\,ns$. σ at the peak is 2.0 ns.

The values obtained in the fits are almost the same that in the case where the muon direction was used. This illustrates that the pre-fit does not need an accurate knowledge of the θ and ϕ parameters to work, a reasonable guess is enough. Again, the gaussian fit fails to fit the tails of the distributions but reproduces very well the peaks. The observed offsets in the mean of the distributions are small compared with the parameter ranges, especially for the y parameter whose mean of the distribution is compatible with 0. For the x and t_0 parameters the values returned by the pre-fit when it fails are, again, slightly smaller and larger respectively.

For comparison, the results obtained with the pre-fit of the standard strategy are shown in figure 3.16. These results give us an idea of the different performances, since for the standard strategy pre-fit also the direction of the track (θ and ϕ) is obtained.

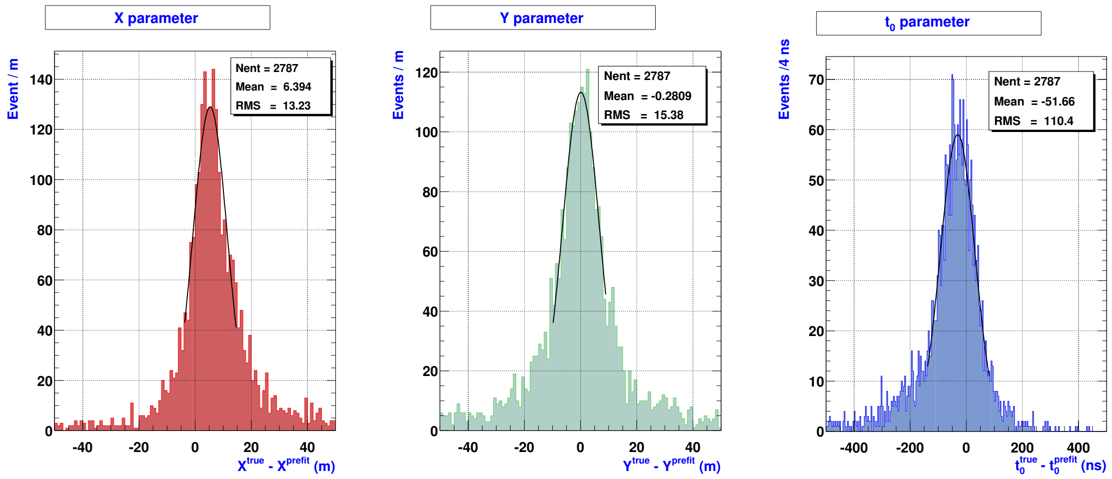

Figure 3.16: Difference between the true track parameter and the value estimated by the old standard reconstruction method (linear fit).

In this case, the pre-fit is only applied to those events that meet the condition to initiate the reconstruction, namely: having more than 6 hits in at least 5 optical modules of more than 2 storeys in at least 2 different strings. This condition is much harder than the trigger condition and thus the reconstruction is only applied to 2787 events. The results are the following:

- x **parameter from the pre-fit**: **23%** of the triggered events have $|x_{True} - x_{Pre-fit}| \leq 10\,m$. σ at the peak's center is 6.1 m.

- y **parameter from the pre-fit**: **24%** of the triggered events have $|y_{True} - y_{Pre-fit}| \leq 10\,m$. σ at the peak's center is 6.5 m.

- t_0 **parameter from the pre-fit**: **12%** of the triggerd events have $|t_{True} - t_{Pre-fit}| \leq 25\,ns$. σ at the peak is 61.2 ns.

The results are much worse than those obtained by the new pre-fit, especially for the t_0 parameter. The old pre-fit computes this number from the average of all the hits used in the pre-fit. Therefore, it is not surprising that worse results are obtained for this parameter. We observe that the distributions exhibit offsets for the x distribution and y distributions in the same direction than in the new pre-fit case. The offsets are, however, larger in this case than in the new prefit, especially for the t_0 parameter.

Concerning the offsets of the distributions, they are observed with both pre-fits. Their origin is related to the geometry of the detector. Since the PMTs are looking down-wards, there is an intrinsic asymmetry in the detector that makes both pre-fits to prefer a slightly smaller x parameter (smaller vertical distance along the strings). The detector is more symmetric for the y parameter, hence the distributions do not exhibit a noticeable offset. Finally, for the t_0 parameter, both pre-fits compute a larger t_0 parameter because usually the wrong pre-fitted events have a small number of Cherenkov hits. When this is the case, the remaining hits are used as if they were Cherenkov hits, what introduces a delay in the estimated t_0 parameter.

In summary, with the new method the track parameters can be obtained with a very good accuracy ($|x_{True} - x_{Pre-fit}| \leq 10\,m$, $|y_{True} - y_{Pre-fit}| \leq 10\,m$, $|t_{True} - t_{Pre-fit}| \leq 25\,ns$) in ~75% of the triggered events[3]. If we compare with the results from the standard reconstruction, we observe that the latter has a much worse estimation of the initial parameters for the reconstruction, especially of the t_0 parameter. Moreover, the number of events where the standard pre-fit can be applied is much smaller.

As a conclusion, provided that the θ and ϕ parameters of the muon track are known, the *new pre-fit* can compute the remaining track parameters with very good accuracy in most of the events that meet the trigger condition.

[3]Notice that the trigger described in [119] is much softer than the trigger required by RECO for reconstruction.

3.5 A fitting algorithm for 5-parameter reconstruction

The previous pre-fit provides very good results but it has an obvious limitation: the direction of the muon/neutrino track must be known in advance in order to apply the technique, which is not the case in most of the events in a neutrino telescope.

The technique can be extended to the general case in which the θ and ϕ of the track are also unknown. A simple approach is to perform a scan in the (θ, ϕ) parameter space. For every θ and ϕ in the scan, the method explained in section 3.2 is applied to obtain the other parameters. For values of θ and ϕ that do not correspond to the true direction, the pre-fit should give a bad estimate of the other parameters. In particular the t_0 distribution should be quite different.

The crossing points of the hyperbolas when the true muon direction is not used can be seen in figure 3.17 for the two previously mentioned events. The intersection point of the track with the plane used in each case is shown in the same figure as a triangle.

Figure 3.18 shows an example of the t_0 histogram for a direction different from that of the true track. For each hit, a $t_{0,i}$ value is computed using the wrong x and y coordinates obtained from the histogram in figure 3.17.

As can be seen, the t_0 distribution is wider and no single narrow peak can be seen. A small window around the highest peak will therefore contain a small number of hits, compared to the number obtained when using the true track's direction. Therefore, one criterion to select the *best direction* is to maximize the number of selected hits in a narrow window ($\sim$20 ns) around the maximum in the histogram. This time window is wide enough to contain most of the hits produced by the muon, as can be seen from the shape of the *pdf* used to compute the hit probabilities. This window is also narrow enough to ensure that the number of selected hits is small when the wrong direction is used.

This is a valid method to obtain the 5 track parameters. Although scanning the whole θ-ϕ space is the safest way to find the true muon direction, it takes too much CPU time. In order to speed up the pre-fit technique, we use an iterative method. In the following, the reconstruction strategy that uses this iterative pre-fit is called ***iterative strategy***. The main purpose of this method is to converge as quick as possible to the 5 track parameters. The steps followed are represented in figure 3.19.

The starting point is the standard RECO pre-fit. We scan a small region around the obtained values of θ and ϕ, and select the direction that provides the largest number of selected hits with our pre-fit technique. This new direction is the starting point of an iterative process that alternates a step where the x, y and t_0 parameters are obtained with a step where a fit is performed. This fit is similar to the standard fit function (product of probabilities for each hit) in RECO, but the x, y and t_0 parameters are constant. The result obtained is compared with the previous iteration. The iteration finishes when the θ and ϕ parameters converge.

Then a new iteration is performed similar to the previous one, but where the fitting function is now the usual 5-parameter function. If a convergence is found in the itera-

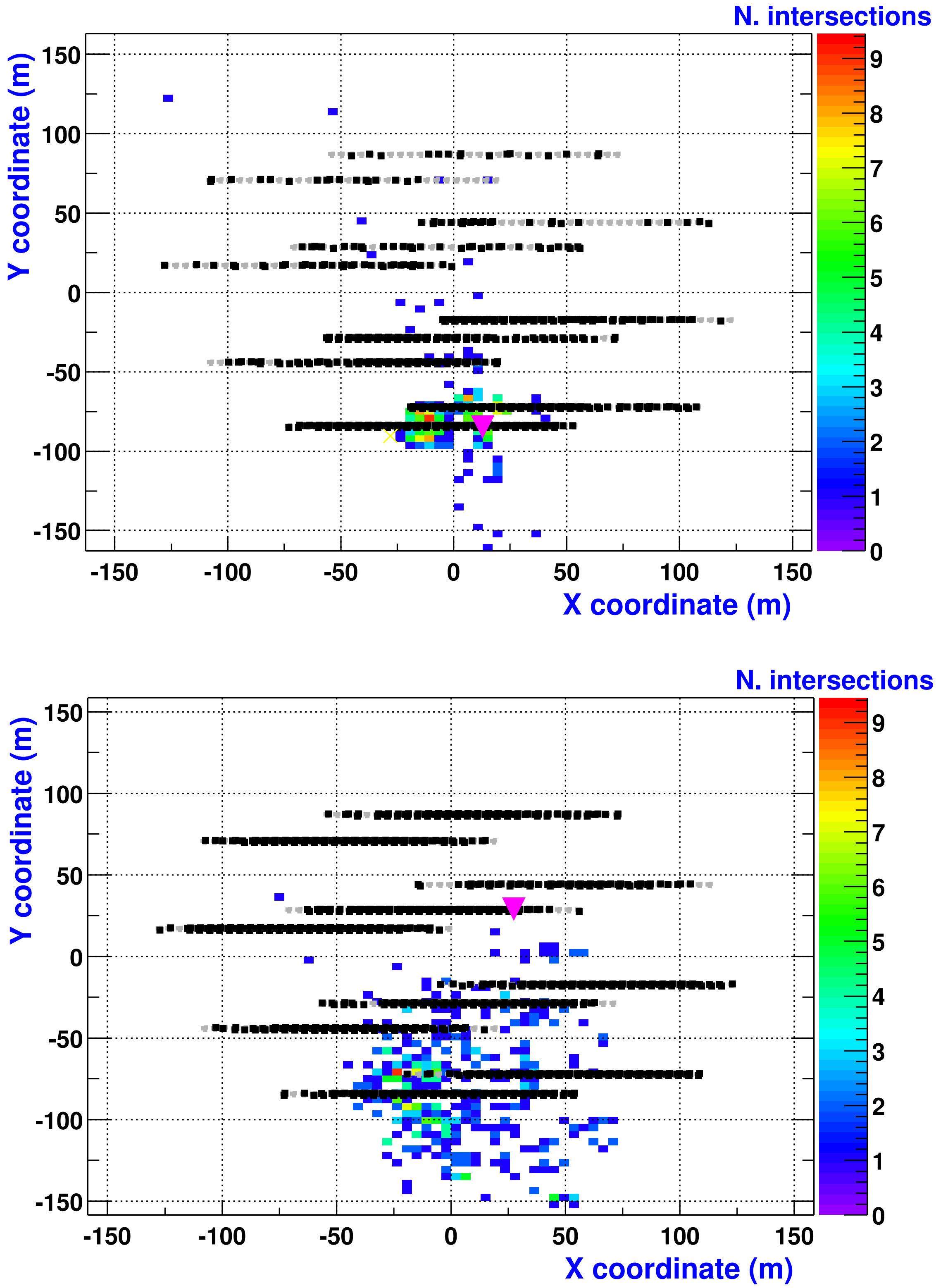

Figure 3.17: Projection of the hits (square points) and the track intersection point with the plane (triangle) together with the intersection points of the hyperbolas for two different events. The direction used is not the true muon direction.

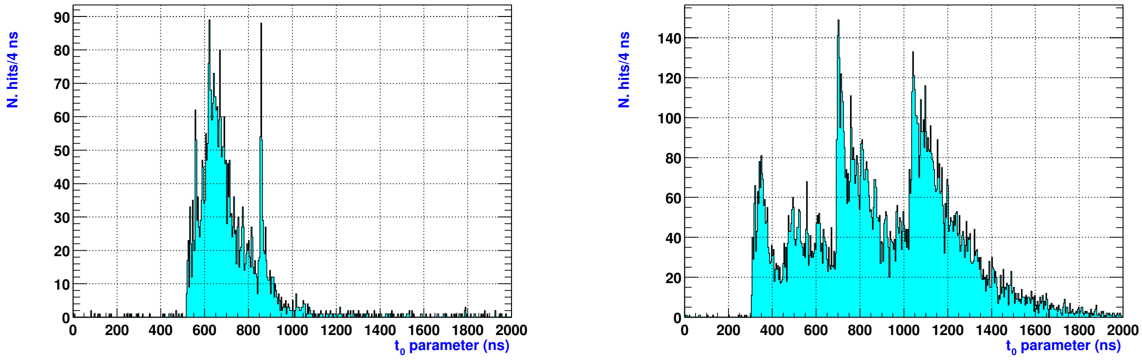

Figure 3.18: Distributions of the t_0 track parameter for the same two events, using the wrong x and y parameters from the previous figure.

tion with the 2-parameter fit, then the result quickly converges with the 5-parameter fitting function. However, sometimes the iteration process with the 2-parameter fitting function is abandoned after several iterations without convergence. Then the second iteration process with the 5-parameter fitting function is second chance. To save CPU time, not all the hits in the events are used for the fits. Instead, we use the same reduced sample used to compute the intersection points of hyperbolas.

Finally, we perform a last scan around the θ parameter to find a better solution that could provide a larger number of selected hits around the maximum in the t_0 histogram. In this way we obtain the set of five parameters that is finally used as starting point for the main RECO fitting routine.

This pre-fitting process is more elaborate than the standard RECO pre-fit and takes more time. However, it is not anymore a guess of the parameters, since it combines the technique for known θ and ϕ direction with calls to the fitting routine. When using the *iterative strategy* for reconstruction, the pre-fit is the most important part of the reconstruction. After the pre-fit, the call to the main RECO fitting routine only performs a fine tuning of the parameters.

3.6 Results with the 5-parameter pre-fit

In the next chapter we present the results obtained after reconstruction using the *iterative strategy* and compare the results with those from the standard strategy. However, in this section we make a comparison of the results obtained with the 5-parameter pre-fit to those from the 3-parameter pre-fit and the standard strategy pre-fit (see section 3.4).

The comparison between the true parameters and the reconstructed parameters can be seen in figure 3.20 for x, y and t_0. A total of 5755 events have been reconstructed,

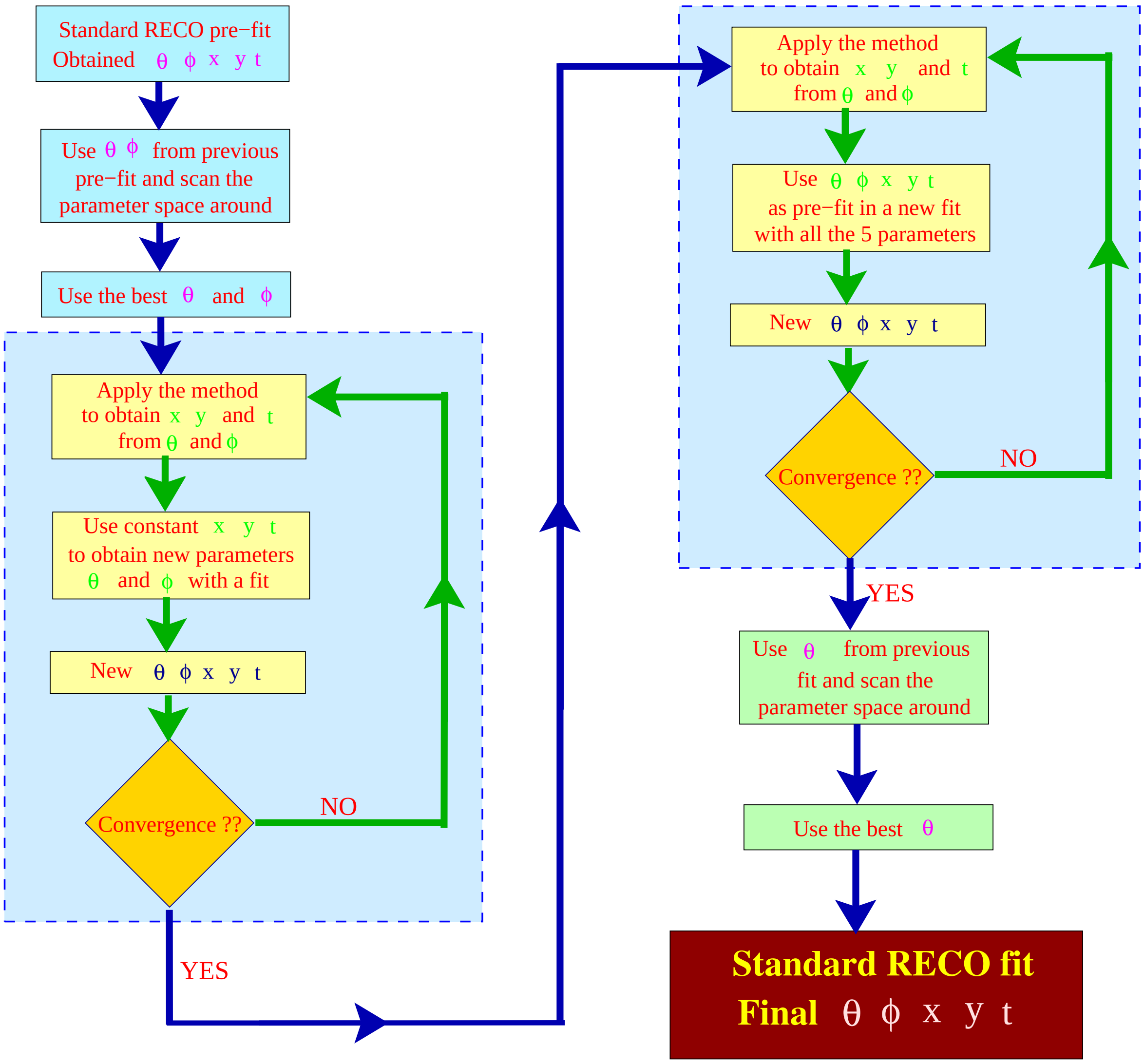

Figure 3.19: Scheme of the process followed in the 5-parameter pre-fit. An iterative process is used to arrive to the correct solution. For each iteration, the 3-parameter pre-fit is used with the candidate θ and ϕ parameters. The iterative process is performed twice, in one case the likelihood function used has two free parameters (θ and ϕ) an in the other case all the five parameters are free.

compared to the 6738 triggered events used in figures 3.14 and 3.15 (the reconstruction is only applied to those events meeting the reconstruction condition, i.e. more than 6 hits in at least 5 optical modules of more than 2 storeys in at least 2 different strings).

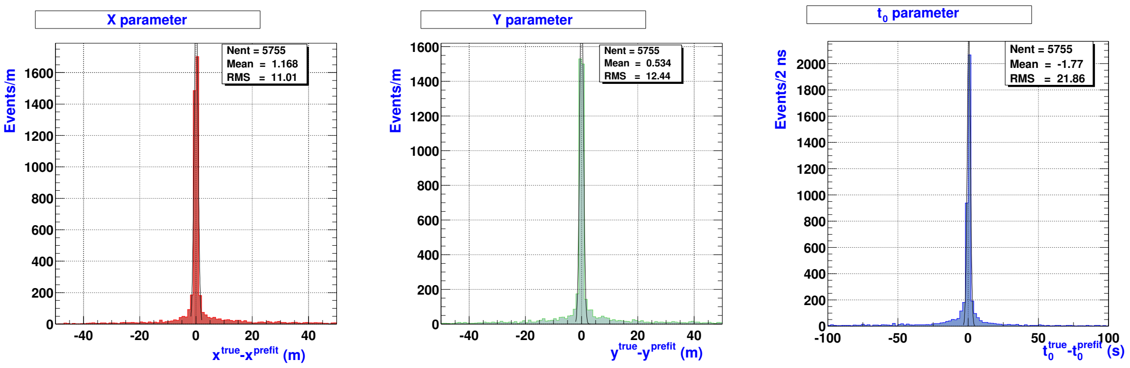

Figure 3.20: Difference between the true track parameter and the value estimated by the 5-parameter pre-fit in the *iterative strategy*.

- x **parameter from the pre-fit**: **73%** of the triggered events have $|x_{True} - x_{Pre-fit}| \leq 10\,m$. σ at the peak is 0.7 m.
- y **parameter from the pre-fit**: **71%** of the triggered events have $|y_{True} - y_{Pre-fit}| \leq 10\,m$. σ at the peak is 0.7 m.
- t_0 **parameter from the pre-fit**: **73%** of the triggered events have $|t_{True} - t_{Pre-fit}| \leq 25\,ns$. σ at the peak is 1.2 ns.

Compared to those from the 3-parameter pre-fit these results show that the percentage of events within the corresponding intervals are similar. However, the total number of reconstructed events is smaller than the total number of triggered events. In contrast, the sigma of the distributions are now smaller. We observe that the 5-parameter pre-fit of the *iterative strategy* provides a very good approximation to the true parameters in a high percentage of the events.

However, from the point of view of neutrino astronomy the important parameters are θ and ϕ of the muon. The results obtained for these parameters are presented in figure 3.21.

For comparison, we have applied the pre-fit of the standard strategy to the same 5755 events reconstructed with the *iterative strategy*. The results are presented in figure 3.22.

We observe that, regardless of the pre-fit used, the $\theta^{true} - \theta^{prefit}$ and $\phi^{true} - \phi^{prefit}$ distributions show again a small offset, although the central peaks are centered at zero. Both pre-fits can not give the correct parameters for all the tracks and when they fail, the tendency for the pre-fits is to compute a larger or smaller θ^{prefit} (the prefit is more

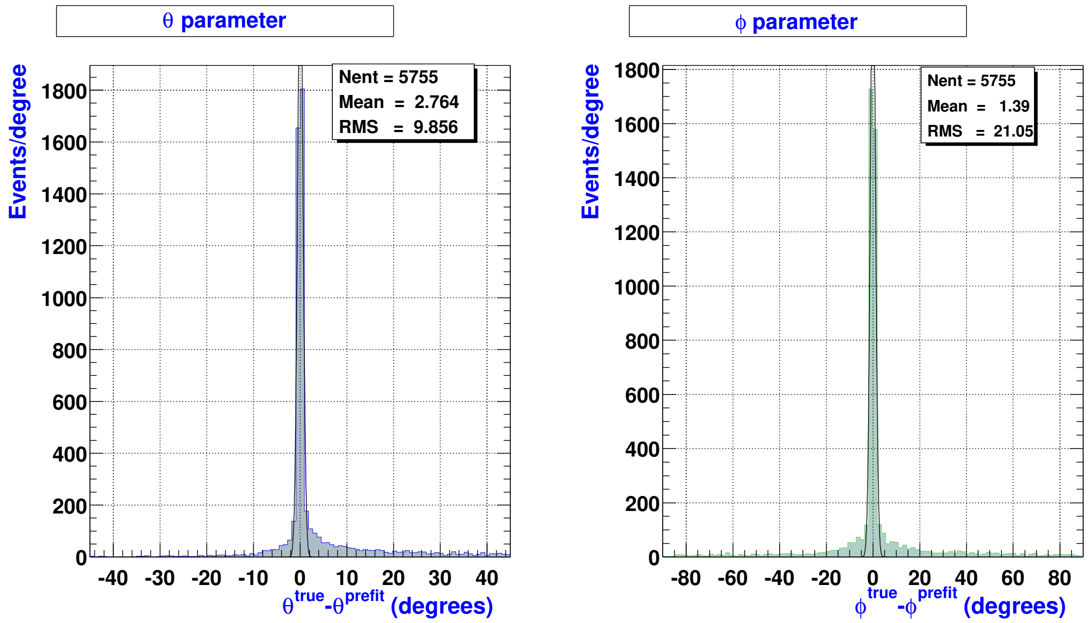

Figure 3.21: Difference between the true track parameter and the value estimated by the 5-parameter pre-fit in the *iterative strategy* for θ and ϕ.

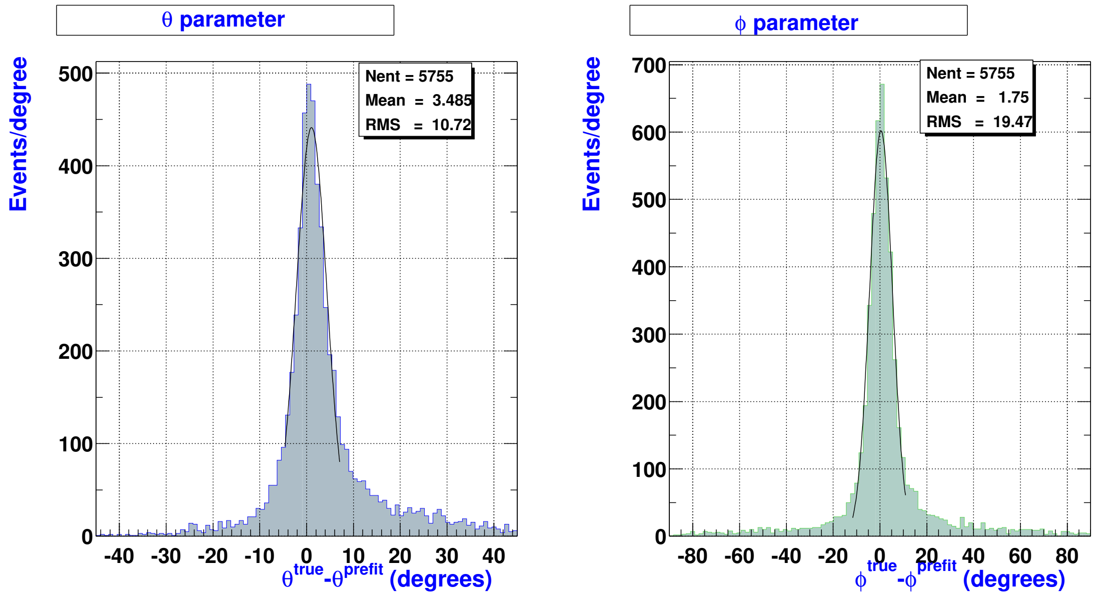

Figure 3.22: Difference between the true track parameter and the value estimated by the old standard reconstruction method (linear fit) for the θ and ϕ parameters.

vertical than the true track) due to the down-wards looking PMTs. With respect to the ϕ parameter, the reason could be the slightly asymmetry of the detector in azimuth. Anyway, the offsets are small compared with the typical values of the parameters (*theta* between 0° and 90°, *phi* between 0° and 360°) and they are smaller for the new pre-fit than for the standard pre-fit.

However, not all the events are well reconstructed after the iterative process. Sometimes the reconstruction fails to find the global minimum, arriving only to a local minimum. In other occasions there is a fake solution that is as good as the true one in terms of timing distribution. This is the case of the tracks reconstructed at twice the Cherenkov angle from the true track (an example can be seen in figure 3.23), a consequence of the ambiguity that exists in some events. The solution is to apply some selection criteria to reject the misreconstructed events. In the next chapter we will present the selection criteria used with the standard reconstruction and the new fitting procedure. The results obtained with our new reconstruction strategy are also compared with those obtained by the standard strategy.

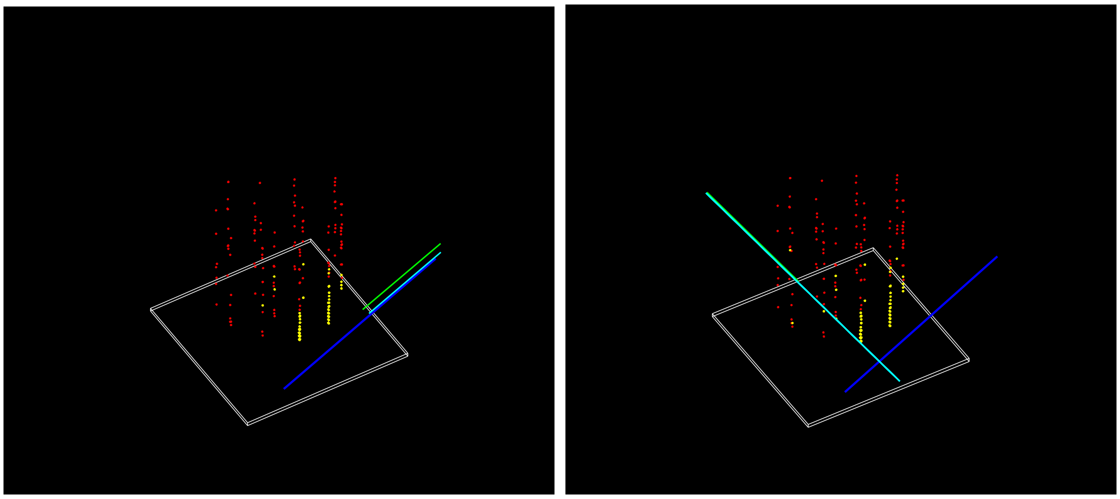

Figure 3.23: Example of event with a fake solution at twice the Cherenkov angle. Left: true muon track (dark blue) and well reconstructed track (light blue). Right: true muon track and fake solution at $\sim 84°$.

To summarise, the performances of the pre-fit in the *iterative strategy* are clearly above those from the pre-fit in the standard strategy. This has important consequences in the results obtained with the two different reconstruction strategies. As we will show in the following chapter, the *iterative strategy* provides a new reconstruction strategy that improves both the number of reconstructed events and the quality of the reconstruction. However, the problem of the misreconstructed fake events will require a new set of selection cuts.

Chapter 4

Performances of the ANTARES detector

In this chapter we present the performances that can be achieved with the ANTARES detector in terms of background rejection, effective area and angular resolution. These performances are calculated with the new fitting strategy (*iterative strategy*) and are compared with those obtained by the old reconstruction strategy. First, we present a rough comparison of the performances at reconstruction level. Then we introduce the selection criteria used with the standard strategy and the new strategy. Later, we compare the performances with both strategies in terms of ν and μ effective area, angular resolution and response to the atmospheric neutrino flux and to a signal with an E^{-2} spectrum. Finally, we study the effect of some environmental parameters in the *iterative strategy*: the influence of the group refraction index and different scattering models.

4.1 Comparison at reconstruction level

In order to perform the proper comparison of the performances of the ANTARES detector between the standard and the new reconstruction strategies, the criteria to select good quality tracks have to be defined in both cases. However, a first rough comparison of performances just after reconstruction can be made. This helps to understand the differences between the *iterative strategy* and the standard strategy. As an example, we have used a flux of 5×10^{10} neutrinos before entering the Earth, with an $E^{-1.40}$ distribution, flat in $\cos\theta$ and ϕ. After reconstruction, there are $14,295$ events reconstructed with the standard reconstruction and $24,407$ events with the iterative technique. This represents an increase of the *iterative strategy* over the standard strategy of **70%**. When the events are weighted by an E^{-2} flux, as expected for signal events, the increase is **69%**. If we compute the increase with events weighted by an E^{-2} flux that are reconstructed at less than $2°$ from the true muon track, the increase is **140%**.

The *muon angular resolution* is defined as the angle between the reconstructed muon track and the real muon track. The distribution of the angular resolution is shown in figure 4.1 for both reconstruction strategies. We observe that the *iterative strategy* has a better angular resolution. However, there is a relative large number of events reconstructed at $2 \times \theta_c$ ($\sim 84°$). As can be seen, the *iterative strategy* not only enhances the reconstruction of good tracks, but also of the ghost tracks at twice the Cherenkov angle. This side effect of the enhancement in efficiency must be corrected when the selection of events is performed.

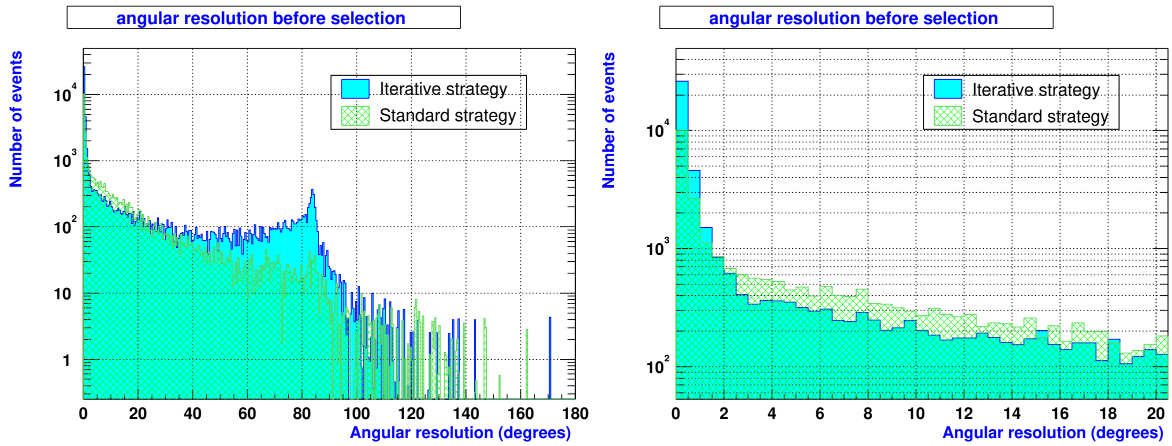

Figure 4.1: Left: Comparison of the angular resolution obtained by the iterative and standard strategies before applying selection cuts. Right: Detail of the angular resolution for both strategies at low angles.

4.2 Selection criteria

We introduce in this section the selection criteria used with each reconstruction strategy. The selection criteria are chosen not only to maximise the fraction of well reconstructed events accepted, but are also optimised to reject misreconstructed events, especially background down-going events reconstructed as up-going events. In chapter 2, we introduced the atmospheric muon background as a dangerous source of background events. It consists of down-going muons produced in cascades after the interaction of the cosmic rays with the atmosphere. In principle, the reconstruction process should be able to separate these events from up-going tracks. However, since the flux of atmospheric muon background events is several orders of magnitude greater than the flux of up-going events, a small fraction of down-going events reconstructed as up-going can dominate over any other kind of events.

The selection criteria used in each of the reconstruction strategies are described below.

4.2.1 Standard strategy

The best solution would be to compute a probability for any reconstructed event, being that probability flat distributed. However, this can not be obtained with the *pdf* used in the fitting routines.

The first set of cuts used with the standard strategy was developed by F. Hubaut [120]. He used a selection based on the following parameters:

- The errors of the reconstructed parameter must be $\delta_x, \delta_y < 5$ m, $\delta_\theta < 1°$, $\delta_\phi < 2°$ and $\delta_t < 6$ ns.

- The spatial and angular distance between the fit and the pre-fit must be $\Delta d < 150$ m and $\Delta\theta < 45°$. The spatial distance is measured between the intersection points of the fit and the pre-fit with the normal planes that contain the detector geometrical center. The angular separation is measured only for the θ angle.

- The ratio between the likelihood for the spherical fit and the conical (track) fit must fulfil: $\frac{\mathcal{L}_{spherical}}{\mathcal{L}_{conical}} < 0.5$.

The limiting factor in the estimation of the rejection of down-going atmospheric events is the available statistics. After ~1 day of simulated time, no event survived the selection cuts, which only ensures less than 1000 down-going events reconstructed as up-going per year.

The selection cuts were updated in the work of A. Oppelt [121]. After the reorganisation and update of the standard reconstruction code, the new selection criteria for the standard strategy were based on the following parameters:

- The difference of zenith angle between the fit and the pre-fit must be $\Delta\theta < 20°$.

- The distance between the fit and the pre-fit must be $\Delta d < 80$ m.

- The product of the errors of all the parameters in the fit should be $\delta_x \times \delta_y \times \delta_\theta \times \delta_\phi \times \delta_t < 0.01$.

Figure 4.2 shows the distribution of the angular resolution of the events reconstructed with the standard strategy versus the parameters used for selection. As can be seen, the selection cuts could yet be optimised by reducing the cut value for the distance and the zenith angle between the fitted and the pre-fitted tracks. The problem is that the selection cuts were developed for a very different detector geometry and have remained unchanged since then, so they are not optimised for the current detector geometry.

The biggest rejection is obtained with the cut based on the product of errors, as can be seen in the figure. The vertical lines in the figures show the cut values of the selection parameters.

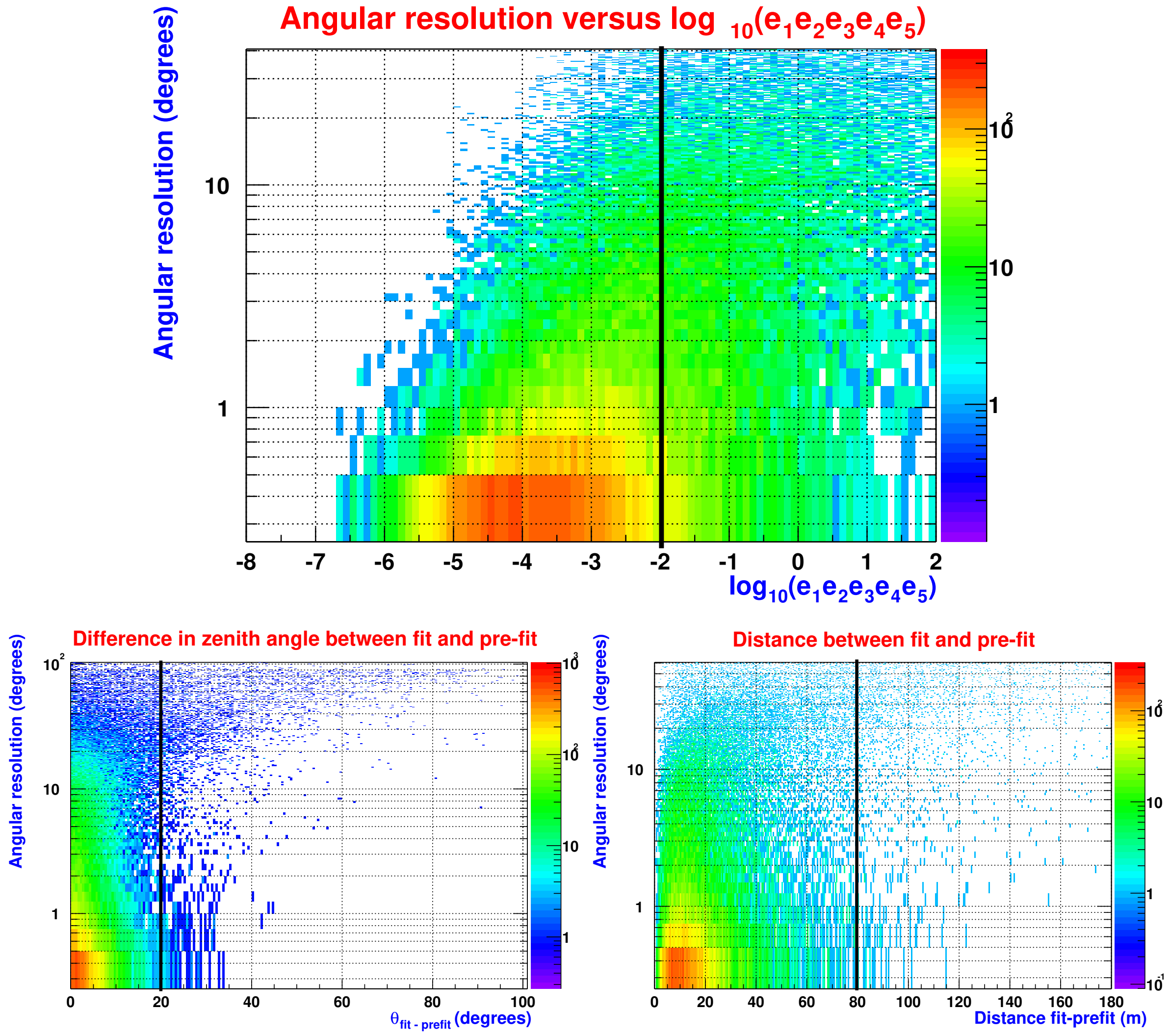

Figure 4.2: Angular resolution of the reconstructed events versus different parameters used for event selection with the standard strategy: the product of all errors (top), the difference of zenith angle between the fitted and the pre-fitted tracks (bottom left) and the distance between the fitted track and the pre-fitted track (bottom right).

In the following, this set of cuts will be used with the standard reconstruction strategy (*standard selection cuts*). The standard selection cuts provide a good angular resolution (low angle between the original track and the reconstructed one), but fail to reject the background of atmospheric down-going events. In order to reject the atmospheric muon background, additional cuts based on the number of hits in the event and the number of strings used in the reconstruction have proved to be very efficient.

4.2.2 Iterative strategy

The selection criteria used with the *iterative strategy* are based on the selection criteria of the standard strategy. As it has been said, the selection criteria have been adopted on the basis that the muon background must be rejected, but still keeping the maximum number of signal events. We have used an existing ANTARES mass production (February, 2001) of simulated atmospheric background events to test the quality of the selection cuts for background rejection. We have also used a large production of events following an E^{-2} spectrum, distributed uniformly in $\cos\theta$ and ϕ to test the response to signal events.

Among the different parameters that we have investigated in order to find the cuts for the *iterative strategy*, the most interesting ones are those used in the standard selection cuts: the angle between the fitted track and the old pre-fit (straight line fit), and the product of all the errors.

In order to increase the signal acceptance we have tried to relax some of the cuts by adding a new variable that helps to distinguish between real and fake up-going tracks. By looking at the angular distribution of the reconstructed down-going events, a maximum between 110° and 130° is observed. Moreover, down-going tracks reconstructed as up-going are very far in angle from the true muon track (specially true for the fake minimum at $\sim 84°$). However, the reconstructed azimuth angle is very close to the correct one (typically $< 15°$). This means that in many cases, for a misreconstructed down-going muon, the real muon has the same ϕ angle as the reconstructed track and a θ angle around 120°.

Using the same techniques as in the *iterative pre-fit*, explained in 3.5, we can take the direction (θ, ϕ) of the fitted track and apply the method to calculate the other parameters and finally obtain the number of selected hits N_1 in a narrow window around the maximum of the time histogram. We can also use the same technique for a direction which is $\theta = 120°$, same ϕ, and obtain another number of selected hits, N_2. For fake down-going tracks, N_2 should be close to (or even greater than) N_1. The following ratio can be computed:

$$X = \frac{N_1 - N_2}{N_1} \tag{4.1}$$

Moreover, the X ratio is calculated at different points ($\theta = 120°$ with $\phi \pm 20°$, $\theta = 115°$ with $\phi \pm 20°$) and the minimum X value obtained is kept. It was checked that fake up-going tracks have values of the X variable typically below 0.50. Therefore, adding a cut in this new variable to our set of cuts the rejection factor for fake up-going events is increased.

Table 4.1 and 4.2 summarise some of the results obtained with different sets of selection cuts. As can be seen, we have adopted the selection cuts that provide the best results according to the goal of having as much signal as possible with as low background as possible. The background has been divided into two categories: **mono-muons** which are down-going single muon events and **multi-muons** which are several down-going muons from the same atmospheric cascade (see section 4.3).

<table>
<tr><th>parameters</th><th>set 1</th><th>set 2</th><th>set 3</th><th>set 4</th><th>set 5</th><th>set 6</th><th>set 7</th></tr>
<tr><td>$\alpha_{fit-prefit}$</td><td colspan="7">$< 50°$</td></tr>
<tr><td>$\delta_1\delta_2\delta_3\delta_4\delta_5$</td><td colspan="2">NONE</td><td colspan="5">$< 10^{-3}$</td></tr>
<tr><td>X</td><td colspan="2">> 0.60</td><td colspan="2">> 0.45</td><td colspan="2">> 0.60</td><td>> 0.50</td></tr>
<tr><td>δ_4</td><td>< 10</td><td>< 2</td><td>< 1.5</td><td>< 2.0</td><td colspan="3">< 1.5</td></tr>
</table>

Table 4.1: Description of the sets of cuts used.

<table>
<tr><th rowspan="2">CUTS</th><th colspan="2">Signal</th><th colspan="2"># of atmospheric</th></tr>
<tr><th># events</th><th># events/year</th><th>mono-μ</th><th>multi-μ</th></tr>
<tr><td>set 1</td><td>33,496</td><td>7.0</td><td>277</td><td>163</td></tr>
<tr><td>set 2</td><td>28,557</td><td>6.0</td><td>8</td><td>2</td></tr>
<tr><td>set 3</td><td>28,089</td><td>6.0</td><td>7</td><td>3</td></tr>
<tr><td>set 4</td><td>27,138</td><td>5.7</td><td>2</td><td>1</td></tr>
<tr><td>set 5</td><td>26,161</td><td>5.4</td><td>1</td><td>0</td></tr>
<tr><td>set 6</td><td>25,867</td><td>5.4</td><td>1</td><td>0</td></tr>
<tr><td>set 7</td><td>27567</td><td>5.8</td><td>1</td><td>0</td></tr>
</table>

Table 4.2: Number of reconstructed events after applying the corresponding set of selection cuts. The last row corresponds to the selection cuts used in this work.

In the previous table, the number of events per year has been computed using an arbitrary flux normalisation of $2 \times 10^{-4} m^{-2} s^{-1} sr^{-1} GeV^{-1}$, that corresponds to the Waxman–Bahcall limit for neutrinos (anti-neutrinos not included).

The final selection cuts adopted for the *iterative strategy* are these on the last row of the table, namely:

1. Angle between straight-line pre-fit and the final fit $< 50°$.

2. X ratio larger than 0.5.

3. Error in the fourth parameter (δ_4) given by the fit < 1.5.

4. Product of all the errors given by the fit $< 10^{-3}$.

Figure 4.3 shows the angular resolution of the events reconstructed with the *iterative strategy* as a function of the different parameters used for selection. As can be seen, the proposed set of selection cuts (represented as vertical lines in the figures) can reject most of the misreconstructed events, while keeping most of the well reconstructed ones.

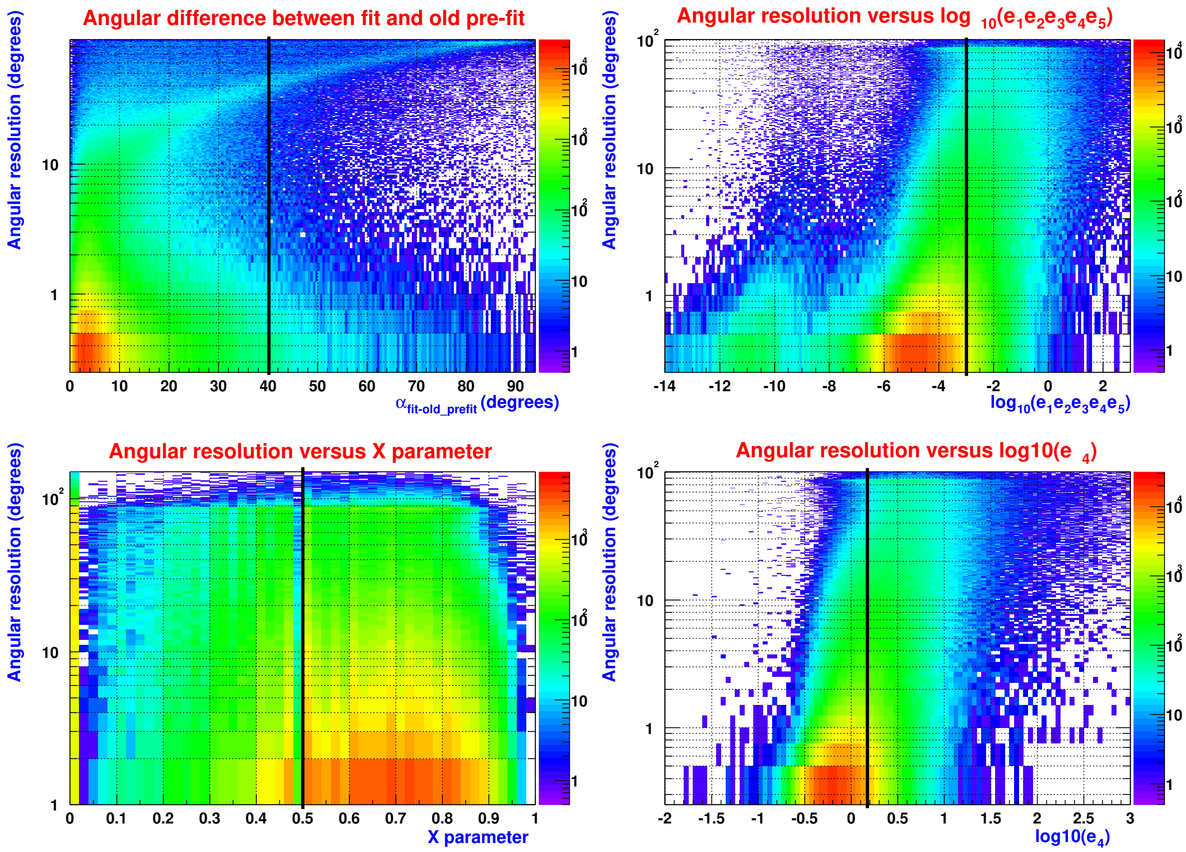

Figure 4.3: Angular resolution of the reconstructed events versus different parameters used for event selection with the *iterative strategy*: the product of all errors (top), the difference of zenith angles between the fitted and the pre-fitted tracks (bottom left) and the distance between the fitted track and the pre-fitted track (bottom right).

In principle, quality cuts should be based on the reconstruction's likelihood or goodness of fit which implies that the reconstruction probability has been thoroughly tested to follow the expected distribution function. This will hopefully be the case when real data will be available. However, in all the previous studies at the Monte Carlo level in ANTARES ([120–124]) cuts based on the errors of the fitted parameters have been used (lately a study based on likelihood cuts has been made, see [116]). Our quality cuts based on errors show that it is possible to separate well from badly reconstructed tracks. Cuts based on errors are not an advisable practice, though, because they can introduce biases.

In figure 4.4 we show a comparison of the distribution of several parameters for the selected and reconstructed tracks. As it is shown in the top-left plot of figure 4.4, the selection cuts with the *iterative strategy* do not bias the distribution of selected tracks as a function of neutrino energy. The main difference is that no tracks are selected below $log_{10}[E_\nu(GeV)] = 1.3$. This is due to the poor quality of the reconstructed tracks at very low energies ($E_\nu <$ 50 GeV). A similar result is shown in the top-right plot, where it is plotted the distance of the neutrino interaction point to the centre of the detector. As can be seen, the ratio of selected events to reconstructed events is constant regardless of the origin point of the track.

Concerning the reconstructed direction of the tracks (a key point in any telescope), we observe a different behaviour in the distribution of zenith angles after reconstruction or selection (bottom-left plot). However, this result is expected because of the asymmetry of the detector which has a spacing between storeys of 14.5 meters in the same string but ∼65 meters (on average) from one string to the others. The result is that the quality of the reconstruction degrades as the direction of the tracks are closer to the horizontal. As a consequence, the ratio of selected to reconstructed tracks is smaller as the zenith angle is closer to 90°. As can be seen, the selection cuts do not add any bias to this expected behaviour. Finally, no bias is observed in the distribution of azimuth angles after selection. Only a slight modulation of the number of selected tracks is observed due to the slight asymmetry of the detector over the ϕ angle. This effect is more noticeable at low energies but it is not due to the selection cuts.

The selection cuts proposed for the *iterative strategy* do not produce a significant bias in the distribution of the fitted parameters. Hereafter, all the results presented include the corresponding selection cuts for each reconstruction strategy.

4.3 Atmospheric muon background rejection

In this section we present the results obtained by both reconstruction strategies and their selection cuts in terms of atmospheric background rejection. Generation of atmospheric muon background events is a complex process when full simulation of the events from the cosmic ray interaction is required. In that case, the cosmic ray interaction and cascade development is performed with dedicated simulation packages as HEMAS [101]. Later the muons from the atmospheric cascade must be propagated to the can surrounding the detector. This is done with the program PROPMU [103]. Then, the simulation of the track propagation and detector response is performed. This process is so time consuming that up to now only a small amount of fully simulated events is available. These events represent a very short time period and they are not useful for testing the background rejection power.

For the time being, the strategy has been to produce two separate samples of down-going atmospheric muons. Each of the samples represents a large amount of real

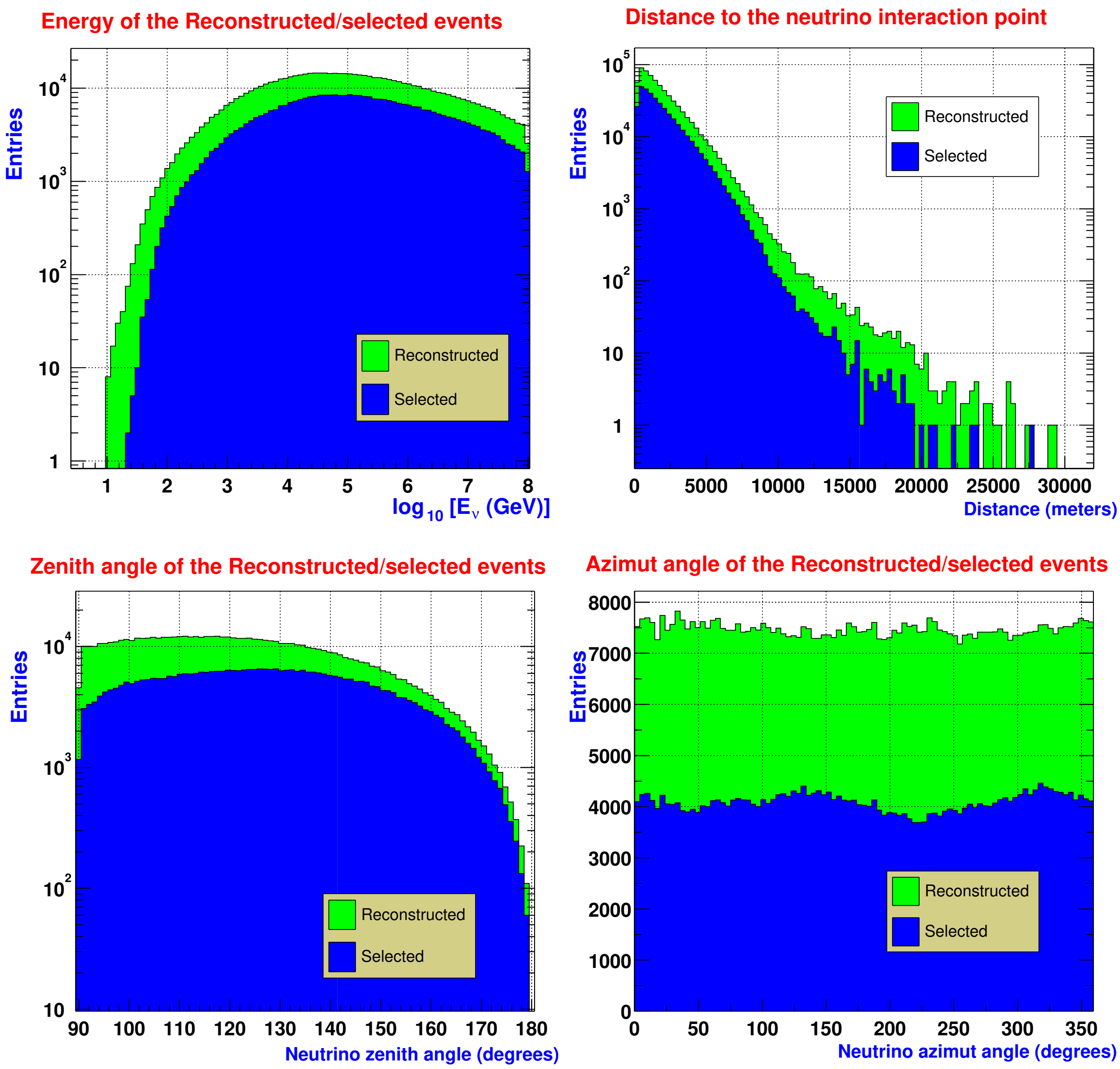

Figure 4.4: Comparison of the track parameters between the reconstructed tracks and the selected tracks. No significant bias is found in the track parameters after applying the selection cuts.

Type of events	Generator	N. of primaries	Real time
Single muons	GEM	3.367×10^8	~ 8.9 days
Multi-muons	HEMAS	4×10^7	~ 9 days
Fully simulated	HEMAS	9.9×10^6	~ 84 minutes

Table 4.3: Details of the productions of atmospheric background events used to test the reconstruction strategies.

time for a particular type of events. One of them consists of single muons generated following the Okada [125] parametrization with the GEM [126,127] program. The other sample, produced with HEMAS, consists only of events where at least 2 muons from the same cascade arrive to the detector. These kind of events are called *multi-muon events*. From the point of view of reconstruction, the multi-muon events are dangerous because they can mimic the signal of an up-going event. These parametrizations of the single muon and multi-muon flux are only approximate. In order to have an accurate estimate of the background rejection power, a full simulation is required. For the time being, these productions illustrate how the atmospheric backgrounds can be separated from the data at a reasonable cost.

Finally, we have used the available fully simulated sample. The simulated real time is too small but no significant differences are observed in comparison with the other samples studied. This is an indication that no major problems have been ignored. However, new productions with full simulation of single and multi-muon events should be studied in the future for a better estimation of the atmospheric backgrounds.

4.3.1 Single muons

For single muons we have used a production consisting of 962 files with 3.5×10^5 primaries per file. In this case, muons are generated at can level using the GEM program and the Okada parametrization.

In figure 4.5 we present the angular resolution (left) and zenith angle distribution of the reconstructed and selected tracks with the standard strategy. The sample used with the standard strategy consists of 4.2×10^7 events (~ 24 hours of real data according to Okada parametrization). In this sample, $175,732$ events have been reconstructed. Only $2,511$ events have passed the standard selection criteria, and 35 of them have been reconstructed as up-going events.

The 35 events represent more than $12,000$ events/year. These events would dominate over any other source of up-going events overtaking even the atmospheric neutrino flux. This problem could be solved by tightening the standard selection cuts but the performances of the reconstruction will be reduced. When the standard selection cuts where developed [120] [121], these samples of atmospheric backgrounds where not available and the choice of the selection cuts was based on other criteria. Since then, these cuts have remained unchanged, but they should be modified in order to reduce the

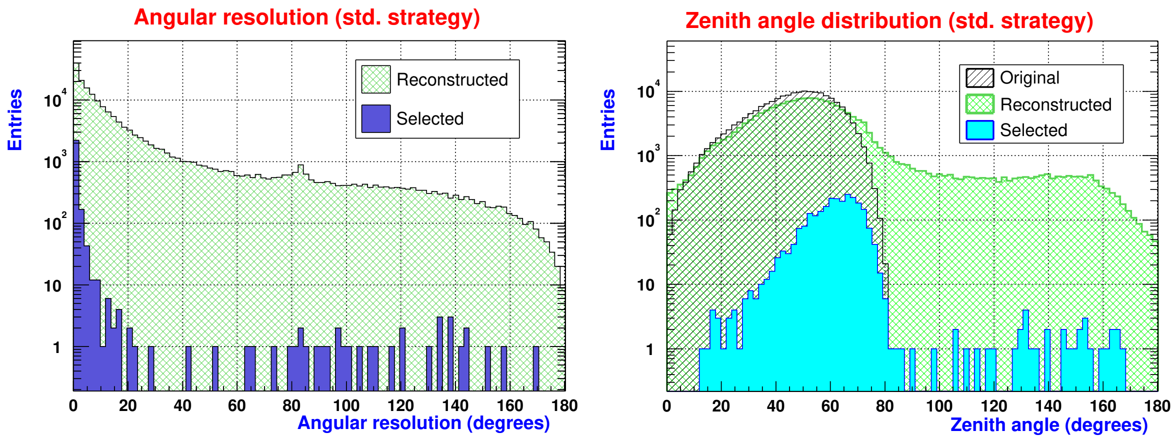

Figure 4.5: Single muon results with the standard strategy. Left: Angular resolution of the reconstructed and selected events. Right: Reconstructed zenith angle distribution for the reconstructed and selected events. For comparison, the true zenith angle distribution of the reconstructed events is also shown ("original").

atmospheric backgrounds.

With the *iterative strategy*, however, 87,534 events have been reconstructed with a sample covering a real time period of $\sim$ 9 days. Only one of the events passes the selection cuts and is reconstructed as up-going (see figure 4.6 for details). This result is far much better than the result of the standard strategy. In part, this is because the number of reconstructed events is much smaller ($\sim$ 9,730 events/day) than the number of reconstructed events with the standard strategy (175,732 events/day). Looking at the distribution of the angular resolution, we observe that the maximum of reconstructed tracks is at $2 \times \theta_c$, the ghost solution. Since the *iterative strategy* has been optimised for up-going tracks, the reconstruction prefers the ghost solution if it is up-going.

4.3.2 Multi-muons

For the multi-muons, 4.00×10^7 primaries generated in the range $0° < \theta < 70°$, have been studied. The sample covers a real time period of $\sim$ 9 days. In this case we find similar results to those obtained in the single muon case for both reconstruction strategies.

For the standard strategy we have finally reconstructed 1.256×10^6 events out of which 61,689 have passed the selection cuts (see figure 4.7) and 346 selected events have been reconstructed as up-going. This represents 38.4 up-going events/day due to atmospheric multi-muon background, very similar to the 35 events/day from the atmospheric single muon background. The same conclusion is drawn from this result, the standard selection cuts must be tightened to eliminate the down-going atmospheric

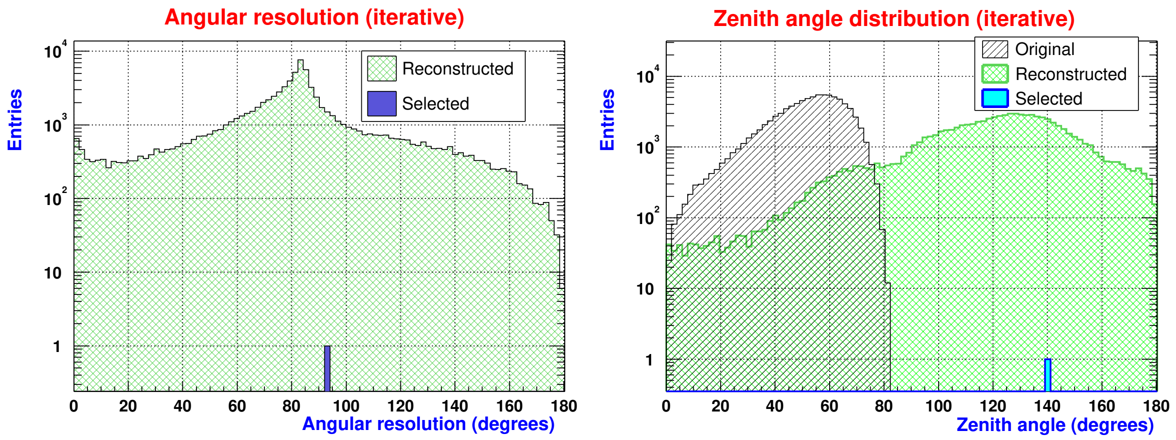

Figure 4.6: Single muon results with the *iterative strategy*. Left: Angular resolution of the reconstructed and selected events. Right: Reconstructed zenith angle distribution for the reconstructed and selected events. The true zenith angle distribution of the reconstructed events is also shown.

backgrounds.

For the *iterative strategy*, the results can be seen in figure 4.8. In this case, 144,188 events have been reconstructed, but none of them has passed the selection cuts. Again, less atmospheric background events have been reconstructed, what reduces the chance for one of these events to be reconstructed as up-going. The angular resolution and zenith angle distributions are very similar to those obtained with the single muon sample.

4.3.3 Combined single muons and multi-muons

A new sample of fully simulated single and multi-muon combined events has been studied. A sample of 9.9×10^6 primaries has been produced to simulate a real time period of ~ 100 minutes. This reflects the enormous computation power needed to simulate a large amount of real time. This production is useful to check that no major problems have been underestimated by separating single muons and multi-muons. Moreover, in the multi-muon sample the muons were generated with zenith angle between $0°$ and $70°$. In this case, however, the down-going tracks have been generated between $0°$ and $80°$. This sample can show whether the nearly horizontal tracks represent a danger that was not studied in the previous multi-muon sample.

The results obtained with the *iterative strategy* can be seen in figure 4.9. As expected, we do not observe any event passing the selection cuts. If only one of such events was selected, the atmospheric background would dominate over any other signal (the problem found with the standard strategy and its selection cuts). The shapes of the distributions are similar to those in the previous single and multi-muons productions.

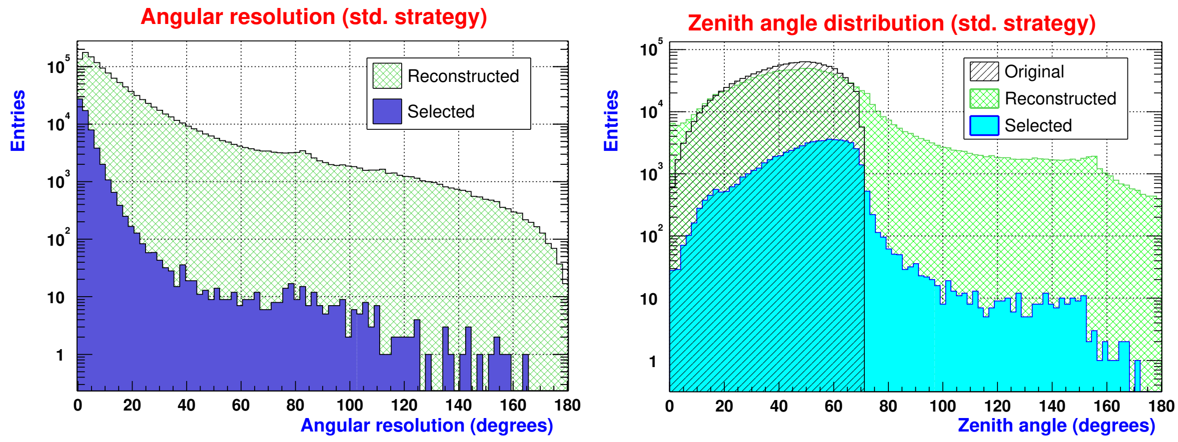

Figure 4.7: Multi-muon results with the standard strategy. Left: Angular resolution of the reconstructed events and the selected events. Right: Reconstructed zenith angle distribution for the reconstructed and selected events. The true zenith angle distribution of the reconstructed events is also shown.

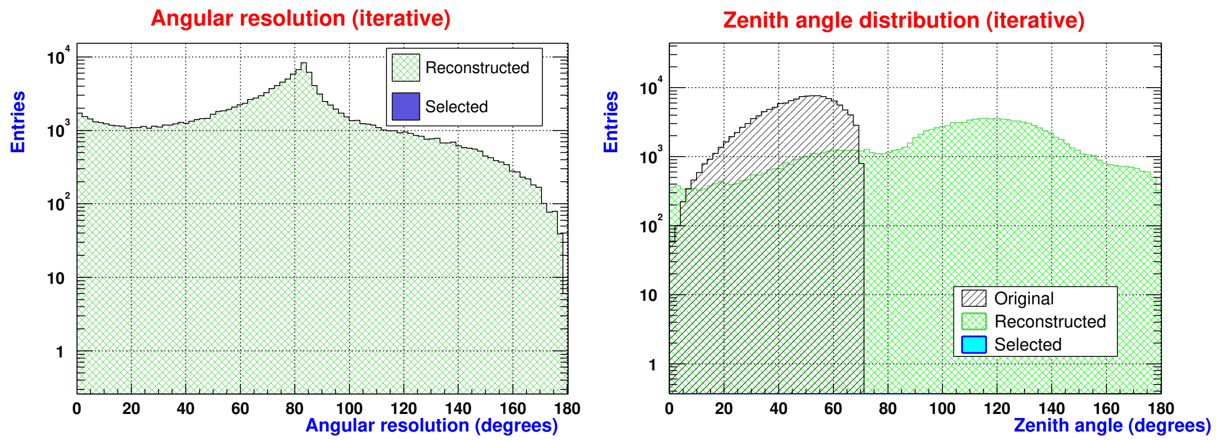

Figure 4.8: Multi-muon results with the *iterative strategy*. Left: Angular resolution of the reconstructed and selected events. Right: Reconstructed zenith angle distribution for the reconstructed and selected events. The true zenith angle distribution of the reconstructed events is also shown. In this case, no event is reconstructed as up-going.

Since the simulated time covered by this sample is very small, we can only say that this result does not contradict the results obtained with the other samples.

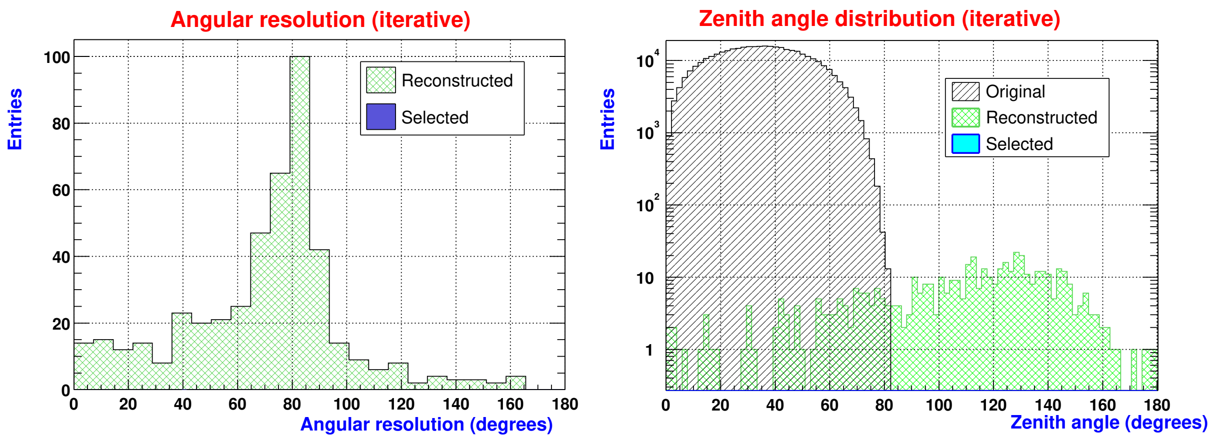

Figure 4.9: Results of the *iterative strategy* for the fully simulated sample. Left: Angular resolution of the reconstructed events and the selected events (none). Right: Reconstructed zenith angle distribution for the reconstructed and selected events (none). The true zenith angle distribution of all the events in the sample is also shown.

4.3.4 Summary

The *iterative strategy* is less efficient for down-going tracks than the standard strategy. This is an interesting feature because it provides a natural protection against down-going atmospheric muon events. On the other hand, it is not an adequate reconstruction strategy for studying the flux of down-going events.

The reason is that the *iterative strategy* has been optimised for up-going events. The *iterative strategy* uses combinations of 3 Cherenkov hits in the same event. These hits are much more likely for up-going tracks because the optical modules in the detector are looking downwards (at 45° degrees from the vertical). It is therefore unlikely that a down-going track produces enough Cherenkov hits for the method to work properly. Moreover, the *iterative strategy* has been optimised to reject atmospheric down-going tracks during the development of the code, which was not the case for the standard strategy.

Finally, the cuts we have selected are also optimised to reject as much atmospheric background as possible, as we showed in section 4.2. The results obtained with the *iterative strategy* using different sets of selection cuts are summarised in table 4.2.

4.4 Signal performances

The performances of the ANTARES detector are studied in this section. We compare the results obtained with the *iterative strategy* with those obtained with the standard strategy. The main parameters studied are the detector effective area and the angular resolution. The predicted number of detected events for an isotropic neutrino flux following an $E^{-\alpha}$ energy distribution is also compared for both reconstruction strategies. This gives an idea of the performances of the detector for signal events[1].

4.4.1 Effective Area

To express detector efficiency we essentially use the ratio of selected events with respect to incident events. However, this quantity can be expressed in a more convenient way as an *effective area*. The effective area is not only a suitable way of expressing the detector efficiency, but also has an intuitive meaning. This parameter reflects the size of a 100% efficient flat surface that observes the same number of through-going neutrinos/muons than the detector. The same parameter can be expressed in terms of neutrinos or muons, known as neutrino effective area and muon effective area respectively.

Neutrino effective area

The effective area for neutrinos is computed from the number of events selected with respect to the total incident neutrino flux. The neutrino flux is considered before traversing the Earth. The resulting effective area is a parameter independent of the incident neutrino flux. It is a function of neutrino energy (E_ν) and neutrino direction (θ_ν and ϕ_ν). The definition of effective area is given by:

$$A^{\nu}_{eff}(E_\nu,\theta_\nu,\phi_\nu) = \frac{N_{selected}(E_\nu,\theta_\nu,\phi_\nu)}{N_{generated}(E_\nu,\theta_\nu,\phi_\nu)} \times V_{generation} \times (\rho N_A) \times \sigma(E_\nu) \times P_{Earth}(E_\nu,\theta_\nu) \quad (4.2)$$

where $N_{selected}$ is the number of selected events (after applying the selection cuts) and $N_{generated}$ is the number of events in the generated neutrino flux. $V_{generation}$ is the volume where the generation was made, as explained in chapter 2. This volume is much larger than the simulation volume to make sure that it contains all the possible neutrino interactions. The parameter ρ accounts for the average Earth density and N_A stands for Avogadro's Number. Finally, $\sigma(E_\nu)$ is the neutrino interaction cross–section, whereas $P_{Earth}(E_\nu,\theta_\nu)$ represents the probability for a neutrino of energy E_ν and zenith angle θ_ν to cross the Earth up to the interaction point.

The effective area allows to compute the number of selected events for any incident flux (before traversing the Earth) using the following equation

[1]Remember that signal events are expected to follow a distribution characterised by a spectral index $\alpha \sim 2$.

$$N_{selected} = \int A_{eff}(E_\nu, \theta_\nu, \phi_\nu) \times \frac{d\Phi_\nu}{dE_\nu d\theta_\nu d\phi_\nu} \, dE_\nu \, d\theta_\nu \, d\phi_\nu \tag{4.3}$$

where $\frac{d\Phi_\nu}{dE_\nu d\theta_\nu d\phi_\nu}$ is the differential neutrino flux before entering the Earth.

In figure 4.10 (top) we can see the neutrino effective area as a function of neutrino energy for the standard and the *iterative* strategies after applying the selection cuts. An upward incident neutrino flux, uniform in $\cos\theta$ and ϕ, i.e. isotropic, has been used. We observe that below $E_\nu = 10^2$ GeV the neutrino effective area obtained with both strategies is almost the same or it is even better in the case of the standard strategy. This is because the selection cuts are more restrictive in the *iterative strategy* than in the standard strategy. These cuts are specially hard at lower energies where the number of hits is smaller and the reconstruction of the events is more difficult.

As the energy of the neutrinos increase, the *iterative strategy* effective area increases faster than the standard strategy one. As it is shown in figure 4.10 (bottom), the relative increase of the *iterative strategy* with respect to the standard one is moderate up to 10^5 GeV, where a 100% increase is achieved. Above this energy the relative increase of the new strategy over the standard one accelerates. At 10^8 GeV the *iterative strategy* is able to reconstruct and select 4 events for each event reconstructed and selected with the standard strategy.

The effect of the selection cuts and their quality is shown in figure 4.11. This figure contains the effective area computed with four type of events: all the reconstructed events; events reconstructed with an angular resolution smaller than 1°; all the selected events; events selected with an angular resolution smaller than 1°.

In figure 4.11 we observe a clear difference between both reconstruction strategies. For the standard strategy, there are more selected events than events reconstructed with an angular resolution smaller than 1°. The selection is not very hard and most of the events well reconstructed are selected, but also many of the events that are not properly reconstructed pass the selection cuts.

The situation is different with the *iterative strategy*, here the selection is very restrictive and we observe that the selected events as well as the events reconstructed and selected with an angular resolution smaller than 1° produce almost the same effective area. So, very few events badly reconstructed pass the selection cuts but yet most of the events well reconstructed ($< 1°$) are selected.

Muon effective area

The detector efficiency can also be expressed in terms of muon effective area. The effective area for muons is the quantity used to compare the size of different detectors. Although it is a quite intuitive concept (the size of a 100% efficient flat surface that observes the same number of through-going muons than the detector), its definition is not straightforward. The problem of defining an effective area for muons is addressed in [128]. There, it is shown that the number of observed events in the detector can be

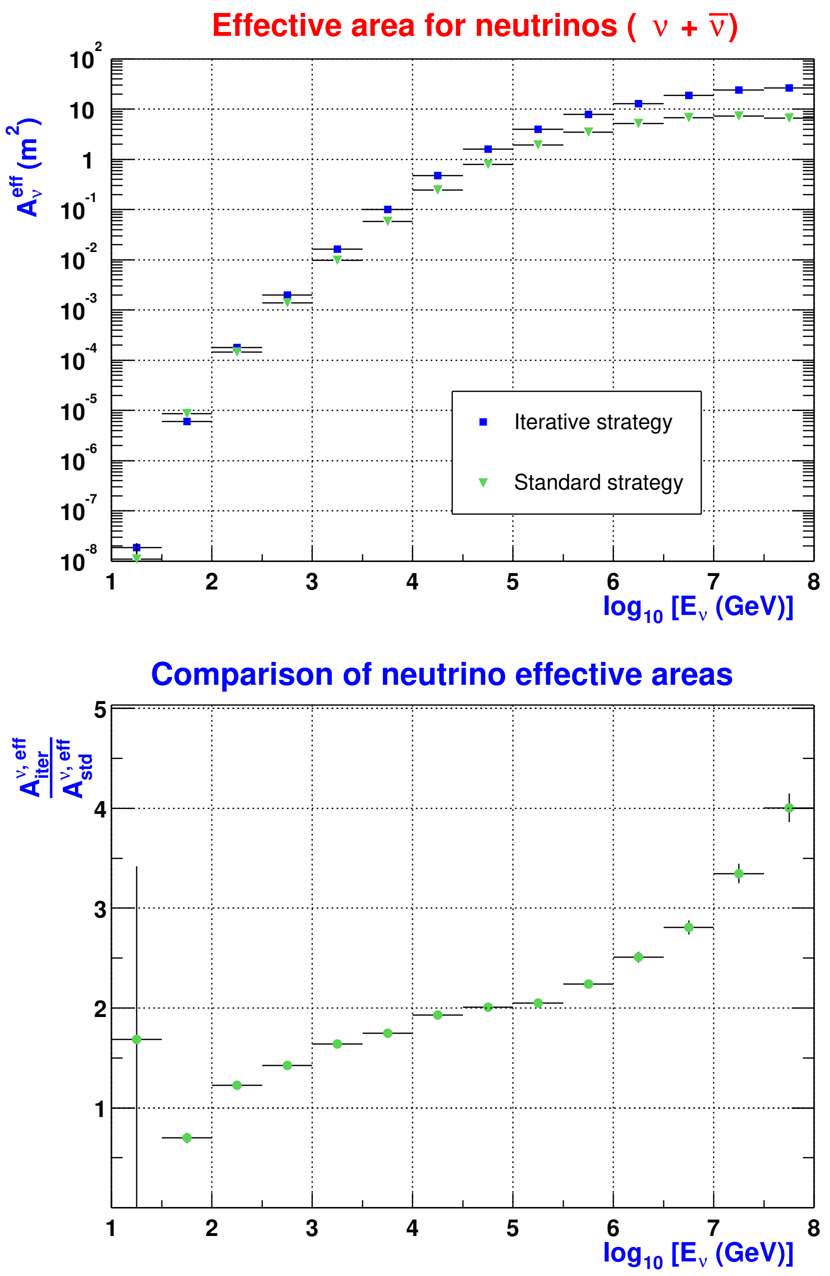

Figure 4.10: Top: Effective area for neutrinos with the iterative and the standard strategies after their respective selection cuts. Bottom: Ratio of the *iterative strategy* neutrino effective area and the standard strategy neutrino effective area.

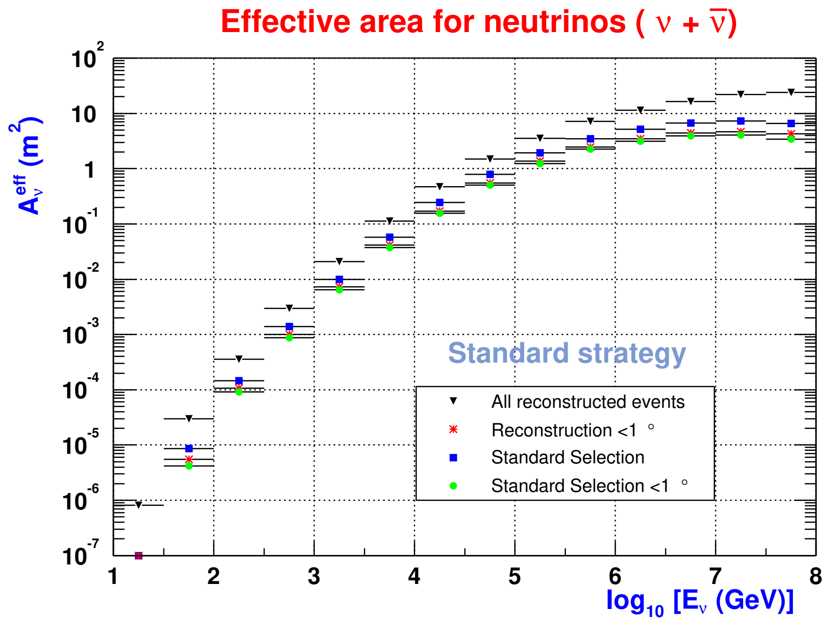

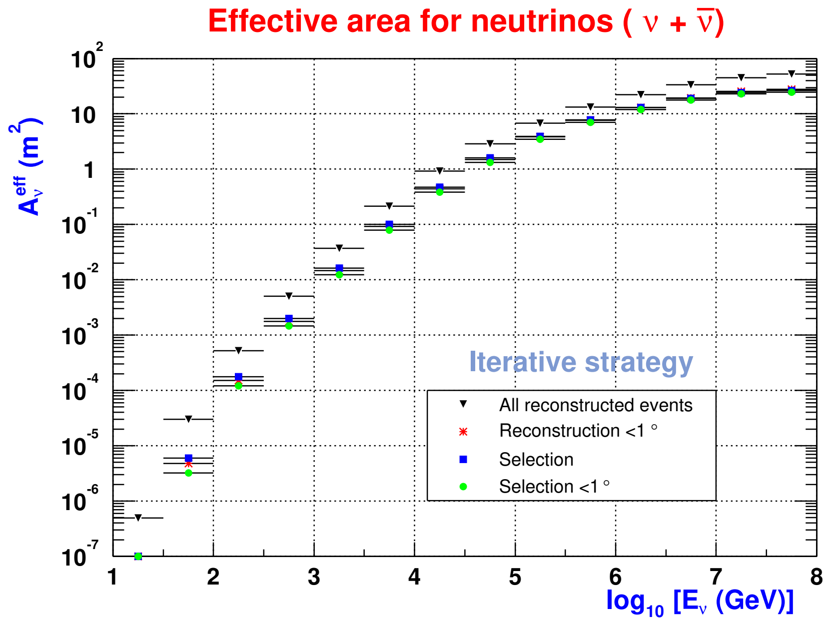

Figure 4.11: The quality of the reconstruction and the selection cuts for the standard strategy (top) and the *iterative strategy* (bottom) in terms of effective area for neutrinos.

expressed in terms of the muon flux, when omitting the dependence on the direction and the absorption in the Earth, as:

$$N_{observed} = \int \frac{V_{eff}(E_\nu)}{\langle R^\mu_{eff}(E_\nu)\rangle} \frac{d\Phi_\mu}{dE_\nu} dE_\nu \tag{4.4}$$

where V_{eff} is the effective detector volume, which is defined as the ratio of the number of selected events to the total generated events times the generation volume. $\langle R_{eff}(E_\nu)\rangle$ is the average effective range for muons coming from neutrinos with energy E_ν. The effective range (R^μ_{eff}) is, in turn, the average distance travelled by muons with a given starting energy up to the point where their energy goes below a given threshold. Finally $d\Phi_\mu/dE_\nu$ is the muon flux in terms of neutrino energy.

The first quantity in equation 4.4, $V_{eff}(E_\nu)/\langle R^\mu_{eff}(E_\nu)\rangle$, multiplied by the muon flux gives the number of observed events. By definition this quantity is the effective area, that can be expressed as

$$A^\mu_{eff}(E_\nu, \theta_\nu, \phi_\nu) = \frac{N_{selected}(E_\nu, \theta_\nu, \phi_\nu)}{N_{generated}(E_\nu, \theta_\nu, \phi_\nu)} \times \frac{V_{generation}}{\langle R^\mu_{eff}(E_\nu)\rangle} \tag{4.5}$$

In the previous expression, the muon flux, $d\Phi_\mu/dE_\nu$, is written in terms of muons produced by neutrinos in the energy range $E_\nu \to E_\nu + dE_\nu$. This quantity is well defined but it is not the most intuitive representation of the muon flux. However, there is no unique definition of the muon energy, since it changes as the muon propagates, and there is no common surface crossed by all the muons that could be used as reference. This, and the fact that using the muon flux in terms of neutrino energy simplifies the computation of the effective areas make the representation of the effective area for muons as a function of neutrino energy widely accepted.

A comparison between the effective area obtained with both strategies is shown in figure 4.12. This figure shows again that the *iterative strategy* offers a considerable increase of performances compared with the standard strategy. The difference between the reconstruction strategies increases with the neutrino energy. However, the increase in terms of muon effective area is not as important as in terms of neutrino effective areas. Figure 4.12 (bottom) shows that the maximum increase is a factor 2.5 with respect the standard strategy above 10^7 GeV. The ratio between reconstruction strategies is quite different between A^ν_{eff} and A^μ_{eff}. This is because the A_{eff} is also a function of the angles θ and ϕ. The A_{eff} values shown up to now are represented only as a function of E_ν, so they have been averaged over the *hidden* parameters using an isotropic neutrino flux. Hence, the different behaviour of the reconstruction strategies as a function of the zenith angle explains the difference.

Below $\sim$ 300 GeV, however, and due to the selection cuts, the *iterative strategy* produces a muon effective area after selection which is below the one produced with the standard strategy.

The quality of the selection cuts for each of the reconstruction strategies is shown in figure 4.13. As in the case of the neutrino effective areas, we observe that the selection of the standard strategy contains most of the events well reconstructed but also contains

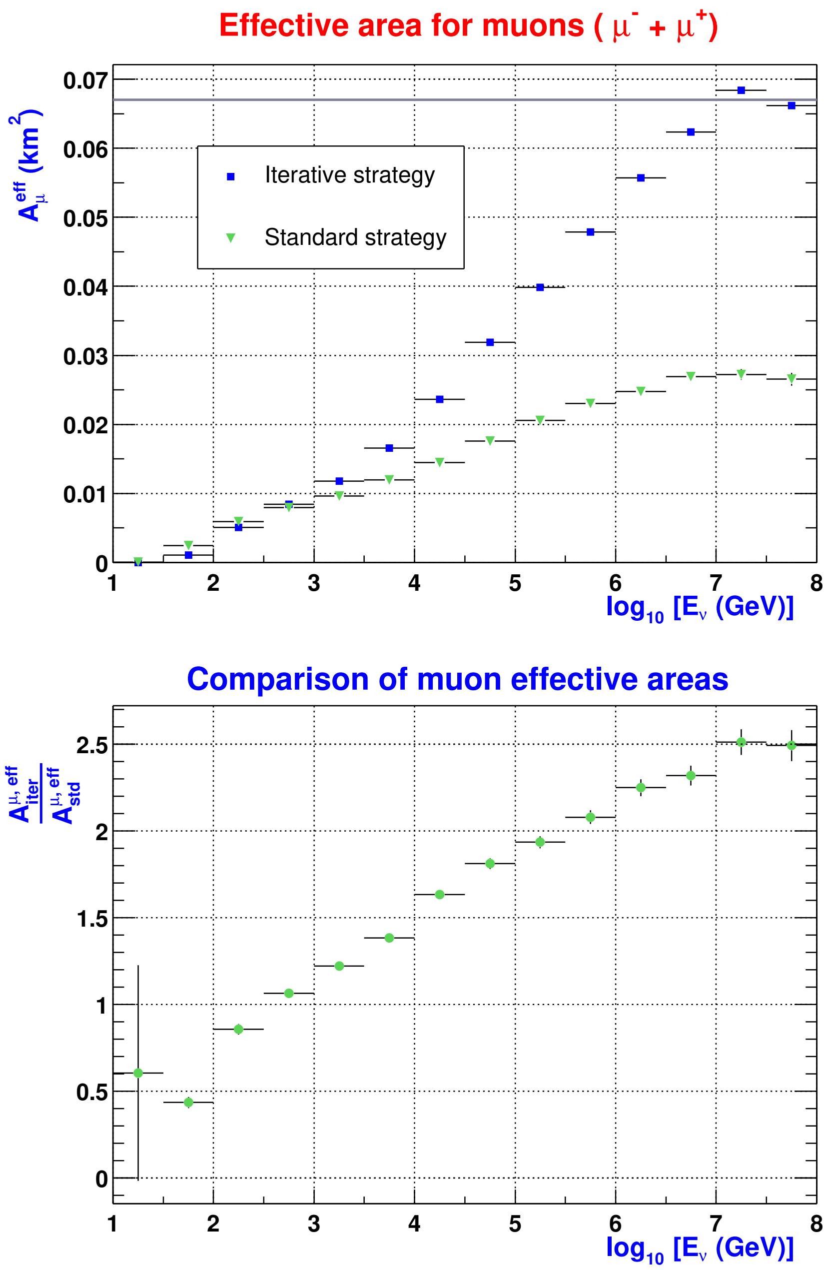

Figure 4.12: Top: Effective area for muons with the iterative and the standard strategies after their respective selection cuts. The continuous straight line indicates the geometrical size of the instrumented volume of the detector. Bottom: Ratio of the *iterative strategy* muon effective area and the standard strategy muon effective area.

many events that are not well reconstructed. In the *iterative strategy* the A_{eff} obtained with the selected events is very close to the A_{eff} with the well reconstructed events ($< 1°$). However, the cuts are so strict that part of the well reconstructed events do not pass the selection. The selection used with the *iterative strategy* rejects more events that are badly reconstructed than the selection for the standard strategy which is very important for the atmospheric background rejection. The price paid for this is that the *iterative strategy* is less efficient below $\sim$ 300 GeV and some of the well reconstructed events are not selected.

4.4.2 Angular resolution

The angle between the muon track and the reconstructed track is called the *angular resolution of the event*. The distribution of the angular resolution of all the events is usually described with the median of the distribution[2] and it is called the *muon angular resolution* of the sample. We also define a *neutrino angular resolution*, described by the median of the distribution of the angles between the neutrino and the reconstructed track in each event (*neutrino angular resolution of the event*).

The muon angular resolution is more adequate to describe the detector performances and to compare reconstruction efficiencies since the neutrino angular resolution contains the unavoidable physical angle between the neutrino and the muon. The angular resolution is, hence, a measure of the pointing accuracy that can be achieved with the detector while the neutrino angular resolution reflects the pointing accuracy that can be achieved when observing a point-like neutrino source.

Figure 4.14 (top) shows the angular resolution obtained with the standard strategy as a function of the neutrino energy. For comparison the neutrino angular resolution has been also plotted in the same figure. In the case of the *iterative strategy*, the results are also shown in figure 4.14 (bottom). With the standard strategy, the angular resolution improves with the neutrino energy up to $log_{10}(E_\nu) = 5.5$ GeV. Above this value, the angular resolution worsens as the energy of the neutrino increases. On the contrary, with the *iterative strategy* the angular resolution improves continuously with the neutrino energy.

At low energies (below 1 TeV) the neutrino angular resolution is dominated by the physical unavoidable angle between the neutrino and the muon. The neutrino angular resolutions obtained with both reconstructions are almost the same. However, the muon angular resolution obtained with the *iterative strategy* is slightly better. At higher energies, the neutrino and muon angular resolutions improve. Above $10^{4.5}$ GeV the neutrino and muon angular resolution are the same because the angular resolution is dominated by the reconstruction angle. With the standard strategy, the best angular resolution is obtained at a neutrino energy around $\sim 10^{5.75}$ GeV and it is 0.4°. Above this energy, the angular resolution degrades as the energy increases. With the *iterative strategy*, however, the best value of the angular resolution (median of the distribution) is

[2]The use of the median instead of the mean avoids an overestimation of the long, but poorly populated tails of the distribution.

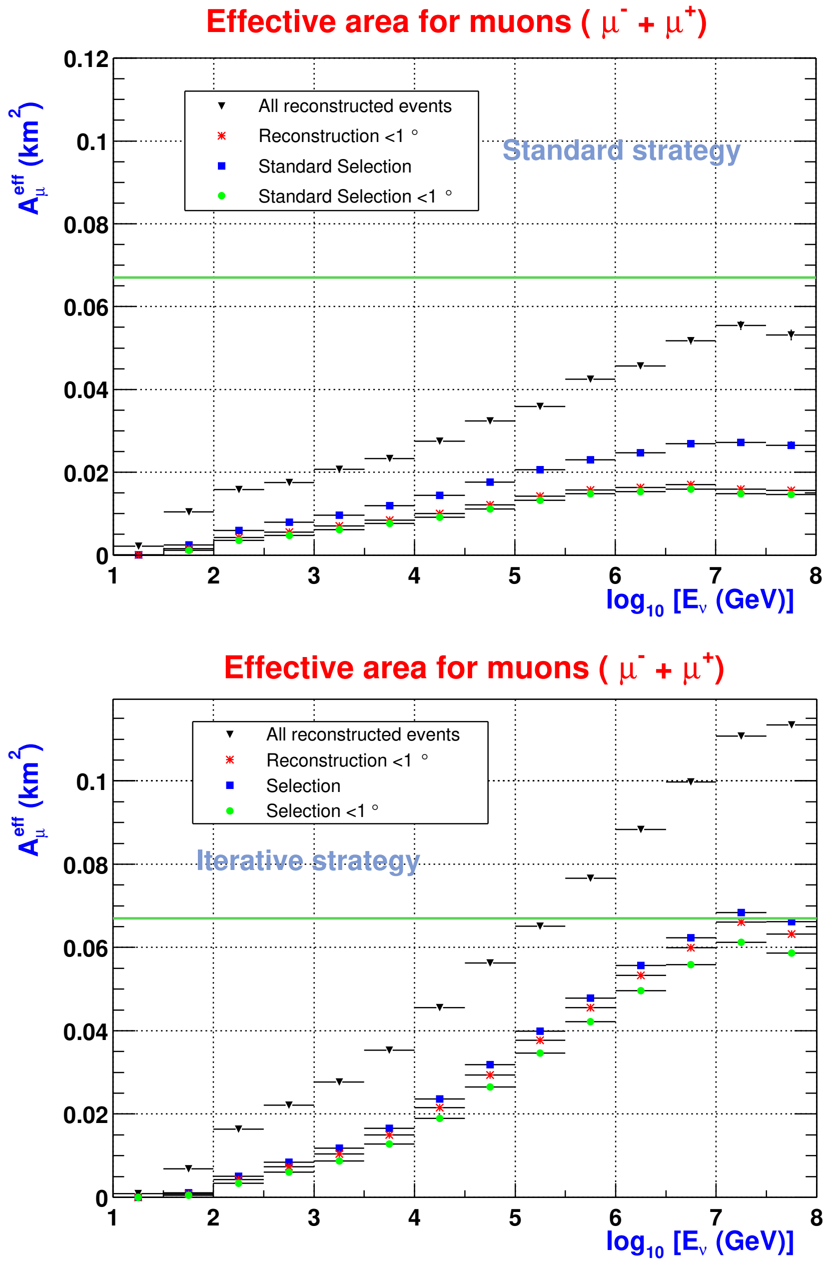

Figure 4.13: The quality of the reconstruction and the selection for the standard strategy (top) and the *iterative strategy* (bottom) in terms of effective area for muons.

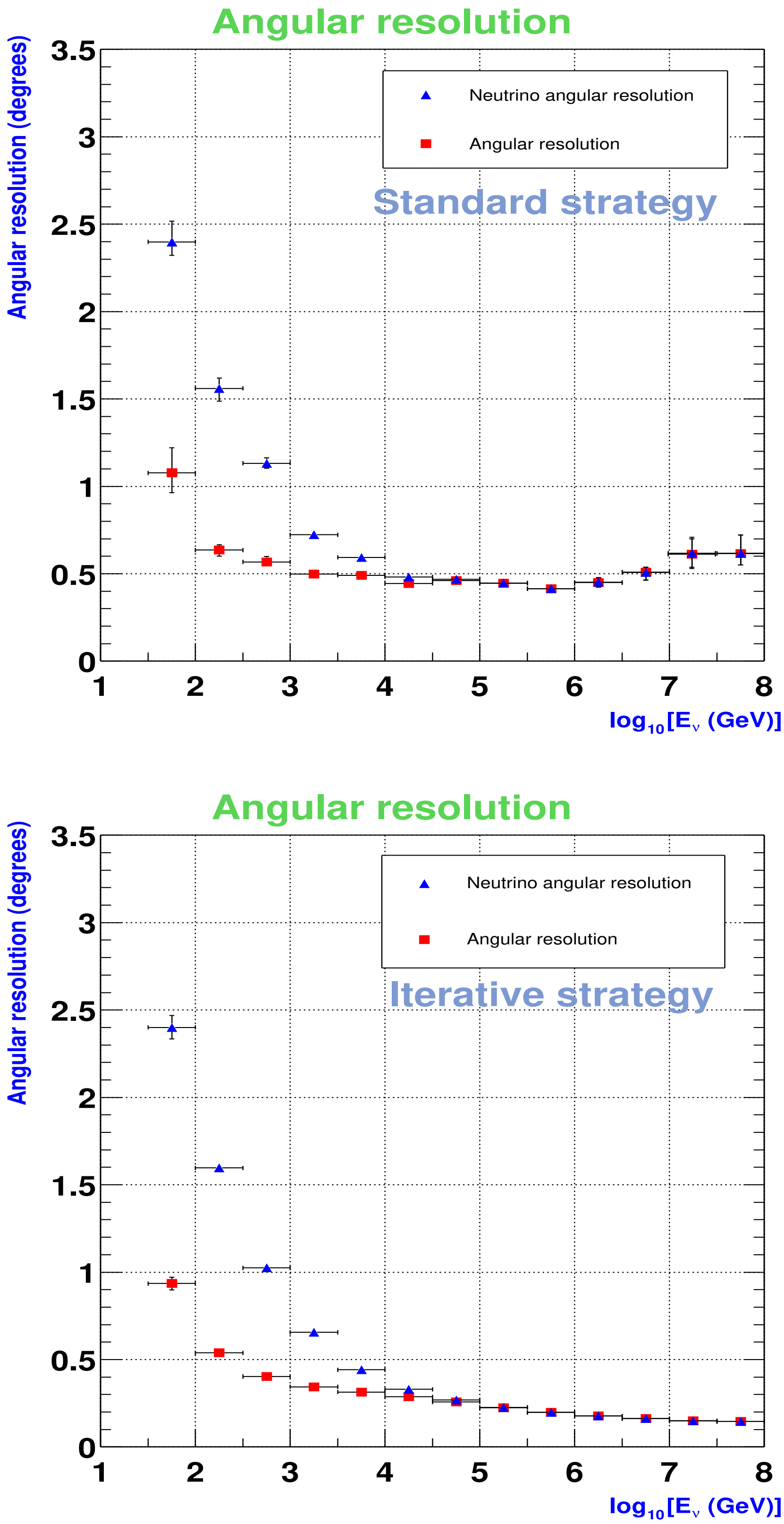

Figure 4.14: Neutrino angular resolution and muon angular resolution after selection for the standard strategy (top) and the *iterative strategy* (bottom).

obtained for the tracks with the highest energy. Above 10^7 GeV the angular resolution for both neutrinos and muons is below $0.15°$.

4.4.3 Response to an $E^{-\alpha}$ flux

Effective areas and angular resolution presented in previous subsections allow a comparison between reconstruction strategies in a flux-independent way. However, under real circumstances the final performances of the detector are a convolution of the flux independent performances and the incident neutrino flux. For instance, the effective area is not measured by the experiment, instead, the effective area convoluted with the neutrino flux produces the number of detected events, which is the number of events actually seen in the detector. In a similar way, the angular resolution in figure 4.14 must be convoluted with the neutrino flux to obtain the angular resolution of the actually observed events.

Since the signal events from an astrophysical source are expected to follow a power law with spectral index of 2.0 (or slightly higher) this flux is used to estimate the performances of the detector for signal events and to compare the reconstructions. Another interesting neutrino flux is that of atmospheric neutrinos. As it was already explained in chapter 1 and 2, these events are an unavoidable source of background that can hide the events from an astrophysical origin. However, this flux is the most guaranteed source of events in a neutrino telescope, hence the importance of knowing the detector response to atmospheric neutrinos.

In the case of the number of events, figure 4.15 shows the distribution of the number of selected events for neutrinos and anti-neutrinos from the atmospheric neutrino flux and a $E^{-2.0}$ isotropic diffuse flux with the normalisation of the Waxman–Bahcall upper limit. From the atmospheric neutrino flux, the standard strategy produces on average 760.4 events per year and the *iterative strategy* produces on average $1,832.6$ events per year, what represents an improvement larger than 140% with respect to the standard strategy. For an isotropic $E^{-2.0}$ neutrino flux and the standard strategy, the average total number of selected events per year is 6.8. In the case of the *iterative strategy*, the average total number of selected events per year is 14.5, what represents an improvement larger than 100%.

Figure 4.15 showed the number of events as a function of the neutrino energy. However, we want to know the angular resolution for the signal events produced by a point-like neutrino source, which is very important for point-like source searches as we will show in chapter 5. In this case, the angular resolution must be weighted by the neutrino spectrum in order to estimate the average angular resolution. Figure 4.16 shows the distribution of the angles between the real muon track and the reconstructed one for events produced by atmospheric neutrinos and events produced by a $E^{-2.0}$ flux. As can be seen, for the standard strategy the muon angular resolution is $0.67°$ for the events coming from the atmospheric neutrino flux and $0.49°$ for the events coming from a spectral index of -2.0. With the *iterative strategy*, the atmospheric neutrino events muon angular resolution is $0.48°$, for a neutrino flux with spectral index of 2.0 the

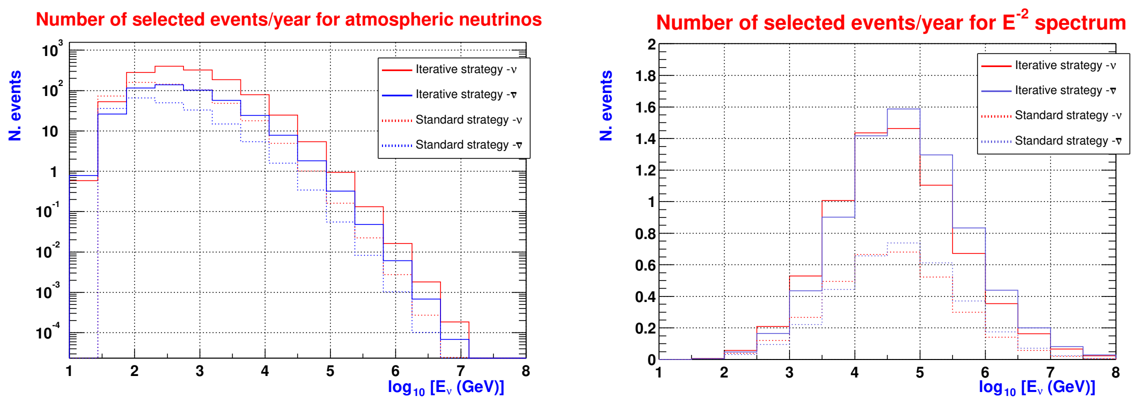

Figure 4.15: Number of selected events as a function of neutrino energy for two different neutrino fluxes with both reconstruction strategies: atmospheric neutrino flux (left) and isotropic $E^{-2.0}$ flux (right).

angular resolution is 0.26°.

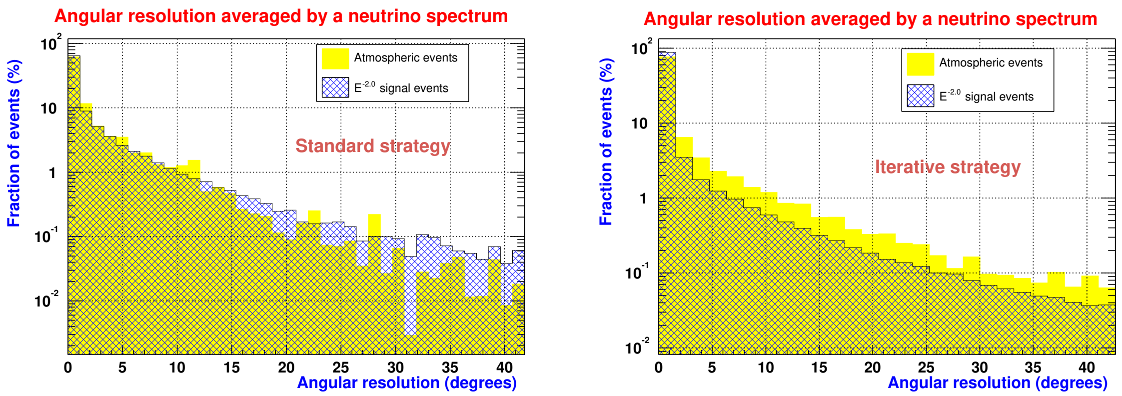

Figure 4.16: Distribution of the angular resolution from the atmospheric neutrino flux and the isotropic E^{-2} neutrino flux after selection for the standard strategy (left) and the *iterative strategy* (right).

4.5 Sensitivity of the reconstruction to environmental parameters

In this section, we investigate the effect of some environmental parameters on the reconstruction. The environmental parameters, especially those related with the water optical properties, can affect the reconstruction performances if they are different from the ones being used in the reconstruction programs. For that reason, the ANTARES collaboration has devoted a great effort to properly measure and parametrise the water optical properties at the ANTARES site [86, 87, 129, 130]. The results obtained have been included in the simulation and reconstruction packages. However, it is important to estimate what is the effect that a change on those parameters can have in the reconstruction and hence in the detector performances.

In section 4.5.1 we study the effect produced by the dispersion of non monochromatic light pulses due to the different refraction indexes at different wavelengths on the reconstruction with the *iterative strategy*. For comparison, we also show the results of the same effect on the standard strategy. Finally, in section 4.5.2 we show the effect that different scattering parameters of light in water can produce in the detector performances.

4.5.1 Speed of light in water. Group velocity

The propagation of light in matter is usually described in the Monte Carlo programs in terms of photons moving with a speed equal to their phase velocity. However, as pointed out in [128, 131], this is not correct and the group velocity must be used instead. The speed of light pulses (instead of photons) is given by $v_g = \frac{dw}{dk}$, where w is the angular frequency ($2\pi\nu$) and k is the wavenumber ($2\pi/\lambda$). The group velocity is then given by:

$$v_g = \frac{c}{n}\left(1 + \frac{\lambda}{n}\frac{dn}{d\lambda}\right) \tag{4.6}$$

where $n = n(\lambda)$ is the refraction index of water, λ is the light wavelength, and c is the speed of light in vacuum. This velocity can be compared with the phase velocity, $v_{ph} = \frac{c}{n}$. Let us, also, call n_{ph} to the usual refractive index n in opposition to the *group refractive index* n_g that is introduced as:

$$n_g = \frac{c}{v_g} = \frac{n_{ph}}{1 + \frac{\lambda}{n_{ph}}\frac{dn_{ph}}{d\lambda}} \tag{4.7}$$

The reconstruction algorithms need to know the refraction index of light in water to compute the arrival time of the photons from the track estimate to the optical modules. Unfortunately, the photomultipliers cannot discriminate between different wavelengths within their response window. Thus, from the point of view of reconstruction, a mean value for the water refractive index is used. This value corresponds to a wavelength of 460 nm, which matches with the maximum sensitivity of the ANTARES optical modules. In figure 4.17 we can see the values of the refractive indexes at the ANTARES site in the wavelength range from 250 to 620 nm.

For λ=460 nm the corresponding values are n_{ph}=1.3499 and n_g=1.3797. We also observe that, apart from the difference between the values of n_{ph} and n_g at a given λ, n_g has a stronger dependence on the wavelength. As shown in [128], the result is that the time offset computed between a direct Cherenkov photon with phase velocity and a group velocity Cherenkov photon is increased. Furthermore, the spread in the arrival time of the group Cherenkov photons is also increased. This can have an important effect on the reconstruction that is neglected when the phase velocity is used in the Monte Carlo instead of the group velocity. For that reason, the latest version of all Monte Carlo programs in ANTARES use the value of n_g at 460 nm, which reproduces more accurately the reality and some of them (KM3) even add the dispersion of the photons with different wavelengths. In any case, the Cherenkov angle is obtained from the value of n_{ph} at 460 nm, since the group velocity affects only the speed of the propagation of light in matter, but not the Cherenkov angle.

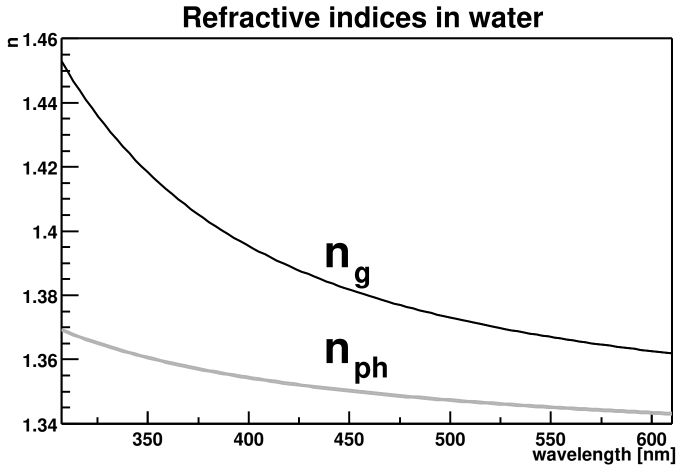

Figure 4.17: Dependence of the phase velocity refractive index (n_{ph}) and group velocity refractive index (n_g) on the photon wavelength.

We have studied the influence of the group velocity in three cases where different combinations of refractive indexes have been made as shown in table 4.4. The three studied cases are:

- In the first case, that we call **no-group velocity**, we used the phase velocity for the propagation of light in water in the simulation and in the reconstruction. This case is used as a reference for comparison with the other cases.

- In the second case, which will be referred to as **not corrected**, we used the group velocity for the propagation of light in water but not for the reconstruction. This case illustrates the situation that could be produced if the real water refractive index is not the one used in the reconstruction programs.

- Finally, in the third case, denoted by the term **full account**, we used the group velocity for both propagation and reconstruction. Comparing this case with the previous ones, in particular with the no-group case, we can get an idea of the effect of the group velocity and the correction that can be achieved when the proper refractive index is used in the reconstruction.

CASE	simulation	reconstruction
no-group velocity	n_{ph}	n_{ph}
not corrected	n_g	n_{ph}
full account	n_g	n_g

Table 4.4: Refractive indexes used for simulation and reconstruction in the three cases under study.

The results obtained can be seen in figure 4.18. We can see the ratios of effective areas obtained with the *iterative strategy* for the **not-corrected** and **full account** cases with respect to the **no-group velocity** case. The upper plot corresponds to the ratios of neutrino effective areas and the lower plot to the muon effective areas. As can be seen, the difference with respect to the **no-group velocity** case is small for both areas. This means that the dispersion produced by the group velocity effect does not affect the reconstruction and the detector performances. In fact, we observe an increase of performances around $\sim 5\%$. The worse scenario is found when the group velocity effect has been added to the simulation but not to the reconstruction of the events. We observe a reduction of $\sim 15\%$ in all energy bins with respect to the **no-group velocity** case for both A_{ν}^{eff} and A_{μ}^{eff}. Finally, if we compare the effective areas between the not corrected and the full account cases, we observe a loss around 15% of the not-corrected with respect to the full account case.

Since, unlike the *iterative technique*, the standard strategy uses a simple pre-fit that does not make use of the water optical parameters, it may seem that any change in the water parameters has a deeper impact on the *iterative* reconstruction than on the standard one. As can be seen in figure 4.19 this is not the case. For this reconstruction, we observe a decrease of $\sim 30\%$ in the **not-corrected** case with respect to the **no-group** velocity case. We also observe that when the group velocity is used for both simulation and reconstruction, both effective areas decrease around 5% with respect to the **no-group** velocity case, in contrast with the *iterative strategy* where we found a $\sim 5\%$ increase. Finally, comparing the **not-corrected** and the **full account** cases we observe a decrease of $28-29\%$ of the **not-corrected** case with respect to the **full account**.

As the *iterative strategy* represents a significant increase ($> 100\%$ in some cases) in effective area compared to the standard strategy, we conclude that even in the worse scenario (the photon propagates with group velocity, but the reconstruction uses the phase velocity) the *iterative strategy* is still superior to the standard strategy. Moreover, the *iterative strategy* is less affected ($\sim 15\%$) than the standard strategy ($\sim 30\%$) by the change in the velocity of the photons.

However, changing the speed of light in water from the phase to the group velocity is more important in terms of angular resolution. Figure 4.20 represents the angular resolution in the three cases studied for the *iterative strategy* (upper plot) and for the standard strategy (lower plot).

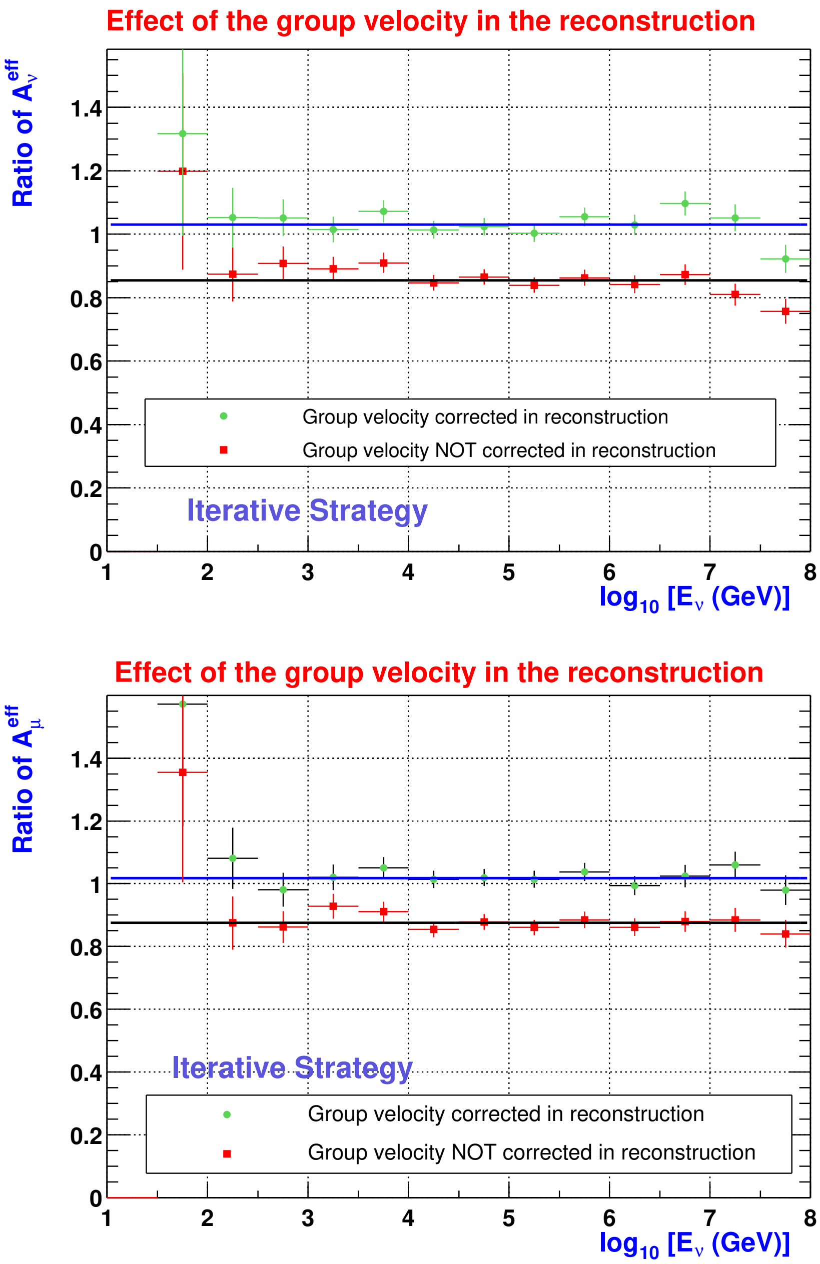

Figure 4.18: Top: Ratio of neutrino effective area for events reconstructed in the **not corrected** and **no-group velocity** cases with respect to the **no-group velocity** case. Bottom: The same plot for muon effective areas. All the events have been reconstructed with the *iterative strategy*.

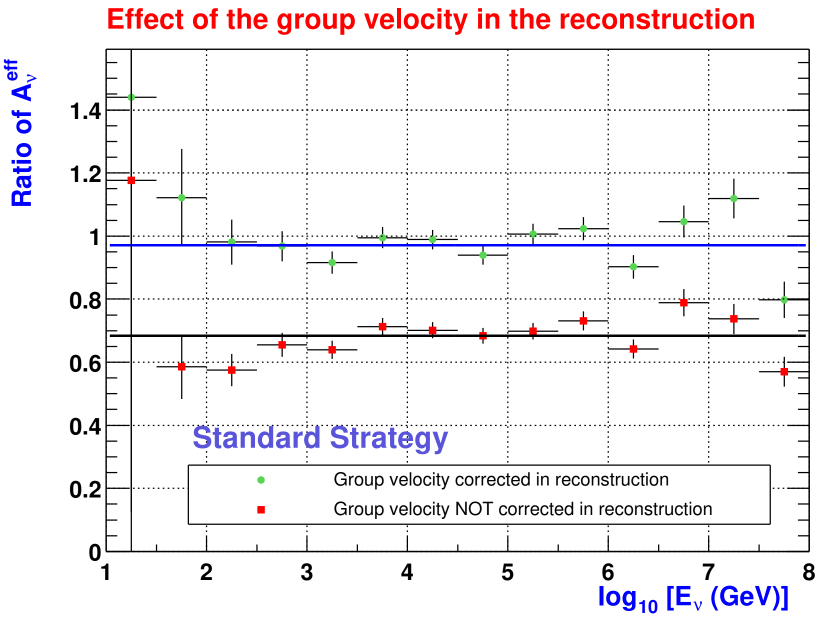

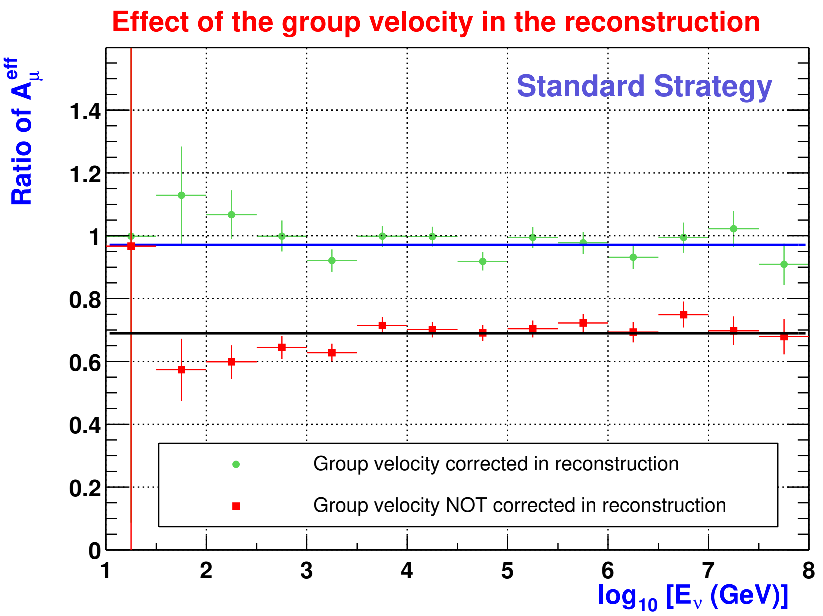

Figure 4.19: Top: Ratio of neutrino effective area for events reconstructed in the **not-corrected** and **no-group** velocity cases with respect to the **no-group** velocity case. Bottom: The same plot for muon effective areas. All events reconstructed with the standard strategy.

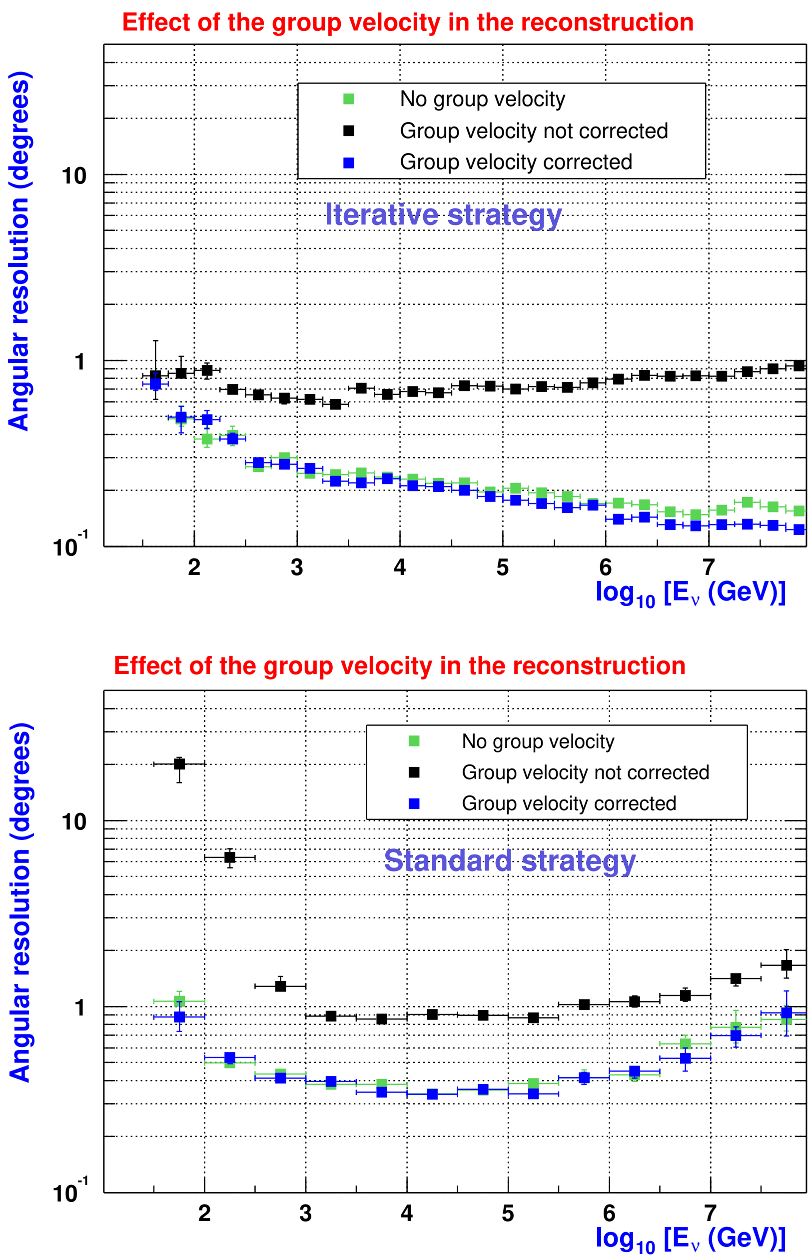

Figure 4.20: Top: Angular resolution as a function of neutrino energy for all the studied cases obtained with the *iterative strategy*. Bottom: Angular resolution as a function of neutrino energy for all the studied cases obtained with the standard strategy.

As can be seen, when the value of the speed of light in water used for the reconstruction is not the value used in the simulation, the angular resolution degrades. Such a degradation depends on the energy and on the reconstruction strategy. We observe that the *iterative strategy* always provides a better angular resolution than the standard strategy under the same circumstances. In the worst scenario, the angular resolution can reach 1.0°, which is much worse than the 0.11° that it is achieved in the best scenario, i.e. when the group velocity is used for both, the simulation and the reconstruction.

When the same value is used for the propagation of light in water in the simulation and the reconstruction, the angular resolution exhibits its typical behaviour for both reconstructions. In particular, the group velocity produces better results than the phase velocity, being this effect more noticeable for the *iterative strategy*.

The conclusion is that the correct value of the speed of light in water must be used in the reconstruction. A wrong value will not change dramatically the effective areas, but can degrade significantly the angular resolution, regardless of the reconstruction used. When the correct value is used, even if we consider the group velocity (what notably increases the fluctuation of the arrival times of the Cherenkov photons to the optical modules) the performances of the reconstruction change slightly with respect to the no-group velocity case. Concerning the reconstruction strategies, in all cases the *iterative strategy* provides better results compared to the standard one.

4.5.2 Scattering of light in water

In this section we study the influence of the scattering on the reconstruction with the *iterative strategy*. We want to check that any change on the optical properties of the water has a limited effect on the reconstruction performances. The reason is that when the reconstruction will be applied to real data, even if the water optical properties are not perfectly known, we want to be reasonable confident that the reconstruction works properly and the performances are not severely affected.

KM3 is the only Monte Carlo program in the ANTARES software scheme that takes the effect of the scattering into account when simulating the detector response. The details of the implementation of the scattering process in KM3 are available in [105, 128]. Different scattering models are available for simulation. The choice is based on theoretical expectations and measurements at the ANTARES site. A great deal of work has been done and is still being done within the ANTARES Collaboration on modelling and measuring the optical properties of sea water [87, 130, 132].

Scattering in the simulation is divided into two components with separate scattering lengths and angular distributions. The first type of scattering is Rayleigh scattering in pure sea water. The second component is the so-called "particle" scattering, produced by small sedimentary particles and microscopic organisms. For the last, two models are considered: one based on measurements by Petzold [133] of the angular distribution of light in water with high particle load. The other model is based on the Henyey-Greenstein function [134]. In this case, a linear combination of two Henyey-Greenstein functions can be fitted to the Petzold data.

There are two types of models implemented in KM3. **P-Models** use the Petzold data for the particle angular distribution. These models use a parameter (η) to measure the probability for a scattering to be Rayleigh. **M-Models** use a combination of two Henyey-Greenstein functions. In this case, the parameter α represents the relative importance of each Henyey-Greenstein function and the parameters g_1 and g_2 are the average $\cos\theta$ of each angular distribution.

The different scattering models differ from each other on the scattering parameters: the scattering length (λ_{scatt}) and the mean cosines of the angular distribution of scattered photons ($< \cos\theta >$). Another parameter used to characterise the scattering models is the "*effective scattering length*", defined as $\lambda_{eff} = \frac{\lambda_{scatt}}{1-<\cos\theta>}$ (see chapter 2). Table 4.5 shows the models used in our study with their optical properties, and the parameters used in each of them. Figure 4.21 represents all the available scattering models in the parameter space. For comparison, we have also included in our study the *nwater* model, that corresponds to water without scattering. According to the available data of the *in situ* tests, the *partic0.0075* model seems to be the most realistic model.

Ref.	**Model Name**	λ_{scatt} **(m)**	$< \cos\theta >$	λ_{eff} **(m)**	**Parameters**
P1	partic-0.01	40.8	0.77	175.0	$\eta = 0.17$
P2	partic-0.0075	52.0	0.77	223.0	$\eta = 0.17$
M2	n2	22.3	0.90	223.0	$\alpha = 1.0$ $g_1 = 0.9$ $g_2 = 0$
M6	medsea-0.0075	52.8	0.90	506.0	$\alpha = 0.985$ $g_1 = 0.92$ $g_2 = -0.6$
N	nwater	∞	-	-	-

Table 4.5: Water models used in this study and their optical properties.

We have studied five of the available scattering models in KM3 using the *iterative strategy*. The simulation was done with the old 10 strings detector (90 PMTs/string) so the results are different from those obtained in previous sections. However, the effect of the water optical properties on the reconstruction performances are the same regardless of the detector geometry used.

In figure 4.22 (left) we can see the neutrino and muon effective areas obtained with the studied scattering models that produce the best performances: *nwater* and *medsea-0.0075*. They are plotted together with the reference model *partic-0.0075*. On the right part of figure 4.22 we can see the neutrino and muon effective areas obtained with the scattering models that produce worst results: *n2* and *partic-0.01*.

The best performances are obtained for the *nwater* model, the model without scattering. This model produces, on average, a $\sim 30\%$ more effective area for muons than the reference model. The *medsea-0.0075*, however, produces a $\sim 9\%$ more effective area for muons than the reference model. On the contrary, the *partic-0.001* and the *n2* models produce lower effective areas. On average, the muon effective area for *partic-*

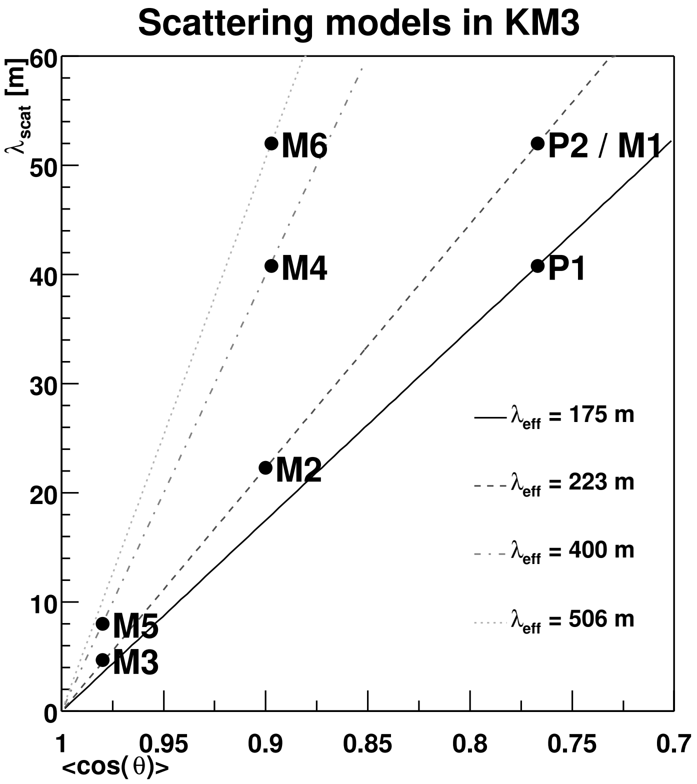

Figure 4.21: Different water models for the simulation of scattering of light in water. The most realistic models according to the existing *in situ* data seems to be the *partic-0.0075* model (also named *P2*).

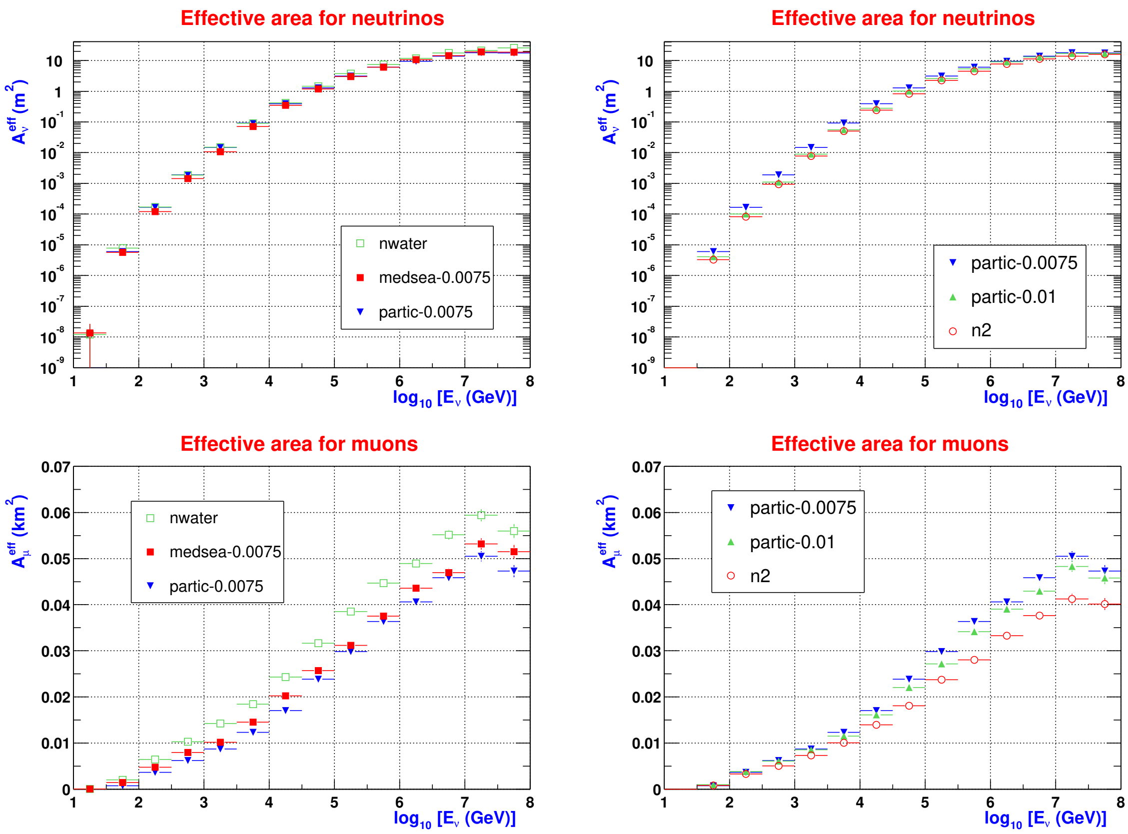

Figure 4.22: Effective areas for neutrinos (top) and muons (bottom) with different scattering models. The reference model is *partic-0.0075*, the model that better reproduces the *in situ* measurements. *Nwater* and *medsea-0.0075* produce better results while the *partic-0.01* and *n2* models produce worse results.

0.001 is on average a $\sim$ 6% lower and for *n2* is on average a $\sim$ 20% lower than the effective area of the reference model.

Concerning the angular resolution, the results are shown in figure 4.23. The *nwater* model produces the best angular resolution of all the studied models. In absence of scattering, the angular resolution is on average a $\sim$ 25% better than in the case of the reference model (*partic-0.0075*). In the case of the *medsea-0.0075* model the angular resolution is on average the same as for the reference model. On the contrary, the other scattering models studied produce worse angular resolutions. The muon angular resolution with the *n2* model is, on average, a $\sim$ 46% worse than the reference model. In the case of the *partic-0.01* model, the angular resolution is only a $\sim$ 5% worse than the reference model.

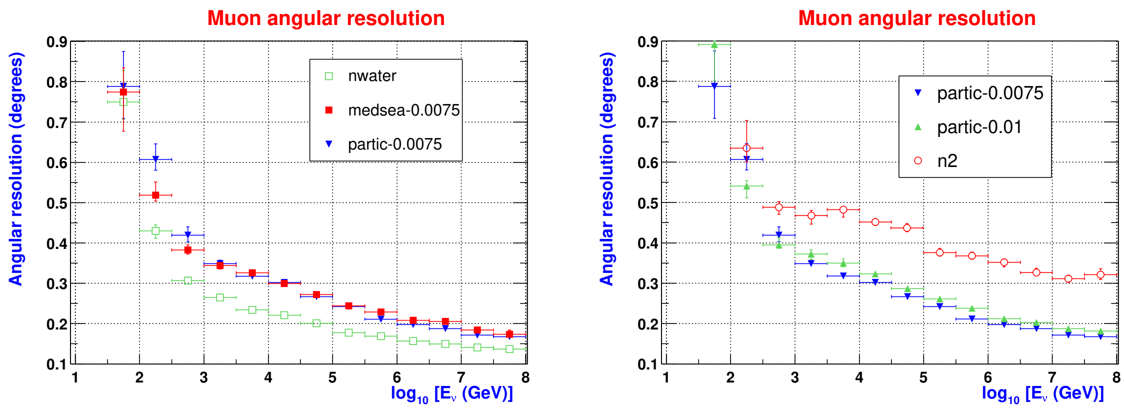

Figure 4.23: Muon angular resolution for different scattering models as a function of neutrino energy.

As a summary, we can conclude that the more diffusive the model is, the worst the performances are. Regardless of the other scattering parameters, the results are very different according to the value of the λ_{scatt} parameter. For lower values of this parameter the medium is more diffusive and the performances degrade. This is particularly true for the *n*2 model (λ_{scatt} = 22.3 m), the worst model. On the contrary, the best results are obtained with the model without scattering (*nwater*).

Concerning the behaviour of the *iterative strategy* under the different scattering situations studied, the performances achieved with the *iterative strategy* are similar among the different models. Only for the extreme cases (*nwater* and *n2* models) the performances showed a larger variation. If we compare these results with the results obtained with the standard strategy in previous sections, the *iterative strategy* is always better, regardless of the scattering model used. This is true, even taking into account that the results of the standard strategy in previous sections were computed with the 12 strings detector and the *partic-0.0075* model. The *iterative strategy* is hence superior to the standard strategy, regardless of the scattering parameters of the water.

Chapter 5

Search for point-like neutrino sources

The possibility of detecting astrophysical point-like sources of high energy neutrinos is one of the main motivations for building a neutrino telescope. Several models predict the emission of high energy neutrinos from compact objects that appear as a point-like source when observed from the Earth. Although the predicted neutrino fluxes are in general too small to be detected with a 0.1 km^2 detector — being the km^2 the natural scale to perform searches for point-like sources — a ~0.1 km^2 detector will be able to put more restrictive flux limits to various point-like source candidates. This will allow to confirm or reject the most optimistic models for point-like emission of neutrinos (e.g. micro-quasars). At the same time, the sensitivity to unknown point-like sources (i.e. not predicted by any model) must be studied in order to optimise the detector performances and the chance of observation of unexpected phenomena.

In this chapter, we present a description of the methods that we have used for this analysis and the results obtained on sensitivity to point-like sources. Flux limits that can be reached after 1 year of data taking (12 strings) if no signal is observed will be given in the following chapter.

5.1 Introduction

From an astronomical point of view only the events that have been reconstructed as up-going are considered. Most of the expected up-going events in a neutrino telescope, namely atmospheric neutrinos, misreconstructed atmospheric muons or multi-muons and neutrinos from diffuse fluxes, act as background in the point-like source analysis. These events are randomly distributed in the visible sky following a different distribution depending on their origin.

On the other hand, the signal consists of events produced in a particular point-like source, following a particular energy distribution (a power law spectrum is typically assumed, $d\phi_\nu/dE_\nu \propto E_\nu^{-\gamma}$ with $\gamma = 2.0$). These events cannot be distinguished from the background. However, after reconstruction, the position of a particular signal event can be anywhere in the sky. Only the distribution of events, according to the reconstruction spread function, can distinguish signal events from background events[1]. Taking into account the ANTARES pointing accuracy, this means that most of the signal events will be reconstructed in a narrow region around the source location. However, since the comparison is made on a distribution basis, a significant number of events is needed to claim the presence of a point-like source.

Basically, binned methods involve making bins in all the visible sky and comparing the number of events in those bins. This means that the comparison of distributions is simplified to a comparison of the number of events contained in the bins. In ANTARES, the use of binned methods is justified by the excellent pointing resolution that can be achieved[2]. In our approach, the source location is unknown and we perform a *blind search* in order to find one or various point-like sources. In this work, we have used two methods (*grid* and *cluster*) to perform the statistical analysis in order to claim or reject the presence of a point-like source. The bins used for the point-like source searches will also be used in the following chapter to establish flux-limits when no source is found.

Binned methods offer several advantages but also have some drawbacks compared to other search techniques. Among the advantages we can mention the following:

- These techniques only require the data themselves to be applied. No further knowledge of the background, the detector or the signal is needed. In neutrino physics and specially in neutrino astronomy, the uncertainties associated with neutrino cross sections, neutrino fluxes or neutrino oscillation parameters are very important. If these parameters are used in the search techniques, the search results would be affected by their uncertainties. On the contrary, the binned methods do not use those physical parameters and rely on a statistical analysis.

- The binned methods can be applied directly to data, as soon as data are available. These techniques can be applied without a perfect description of the results with Monte Carlo.

- Since they do not need external parameters to work, the binned methods are more robust against any change in the detector, the knowledge of the background or changes in environmental parameters. Other techniques may need some adaptability to add any change in the performances to the search technique. Besides, they will require a very accurate description of the detector in order to obtain meaningful probability estimates. However, with the binned methods any change in the performances of the detector affects the data but not the technique.

[1]For simplicity, we have not mentioned the distribution of reconstructed energy of the events. This distribution can be used to distinguish between signal and background thanks to their different spectral indexes. We have preferred not to use the reconstructed energy of the events in our analysis. This is explained later in the text.

[2]This means quite a narrow distribution, easy to distinguish from the background distribution of events.

- An estimate of exclusion or discovery limits intrinsically implies computations of integrated probabilities of the tail of a likelihood distribution. The more complicated the distribution, and the more it depends on the correct Monte Carlo description of the detector, the lower the certainty in the correct description of its tail. Conversely, bin methods allow to extract this estimate from simple analytical distribution functions, in our case essentially the binomial distribution. This provides greater confidence in the determination of probabilities which in some cases are as low as one part in ten millions (e.g. 5σ effects).

- Furthermore, binned methods exploit the fact that the background follows a uniform distribution in right ascension.

- Binned methods have been widely used in other experiments. This allows a direct comparison of the performances attained by each experiment, without involving comparison of statistical techniques.

As a drawback, the binned methods could be less powerful than other search techniques that include some physical parameters to optimise the search. The binned methods need some detector performances too to optimise the search and produce optimal results. These performances must be obtained by Monte Carlo unless an experimental calibration can be carried out.

5.2 The Monte Carlo data sample

As just mentioned, in order to apply the binned methods to real data we do not need a precise knowledge either of the background or the detector. However, Monte Carlo simulated data will be used in this work for the following two purposes. First, to optimise the size of the binning. Secondly, to be used as real data in absence of the latter at the present stage of detector construction.

A good estimation of the background is needed to produce realistic Monte Carlo data samples on which to apply the search techniques. The realistic Monte Carlo data samples include all the guaranteed neutrino events after 1 year of data taking[3]. These samples will be called "*Monte Carlo data samples*", but in this work they are also called *1-year data sample*, *3-year data samples* or *5-year data samples* depending on the time period covered by the sample and omitting the Monte Carlo term. Atmospheric neutrinos and anti-neutrinos constitute the main contribution to the background. However, events from other sources like misreconstructed atmospheric muons, the diffuse neutrino flux and others can also contribute to the background. Figure 5.1 represents all the contributions added to build a *1-year sample*. The signal events from a point-like source are added only when investigating the search performances of the proposed techniques.

[3]Samples containing 3 or 5 years of data have been studied too.

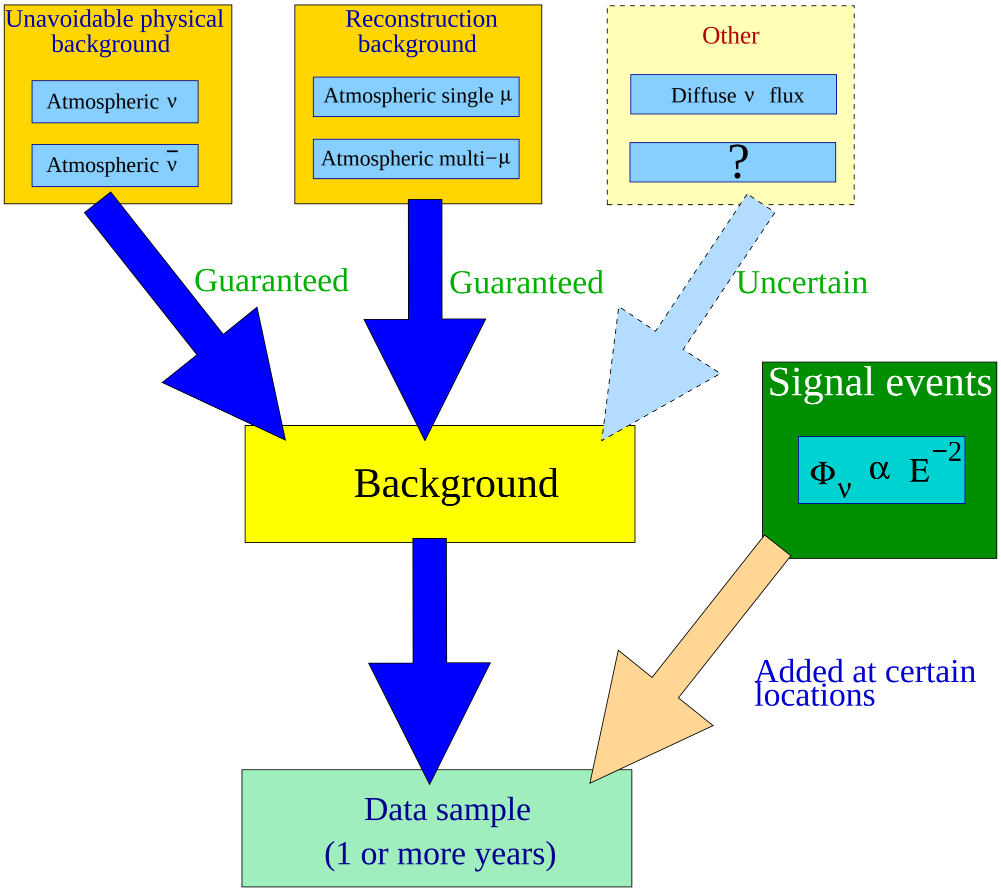

Figure 5.1: Scheme of the subsample composition of the *1-year sample*.

The main contribution to the *1-year sample* is background. More precisely, if no point-like sources are present, the events in the sample are all produced by background sources.

The events from each different source are added to the *1-year sample* following the theoretically predicted amounts and angular distributions. In the case of the background, the main contributions considered are the following (see 2.2):

- **Atmospheric ν and $\bar{\nu}$**: These neutrinos are indirectly produced by the interaction of high energy cosmic rays with the Earth's atmosphere. They constitute an unavoidable physical background because they are indistinguishable from astrophysical neutrinos.

- **Atmospheric μ and multi-μ**: These background events are produced by down-going atmospheric events (muons and multi-muons) that the reconstruction algorithm reconstructs as up-going. The *iterative strategy* provides a natural protection against down-going events, since it uses coincidences of photomultipliers in groups of three that are more likely produced with up-going events than with down-going events due to the orientation of the photomultipliers. Apart from that, the selection cuts have been chosen to reject as much atmospheric background as possible (see 4.2).

- **Other background events**: Finally, another type of events (events produced by astrophysical sources) can contribute to the background in the point-like source searches. However, this contribution is very small and can be neglected when compared to the other sources of background.

The previous components are mixed to build the Monte Carlo data samples consisting of background only. The number of events that is added to the samples depends on each type. In each case, the event has a probability (obtained in the Monte Carlo) to appear in the experiment. This probability is stored in the Monte Carlo data files as the event weight that depends on parameters like the physics of the event, the energy and the direction (see [135] for a description of the event weights).

The selected events (those which meet the selection criteria) are converted from local (θ, ϕ) to equatorial coordinates (δ, RA). This is the only information stored in the *1-year sample* files. After the reconstruction of the event in the detector, the only information needed in the proposed binned methods is the location in the sky (δ and RA coordinates) corresponding to the direction of the reconstructed muon.

Finally, in order to test the point-like search techniques, some signal events can be incorporated to the Monte Carlo data samples. These events are added to the sample as if they came from a given point-like source in the sky. The events follow the distribution of angular resolution expected for reconstructed muons coming from a E^{-2} neutrino flux. The number of signal events added to the sample is varied in order to test the efficiency of the searches with different number of signal events.

Each event of the 1-year sample is represented by its declination and right ascension (see fig. 5.2). The goal is then to detect one or several point-like sources among this background.

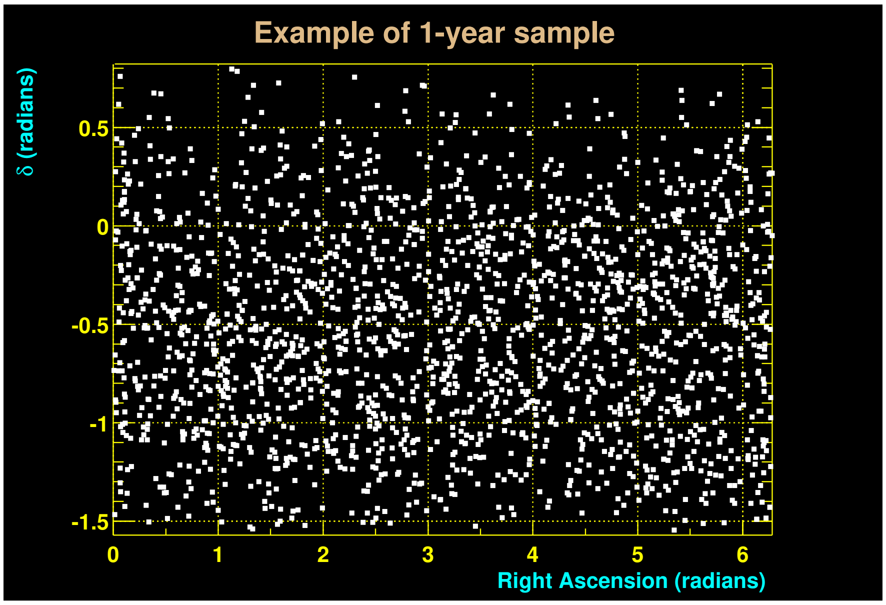

Figure 5.2: An example of a *1-year sample.*

In the following subsections we describe in more detail which are the characteristics of each type of events introduced in the Monte Carlo data samples.

5.2.1 Atmospheric neutrinos

The general *atmospheric neutrinos* description usually comprises both neutrinos and anti-neutrinos produced in the Earth's atmosphere. These neutrinos represent the most guaranteed source of events in any neutrino telescope (see section 2.2). However, from the point of view of the search for point-like sources, they represent the most important source of background.

In order to simulate this kind of events we have used a Monte Carlo simulation production consisting of 112 neutrino event files and 112 anti-neutrino event files. Each file corresponds to 10^{10} neutrinos distributed in the energy range from 10 GeV to 10^8 GeV. This production was generated with Genhen v5r1 [99]. The simulation was performed in two steps. First KM3 v2r0 [136] simulates the scattering of light in water and group velocity dispersion. Then GEASIM v4r8 [106] simulated the hadronic cascade of the events and other processes like the ^{40}K simulation. The water model used in the simulations with KM3 was partic-0.0075, the most realistic parameterization of the water optical properties at the ANTARES site up to now. For the reconstruction we have used the *iterative strategy*. The total number of selected events is $719,044$

($350,929\,\nu$ events and $368,115\,\bar{\nu}$ events). This represents $\sim$ 258 years of simulated data for neutrinos and $\sim$ 775 years of simulated data for anti-neutrinos. The average number of atmospheric neutrino events expected in 1 year of data taking with the 12 strings detector is $1,832.0$ events, $1,357.4$ neutrino events and 474.6 anti-neutrino events.

Not all the simulated events participate in a given Monte Carlo sample. For each particular event, the decision of whether it has to be included or not is randomly taken according to the rate corresponding to that particular event in the atmospheric neutrino flux. The atmospheric neutrino flux used in the simulation follows the Bartol model [137]. The contribution of prompt neutrinos to the atmospheric neutrinos has been neglected since the predicted number of prompt neutrinos is small compared to the total number. Notice that this is allowed as far as the reconstructed energy of the events is not considered. Otherwise the prompt neutrinos must be considered carefully, since their energy distribution is different from the rest of atmospheric neutrinos.

A random time is assigned to the events participating in a Monte Carlo data sample. With this time and the local coordinates we can compute the equatorial coordinates of each event in the sample. After reconstruction, the sample can be reduced only to the equatorial coordinates of the reconstructed events. This is the only information needed to apply the binned search methods that we propose. We have produced 1000 of these Monte Carlo data samples, each one covering a 1-year time period, which is longer than the simulated one. However, each event has been assigned a random time and the assignment of the events to the samples is also random. So, the simulated sample is large enough for our purposes.

Figure 5.3 (left) shows the declination of the reconstructed events. The data have been normalised to one year of data taking. The average number of expected events per year is $\sim 1,832$, $\sim 1,357$ ν events and ~ 475 $\bar{\nu}$ events. Figure 5.3 (right) shows the distribution of right ascension for the selected events.

5.2.2 Atmospheric muons and multi-muons

For multi-muons, due to the large CPU time required, the available simulation production represents $\sim$ 9 days of real time simulated data for $E_p < 2$ TeV or $\sim$ 20 days of data for $E_p < 200$ TeV. In this production, **no events** have been reconstructed as up-going (see sect. 4.3.2). This means that after one year of data taking, we can expect less than 98 events at 90% CL (calculated using Feldman and Cousins [7]).

For single muons, we have used a production of muons with the Okada parameterization [138]. However, this production covers only $\sim$ 24 hours of real time simulated data. We increased the production up to 8.9 days of real time data using the same parameters for the simulation. In this case, after applying the cuts only **1 event** survived (see sect. 4.3.1). This amounts to less than $\sim$ 138 events per year at 90% CL (Feldman and Cousins).

Therefore, in the case of the background from atmospheric muons, we have only a limit to the maximum expected number of events after cuts. We have assumed that

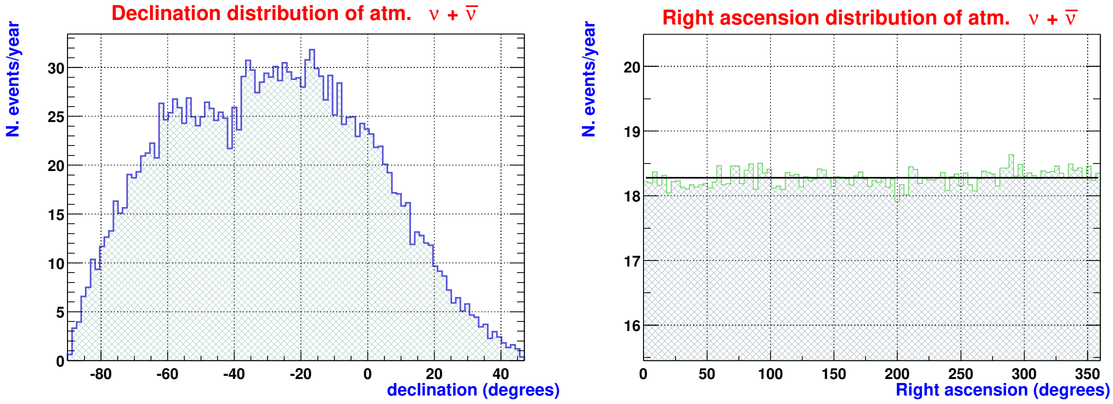

Figure 5.3: Results with the iterative strategy and the fully simulated atmospheric neutrino sample. Declination distribution of the selected events (left) and their right ascension distribution (right).

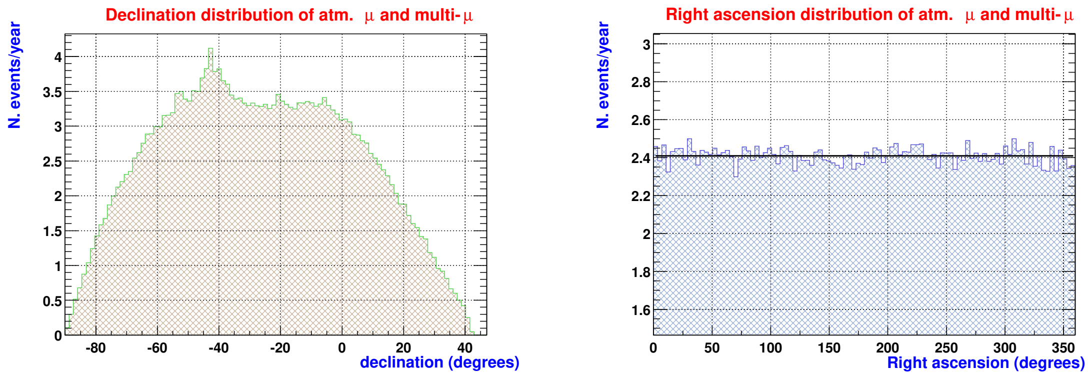

Figure 5.4: Declination (left) and right ascension (right) distribution of the reconstructed multi-muon atmospheric events.

the selection cuts do not introduce any bias, so that the events that pass the selection cuts follow the same distributions in local coordinates as the reconstructed ones. The equatorial coordinates of the reconstructed events from atmospheric muon backgrounds can be seen in figure 5.4. We have used these distributions to randomly produce the δ (only between 90° and 180°) and RA coordinates of the expected events.

5.2.3 Other sources of background events

The relative importance of other sources of background is small and they can be safely neglected.

The diffuse neutrino flux from astrophysical sources is one of the most important additional source of events. From the estimate of the neutrino flux produced in a particular astrophysical source or type of sources, it is possible to compute the diffuse flux produced by all the sources of the same type in the Universe. One of the possible choices for the distribution of sources is assuming that the sources are uniformly distributed in the Universe. For that reason, most of the diffuse fluxes predict a flux of neutrinos uniformly distributed in local coordinates ($\cos\theta$ and ϕ). However, different models predict very different fluxes due to the problem of establishing the normalisation constants of the fluxes. Some of the predictions establish an upper limit for the neutrino fluxes based on other observations. Figure 5.5 [139] shows different generic bounds and the flux limits from the Frejus [140] experiment and the Waxman–Bahcall upper limits [6]. In general, all the upper limits as well as most of the predicted diffuse neutrino fluxes predict a very small number of selected events in ANTARES [141], hence their contribution to the point-like searches background can be neglected. Just an example, assuming that the Waxman–Bahcall upper limit is the actual diffuse neutrino flux, this would represent ~ 7.1 selected events/year from the neutrinos and ~ 7.4 events/year from anti-neutrinos. These events, which are randomly distributed over the visible sky, can be neglected when compared with the expected numbers of atmospheric neutrinos (and anti-neutrinos) or atmospheric backgrounds.

The predicted fluxes from other sources of background, such as the neutrinos produced in the Galactic Plane, are even smaller and have also been neglected. Other unknown sources of high energy neutrinos could exist, but given the present experimental limits offered by other detectors they must also be negligible compared to atmospheric neutrinos.

5.2.4 Signal events

As previously mentioned, signal events are produced by a point-like source. They are indistinguishable from those produced by background but their distribution in the visible sky can be used to separate them. The events produced in the same source will be reconstructed in a narrow cone around the real source location. Even if the source is unknown, a large enough number of signal events reconstructed in a small region of the sky points out the presence of a point-like source. Figure 5.6 shows an example of

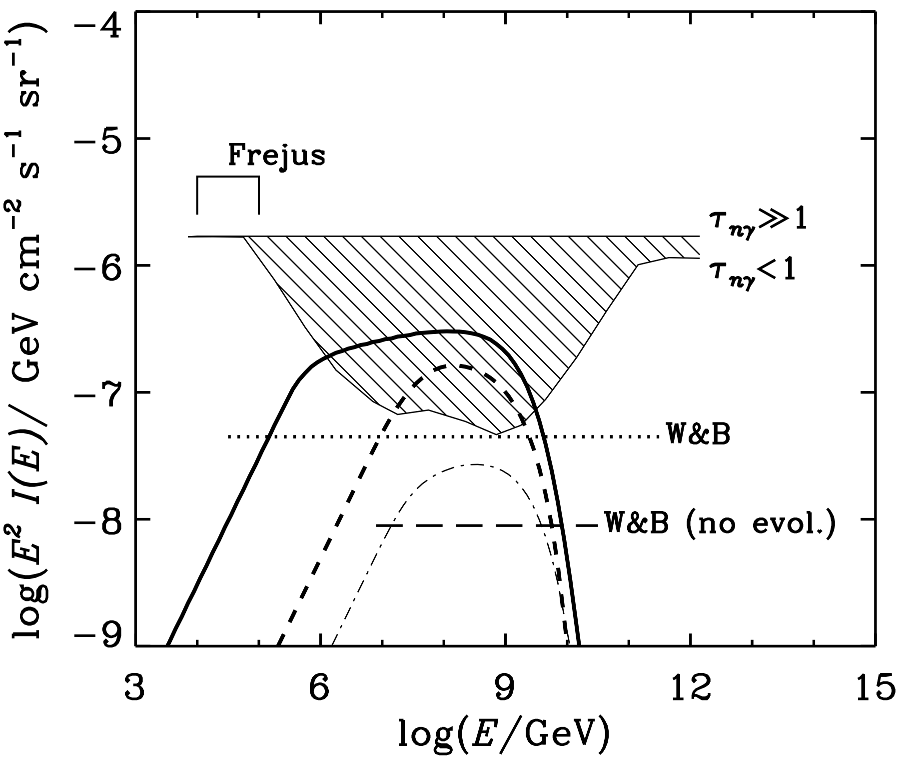

Figure 5.5: In the figure it is shown the generic bound for the optical thin ($\tau_{n\gamma} < 1$) and thick case ($\tau_{n\gamma} \gg 1$), the generic blazar bound (solid line), the EGRET blazar bound ($E_{\tau=1} \approx 10^8$ GeV and L=10^{48} erg/s) –dashed curve–, the BL Lac bound ($E_{\tau=1} \approx 10^{11}$ GeV and L=3×10^{44} erg/s) –dot-dashed curve–, the Waxman–Bahcall limits (with and without evolution) and the Frejus limit.

a data sample for 1 year of data taking where 7 signal events produced by the same source have been added.

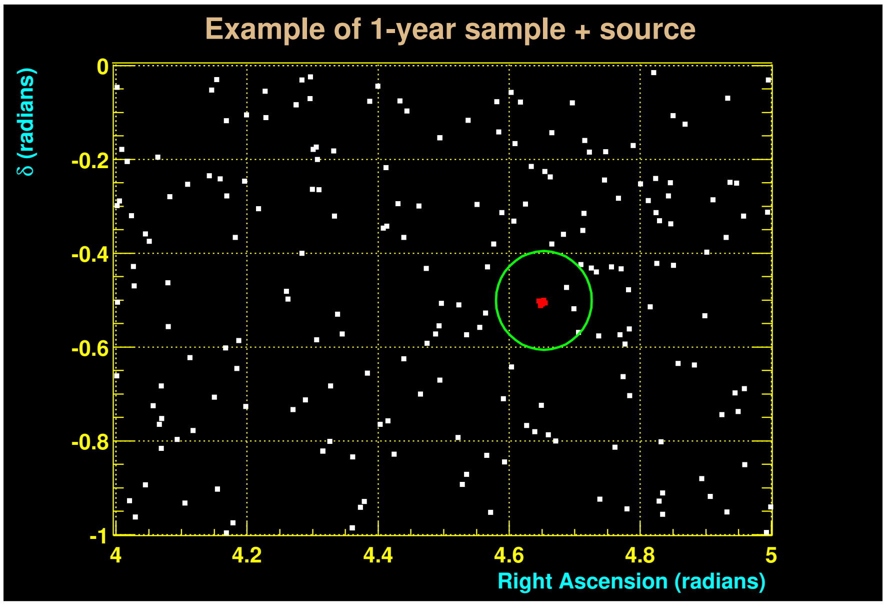

Figure 5.6: An example of a *1-year sample* with 7 *signal* events added. The region of the sky with the source has been zoomed to be able to see the signal events and a circle has been drawn around them.

The signal events emitted by a point-like source are also characterised by the energy distribution that they are produced with. As usual, this distribution is expected to be a power law with a spectral index around 2.0. However this can not be assured and it is only a reasonable guess. Since the techniques proposed in this work do not use the reconstructed energy of the events, the importance of the spectral index on the results is not very strong. However, it is still important because the angular resolution of the reconstructed events changes with their energy (see chapter 2).

In order to test the discovery potential, a point-like source with a given number of events is added to the data sample assuming that the neutrinos come from the source's location in the sky and taking into account the angle between the neutrino and the reconstructed track due both to the physical angle between the parent neutrino and its produced muon and the angle between the latter and the reconstructed track. Therefore, signal events will be distributed in the sky around the point-like source following the angular distribution expected for that declination. Concerning energy we will assume that the events are emitted following a E^{-2} flux (the reconstruction efficiency depends on the energy of the muon in the detector surroundings).

Figure 5.7 shows the actual distributions used to add the events from the point-like source to the data sample. On the left, the angle between the neutrino and the reconstructed track for different declinations can be seen. Each declination band is normalised to 1. On the right, the average over all declinations (weighted by their visibility from the ANTARES site) can be seen. The median of the distribution, known as angular resolution, is 0.3°.

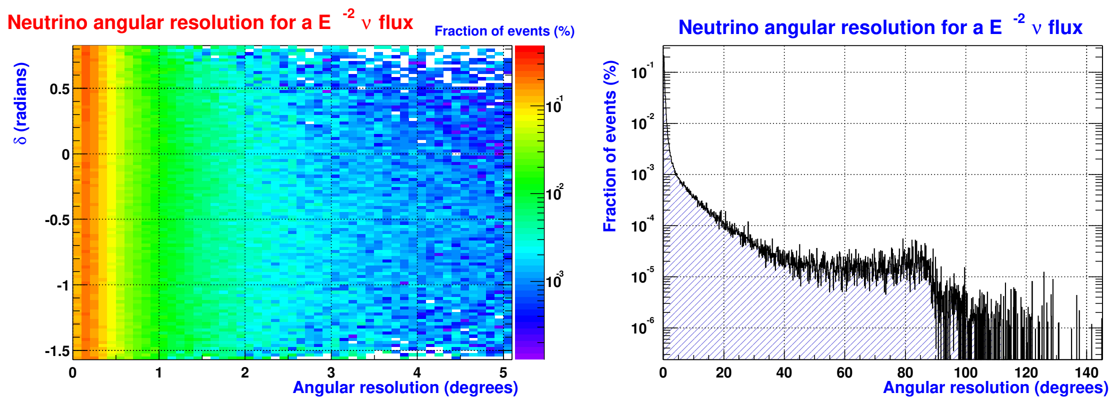

Figure 5.7: Left: Neutrino angular resolution for different declinations. Right: Neutrino angular resolution averaged over the different declinations.

The effect of the spectral index can be appreciated in figure 5.8. The plot on the left shows the distribution of the angles between the neutrino and the reconstructed muon. As the spectral index increases, the fraction of high energy events decreases and hence the angular resolution of the reconstructed events also decreases. This effect is clearly reflected in the right plot of figure 5.8. As we can see there, the angular resolution degrades as the spectral index increases. The effect is more important for the neutrino angular resolution since this one includes the physical angle between the neutrino and the muon tracks which dominates the angular resolution at low energies. In the case of the neutrino angular resolution it varies between 0.30° and 0.94° for $\gamma = 2.0$ and $\gamma = 3.0$ respectively. In the case of the muon angular resolution the range is smaller ant it varies between 0.26° and 0.42° in the same range.

From the point of view of point-like searches, the optimisation of the techniques is performed for sources emitting with $\gamma = 2.0$. It is very unlikely to detect a point-like source emitting neutrinos with a spectral index above 2.0. The reason is that the energy averaged effective area of the detector decreases quickly as the spectral index increases (see next chapter for the details). As a consequence if a given number of events is required to claim that they come from a point-like source, this number is not going to change dramatically with the spectral index, but the required flux from the source to produce those events will be very different from one spectral index to another. Taking into account the size of the ANTARES detector, the optimisation of the search techniques is performed for $\gamma = 2.0$ where the possibility of a discovery is higher.

Finally, the problem when searching for point-like sources is how to distinguish the signal events from random accumulations of events. Actually this problem is intimately

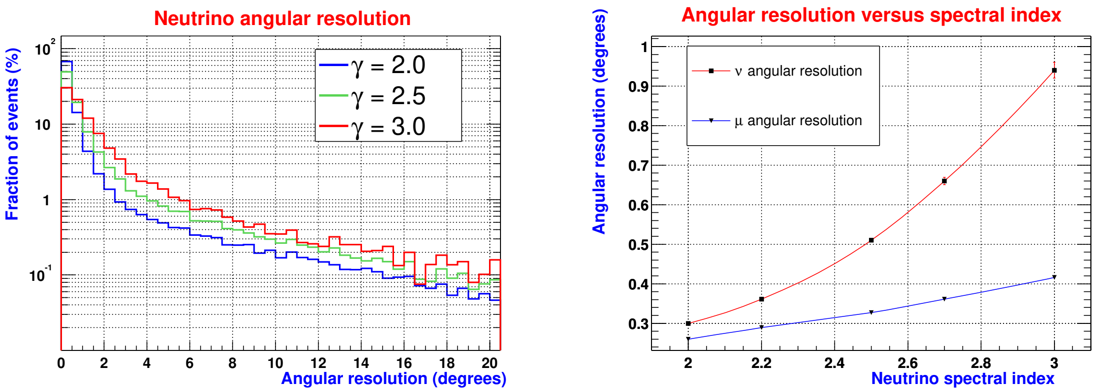

Figure 5.8: Left: Neutrino angular resolution distributions for different values of the spectral index. Right: Neutrino an muon angular resolutions for different values of the spectral index.

related with two questions: what is the number of signal events that ensures that it is a point-like source and how small should be the region where they must be concentrated. Both questions depend not only on the signal distributions but also on the background distribution of events. In the following sections this problem is studied in detail.

5.3 Analysis with binned methods

In this work we have chosen a robust approach to the problem of locating one or several point-like sources in the visible sky. In the absence of real data, the methods developed here have been applied to Monte Carlo simulated data. However, these methods and the results obtained do not depend critically on Monte Carlo estimated detector performances. This is because our approach is more conservative than other methods that can offer more sensitivity at a price of being very dependent on Monte Carlo estimations. In our case, the methods used are characterised by:

- **No use of energy estimators.** The atmospheric neutrino flux drops faster for increasing energies than the $E^{-(2+\epsilon)}$ expected signal from astrophysical objects. Selecting events above a reconstructed energy threshold should enhance the signal to background ratio. Although much work is being carried out on energy reconstruction in ANTARES, this is based on Monte Carlo studies and will depend critically on the final water parameters and detector performance, which cannot be fully estimated at the present stage.

  Moreover, the energy of a single event cannot be accurately estimated because of the nature itself of the interaction of charged particles with matter. At the present moment, the energy reconstruction of the events is based on the average behaviour of large samples of events. In the case of point-like sources, one event makes a great difference between background and a significant point-like candidate.

Furthermore, the contribution of prompt neutrinos to the total number of atmospheric background events varies significantly from one model to another [142]. These neutrinos follow a much softer spectrum and become an important part of the atmospheric neutrino spectrum at high energies. However, their relative importance is small when compared with the total flux. By applying a cut based on the reconstructed energy the contribution of prompt neutrinos is enhanced, so that the results depend on the particular atmospheric neutrino model used.

To avoid these problems we have chosen not to include cuts based on the reconstructed energy. The results become more robust and independent of the energy reconstruction performances, the Monte Carlo and the atmospheric neutrino models. In the future, when these parameters will be well known in the real detector, this analysis can be upgraded by adding the reconstructed energy of the events in order to increase the sensitivity of the method.

- **No hypothesis about the source.** The proposed methods rely only on the statistical analysis of the direction of the reconstructed event. We have not introduced any hypothesis on the source location, energy spectrum or flux normalisation. The only exception is the reasonable hypothesis that the source emits according to a power law with spectral index of 2. Additional hypotheses could increase the sensitivity of the analysis at the price of making it model dependent. Our objective, for the time being, is to perform a *blind search* with as few input parameters as possible. Once more, the analysis could be upgraded in the future with hypotheses based on physical or astrophysical arguments.

The point-like search is performed by looking for a significant excess of events in a particular sky region. We make no assumption about the location or the number of sources. The sources can be located anywhere in the sky with equal probability and their number can be any (zero, one or more than one). In order to perform the searches we use two complementary methods: the **grid method** and the **cluster method**.

- In the **grid method** the ANTARES visible sky is divided using a grid in declination and right ascension. The events from a data sample are distributed in the different bins of the grid. Given a bin, the corresponding significance is obtained by computing the probability for that bin to contain the observed or a higher number of events, if all the events are produced by background.

- In the **cluster method** we use a cone around each of the events in the sample and count the number of events inside the cone. A significant excess of events in one of the cones would indicate the presence of a point-like source. In this case, the relative significance is obtained by computing the probability for the background to produce the observed or a higher number of events in the cone.

5.4 Choice of search bins and cones

In both methods, grid and cluster, exist a certain freedom when choosing the bin size or shape, or the cone size. In the case of the grid method, we can select to use rectangular or square bins, equal solid angle bins, bins with equal signal efficiency, etc. In the case of the cluster method we can have cones with equal radius, equal efficiency or equal background. This is not a problem provided that, whatever the election, we use the optimal bin/cone choices. If that is the case, the optimal performances should be on average the same or very similar for all the bins/clusters. Moreover, we will show that it is not possible to obtain an optimal choice under all circumstances, and in some cases (a given declination, a particular number of signal events), one choice could be more advantageous at the price of being less efficient in other particular situations.

We present below the choice we have made for the bins in the grid method and for the cone size in the cluster method, as well as the advantages derived from that particular choice.

5.4.1 A choice for the grid and the cones

In figure 5.2 we observe that the background from the 1-year sample is not uniformly distributed in the visible sky. In principle, for an isotropically distributed background, the number of background events in a small region of the sky is proportional to the solid angle covered by this region multiplied by the time fraction that the region is visible from the ANTARES site (42° 50' N, 6° 10' E). However, the distribution in figure 5.6 is different because the angular distribution of the atmospheric neutrino (the main contribution to the background) is not isotropic.

The background is, as expected, right ascension independent, but it changes with declination. Therefore, if we use bins of equal size in declination and right ascension, the number of background events changes from one declination to another. In our search, we assume that a possible point-like source can be located with equal probability at any position in the visible sky. For that reason, we want our grid to have the same sensitivity at all sky positions. Since the sensitivity is related to the mean background per bin, we have chosen for our studies square bins with the same number of background events.

An additional advantage of this choice is that only one free parameter, the average background per bin, needs to be varied to obtain all the possible grids with square bins and equal background. This simplifies the process to obtain all the possible grids that can be made with equal background and square bins. However, the signal efficiency in each of these bins, even with the same background, is different from one declination to another. The result is that the response of the detector to different declinations is necessarily different, even when equal background bins are used.

In order to build a grid whose bins are square and have on average the same number of background events we carry out the following process. First, we use a reference declination that corresponds to the maximum in the distribution of number of background events. This election is absolutely arbitrary, there is no real reason to choose a particular reference declination. According to the Monte Carlo, this maximum is located at $-20°$, as can be seen in figure 5.9 (left). Starting at that position we make a declination band with a given width. Then we divide this band into right ascension bins whose size ensures that the bins are square when projected over the surface of the sphere[4]. Each declination band contains a different number of right ascension bins, but since the background does not depend on right ascension, we can compute the average number of background events per bin ($< N_{back} >$). The final goal is to build a grid where all the bands have on average $< N_{back} >$ events per bin. Notice that when real data will be available, we can perform the same process using the data themselves.

For simplicity, each grid is described by the width of the first constructed declination band. This parameter completely determines the grid according to the previously explained procedure. However, the actual figure of merit is the average number of background events per bin in each grid. Size and average background are related, since the latter should be proportional to the square of the former. In the future, we only use the initial band width as a reference for each grid. The corresponding average background per bin can be obtained from figure 5.9 (right), where the average background is represented as a function of the initial band width. The data have been fitted with a second degree polynomial.

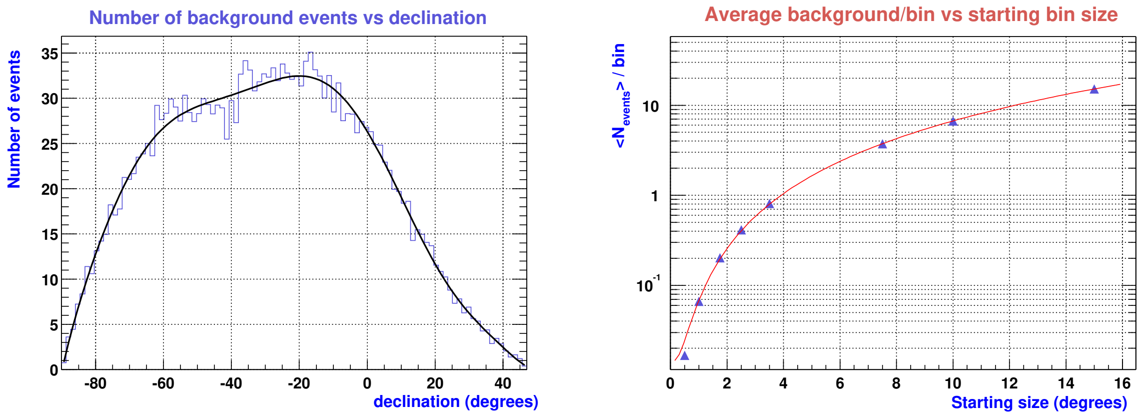

Figure 5.9: Left: Number of background events per declination band (obtained by Monte Carlo) as a function of declination, using declination bands with the same size. Right: Average number of background events per bin as a function of the initial band width. Data have been fitted with a second-degree polynomial, shown in the figure.

An example of equal background grid can be seen in figure 5.10. The number of events per bin using that grid averaged over 1000 experiments can be seen in figure 5.11.

[4]In practise the bins are not exactly square because the band must be divided into an integer number of bins.

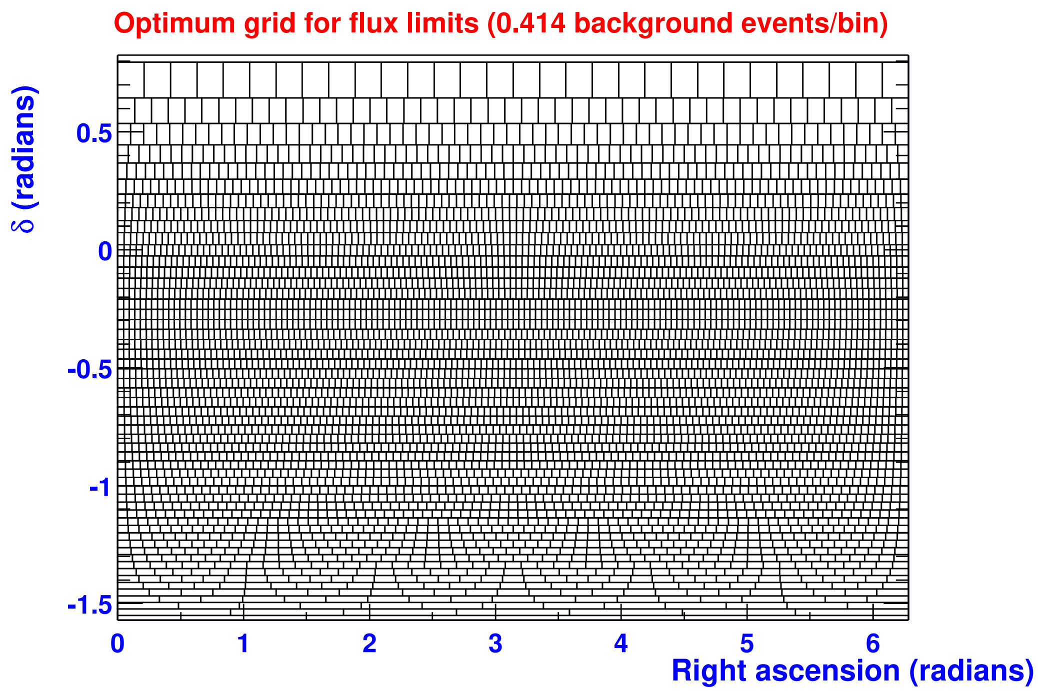

Figure 5.10: Example of a grid with an initial band of 2.5 degrees in declination.

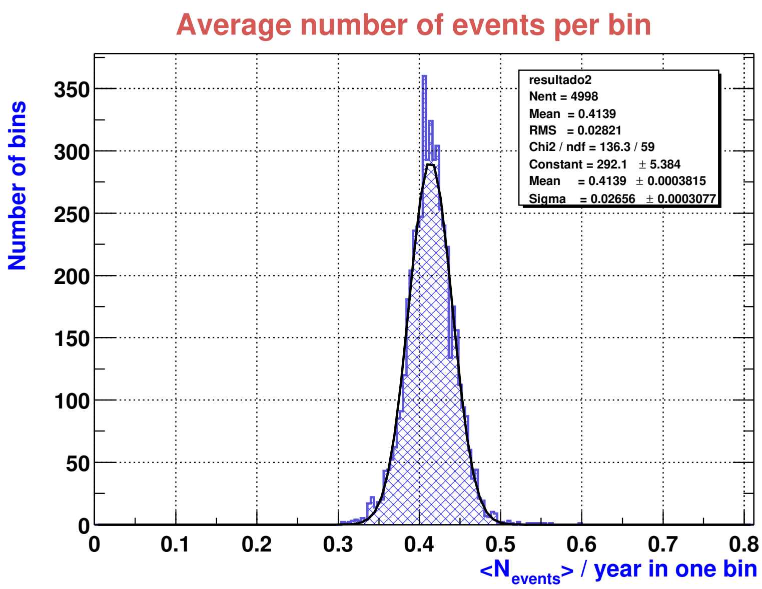

Figure 5.11: Distribution of the average number of events per bin when using the grid in figure 5.10. As can be seen, the mean value is 0.41 events.

5.4.2 Cones for the cluster method

For the same reasons as before we use cones of equal background. Starting at the same declination (-20°) as in the grid case, for a given cone radius there is a certain average number of background events per cone. Using that number as a reference, the radius for other cones is such that the average background is always the same, regardless of the declination. Figure 5.12 shows the cone size (diameter) as a function of declination to have the same number of background events at all declinations for two different initial cone sizes.

As in the grid case, the average background per cluster is the reference parameter used to compute the cone radii for the different declinations. However, for convenience we use the initial cone diameter as the reference value. The average background and the initial cone radius are correlated, as in the grid case. Figure 5.13 shows the average number of background events per cone as a function of the initial cone diameter. Data in the figure have been fitted with a second-degree polynomial. This is expected since the average background should be proportional to the area of the initial cone and therefore to the square of the radius.

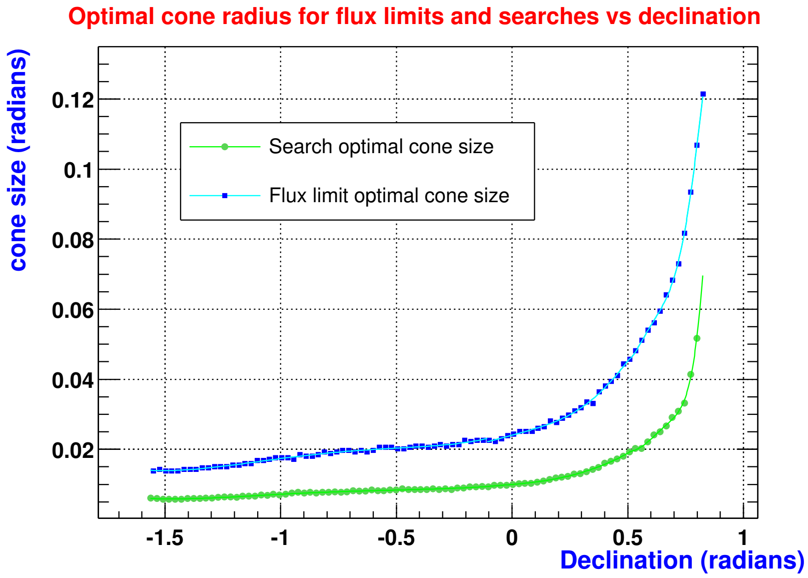

Figure 5.12: Cone diameter as a function of declination to have the same number of background events at all declinations for two different values of the average background.

5.5 Searches with the binned methods

In this section we present the technique used to decide whether a particular bin or cone contains a point-like neutrino source. In our search, neither a a-priori assumption

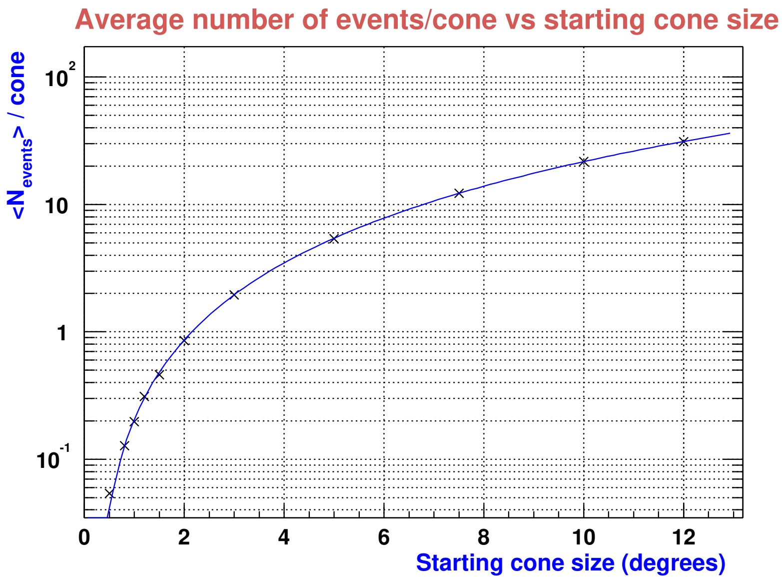

Figure 5.13: Average number of background events per bin as a function of the initial size for the grid. Data have been fitted with a second-degree polynomial, shown in the figure.

is made about the location of the sources (*blind search*) nor about the number of point-like sources.

A point-like source is visible if there is a significant excess of events in one of the bins (grid method) or in one of the cones (cluster method) with respect to the number of events expected from the background. The expected number of events is obtained from the average background in similar bins and clusters and thus is given by the experimental data themselves. So, the problem of finding a point-like source is translated into the problem of finding an excess with respect to the average number of events.

The decision of whether a point-like source is present or not is based on the probability for the background to produce the observed number of events. The expected number of background events could also be estimated from a theoretical expression for the background neutrino fluxes convoluted with the detector response obtained by Monte Carlo simulation. However, the values obtained in this way depend on the correctness of the theoretical models and on the exact description of the detector. Instead, using the data themselves to estimate the average background, as we do in this work, provides more robust and sounder results.

From the comparison of the expected to the observed number of events a significance of the possible deviation of the observations to the expectations can be computed for each bin or cluster. This significance is then used to set statistical criteria to decide when a source has been found or, on the contrary, to which extent — in terms of confidence levels — it can be excluded.

In the following sections, we clarify the exact meaning of significance and show the way to compute it.

5.5.1 Significance in the grid method

The probability for the background to produce the observed number of events in the $i-th$ bin is computed comparing that number, N_i, to the number of expected events which is estimated from the average background, $\bar{N}_{bg}$, in the declination band containing the bin.

As already mentioned, the distribution of background events in declination depends on the particular origin of the events, but the distribution of those events in right ascension is, due to the Earth's rotation, uniform, i.e. background events have a constant probability as far as right ascension is concerned. The visible sky can be divided in square bins using each of the grids that can be built according to the process explained in section 5.4. For a particular grid, we consider the declination bands whose bins are all at approximately the same declination. Within a given declination band with m bins in right ascension, we can compute the probability for the observed number of events in each particular bin. Since the background events are distributed uniformly in right ascension and all the bins in a declination band have, by construction, the same size, the probability for an event to lie in a particular bin is $P = \frac{1}{m}$. If there are N_{total} events in the declination band and N_i events in its $i-th$ bin, the probability for the background to produce in that bin N_i or more events can be computed from the binomial distribution [5]:

$$P_i = \left(\frac{1}{m}\right)^{N_{total}} \sum_{n=N_i}^{N_{total}} \left(\begin{array}{c} N_{total} \\ n \end{array} \right) (m-1)^{N_{total}-n} \tag{5.1}$$

We define the significance of one bin as $S_i = -log_{10}(P_i)$. This significance quantifies the unlikeliness of observing N_i or more events out of N_{total} in *just one particular bin* of the m bins of that declination band. To define an overall significance, *sample significance*, valid for the whole sample, the fact that there are N_{bins} bins in the grid must be taken into account. The sample significance is the parameter used to determine whether one particular experiment contains or not a point-like source. A bin with a high significance (i.e. very low probability of being produced by background) may indicate the presence of a point-like neutrino source. And vice-versa, if all the bins in the grid have a significance distribution compatible with that from the background distribution, then no point-like neutrino source can be claimed.

In order to present the results in a more intuitive way, we express the significances as a number of *standard deviations of the normal probability distribution function.* We

[5]Notice that the binomial distribution instead of the Poisson distribution is used, since the total number of events in a declination band is assumed to be fixed to the actual number obtained in the experiment and therefore not a random variable itself

usually use the expression *a significance of $n\sigma$* meaning that the probability is:

$$P = 1 - \int_{-n}^{n} \frac{dx}{\sqrt{2\pi}} \exp\left(-\frac{x^2}{2}\right) \tag{5.2}$$

The previous definition may differ from the definition used somewhere else.[6]

In figure 5.14 we can see the distribution of significances for three samples which correspond to 1 year of data taking plus 5, 10 and 15 signal events, respectively, from a point-like neutrino source. In each figure we also show the background-only distribution for comparison. The significances computed with equation 5.2 are bin significances. In order to translate it to sample significances, the 1-bin probability must be divided by the total number of bins in the grid.

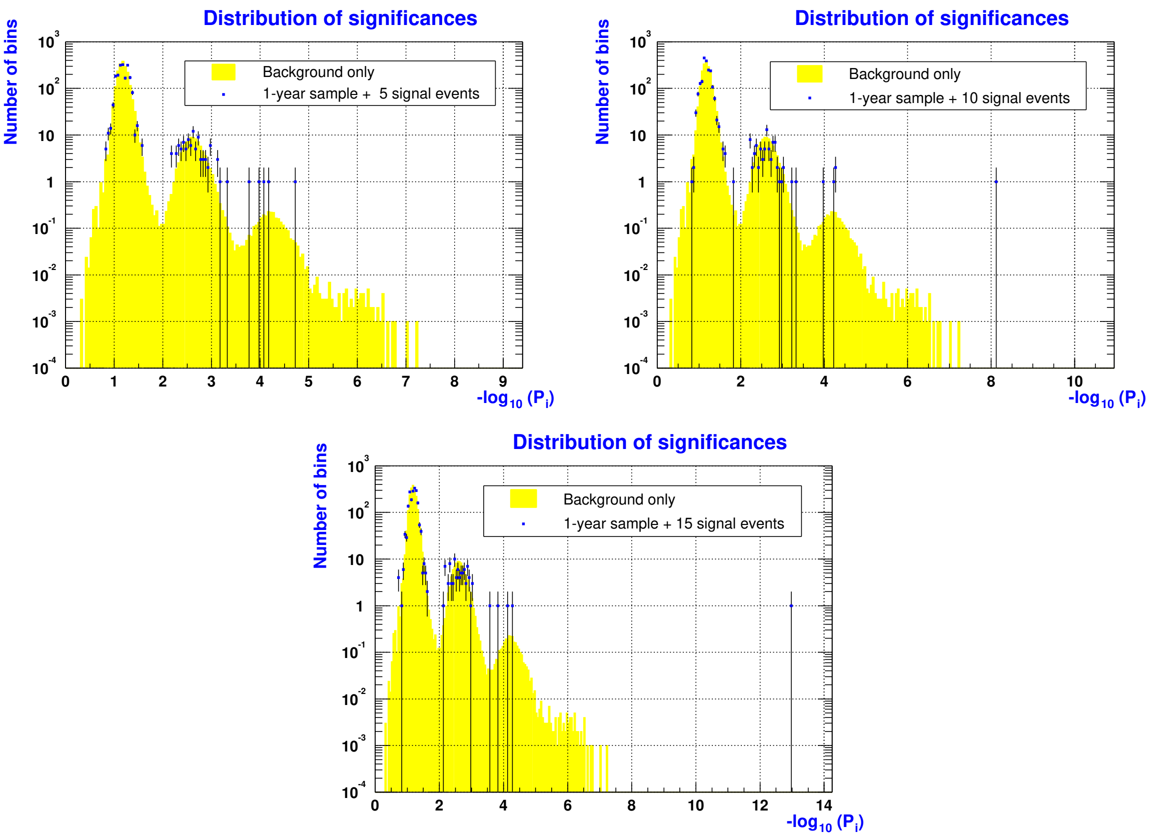

Figure 5.14: Three examples of distribution of 1-bin significances in a 1-year sample. A point-like neutrino source has been added, emitting 5 events (top left), 10 events (top right) and 15 events (bottom).

[6]The $n\sigma$ significance is also defined as $P = \int_{n}^{\infty} \frac{dx}{\sqrt{2\pi}} \exp\left(-\frac{x^2}{2}\right)$. In practise, this difference has little effect on the results because the significances are computed for a discrete distribution (binomial).

As can be seen in the figure, the bin containing the point-like neutrino source is noticeable as the bin with the largest significance in the distributions. This is not enough to claim the presence of a point-like neutrino source. The significance of the excess must exceed a previously defined threshold in order to guarantee that the background is excluded at certain confidence level as the origin of the excess. The confidence levels are defined as *$n\sigma$ significances* and must also take into account the number of bins in the grid. To this end, we divide the $n\sigma$ probability by the number of bins. For instance, for a 5σ level the probability for the background to produce the excess is 5.733×10^{-7}. If there are 1000 bins in the grid, one should expect 5.733×10^{-4} bins with a 5σ excess in each sample. Instead, if we want to use a 5σ threshold for the whole experiment, the threshold that must be used for each particular bin is $\frac{5\sigma}{N_{bins}}$, to ensure that on average there will be 5.733×10^{-7} bins in each sample where the background has been able to produce a significant excess.

Increasing the efficiency of the grid

The grid method performs a division of the sky in bins that can be studied individually to test the presence of a point-like source. However, the point-like source may not be located at the centre of the bin, but between two adjacent bins, instead. This limits the number of events collected in each bin and reduces the chances of detecting the source. To avoid this problem, we apply the same grid four times with the same data sample. In the first grid, the coordinates of the events are those contained in the data. In the second grid, a small offset is added to the right ascension coordinate of the events. In the third grid, a small offset is added to the declination coordinate of the events. Finally, in the fourth grid, a small offset is added to both the right ascension and the declination coordinates of the events. The magnitude of the offset corresponds to half the size of the smallest bin in the grid. If a point-like source is found in the second, third or fourth grids, we can obtain the real coordinates of the source by removing the corresponding offsets.

Figure 5.15 shows the distribution of significance obtained for the four grids. As can be seen, there is no difference between the four grids used, as it was expected taking into account that the background is randomly produced.

Finally, using four grids to look for a point-like neutrino source increases the total number of bins used to compute the significance of an observed excess. To correct for the increase in the total number of bins, we compute the significance thresholds using the total number of bins used in the four grids. This means that in order to exclude that the background has produced an excess of events in one bin at a level of 5σ, the probability computed for that particular bin (using the binomial distribution) should be equal or smaller than $\frac{5\sigma}{4\times N_{bins}}$, where N_{bins} is the number of bins in the grid (the same number in the four cases).

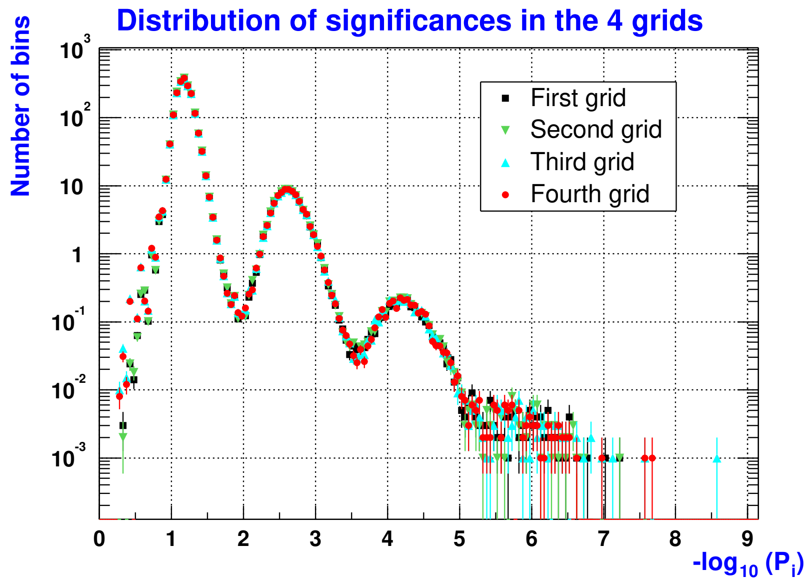

Figure 5.15: Comparison of the distribution of significances in the four grids used to increase the efficiency of the grid method.

5.5.2 Significances in the cluster method

In the cluster method, the situation is very similar to the grid method. However, the probability for the background to produce the observed number of events cannot be computed as easily as in the grid case, due to the correlations between different cones. In contrast with the grid method, where an event can only fall in one bin, in the cluster method a given event can lie in more than one cone. Our strategy to solve this problem is to compute a probability for each cone as if they were independent and consider only the cone with the largest significance in those cases where more than one cone with high significance overlap. Considering only one cone avoids the problem of correlations, although it reduces the efficiency of the method.

To compute the probability of each cone we make use again of the fact that the background events should be distributed uniformly in right ascension. Let us imagine for example a situation as that depicted in figure 5.16. There are 8 events in the figure. We draw a cone around one of them. With the selected radius for the cone, only one of the other events is inside the cone. The events produced by the background have their right ascension coordinate uniformly distributed. Therefore, the events can be located anywhere along the horizontal lines drawn in the figure. Thus for the cone in the figure at most 5 background events could have been located inside the cone. The probability for one of those events to be inside the cone is the fraction of the horizontal line intersected by the cone. We can compute analytically the intersection probabilities and use them to compute the probability of having observed 0, 1, 2, 3, 4 or 5 events inside the cone if all the events come from background. The event used to set the centre of the cone is not used in the computations because by definition the cone always contains that event.

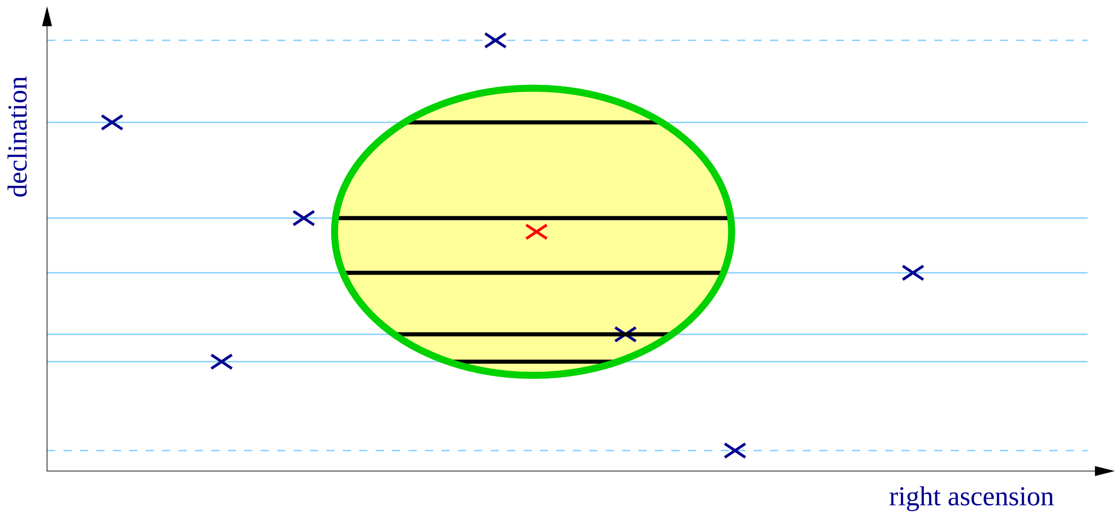

Figure 5.16: Example of one cone containing only 1 event inside.

In practise, what we compute is the probability of having one or more than one (up to 5 in the previous example) events inside the cone. This probability can be obtained in the most general case as:

$$P_i = \sum_{n=N_0}^{N_{total}} \left(\sum_{\sigma \in C_n^{N_{total}}} \left(\prod_{j \in \sigma} p_{j,i} \times \prod_{k \notin \sigma} (1 - p_{k,i}) \right) \right) \tag{5.3}$$

where

- N_0 is the observed number of events inside the cone defined by the $i-th$ event. In the previous example $N_0 = 1$.
- N_{total} is the maximum number of events that could be inside the cone i. In the previous example $N_{total} = 5$.
- P_i is the probability for the background to produce the observed number of events (N_0) or a larger number (up to N_{total}).
- $C_n^{N_{total}}$ is the set of combinations of N_{total} elements in groups of n elements.
- σ is one element of the set $C_n^{N_{total}}$
- $p_{j,i}$ is the probability for the event j to be inside the cone defined for the event i. As explained before, this probability is given by the fraction of the horizontal line through the event j that intersects the cone of the $i-th$ event.

By computing P_i for each event in the data sample, we can assign a significance to it in a similar way as we assigned a significance to each bin in the grid method. In this case, however, we must take into account that the events can be shared by several cones and this will produce several cones with high significance. To avoid the problem of correlations, we use only the cone with the highest significance as the signature of a point-like source. If there is more than one cone with high significance and they are far away enough from each other to be un-correlated (they do not share events) then this can be considered as the signature of one or more new point-like sources.

Computing all the combinations in equation 5.3 takes too much CPU time when the number N_{total} is very large. We have checked that when the number of events per cone is large, we can compute the probabilities P_i substituting the probabilities $p_{j,i}$ by an average probability $\bar{p}^i$ that is the average of all the $p_{j,i}$. In that case, equation 5.3 is reduced to the binomial probability distribution function.

We can compare the measured distributions of number of events inside a cone to those expected according to the probabilities computed as explained above. Figure 5.17 shows this comparison in the case when no point-like source is added and when a point-like source producing 5 and 10 events is added.

As can be seen in the figure, the point-like source is noticeable as an excess of events in one or various cones. In order to decide whether the excess was or not produced by the background we use the analytically computed probability for the observed number of events in the cone containing the largest number. This probability (previously named P_i) is used to test the significance of the excess.

The confidence level thresholds of 3σ or 5σ correspond to a probability of less than 2.70×10^{-3} and less than 5.73×10^{-7}, respectively. Again, we want these values to represent the probability for the background to produce the observed excess in any of the available cones, rather than in a particular cone. To this end, we need the individual cone significance to be smaller than the equivalent 3 or 5σ probability divided by the total number of cones in the sample. This is similar to dividing the significances of the grid method by the total number of bins in the grid. If the probability of a cone (P_i) is smaller than a previously fixed threshold (3σ or 5σ) divided by the number of cones, we can exclude at the corresponding confidence level that the background has produced the observed number of events.

Notice that only the bin with the largest number of events is used for the searches in order to avoid the problem of correlations between cones. However, using only one bin reduces the efficiency of the searches although this can be compensated by choosing the optimal cones for the searches.

5.5.3 Criteria used for point-like neutrino searches

In order to claim the presence of one or various point-like neutrino sources in a data sample, we have adopted the following criteria:

- The bin with the largest significance (grid) or number of events (cluster) is used

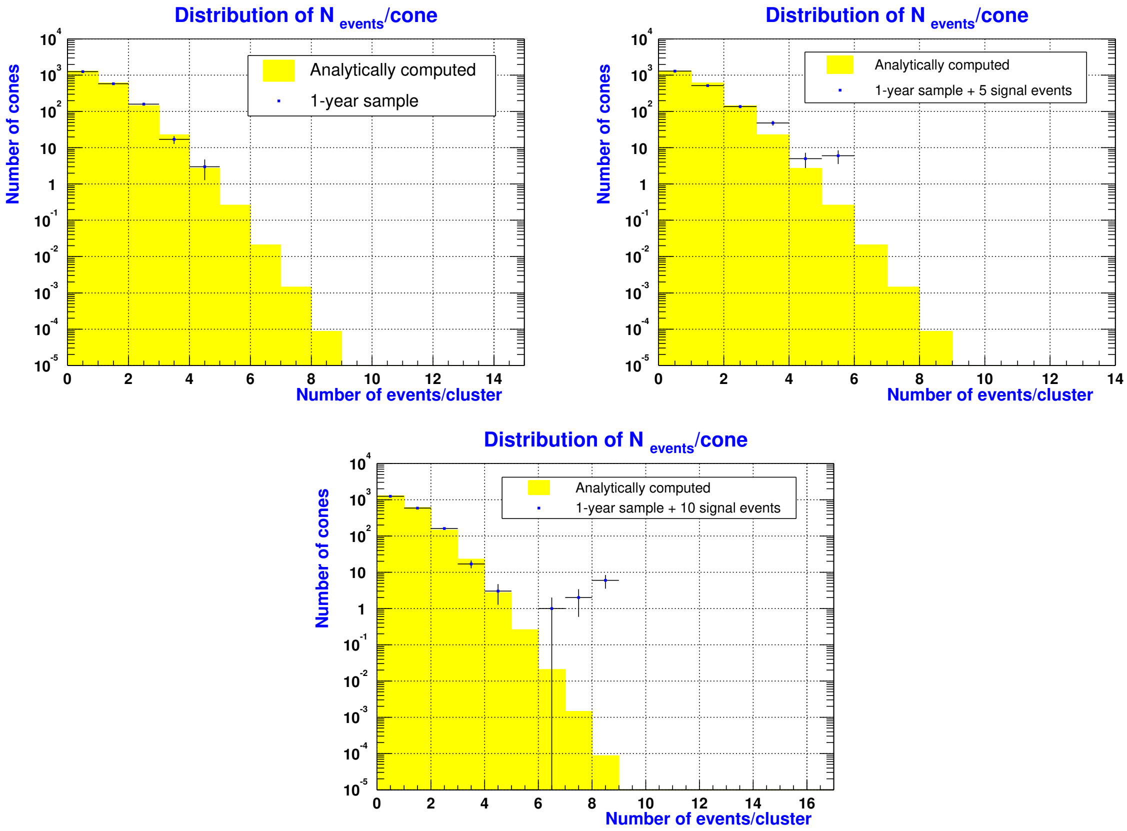

Figure 5.17: Three examples of the distribution of $N_{events}/cone$ in a 1-year sample where no point-like source is added (top left), a point like source emitting 5 signal events is added (top right) and a point-like source emitting 10 signal events is added (bottom).

as a candidate point-like source. This avoids the problem of correlations between the four grids or between the cones.

- Only when two bins/cones containing a significant excess of events are far enough from each other, we consider that there are two point-like sources in the data sample. Taking into account the angular resolution of ANTARES, one degree is enough to ensure that both sources are un-correlated. On the contrary, a bright enough point-like source could produce a large number of events in one particular bin/cone, contributing also to the adjacent bins/cones. As a consequence, significant excesses in the surroundings of the true neutrino source could be found, not meaning necessarily that those bins/cones contain other neutrino sources.

Considering only one bin or one cluster might reduce the efficiency of the method because we do not use the information contained in the adjacent bins/cones. However, if the bins/cones are chosen with the optimal size to detect a weak signal (small number of events), the information contained in the adjacent bins/cones does not make an important difference. Finally, when the number of signal events is large enough, the optimal bin/cone should always have a significant excess of events.

With the binned techniques and following the two considerations above, we have performed the search for point-like neutrino sources in the Monte Carlo generated data samples. Of course, the procedure used is the same that can be applied to real data once they become available.

A last step must be performed before applying the search procedure, namely to obtain the optimal grid/cluster, i.e. to determine the best bin/cone size. This question is tackled in the following section.

5.6 Optimal bins and cones for searches

In this chapter the optimisation of the grids/clusters is presented within the context of searches for point-like sources, while the optimisation for the case of flux limits will be treated in the next chapter.

The performance of the search procedure depends on the **background** and the **signal**, i.e. the number of background and signal events within each bin/cone. As the size of the bin/cone is increased, both the number of background and signal events inside are also increased. Our goal is to select the optimal bin/cone size so as to reach the best signal to background ratio.

In the grid/cluster choice that we made in section 5.4, only one free parameter can be varied, namely the average number of events in each bin or cone. For convenience we will present the results in terms of the initial bin declination width or cone diameter, which as has been shown is equivalent to the average background.

The study to find the optimal grid and cones is performed with Monte Carlo data samples and using the Monte Carlo estimated detector performances. When real data is available, we will still need the Monte Carlo performances in order to know the angular resolution of the reconstructed events. However, these Monte Carlo estimates will benefit from the more accurate detector description thanks to the real data themselves.

5.6.1 Optimal grid for searches

For the searches we define the optimal grid as the grid that can find a point-like source with the minimum number of signal events in the data sample. In practice, this simple definition is more complex because we need to use a threshold in probability to be sure that the background did not produce the excess of events of the point-like source. We are going to call this parameter the *Security Threshold*, to emphasise that it is used to ensure that the excess could not have been produced by the background. A typical value is 3σ and means that the probability for the background to produce a sample where at least one of the bins has the observed significance is smaller than 0.27%.

Apart from that, all the processes involved in these searches have a statistical nature. The source is only detected in a given percentage of the data samples. As a consequence, a second value must be used to describe the success fraction in the searches. Typical values can be 50%, 90% or 99%.

Since the grids we have chosen to perform the searches can be described by one parameter, the average background per bin, we need to find the optimal value. We can build different grids using different values of the average background (equivalently, using different initial sizes of the bins in the grid), and check the percentage of success in the searches. However, there are too many free parameters so we set the security threshold to 3σ.

In the following, we study the search of one point-like source in samples corresponding to 1 year of data taking. In case that more than one point-like source are present, the technique is the same provided that they are so far away that their relative excesses of events can be considered uncorrelated.

The process to locate one point-like source in the data sample using the grid method is the following. First, we compute the significance of all the bins in the grids (the 4 grids used to increase the sensitivity of the method). Only the bins with a significance above the security threshold (3σ) are considered. We check if the source is located in one of the bins over the security threshold. If that is the case, then the method succeeded in finding the point-like source. We count the number of remaining bins over the security threshold because these are *false positives*. However, using a high security threshold like 3σ ensures that the number of *false positives* is well controlled.

The results obtained by adding different number of events from the point-like source and using different grids can be seen in figure 5.18

All the results in figure 5.18 have been obtained using a security threshold of 3σ. Using as a reference a percentage of success of *50%* we observe that the optimal grid depends on the declination. The optimal grid (the grid that needs less events to detect the point-like source at least 50% of the times) is different for the different declinations. At $\delta = -73.4°$ the optimal grid is the 1.25° **grid** (the grid whose initial bin size is 1.25°,

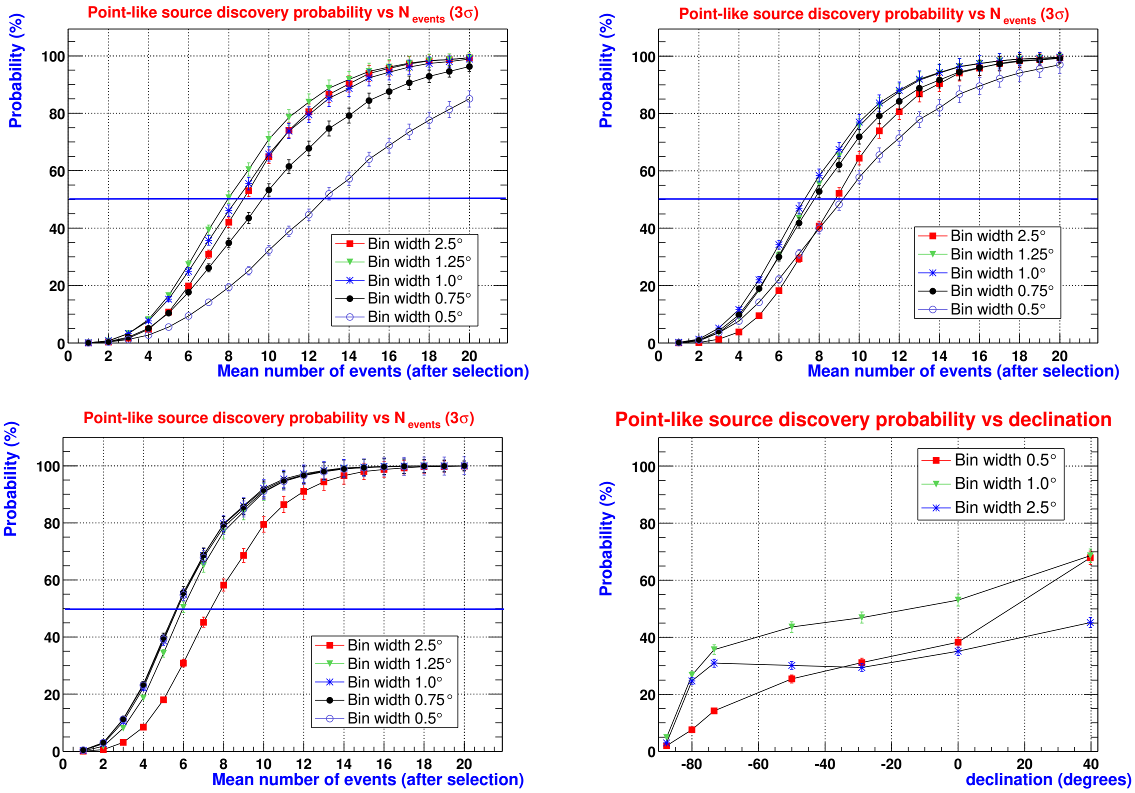

Figure 5.18: Top left: Percentage of success for discovering a point-like source located at $\delta = -73.4°$ (SMC X-1) as a function of the number of signal events from the source. Top right: Percentage of success for discovering a point-like source located at $\delta = -28.9°$ (Galactic Center). Bottom left: Percentage of success for discovering a point-like source located at $\delta = +39.8°$ (MRK 501). Botton right: Percentage of success as a function of declination when 7 events in the data sample come from the point-like source.

what corresponds to an average background of 0.103 events/bin). At $\delta = -28.9°$ the optimal grid is the 1.0° **grid** (~ 0.066 events/bin) and at $\delta = +39.8°$ the optimal grid is the 0.75° **grid** (~ 0.037 events/bin).

Concerning the number of signal events needed to reach the 50% of samples with a positive discovery of the point-like source, this number also changes with declination. In general, we observe that as the declination increases, the number of signal events needed to find the source is smaller. For instance, at $\delta = -73.4°$ and the optimal grid for that declination we need **8.0** events, at $\delta = -28.9°$ **7.3** events and at $\delta = +39.8°$ **5.6** events. This effect is due to the efficiency of the bins, at lower declinations the bin size is smaller (see figure 5.10) and hence the efficiency collecting the events inside the bin is smaller. The source must emit a larger number of events in order to keep inside the source bin a significant number of events. For the same reason, the optimal grid at lower declinations has larger bins.

We also observe that the differences between the different grids become smaller as the declination increases. The differences between grids are mainly due to the efficiency collecting events inside the bins. As the declination increases, by construction all the grids have larger bins (in order to keep the same background per bin). If the size of the bins is large enough, increasing the size of the bin has little effect because most of the signal events are collected inside the source bin. In that case, increasing the bin size has the adverse effect of increasing the number of background events per bin, but at high declinations this effect is small because the number of background events per solid angle is much smaller than at low declinations.

This result has an important consequence from the point of view of point-like searches. As can be seen in the results, the difference between the optimal grid and the other grids is small as far as we are close to the optimal one. And the differences even reduce as the declination increases. Since the optimization of the grid needs some Monte Carlo information, we see that even if this information is not very accurate and we choose a non optimal grid, the results are not going to be very different from the optimal ones.

A second important consequence is that we can use the same grid for all the declinations because the results do not change much from the optimal grid to the others, provided that the grid is close to the optimal one. If we use the mean value of 1.0° for the grid, the required numbers of events to detect the point-like source at least 50% of the times are 8.4, 7.3 and 5.7 for $\delta = -73.4°$, $\delta = -28.9°$ and $\delta = +39.8°$ respectively.

Finally, we must keep in mind that the required number of events is important at the level of the data sample. However, if we want to compare the relative strength of the source in order to be detected we need to consider the source visibility (given by the declination of the source) and the effective area of the detector. In the following chapter, we use the results obtained for the source flux-limits to also compute what is the neutrino flux needed in order to observe the required number of events for the discovery (discovery flux).

5.6.2 Optimal cone for searches

With the cluster method the situation is similar to the previous one for the grid method. In this case, we are going to find what is the best cone size choice in order to find a point-like source with the minimum required number or signal events in the sample. As in the grid case, we use a security threshold, a threshold in significance that excludes the background as the origin of the observed excess of events.

With our cone choice, all the cones have the same average background per cone. There is only one free parameter that can be tunned and it is the average background per cone, which is related to the cone size at each declination. By changing that free parameter, we can have different sets of cones that have all of them the same average number of background events. For convenience, instead of using the average background per cone, we usually use the cone size at $\delta = -20°$, which is the initial declination used to compute the cone radius at other declinations.

As in the grid case, we are going to compare the chances of success finding a point-like source (previously added at certain locations) with the different cone choices. For this comparison, we fix the security threshold to 3σ. The data samples used in this comparison correspond to 1 year of data taking. If more than one point-like source was present in the same data sample, we apply the same criterion as in the grid case: consider that their relative excesses are uncorrelated when they are far enough from each other. This is specially important for the cluster method because different cones can share the same events inside their respective cones.

To locate the point-like source we compute the significance for each of the cones as explained in a previous section. Only the cones whose significance exceeds the security threshold (3σ for instance) are considered. In the cluster case, since the events are shared by various cones, we only use the cone with the largest significance. For that cone we check whether the point-like source is contained there. If the source is in the cone, the search succeeded. If not, the search found a false positive. By using a high security threshold, the chances of finding a false positive are very suppressed.

The results obtained for the cluster method using a 50% of successes as a reference and a security threshold of 3σ when adding different number of events from the point-like source and using different cone choices (different backgrounds expressed as different initial cone sizes) can be seen in figure 5.19.

As in the grid method, there is little difference between the results obtained for the different initial cone diameters (i.e. the average background per cone). The exception are the results obtained for an initial cone diameter of 0.1° and 0.2° for $\delta = -73.4°$ and $\delta = -28.9°$, and the results with the initial cone diameter of 1.2° for $\delta = +39.8°$. As in the grid technique, the results with different cone diameter are close to the optimal ones provided that they are close to the optimal value. When that is not the case, the performances degrade quickly.

Concerning the optimal cone parameters, these depend on the declination, security threshold and reference success probabilities. However, by fixing the threshold significance to 3σ and using as a reference a 50% of successes, we obtain for three different

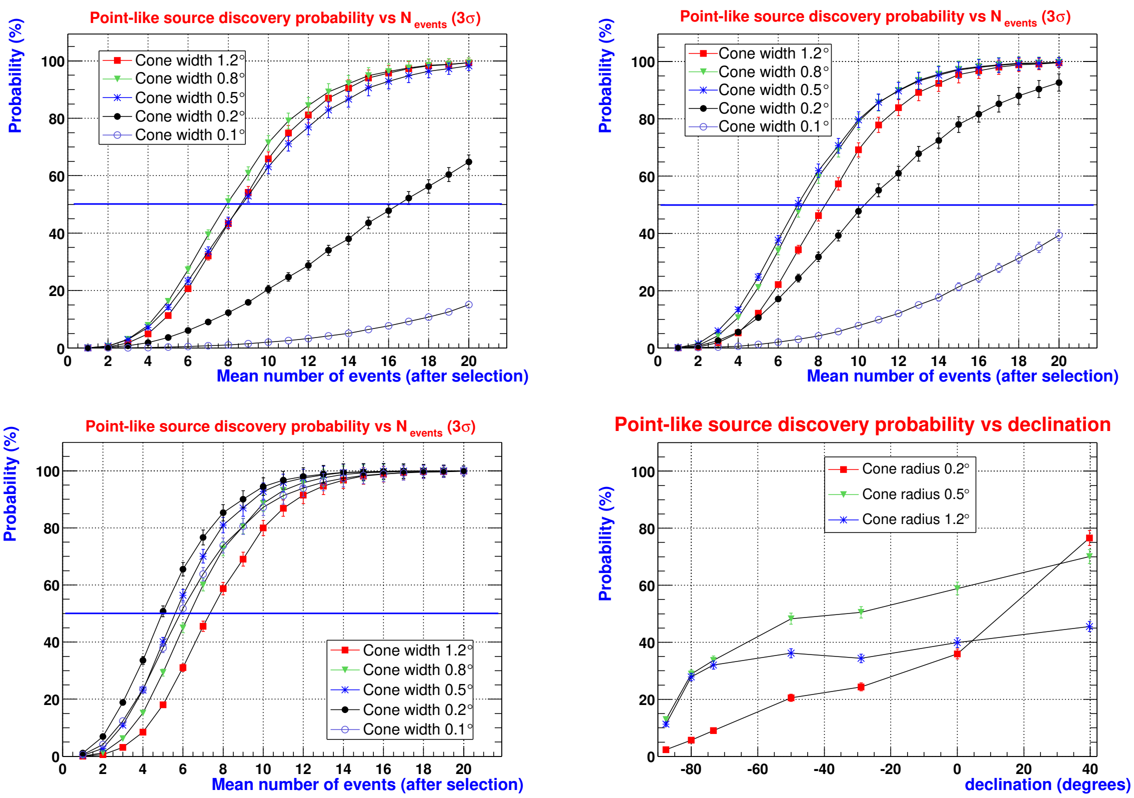

Figure 5.19: Top left: Percentage of success for discovering a point-like source located at $\delta = -73.4°$ (SMC X-1) as a function of the number of signal events from the source. Top right: Percentage of success for discovering a point-like source located at $\delta = -28.9°$ (Galactic Center). Bottom left: Percentage of success for discovering a point-like source located at $\delta = +39.8°$ (MRK 501). Botton right: Percentage of success as a function of declination when 7 events in the data sample come from the point-like source.

declinations:

- For a source located at $\delta = -73.4°$, the optimal cones are those that have the same background than the cone with diameter 0.8° at $\delta = -20°$ (that is, 0.127 background events per cone). For 50% of successes the source must emit 7.9 events/year (on average).
- For a source located at $\delta = -28.9°$, the optimal cones are those starting with a cone diameter of 0.5° (5.39×10^{-2} background events/cone). For 50% of successes the source must emit 7.0 events/year (on average).
- For a source located at $\delta = +39.8°$, the optimal cones are those starting with a cone diameter of 0.3° (8.96×10^{-3} background events/cone). For 50% of successes the source must emit 5.0 events/year (on average).

In contrast with the grid, where the same grid is used for all the visible sky, we can use different cones with different backgrounds per cone for the different declinations. However, we will use only one set of cones with the same average background per cone because the differences among the results with different cone sets are not very important. In particular, using a common starting cone diameter of 0.5°, the results at all declinations are close to those for the optimal cone. This simplifies the process of searching for a point-like source. Nevertheless, the method can still provide a better result if the optimal cone size is used at each declination.

5.7 Discovery potential results

In this section we compute the discovery potential of point-like neutrino sources for both methods — grid and cluster. In this search, no a-priori assumption is made about the location of the sources in the sky, i.e. all positions are equiprobable (*blind search*). We need a significant excess in at least one of the bins (grid) or one of the cones (cluster). The average background is estimated from the experimental data themselves, so that we look for excesses relative to the average number of events in the other bins or clusters.

Each of the simulated data samples corresponds to 1-year of data, i.e. they can be considered as data coming from the experiment after one year of data taking. We use the two techniques previously presented, using the same grid (1.0° width at $\delta = -20°$) and cone set (0.5° diameter at $\delta = -20°$) in all the searches.

5.7.1 Grid results

For the grid method, the proposed grid is the one starting with a bin size of 1.0°, and the other 3 shifted grids. The results obtained combining all grids are summarized in figure 5.20 for different values of the security threshold. The study has been performed with 1000 Monte Carlo 1-year data samples.

We observe that as the security threshold increases, a larger number of signal events is required in order to obtain a satisfactory success percentage (for instance 50% or 90%). Using as a reference 50% of successes, we need at least 8.4 signal events from a source located at $\delta = -73.4°$, 7.3 for $\delta = -28.9°$ and 5.7 events from $\delta = +39.8°$. These values are very close to the optimal values obtained with the optimal grid for each declination (8.0, 7.3, and 5.6 respectively).

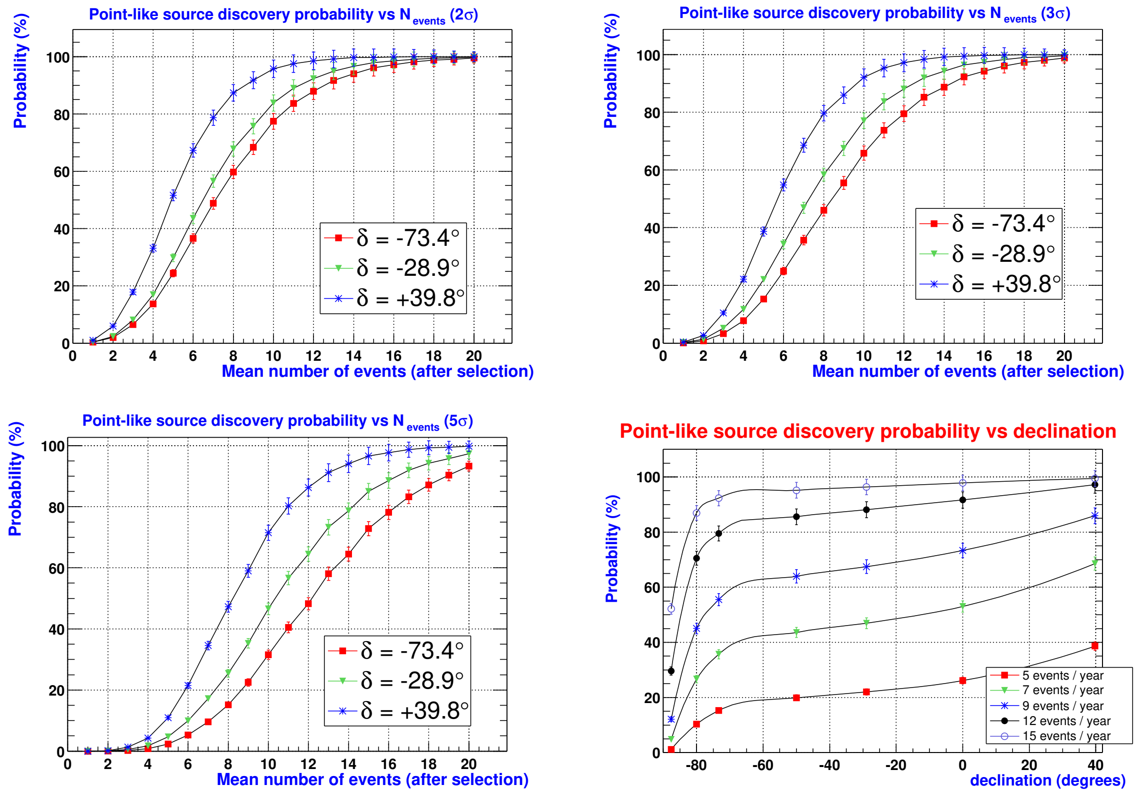

Figure 5.20: Results obtained with the grid method and different declinations for 2σ (top left), 3σ (top right) and 5σ (bottom left) after 1 year of data taking. Bottom right figure represents the probability of discovery for 3σ after 1 year of data taking as a function of the declination for different average number of events per year.

Concerning the background, an increasing security threshold guarantees that a background fluctuation is not the origin of an observed accumulation of events in one bin. In order to have a solid prove that a point-like source is present in the data probably 3σ (background produces the observed excess 2.7 times every 1000 experiments) begins to be enough. However, even a 2σ (background can produce the excess 4.5 times every 100 years) could be used as a hint pointing in the direction of some interesting source.

We have used our 1000 Monte Carlo generated samples to check that the background estimation is correct. We have observed that a random background behaves as expected from our computation of probabilities and the observed number of background fake point-like sources is in agreement with the corresponding nominal value for that security threshold. In fact, it is below the corresponding threshold because the distribution of number of events inside the bins is a discrete distribution. See table 5.1 for a complete comparison.

Significance	Computed from Monte Carlo	Nominal value
2.0σ	(3.1 ± 0.6) %	4.55 %
2.5σ	(0.50 ± 0.22) %	1.24 %
3.0σ	(0.20 ± 0.14) %	2.77×10^{-1} %
3.5σ	< 0.1 %	4.65×10^{-2} %
4.0σ	< 0.1 %	6.33×10^{-3} %
4.5σ	< 0.1 %	6.80×10^{-4} %
5.0σ	< 0.1 %	5.73×10^{-5} %
5.5σ	< 0.1 %	3.80×10^{-6} %
6.0σ	< 0.1 %	1.97×10^{-7} %

Table 5.1: Comparison of the probabilities for the background to produce a bin with a significance over a given threshold with the results observed in 1000 analysed data samples. When no background excess is observed in the studied samples, we can only conclude that the probability is smaller than 0.1 %.

5.7.2 Cluster results

In the cluster method, the proposed cone set is defined by all the cones with the same background as the cone with diameter 0.5° located at $\delta = -20°$. That means that all the cones have an average number of 5.39×10^{-2} background events per cone and year. As it was said, there is no need to choose the same set of cones for all the events in the sample, however we have shown that with the proposed set of cones the results are not very different from the optimal results.

As in the grid case, when increasing the security threshold a larger number of events is needed in order to reach a satisfactory success percentage. Using once more 50% successes as a reference, we need at least 8.7 events for $\delta = -73.4°$, 7.0 events for $\delta = -28.9°$ and 5.6 events for $\delta = +39.8°$. The optimal values we found in a previous section were respectively 7.9, 7.0 and 5.0. In this case, we observe that the difference is larger than in the grid case between the chosen cones and the optimal ones. This is a price to be paid in order to have a less optimal cone choice but much more simple and less dependent on Monte Carlo. Figure 5.21 shows the results obtained for different security thresholds and different declinations after 1 year of data taking.

As for the grid method, a 3σ security is a reasonable prove that the background was not the origin of the observed excess of events. 2σ is also useful as an indication

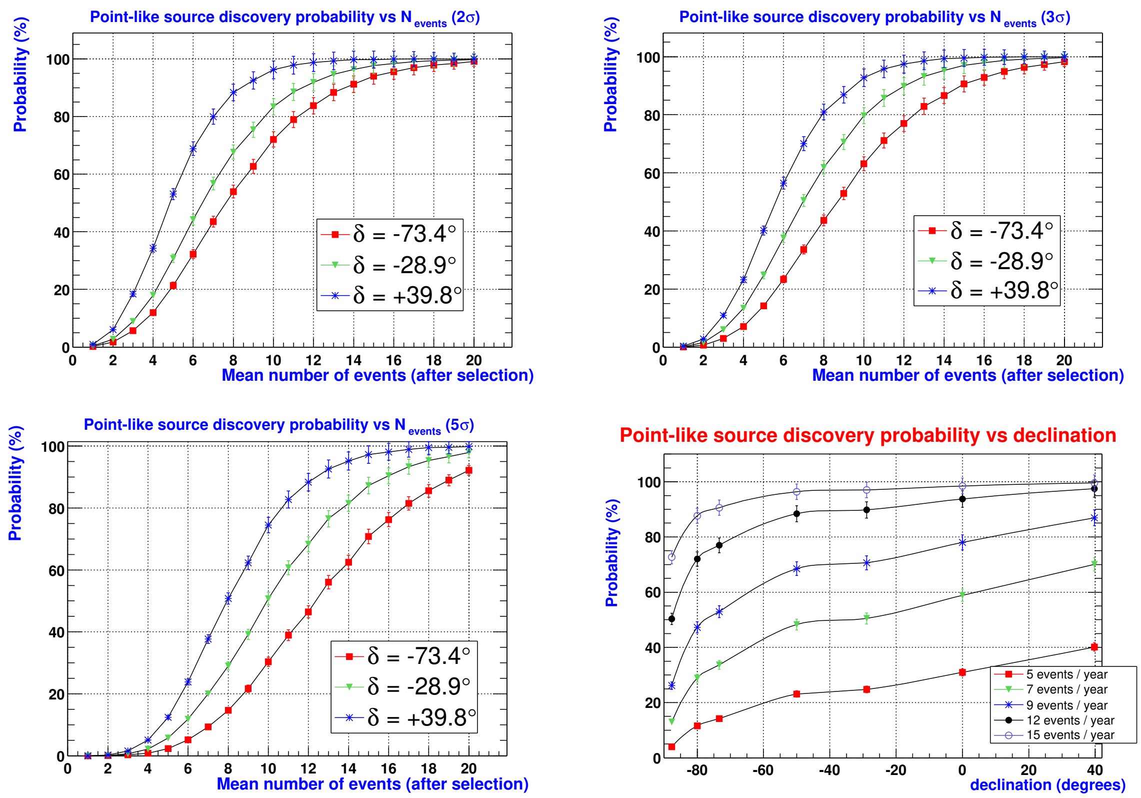

Figure 5.21: Results obtained with the cluster method and different declinations for 2σ (top left), 3σ (top right) and 5σ (bottom left) after 1 year of data taking. Bottom right figure represents the probability of discovery for 3σ after 1 year of data taking as a function of the declination for different average number of events per year.

of something interesting to be studied with higher statistics. We have used the cluster method with the 1000 Monte Carlo generated samples to check that the background behaves as expected. The answer is that the observed number of background sources is below the number of fake sources expected for the corresponding thresholds as far as can be studied with only 1000 data samples. Again, the reason comes from the discrete nature of the distribution of number of events inside the clusters. See table 5.2 for a complete comparison.

Significance	Computed from Monte Carlo	Nominal value
2.0σ	(1.1 ± 0.3) %	4.55 %
2.5σ	(0.50 ± 0.22) %	1.24 %
3.0σ	(0.10 ± 0.10) %	2.77×10^{-1} %
3.5σ	(0.10 ± 0.10) %	4.65×10^{-2} %
4.0σ	< 0.1 %	6.33×10^{-3} %
4.5σ	< 0.1 %	6.80×10^{-4} %
5.0σ	< 0.1 %	5.73×10^{-5} %
5.5σ	< 0.1 %	3.80×10^{-6} %
6.0σ	< 0.1 %	1.97×10^{-7} %

Table 5.2: Comparison of the probabilities for the background to produce a cone with a significance over a given threshold with the results observed in 1000 analysed data samples. When no background excess is observed in the studied samples, we can only conclude that the probability is smaller than 0.1 %.

5.7.3 Comparison of techniques

We can compare the results obtained by both techniques using the proposed search grid (1.0°) and search cones (0.5°) in data samples containing 1 year of data taking. In principle, both techniques are complementary and can be used to independently look for point-like sources. Figure 5.22 shows a comparison of the percentage of success in the search for different average number of signal events from the point-like source.

As can be seen, in figure 5.22, the results obtained for both techniques are almost equal. At low declinations, the differences are more important and the grid method provides better results. However, as the declination increases the differences become smaller and the cluster method seems slightly better. The results is that both techniques seem to reach a common limit that does not depend on the particular technique used, but it depends on the nature of the method itself (binned methods) and the detector itself. This can also be interpreted as a prove that both techniques after optimization reach the same limit that the binned methods can offer.

The differences between the security threshold of 2σ and 3σ, are not very important and they reduce as the declination increases. As a consequence, decreasing the security

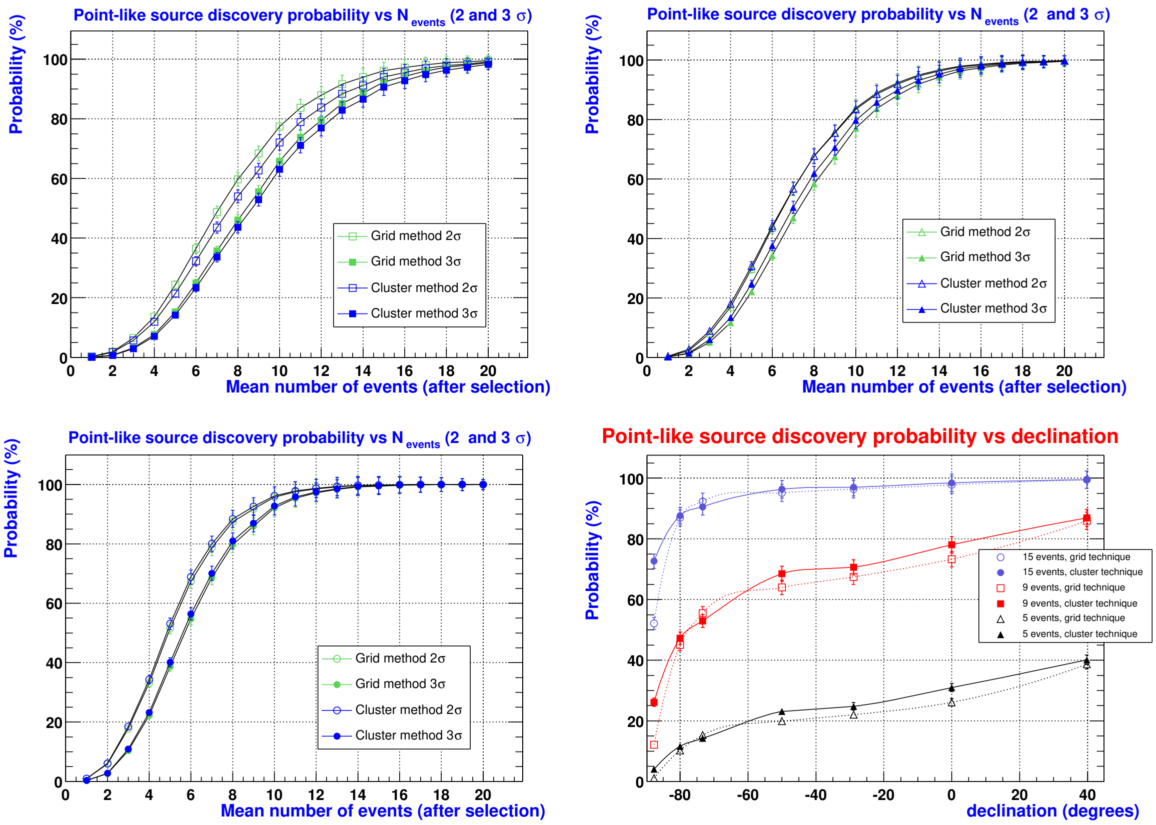

Figure 5.22: Comparison of performances between the grid and cluster techniques for the security thresholds of 2σ and 3σ. The source location is $\delta = -73.4°$ for the top left plot, $\delta = -28.9°$ for the top right plot and $\delta = +39.8°$ for the bottom left plot. Bottom right plot represents the probability of discovery as a function of declination with different number of signal events.

threshold is not going to improve dramatically the sensitivity of the search but is going to enhance by a large factor the probabilities for a false positive.

Since the data sample is the same and the techniques are very similar, we have observed that combining both techniques to perform the search, marginally enhances the results. When we have a significant excess, it is going to be noticeable by both methods, only changing the significance of the excess. Only in some special situations, the differences between methods are going to be important. The main difference between both techniques is found when we use them to set a flux-limit as will be described in the next chapter. In one case, the grid technique, we can put a flux-limit to a small fraction of the visible sky where no point-like source has been observed. In the other case, the cluster technique, we can set a flux-limit to candidate sources, by locating the search cone center at the candidate source.

5.8 Going from 1 to several years of data taking

As we have seen in the previous results, the binned methods need a relatively important number of signal events to find a point-like source with a high security threshold (more than 3σ). One solution to be sensitive to lower neutrino fluxes is to increase the acquisition time. This is something natural in ANTARES because statistics is accumulated over time without any special consideration.

Data covering more than 1 year increases the chances for discovering a point-like source. If the source is not visible in one of the *1-year sample*s, it could be detected in other 1-year samples, or in the cumulative n-years sample. The advantage of accumulating data is that the background, being randomly distributed, tends to be more uniform as the statistics increases. In contrast, the signal will concentrate at the same location in the sky.

We expect a different number of events from the same source per year. This number will follow a Poisson distribution with mean value μ_{events}. We can see in figure 5.23 what is the percentage of success detecting the point-like source over a security threshold of 2σ and 3σ for three different declinations, as a function of the number of signal events per year.

As can be seen in figure 5.23, the average number of events per year needed to detect a point-like source decreases as the observation time increases. For instance, to reach the 50% discovery chance, the needed number of events/year for a 3σ threshold is between 3.7 and 2.4 events (depending on the declination) for 3 years of data taking. In contrast, under the same conditions the required number of events lies between 2.6 and 1.6 events/year after 5 years of data taking. This results reduced significantly the required number of events/year compared with 1 year of data taking (between 8.5 and 5.7 events/year).

If we compute the total number of events required for the discovery we observe that this number increases with time. This is because the background increases with more years of data taking. For instance, for the declination of $\delta = -73.4°$ and the security

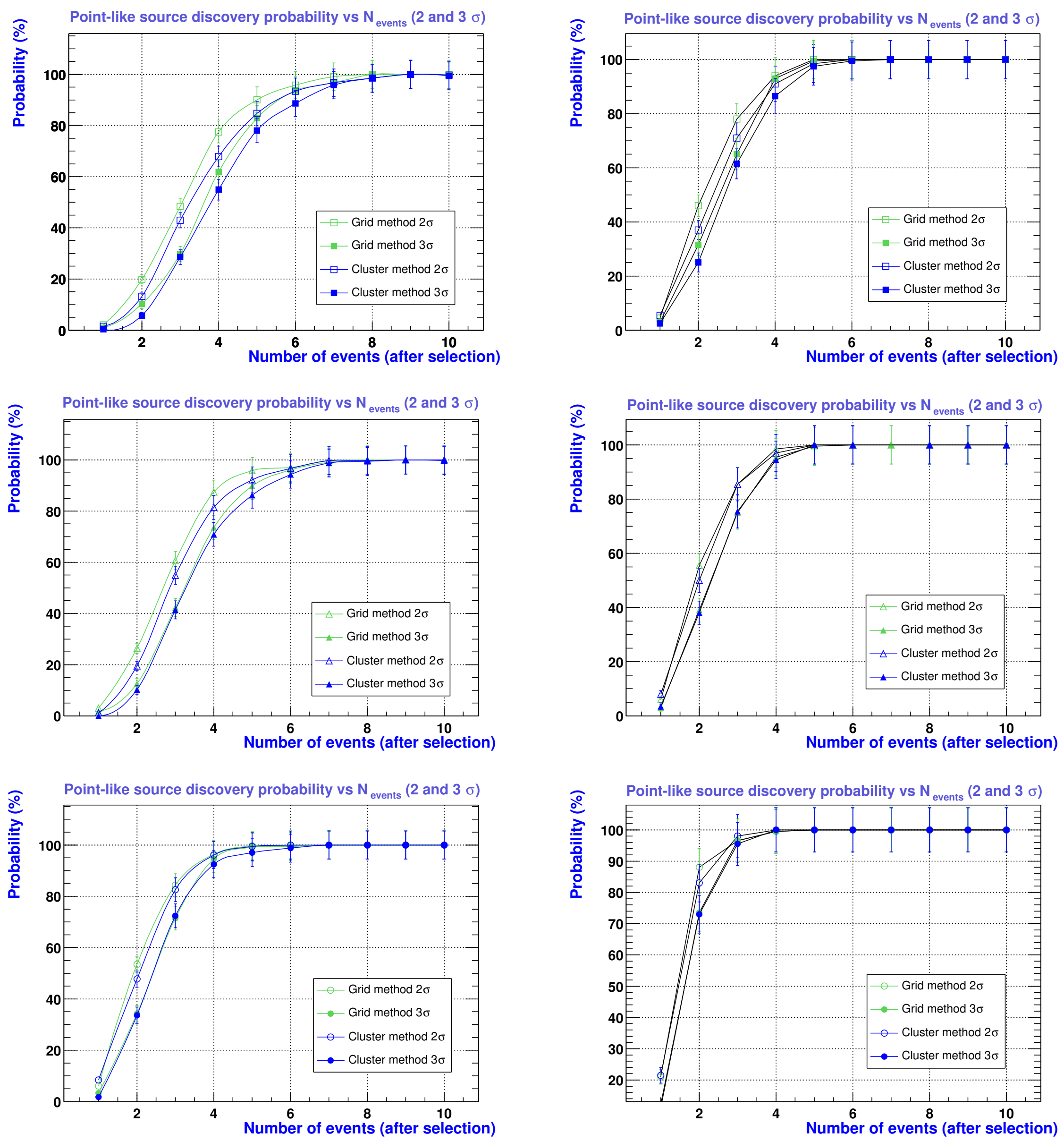

Figure 5.23: Results obtained with the grid and cluster techniques after 3 and 5 year of data taking. The first row contains the results for $\delta = -73.4°$ after 3 years (left) and 5 years (right). The second row contains the results for $\delta = -28.9°$ after 3 years (left) and 5 years (right). The third row contains the results for $\delta = +39.8°$ after 3 years (left) and 5 years (right).

threshold of 3σ, the required total number of events for 50% of successes is 8.5 events in 1 year. For 3 years, the accumulated number of events under the same conditions is, on average, 11.1 events. For 5 years and the same conditions, the total required number of events is 13.0.

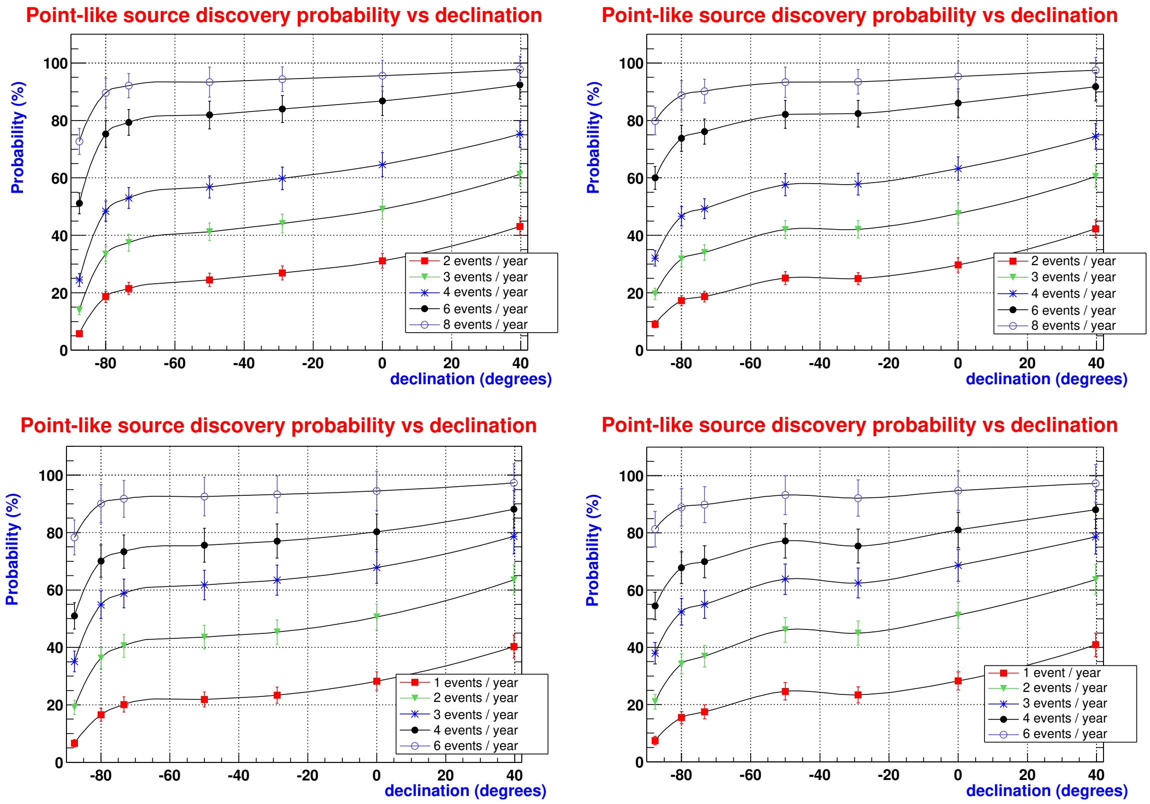

Figure 5.24: Comparison of performances between the grid and cluster techniques for the security thresholds of 3σ as a function of declination. Top left: grid technique and 3 years of data taking. Top right: cluster technique and 3 years of data taking. Bottom left: grid technique and 5 years of data taking. Bottom right: cluster technique and 5 years of data taking.

5.9 Combined effect of several point-like sources

As has been shown, only very powerful point-like neutrino sources can be detected with the ANTARES neutrino telescope. The neutrino flux needed to give raise to the required number of detected and selected events in the detector is too high to be produced in the cosmic accelerators, according to the existing models for particle production and acceleration. It is still open the possibility to other unknown sources or processes that could lead to higher neutrino fluxes. Only by observing the high energy neutrino sky with a neutrino telescope like ANTARES this possibility can be confirmed or ruled out.

However, if several of such cosmic accelerators produce high energy neutrino fluxes that can not be individually detected, they still could be detected by considering the global effect of all this individual point-like sources. We can use the total number of events inside a cone around known sources that can produce high energy neutrinos to investigate how likely is it that the background produces the observed data. The list of candidate sources must be chosen before the results, not to bias them. Otherwise it is very likely to find a list of candidate sources matching the observed data with a high probability not to be produced by background.

We have used a list of 49 candidate sources visible from the ANTARES location, that are suitable to produce high energy neutrino events. See Appendix B for a detailed description of the selected sources. Among these sources, 13 are known to emit gamma rays above 1 TeV, what makes them the best candidates for high energy neutrino emissions. The 13 sources are collected in a reduced list that has also been studied.

To perform this study we have used the cluster technique. In this case, the position of the sources is known, so the best approach is to use cones around each of the sources. In figure 5.25 we can see what is the distribution of the total number of events inside all cones after 1 year of data taking if all the events in the data sample are background. As can be seen in the figure, in both cases (49 sources and 13 sources) the analytically computed distributions match the distributions obtained by Monte Carlo. We can use the analytically computed distributions to know what is the probability for the background to produce an observed number of events inside all cones.

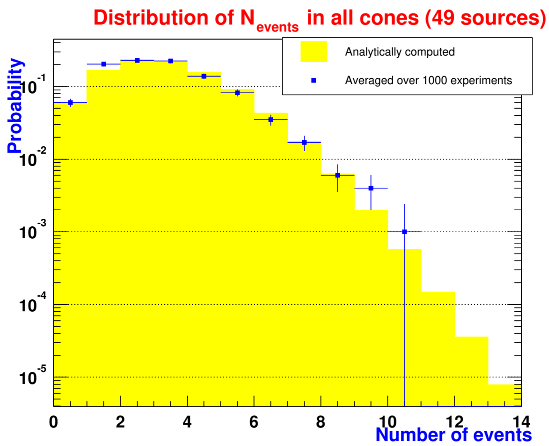

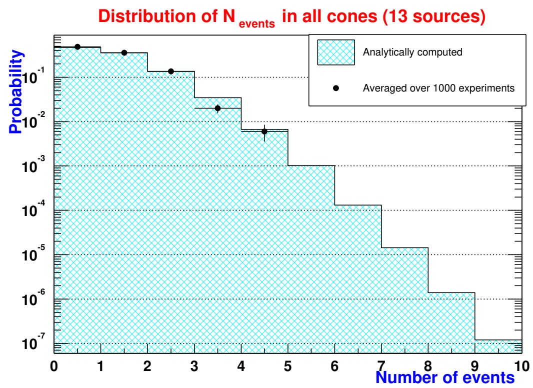

Figure 5.25: Left: Distribution of the total number of background events inside cones around the 49 candidate sources. Right: Distribution of the total number of background events inside cones around the 13 candidate sources emitting gammas above 1 TeV.

As can be seen, the number of needed events to achieve a security threshold of 3σ

(2.700×10^{-3}) is more than 9 events in total when looking to all cones around the 49 pre-selected sources and it is 5 or more events in total for all the cones around the 13 1 TeV sources. These are the numbers of signal events required in all cones (49 or 13, depending the number of studied sources) for a significant excess.

The flux emitted by each point-like source should be different. However, in order to estimate the sensitivity of this kind of searches, we can assume that the emitted flux is the same for all sources. We can then, estimate what is the required number of events in the sample from the studied point-like sources in order to be detected as a significant excess. We can see in figure 5.26 what is the percentage of success to find a total contribution with a security threshold of 2σ, 3σ and 5σ for all the 49 sources (left) and the 13 $\sim$TeV sources (right), after 1 year of data taking with ANTARES.

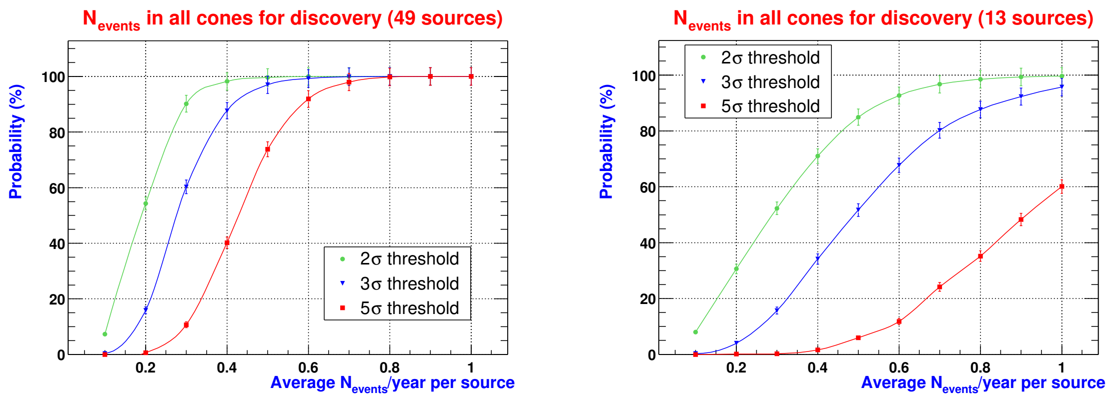

Figure 5.26: Left: Probability of success detecting a 2, 3 and 5σ excess of events for the 49 candidate source as a function of the average number of events per year emitted by each source. Right: The same plot for the 13 candidate 1-TeV sources.

In general, as the number of sources is larger in the long list than in the 1-TeV list, the average number of signal events/source needed to produce a significant excess is smaller in the long list case. This number is, for 90% of successes and a 3σ security threshold, 0.41 events/source for the long list and it is 0.91 for the 1-TeV list. However, we can compute the actual average number of events required for the discovery in the same conditions. This number is the product of the number of sources and the average required number of signal events. In the long list case the average number of required signal events is **20.1** (0.41×49) and in the 1-TeV list case is **11.8** (0.91×13). Both results are somehow complementary. Taking into account that the long list includes a wide variety of sources, it is not very likely that all the sources can emit the same flux (or even high energy neutrinos). For that reason, the short list contains the known sources more likely to produce high energy neutrinos but the required fluxes for discovery are higher.

When the acquisition time increases, it improves the sensitivity to the global flux for both lists. Figure 5.27 shows the discovery probability as a function of the average number of signal events emitted by source and year for different security thresholds.

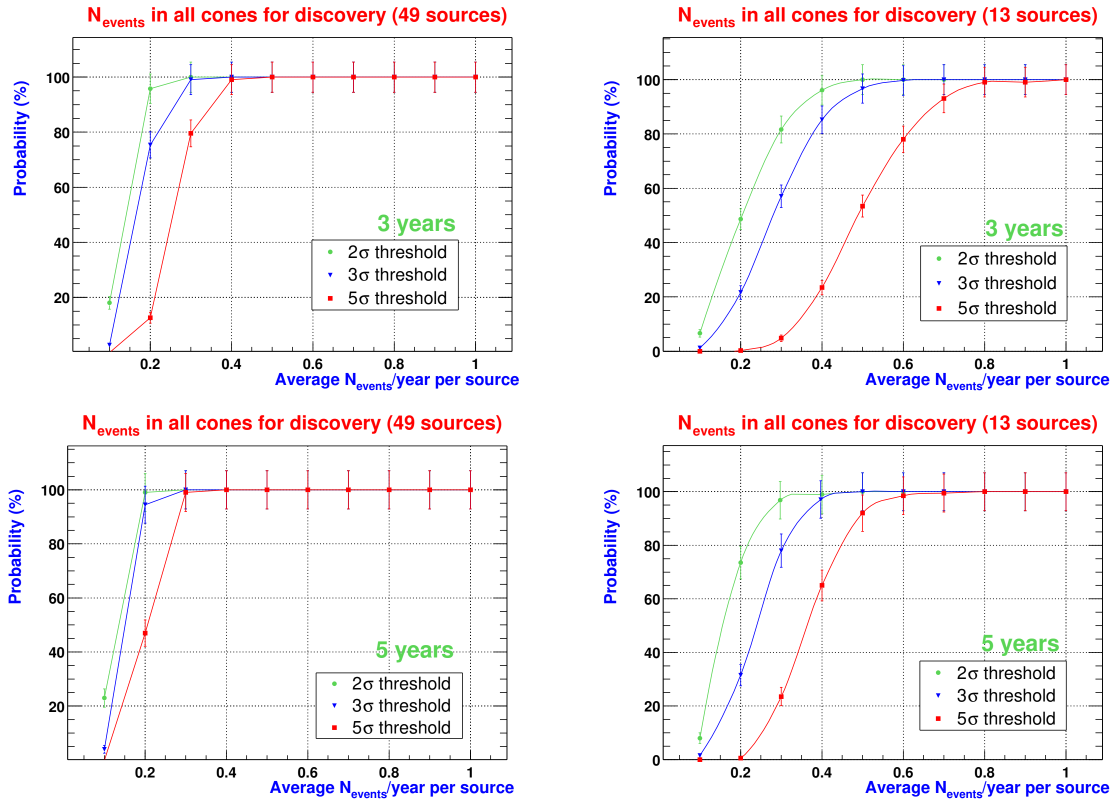

Figure 5.27: Top left: Probability of success detecting a 2, 3 and 5σ excess of events after 3 years of data taking for the 49 candidate sources as a function of the average number of events per year emitted by each source per year. Top right: The same plot for the 13 candidate 1-TeV sources and 3 years of data taking. Bottom left: Results for 5 years of data taking with the long candidate sources list. Bottom right: Results for 5 years of data taking with the 1-TeV sources list.

As can be seen, the required number of events per year for discovery is smaller when the acquisition time increases. For instance, after 5 years of data taking, the required average number of events per source for 90% of successes above a security threshold of 3σ is 0.19 **events per source and year** for the long list. The same result for the 1-TeV list is 0.35 **events per source and year**.

This technique shows that the sensitivity can be increased compared with the single point-like searches. However, less information can be obtained because the signal is distributed among different sources. These results, however, only show some global sensitivity to various point-like sources. There are various problems that must be addressed carefully when applying this method to real data. One problem is that not all the considered sources could emit neutrinos or some different sources could emit them and not be in the lists, what reduces the efficiency of this global search. Another problem is that the choice of the candidate sources must be done without any prior knowledge from the data. Otherwise, it could be almost always possible to choose some convenient sources that match the observed data. This would lead to a wrong interpretation of the data.

Chapter 6

Flux Limits

In this chapter we present the limits that can be obtained with the 12-string ANTARES detector if no point-like source is observed. First, we introduce the concept of energy-averaged effective area for neutrinos and muons. Then, we show how to define a flux limit for unobserved point-like sources and how to apply this definition with the grid and cluster techniques presented in the previous chapter. In order to obtain the best flux limits, we perform an optimisation of the parameters used in the grid and cluster methods. Next, the results that can be obtained with the ANTARES detector using both techniques are presented. The grid technique is used to produce a flux limit for each sky region defined by each bin in the grid, i.e. for the unknown sources located in that region. The cluster method, however, is used to produce a flux limit for known point-like gamma ray sources. Finally, we compare the point-like flux limits with the discovery limits derived from the results obtained in the previous chapter and with the diffuse flux limit results.

6.1 Averaged A_{eff} and fluxes

In order to compute energy-averaged neutrino and muon flux limits, an energy-averaged effective area is needed. In chapter 4 we showed that the effective area is a parameter that characterises the detector performances providing a sort of detector surface effectively seen by neutrinos or muons when they reach the detector. This area, A^i_{eff}, was defined in such a way that $N^i_{det}(E_\nu, \theta_\nu, \phi_\nu) = \Phi^i(E_\nu, \theta_\nu, \phi_\nu) \otimes A^i_{eff}(E_\nu, \theta_\nu, \phi_\nu)$ for $i = \nu$, μ. The actual definition of effective area can be seen in chapter 4. This definition is independent of the neutrino flux, being an intrinsic property of the detector [1].

The flux limits computed in this chapter are integral limits over energy in accordance to what has been published by other experiments like MACRO [143], Super-Kamiokande [144] or AMANDA [145, 146]. To compute such limits we need the corresponding energy-averaged effective areas, i.e. the neutrino or muon effective area

[1] Here *detector* includes not only the instrumented volume, but also all the physical processes involved in the neutrino detection. It includes neutrino interaction in the Earth, muon propagation in rock and water and light propagation in sea water.

properly weighted by the number of neutrinos or muons for each energy. Hence, the neutrino and muon fluxes are required.

In the case of neutrinos, in subsection 6.1.1, we compute the averaged effective area with different neutrino fluxes, each of them characterised by a different spectral index between 2 and 3. In subsection 6.1.2 we compute the energy-averaged effective area for muons. In this case, however, the muon flux is not known and we must first compute it from the known neutrino flux and neutrino effective area. Once the muon fluxes are computed for different values of the neutrino spectral index, they are used to obtain the corresponding energy-averaged muon effective areas.

6.1.1 Neutrinos

The effective area for neutrinos is related to the neutrino interaction and survival probabilities when traversing the Earth as shown in chapter 4. From the Monte Carlo data, the effective area for neutrinos can be computed by the expression 4.2.

In the most general case, A^{ν}_{eff} is a function of E_ν, θ_ν and ϕ_ν. For convenience, however, the effective area is frequently represented as a function of a smaller number of parameters (typically only one). It is common to find the effective area for neutrinos as a function of neutrino energy as can be seen in chapter 4. Since the effective area is actually a function of three parameters, those plots are made by implicitly averaging over the other parameters. For the plots in chapter 4, the generation was done using a neutrino flux uniform in $\cos\theta$ and ϕ, hence the computed effective areas are actually averaged over an isotropic neutrino flux. In general, in order to reduce the number of parameters on which the effective area depends, an average over the corresponding parameters is needed and thus a neutrino flux must be introduced. An averaged neutrino effective area is not a neutrino-flux independent quantity.

The procedure to compute the energy-averaged effective area for neutrinos is the following:

1. We compute the effective area of the detector as a function of the three parameters (E_ν, θ_ν, ϕ_ν). A histogram in 3 dimensions is filled with the corresponding values. As an example, figure 6.1 shows the detector effective area as a function of neutrino energy and $\cos\theta$ (left) or declination (right). In this case, we have averaged over the missing parameter (ϕ or right ascension, respectively). This average has been done assuming that the neutrino flux is independent of ϕ or right ascension, which is a perfectly valid assumption.

2. The neutrino flux used, a typical $E^{-\gamma}$ spectrum uniformly distributed in local coordinates, is introduced in another 3D histogram. Figure 6.2 shows the neutrino flux as a function of E_ν and δ for 3 different spectral indexes. The normalisation constant has been arbitrarily set to the Waxman–Bahcall upper limit [6].

   By definition, the effective area can be used in combination with the neutrino flux to compute the expected number of events in the detector:

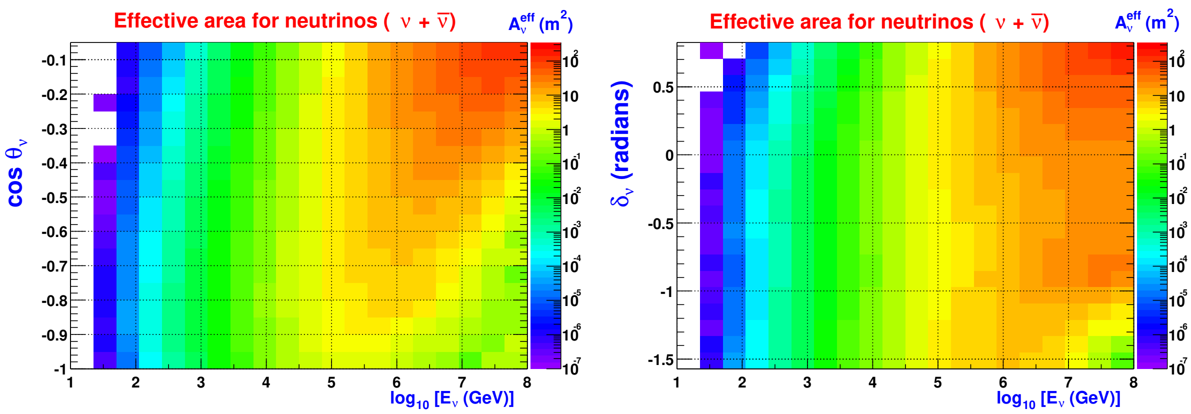

Figure 6.1: A_{eff} of the detector for neutrinos as a function of neutrino energy and $\cos\theta$ (left) or declination (right).

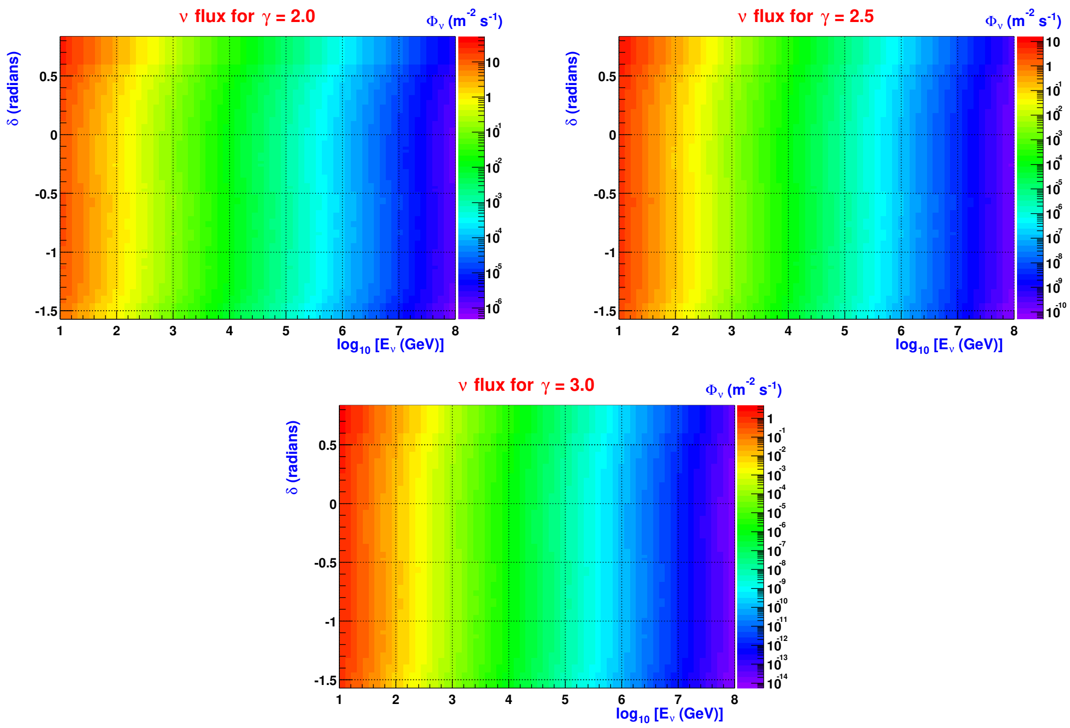

Figure 6.2: Neutrino flux as a function of E_ν and declination for spectral indexes γ = 2.0, 2.5 and 3.0 and a normalisation constant equal to the Waxman–Bahcall upper limit.

$$N_{events} = \int_{E_{min}}^{E_{max}} A^{\nu}_{eff}(E_\nu, \theta_\nu, \phi_\nu) \cdot \frac{d\Phi_\nu(E_\nu, \theta_\nu, \phi_\nu)}{dE_\nu \; d\Omega_\nu} \, dE_\nu \; d\Omega_\nu \tag{6.1}$$

This convolution is performed using the 3D histograms with a suitable binning. In figure 6.3 we can see the expected number of events as a function of E_ν and declination for two values of the spectral index.

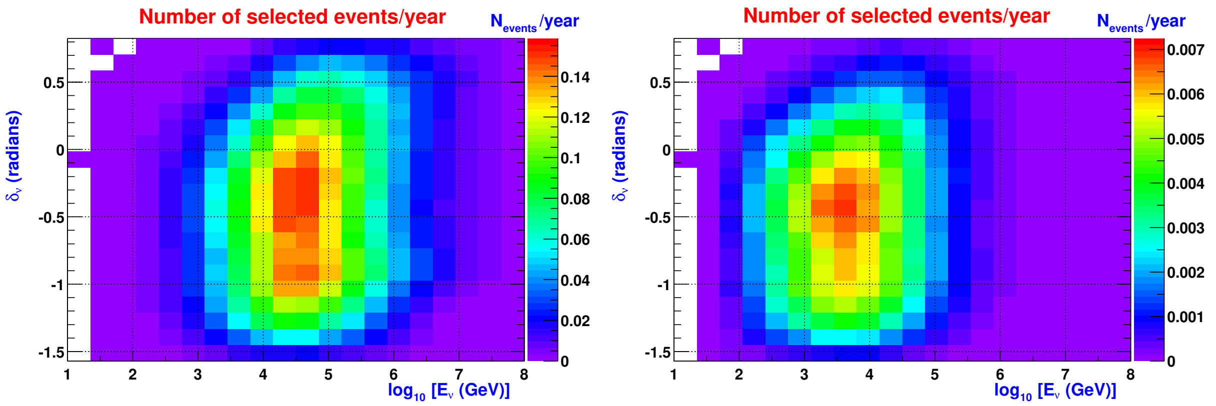

Figure 6.3: Number of events expected in 1 year of data taking for a neutrino flux with normalisation equal to the Waxman–Bahcall upper limit ($4.5 \times 10^{-4} cm^{-2} s^{-1} sr^{-1} GeV^{-1}$), as a function of declination and neutrino energy for a spectral index $\gamma = 2.0$ (left) and for $\gamma = 2.5$ (right).

In addition to computing the number of expected events, the neutrino flux is also used to average the neutrino effective area:

$$\bar{A}^{\nu}_{eff}(\theta_\nu, \phi_\nu) = \frac{\int_{E_{min}}^{E_{max}} A^{\nu}_{eff}(E_\nu, \theta_\nu, \phi_\nu) \cdot \frac{d\Phi_\nu(E_\nu,\theta_\nu,\phi_\nu)}{dE_\nu d\Omega_\nu} \, dE_\nu}{\int_{E_{min}}^{E_{max}} \frac{d\Phi_\nu(E_\nu,\theta_\nu,\phi_\nu)}{dE_\nu d\Omega_\nu} \, dE_\nu} \tag{6.2}$$

Using equation 6.2 we compute the energy-averaged effective area using the 3D histograms. The result is a 2D histogram of the effective area as a function of declination and right ascension. Figure 6.4 shows the effective area as a function of declination only. In this case, a new average over right ascension has been performed. As the neutrino flux is uniformly distributed in right ascension, this average can be trivially computed.

The same procedure could be used to compute an effective area averaged over any other parameter. However, to compute integral flux limits, only the energy-averaged effective area is needed. This quantity is computed in the energy range used in the generation of the events, i.e. between 10 GeV and 10^8 GeV.

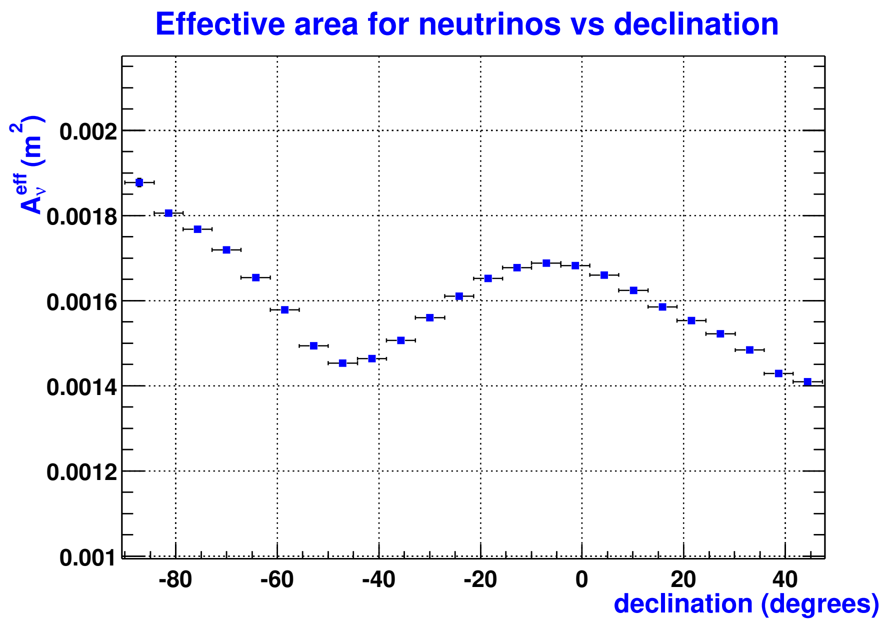

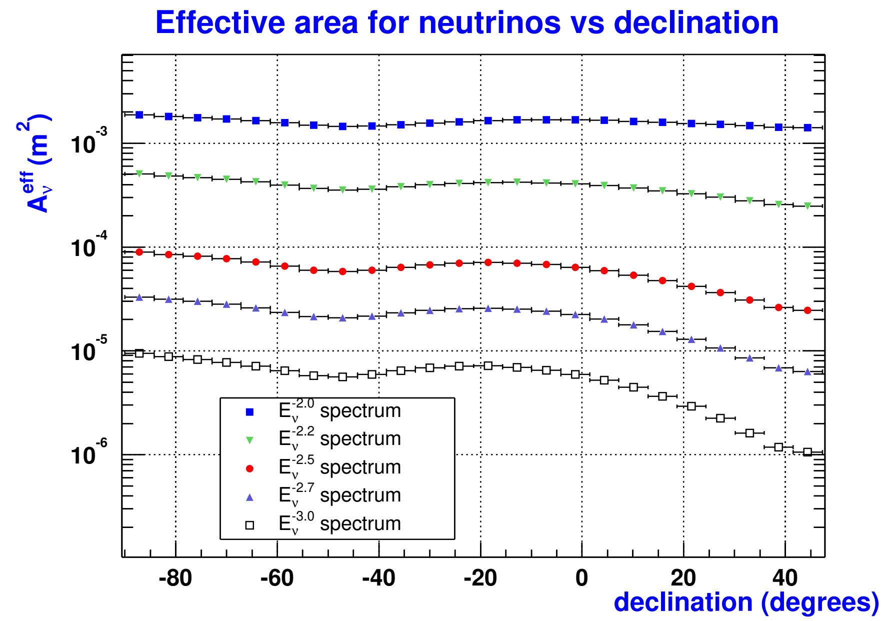

Figure 6.4: Averaged neutrino effective area computed with a neutrino flux $E^{-2.0}$ (top) and a comparison of different averaged neutrino effective areas obtained for different spectral indexes (bottom).

6.1.2 Muons

For neutrinos, the effective area and flux are well defined concepts. However, this is not the case for muons. It was shown in [147] that using events generated on the surface of a can around the detector leads to an underestimation of the detector effective area at low energies. The solution to this problem is to combine the effective area produced by surface events and volume events. The price to pay is that a particular neutrino flux is required in order to determine how to combine both types of events. Later in [148], it was shown how to use volume events and the effective muon ranges to simplify the problem. However, the muon effective area has to be expressed as a function of neutrino energies (it cannot be done as a function of muon energy, since this energy changes as the muon propagates).

Using the solution proposed in [128, 148], the detector effective area for muons can be computed using the Monte Carlo information as it was shown in chapter 4. This solution leads to a muon effective area of the detector expressed in terms of neutrino parameters (E_ν, θ_ν, ϕ_ν). Figure 6.5 shows the effective area for muons as a function of both neutrino energy and declination or right ascension.

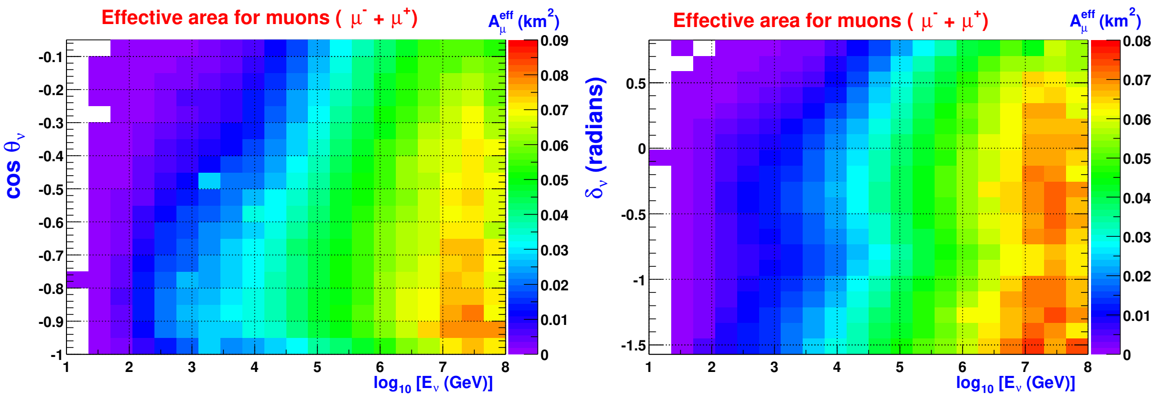

Figure 6.5: A_{eff} of the detector for muons as a function of neutrino energy and $\cos\theta$ (left) or declination (right).

A second problem when working with muons are muon fluxes. A muon flux at the detector is required in order to compute an averaged muon effective area similar to the neutrino case in the previous subsection. While a neutrino flux is something well defined that we usually parametrize by a simple power law in energy, the muon flux at the detector is not known.

As we did for neutrinos, the number of events in the detector can be computed from the muon effective area and the muon flux using equation 6.1 for muons. In practical terms, this is done using the corresponding 3D histograms. Since the number of events in the detector — as a function of three variables — must be the same, independently of whether we use neutrinos or muons to obtain it, we can use this number (as a matter of fact a 3D histogram), obtained through the neutrino effective area and flux, to invert equation 6.1 and obtain the muon flux from the known muon effective area.

Three examples of muon fluxes computed in this way can be found in figure 6.6 for different values of the spectral index. In this case, the fluxes are represented as a function of neutrino declination and energy. As can be seen, the shape of the muon fluxes is different for different spectral indexes. In the figure, the muon fluxes have a normalisation that corresponds to a neutrino flux normalised to the Waxman–Bahcall upper limit for all the different spectral indexes. However, the global normalisation is not important for our purposes since we will use the muon flux to re-weight the muon effective areas.

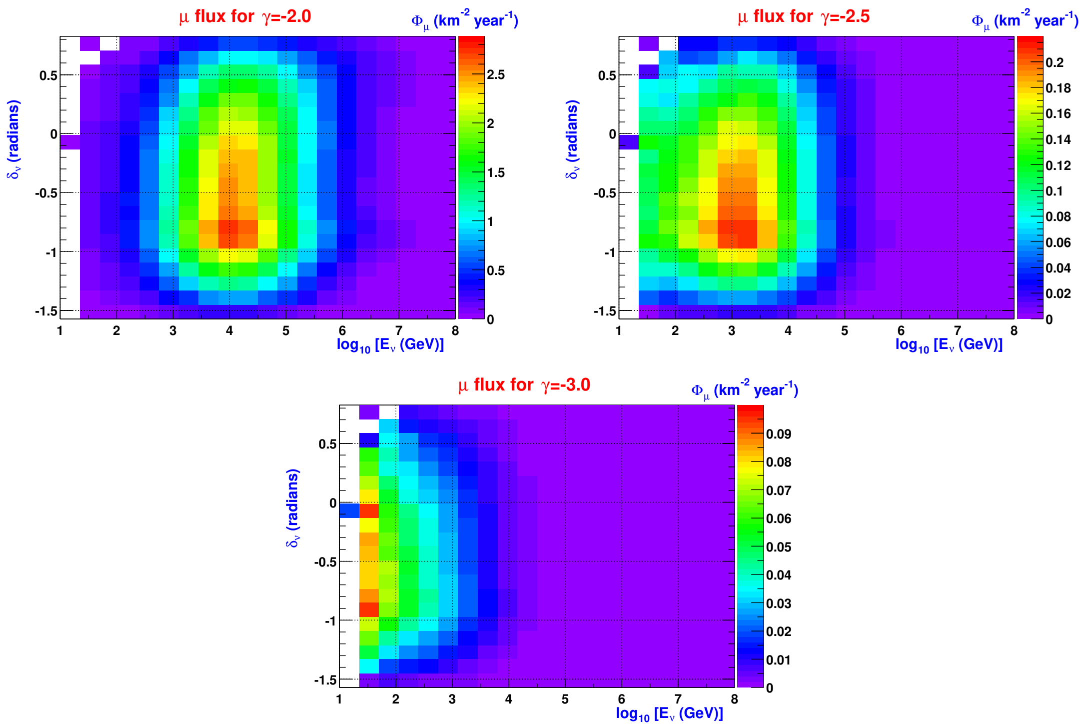

Figure 6.6: Muon flux (including both μ^+ and μ^-) as a function of E_ν and declination for spectral indexes γ = 2.0, 2.5 and 3.0 and normalisation constant $4.5 \times 10^{-4} m^{-2} s^{-1} sr^{-1} GeV^{-1}$ in (Waxman–Bahcall upper limit) the neutrino flux.

Once the muon flux has been established, we can compute the energy-averaged effective area needed to compute the muon flux limits. The energy-averaged effective area is weighted using the muon flux (equation 6.2 for muons). The results after averaging over right ascension can be seen in figure 6.7.

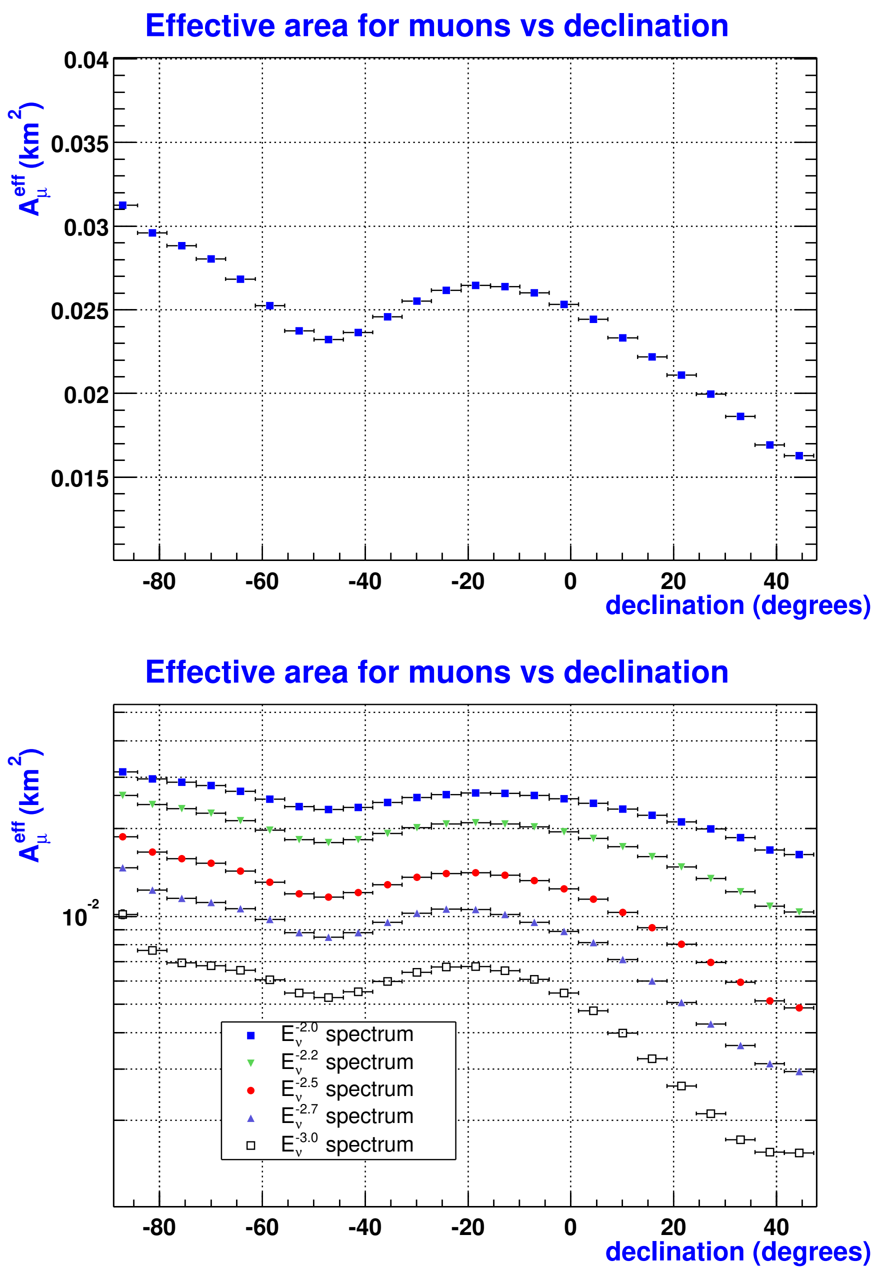

Figure 6.7: Averaged muon effective area computed for the muon flux produced by a neutrino flux E^{-2} (top) and a comparison of the different averaged muon effective areas obtained with different spectral indexes (bottom).

6.2 Flux limits

In chapter 5 we used the grid and cluster techniques to perform searches for point-like neutrino sources in the (Monte Carlo) data. However, when no significant source can be identified in a particular sky region or around a candidate source, the same techniques can be used to derive a flux limit. As we have already mentioned, we compute integral flux limits since integrating the signal over the whole detectable energy range ensures maximum sensitivity. Our integral flux limits are always computed in the range between 10 GeV and 10^8 GeV. This energy range comprises the ANTARES sensitivity range. At lower energies the events can not be properly reconstructed and at higher energies the Earth is opaque for neutrinos.

In order to derive a flux limit, one has to compute the maximum average number of events statistically acceptable at a given confidence level (90% in our case), when N_{bg} background events are expected and N_0 events are observed. We call $\mu_{90\%}^{limit}(N_0, N_{bg}(\delta))$ the upper limit at 90% confidence level computed with the Feldman and Cousins unified approach [7]. An advantage of the Feldman and Cousins approach over classical Poissonian statistics is the smooth transition between an upper limit and a central confidence belt. Using the previously mentioned $\mu(N_0, N_{bg})$ upper limit, we compute the integral (over all energies) flux limit as:

$$\Phi_{90\%}^{limit,i}(\gamma,\delta) = \frac{\mu_{90\%}(N_0, N_{bg}(\delta))}{\epsilon(\gamma,\delta)\cdot \bar{A}_{eff}^{i}(\gamma,\delta)\cdot T_{live}(\delta)} \tag{6.3}$$

where i can be ν or μ, γ is the spectral index and $T_{live}(\delta)$ is the amount of time that a source of declination δ is visible from the ANTARES detector during the corresponding period of data taking. The flux limit expression also requires the energy-averaged effective area computed in the previous section ($\bar{A}_{eff}^{i}$). Finally, the expression also includes the bin/cluster reconstruction efficiency (ϵ) that accounts for the probability that the muon track is reconstructed in the same bin/cone than the original neutrino.

In this work, all the flux limits will be computed with the Feldman and Cousins approach at a confidence level of 90%.

In the following subsections, we will study the all-sky flux limit case using the grid technique and the flux limits for the case of specific sources using the cluster technique. Later, we will show how both techniques can be optimised in order to achieve the best performances.

6.2.1 All–sky flux limits

The next step is to compute neutrino and muon flux limits for hypothetical point-like sources with a given energy spectrum. These spectra are characterised as usual by a power law ($\frac{d\Phi_\nu}{dE_\nu} \propto E_\nu^{-\gamma}$) with spectral indexes (γ) between 2 and 3. We will use the grid technique to produce an *all–sky flux limit* in the sense that a flux limit will be computed for each of the bins made for the whole ANTARES visible sky.

As mentioned, our flux limits are integral flux limits, computed from equation 6.3. This equation is applied to each particular bin in the grid covering the whole ANTARES visible sky. The upper limits are computed from the observed number of events in one bin (N_0) and the expected background (N_{bg}), computed as the average number of events per bin in all the bins of the same declination. The average background is directly obtained from the observed data without any previous knowledge of the background distribution or detector performances. Only the fact that the background is right–ascension independent is used and hence the average background for all the bins at the same declination band is the best estimate of the expected background. Once more, by binning the data the result is more robust because no additional hypothesis about the background is needed. The upper limit ($\mu_{90\%}^{limit}$) is the same for both neutrino and muon fluxes, because it is computed from the number of events N_0 and the average number of events N_{bg}, that includes both the neutrino and the resulting muon.

Equation 6.3 also includes the term $T_{live}(\delta)$, the time that a given region of the sky is visible from the detector. $T_{live}(\delta)$ is a fraction of the total duty time of the detector and depends on declination. For the grid technique, figure 6.8 shows the percentage of time that each of the bins in a grid is visible from ANTARES within one day[2]. The grid used corresponds to the optimal one for flux limits, as will be explained in section 6.3. As can be seen, only $\sim 30\%$ of the declination range accessible from the ANTARES site is seen during 100% of the time. The rest of declinations have different visibilities ranging from 100% between $\delta = -90°$ and $\delta \approx -48°$ to 0% visibility at the limit of the visible sky, $\delta \approx +48°$. The visibility values computed for each of the bins in figure 6.8 correspond to the average visibility associated to all the declinations contained in each bin. In our case, we have studied the results after 1,3 and 5 yeas of data taking.

In equation 6.3 the bin reconstruction efficiency $\epsilon(\gamma, \delta)$ is also included. This parameter takes into account the fraction of events that are reconstructed inside the bin. The efficiency for neutrinos or muons represents the case of a source originally emitting neutrinos or muons, respectively. Since we look for neutrino sources, the parameter ϵ must be the neutrino efficiency. In general, muon efficiency is larger than neutrino efficiency, because the angle between the neutrino and the reconstructed muon includes the physical angle between the neutrino and the muon. With larger bins, the bin efficiency increases and approaches to one. The spectral index also plays an important role, because as it increases the angular resolution degrades (see figure 5.8 in chapter 5).

In the upper part of figure 6.9 we can see the bin efficiency for neutrinos and on the lower part the bin efficiency for muons for different spectral indexes. Only the neutrino efficiency is the reconstruction efficiency (ϵ) to be used to compute the flux limits. As just mentioned, both efficiencies decrease as the spectral index increases (the relative importance of low energy events is larger). The influence of the spectral index is more significant for neutrinos than for muons due to the physical angle between the neutrino and the muon. We observe that as the spectral index approaches 3, the mean angle between the neutrino and the muon increases and the bin efficiency for neutrino

[2]Variations from one day to another are negligible.

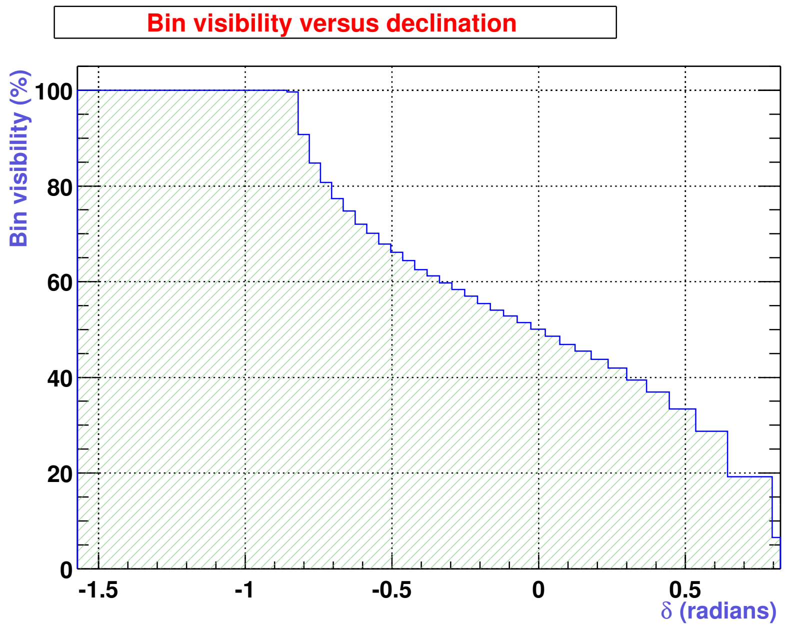

Figure 6.8: Percentage of time that a source is visible from ANTARES as a function of declination. The binning in declination corresponds to equal background bins.

decreases. For muons, the same effect is present but is less important. In both cases we notice that the size of the bins in the grid has a deeper impact in the bin efficiency than the spectral index.

The last ingredient to compute the flux limits is the averaged effective area for neutrinos or muons. The process to obtain the energy-averaged effective areas was described in section 6.1. Those computations can be performed using the same binning than the one used to compute the flux limits. So, the effective area for neutrinos or muons to be used in each particular bin is known.

With all these elements we build an integral all–sky flux limit for neutrinos or muons, by combining the flux limit computed for each individual bin of the grid. However, we first need to estimate the optimal grid to be used for the computation of the flux limits (see section 6.3).

6.2.2 Flux limits for selected sources

When some known sources are suspected to be point-like neutrino sources we can use their position to set a specific flux limit for each source. In the all–sky survey there is no guarantee that the source is located at the centre of the bin. This makes the technique less sensitive, which is reflected as a lower ϵ_{bin} parameter. In this case, we can use the cluster technique to study only the circular region around each candidate source. The source is then located at the centre of the cone and hence the efficiency

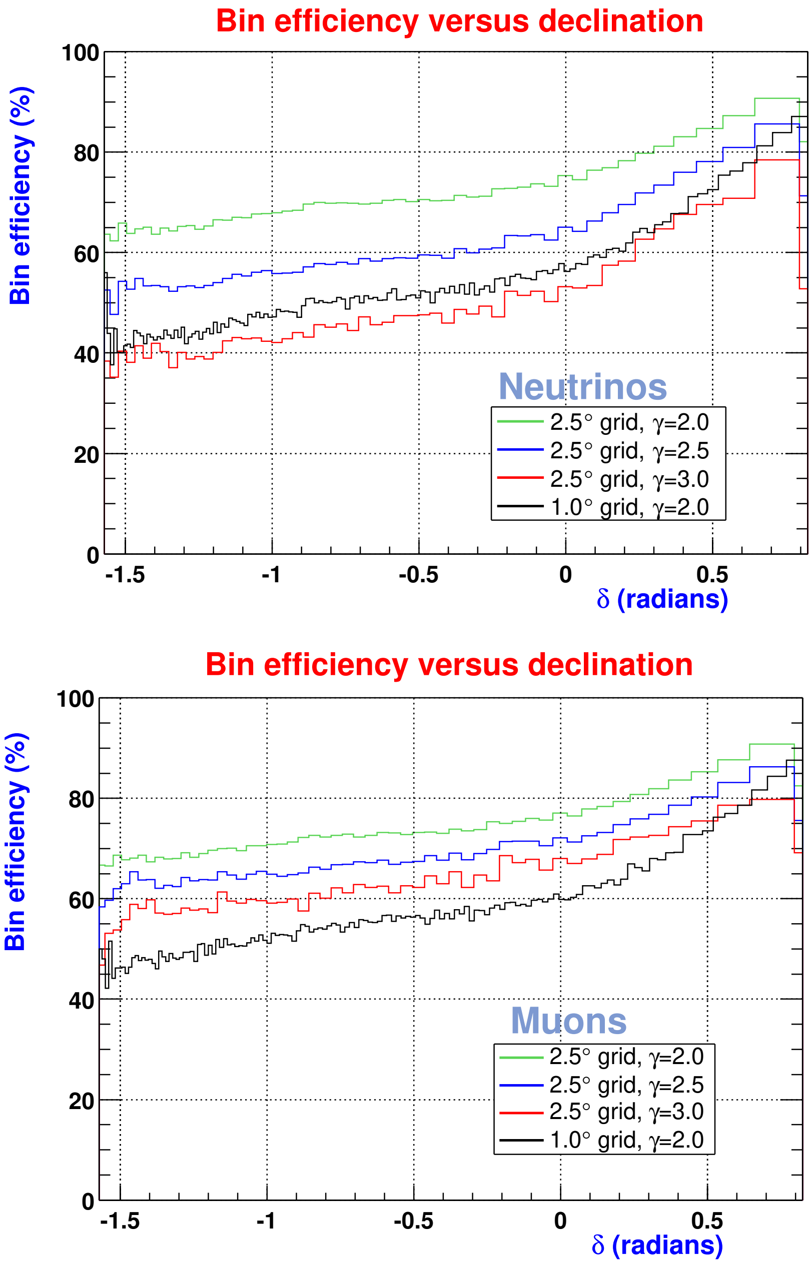

Figure 6.9: Bin efficiency for neutrinos (top) and for muons (bottom) for different spectral indexes between 2 and 3. In both plots the grids used correspond to the optimal case for flux limits (2.5°) except for one of the graphs, in which it corresponds to the optimal grid for searches (1.0°)

parameter (ϵ_{cone}) and the sensitivity of the technique are larger.

From the location of the ANTARES site the sky coverage is 3.5π sr (although this must be weighted by the time fraction that each sky region is visible). This allows to study most of the point-like candidate sources that could emit high energy neutrinos. The ANTARES visible sky region has also a small overlap with the AMANDA visible sky region, what allows a comparison between both experiments. We have selected 49 point-like sources that could emit neutrinos. Most of them are known to be X-ray emitters and 13 of them are also known to be gamma ray emitters above 1 TeV. The complete list of point-like source candidates studied can be found in Appendix B. This selection is not complete and in the future, as new astronomical data from these or other sources are obtained, the list could be extended or reduced.

The flux limits are computed as described in the previous subsection. We use again equation 6.3, where:

- ϵ is now the efficiency of collection of events in a cone of a certain radius, centred in the source under study. Since the cone is located around the source where all the events are supposed to come from, the efficiency for a cone is always higher than the efficiency for a bin. Figure 6.10 shows this efficiency as a function of declination for different cone sets. The different efficiency in declination is mostly due to the different size of the cones since all the cones in the same set have the same average number of background events.

- N_0 is the number of observed events inside the cone around the source.

- $N_{bg}(\delta)$ is the average number of events observed in cones of the same radius at the same declination as the source. However, since the cones are chosen following the criteria mentioned in chapter 5, this background is the same for all the cones in the same cone set.

- T_{live} is again the visibility of the source. In this case, however this visibility corresponds only to the source (figure 6.8 showed the average visibility inside a bin).

- A^i_{eff} is the energy-averaged effective area for neutrinos or muons in the cone. In this case we use the effective area computed for the bin containing the corresponding cone.

Thanks to the knowledge of the source location, the sensitivity of the flux limits obtained with the cluster technique for particular point-like source candidates will be higher than the all sky flux limit for the sky region where the candidate source is located. However, the cluster technique can only be applied to known sources that are suspected to be neutrino emitters while the all sky flux limits can be set for all the sky regions without any previous knowledge. Both techniques, cluster and grid, are complementary, but prior to their use they must be optimised in order to obtain the flux limits with higher sensitivity.

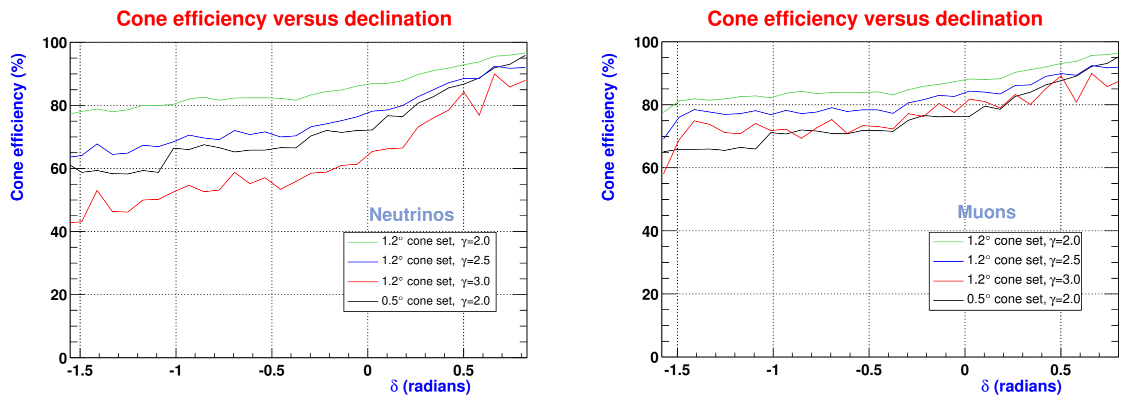

Figure 6.10: Efficiency collecting signal events inside the cones of one particular cone set for neutrinos (left) and muons (right), represented as a function of the declination.

6.3 Signal to background optimisation

In order to obtain the optimal flux limits, the optimal grid and cluster choice must be made. This choice is based on a criterion different from the one used for point-like source searches in chapter 5. However, the grid and cone sets used are the same: all the bins or all the cones contain on average the same number of background events regardless of their declination. For that reason, we use again the average number of background events per bin or per cone as the reference parameter to describe a particular grid or cone choice. This parameter is equivalent (as it was shown in the previous chapter) to the width of the first bin or cone used to obtain the other bins or cones.

For each grid or each set of cones we compute the average signal to background ratio. We will use the grid and the cone set that provides the best signal to background ratio. Let us call ϵ_{bin} the efficiency of reconstructing events within a given bin, i.e. the fraction of events initially directed to that bin/cone that are finally reconstructed inside (see figure 6.9 and figure 6.10). Let us call N_0 the actual number of detected events in a bin and N_{bg} the expected background in that bin. We define $\mu(N_0, N_{bg})$ as the 90% confidence level upper limit for the signal (i.e. the maximum acceptable signal computed with Feldman and Cousins at 90% C.L. for that N_0 and that N_{bg}). Then, a measure of the signal to background ratio in a certain bin/cone is given by:

$$\frac{S}{B} = \frac{\epsilon_{bin}}{\mu_s(N_0, N_{bg})} \tag{6.4}$$

This equation gives us the figure of merit used to optimise the grid and cluster techniques. For both techniques the average background, N_{bg}, is computed from the data themselves, regardless of their origin (real data or Monte Carlo).

In the case of the grid technique, N_{bg} is computed by averaging over the observed number of events in all the bins in the same declination band. The reason is that the background distribution is right-ascension independent and all the bins in the same declination band have the same average background. The S/B value is computed for each bin with the corresponding N_0 and ϵ_{bin}. However, since we are computing the optimal parameters to produce the flux limits, we want a kind of average behaviour. The S/B obtained for each bin is thus averaged over all the bins in the grid. The results obtained with the different bin grids are summarised in figure 6.11. This figure shows the inverse of the average S/B ratio obtained with the different grids studied.

As can be seen in the figure, the optimal value is obtained with the grid characterised by an initial bin width of 2.5° or equivalently a grid that has an average background of 0.41 events per bin. The optimal value for S/B (the inverse of the minimum in the figure) is 0.25. In the case of searches with the grid technique, the optimal grid had an initial bin width of 1.0°, what represented an average background of 6.63×10^{-2} events/bin. So the grid for flux limits has larger bins and hence, a smaller number of bins dividing the visible sky.

For the cluster method, the optimal S/B is computed in a similar way. Equation 6.4 is again used, but in this case N_0 is the number of events from the *1-year sample* inside a particular search cone and ϵ_{bin} is the efficiency of reconstructing the events inside that cone. Since any direction in the sky can be used, the average S/B has been calculated over 49 directions in the sky corresponding to the 49 point-like source candidates in the ANTARES visible sky listed in Appendix B. Figure 6.12 shows a plot with the inverse of the average value of S/B for different cone sizes. As can be seen, the optimal cone size is the cone set with an initial diameter of 1.2° or equivalently the cone set with an average background of 0.31 events/cone. For this technique the optimal value of the S/B ratio (the inverse of the minimum in the figure) is 0.31.

The cone diameters of the selected cone set as a function of the declination is shown in figure 6.13 (left). For comparison, the figure also shows the size of the optimal cone set for searches. As in the grid case, the optimal cone sets are larger for flux limits than for searches.

Concerning the optimal S/B ratio obtained for both techniques, we observe that the optimal value from the cluster technique (0.31) is better than the optimal value obtained from the grid technique (0.25). The difference is mainly due to the different efficiency collecting signal events inside a bin or a cone (ϵ). Although the bin widths are larger than the cone sizes, the efficiency for the cones is better. This is because the signal events are expected to be produced by the point-like source located at the centre of the cone. However, in the grid case the source location is unknown and could be anywhere in the bin, in other words, the bin efficiency is a kind of average efficiency all over the bin. Figure 6.13 (right) shows a comparison of the bin and cone efficiencies obtained with the optimal grid and cone sets.

In both techniques the optimisation has been performed assuming that the signal follows a E^{-2} spectrum. In the following, all the results will be produced using the optimal grid and cone sets obtained for that case, even when the flux limits are computed for spectral indexes different from 2.0. This is justified because the difference

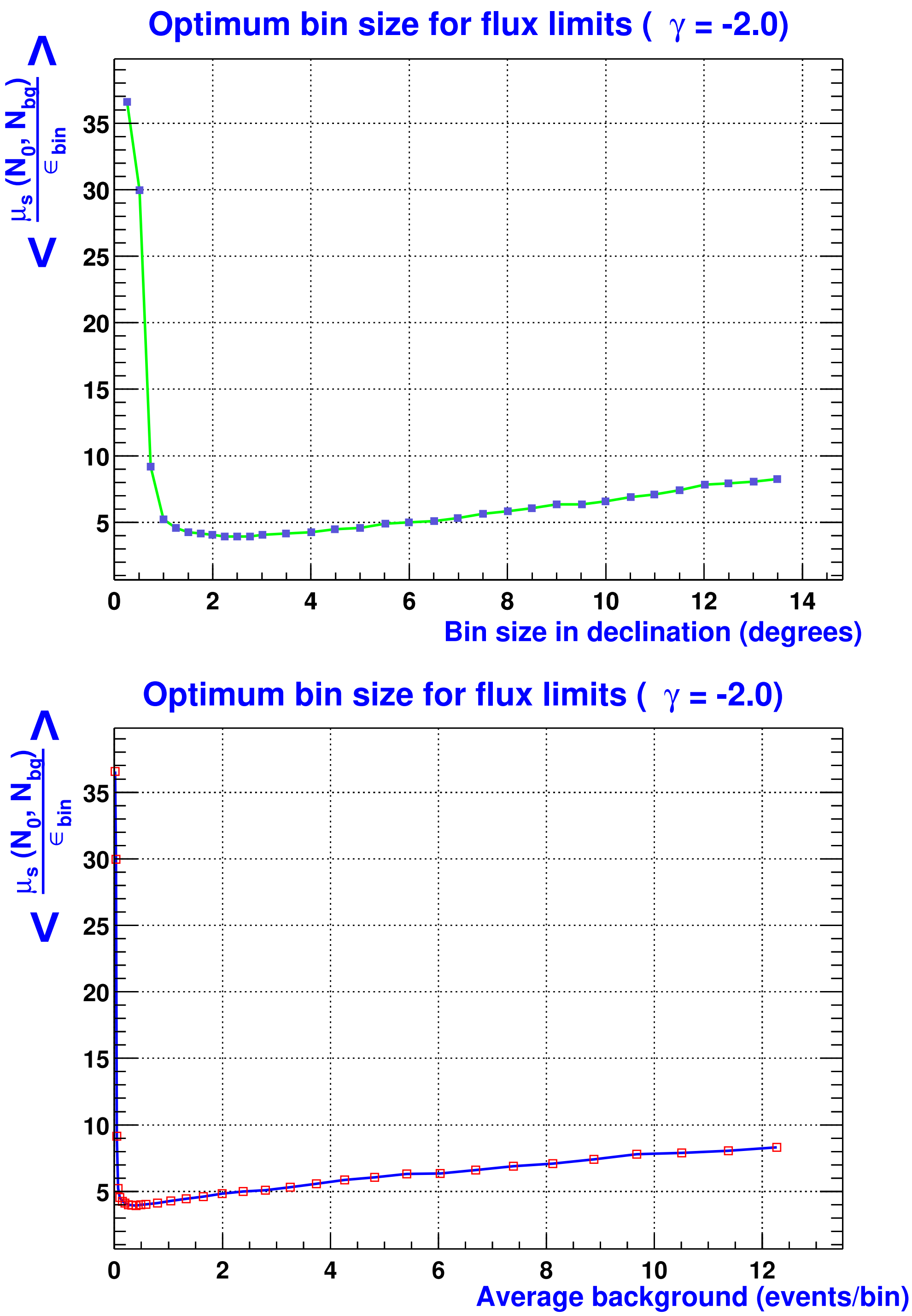

Figure 6.11: Average $\frac{B}{S}$ obtained with different grids. In the upper plot, the B/S ratio is represented as a function of the initial bin width. In the lower plot, the B/S ratio is represented as a function of the average number of background events per bin.

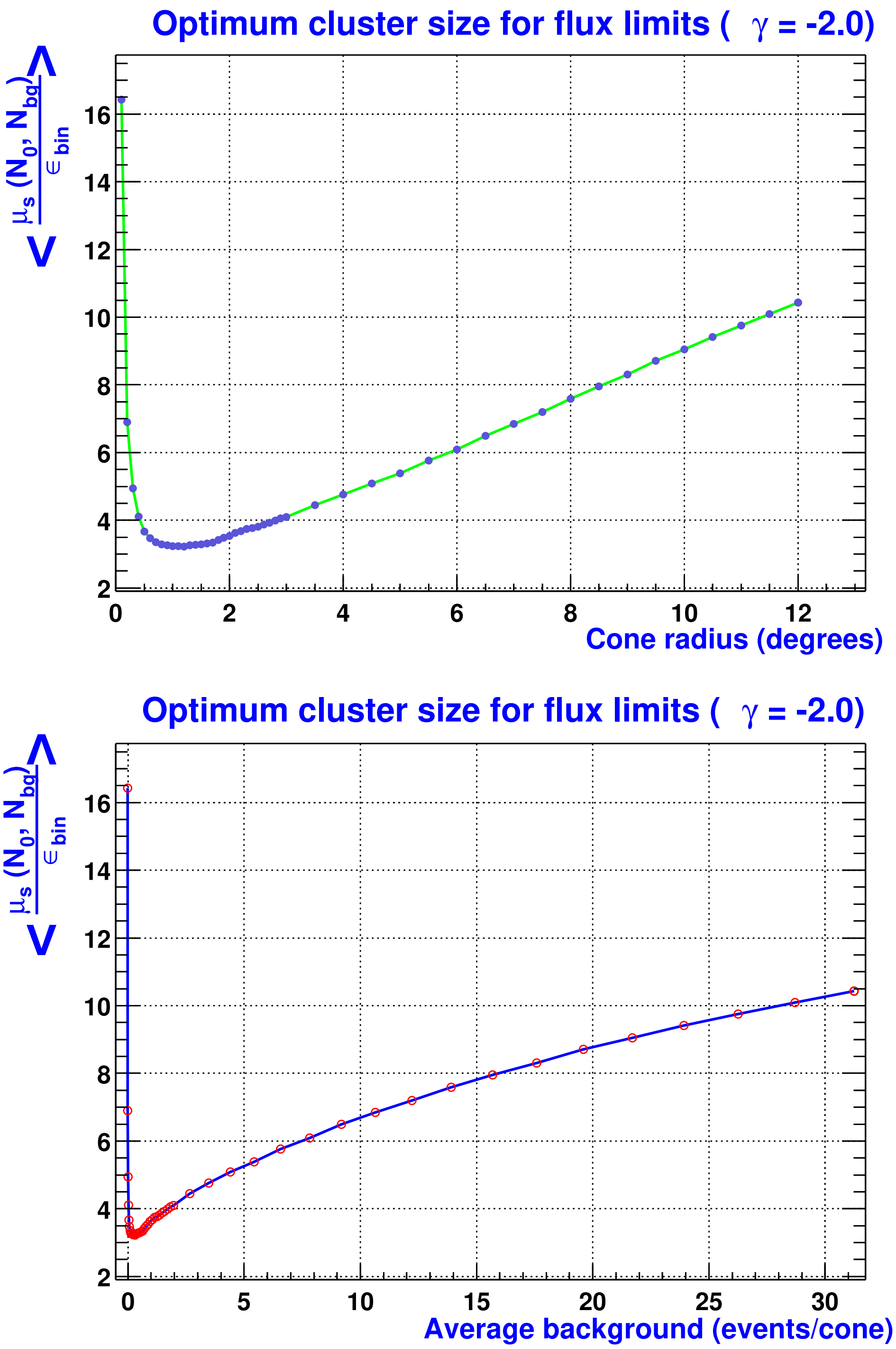

Figure 6.12: Average $\frac{B}{S}$ obtained with different cone sets. In the upper plot, the B/S ratio is represented as a function of the initial cone diameter. In the lower plot, the B/S ratio is represented as a function of the average number of background events per cone.

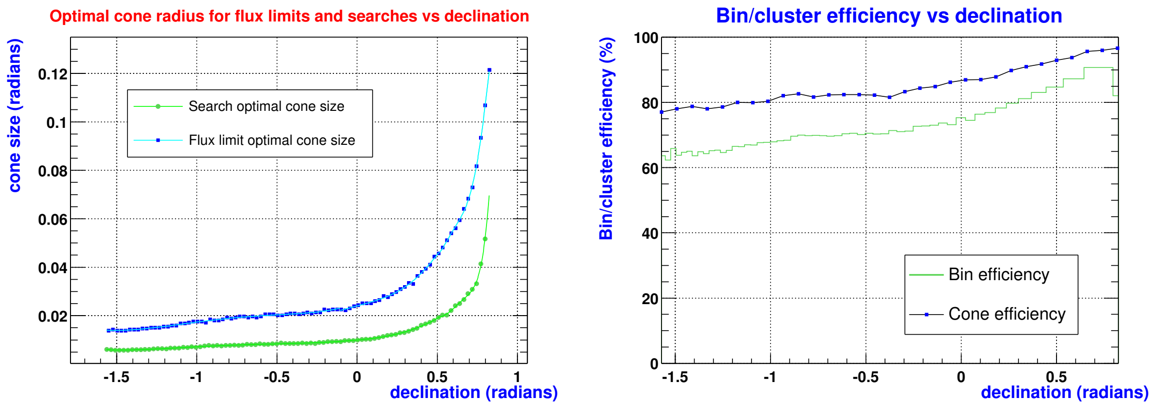

Figure 6.13: Left: Cone diameter for the cluster technique as a function of declination for the optimal cone set for searches and the optimal cone set for flux limits. The size of the cones for searches is smaller than the size of the cones for flux limits. Right: Efficiency collecting signal events as a function of the declination for the optimal grid and the optimal cone sets to compute flux limits.

between the optimal grid and cone sets for E^{-2} with other spectral indexes is very small. Figure 6.14 shows the inverse of the S/B ratio as a function of the initial bin width and cone diameter. As can be seen, the optimal size for $\gamma = 2.5$ and 3.0 is very close to the optimal size for $\gamma = 2.0$. However, as the spectral index increases, the optimal S/B ratio decreases. Table 6.1 summarises the results obtained.

	Best S/B	
γ	Grid	Cluster
2.0	0.25	0.31
2.5	0.21	0.27
3.0	0.17	0.23

Table 6.1: Best values of the S/B ratio obtained with the two techniques and different values of the spectral index.

6.4 All sky flux limits results

In this section, we present the flux limits results obtained with the optimal grid found in the previous section. The grid built with an initial bin width of 2.5° provides the best signal to background ratio for an spectral index of 2.0, after averaging over all the bins. This means that if other grids were used, they might give better results in a particular region of the visible sky, but, on the whole our particular choice produces

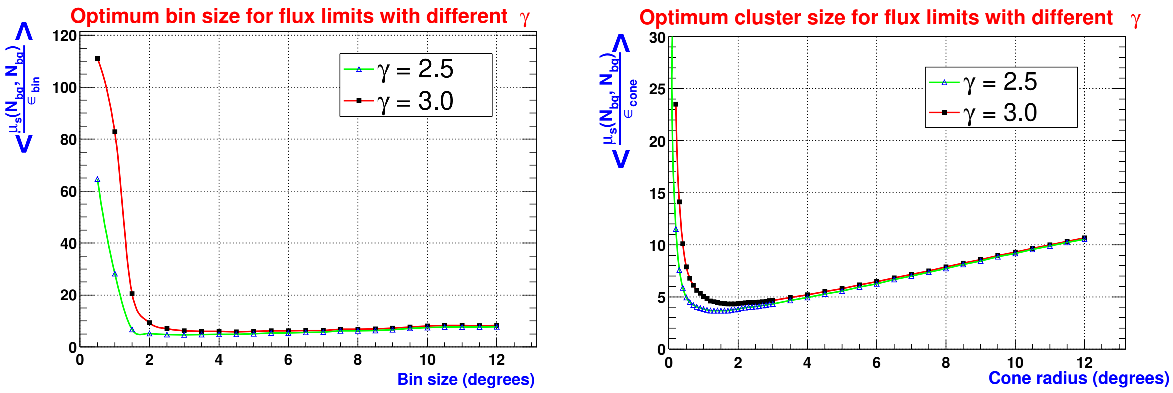

Figure 6.14: Average $\frac{B}{S}$ as a function of the initial bin width (left) and the initial cone diameter (right) for a spectral index of 2.5 and 3.0.

the best results. All the results presented here have been produced with the average optimal grid.

The all sky flux limit is obtained from the limits computed for each bin in the grid and using the data obtained from the data sample (Monte Carlo in our case) and the detector performances (always obtained from Monte Carlo). Using all the bins, we can obtain flux limits for all the visible declinations and hence the name of "*all sky flux limit*". However, each limit computed for each particular bin only applies to that bin. Each limit represents the maximum signal emitted by an unknown source located in the bin that can be admitted, taking into account the observed data. The limits are computed at the 90% confidence level using Feldman and Cousins.

The limits can be expressed in terms of the neutrino flux emitted by the source, or the muon flux arriving at the detector. In one case, we set a flux limit to the neutrino flux emitted by the source that arrives to the opposite side of the Earth (before traversing it). In the other, we set a limit to the muon flux at the detector level. Some experiments, like Super-Kamiokande, only compute the muon flux limit, however, other neutrino telescopes like AMANDA [145,149] compute both types of flux limits. The muon flux limit, has the additional advantage of being much less sensitive to the energy range of the neutrino flux used in the computations, what makes the result more robust. In this work, both types of flux limits are computed.

6.4.1 Results after 1 year of data taking

Figure 6.15 shows the all sky flux limits after one year of data taking assuming a spectral index of 2.0. The upper (lower) plot shows the flux limit for neutrinos (muons) as a function of declination. For each declination band, the flux limits have been averaged over all the bins in that band. These limits have also been averaged in the figure when one point covers more than one declination band of the real grid used to compute the flux limits. These average values and their errors do not show the fluctuations from one experiment to another due to the different number of events observed in a particular bin. This means that the flux limits derived from one real experiment will fluctuate around the mean values shown in the figure 6.15. Since this study is carried out at Monte Carlo level, only the average values of the flux limits and the uncertainties in their determination (error bars) are shown.

As can be seen in figure 6.15, there is roughly a factor $\sim 10^7$ between the neutrino and muon flux limits coming from the $\sim 10^7$ factor between the neutrino and muon effective areas. The flux limits that can be set get worse as the declination increases, a consequence mainly of the time during which those declinations can be observed from the ANTARES location.

The effect of including different values of the spectral index in the calculations can be seen in figure 6.16. This figure shows the neutrino and muon flux limits that can be set for different values of the spectral index between 2.0 and 3.0. As can be seen, the neutrino flux limits change over a larger range when modifying the spectral index. This is a consequence of the behaviour of the energy-averaged effective areas. The shape of the different curves is, however, very similar. The neutrino flux limits increase (worsen) slowly as the declination increases. Then, above $\delta \simeq -10°$, the limits increase faster due to the live time parameter. For the muon flux limits, however, the different spectral index affect the flux limits that can be derived, but the differences are much smaller than in the neutrino case. The general behaviour of the muon flux limits is the same among the different spectral indexes and it is similar to the behaviour of the neutrino flux limits. We find a soft increase of the flux limits as the declination increases, then above $\delta \simeq -10°$ the flux limits worsen quickly due to the visibility of those declinations from the ANTARES site.

All the results in figure 6.16 have been obtained using the same grid, the grid that provided the optimal results for a spectral index of 2.0. In principle, the best results with a given spectral index are obtained when the optimal grid for that spectral index is used. Nevertheless, the optimal S/B ratios with other spectral indexes in the range $2.0-3.0$ are almost the same as the S/B ratio obtained with the 1.2° grid (the optimal grid for the spectral index of 2.0).

6.4.2 Results after several years of data taking

The flux limits obtained by an experiment can be improved by increasing the observation time. In equation 6.3, T_{live} is increased just by increasing the time that the experiment is running. On the other hand, the parameter $\mu_s(N_0, N_{bg})$ also changes when the observation time increases, since both N_0 and N_{bg} should scale by the same factor when the observation time is increased. Hence, $\mu_s(N_0, N_{bg})$ also increases when increasing the acquisition time of the experiment. The result is that after increasing T_{live} by a given factor, the flux limits are improved by a factor slightly smaller: ~ 2.5 for 3 years and ~ 3.8 for 5 years. In addition, the fluctuations of μ_s, produced by the different values of N_0, are reduced. The results obtained for the neutrino and muon

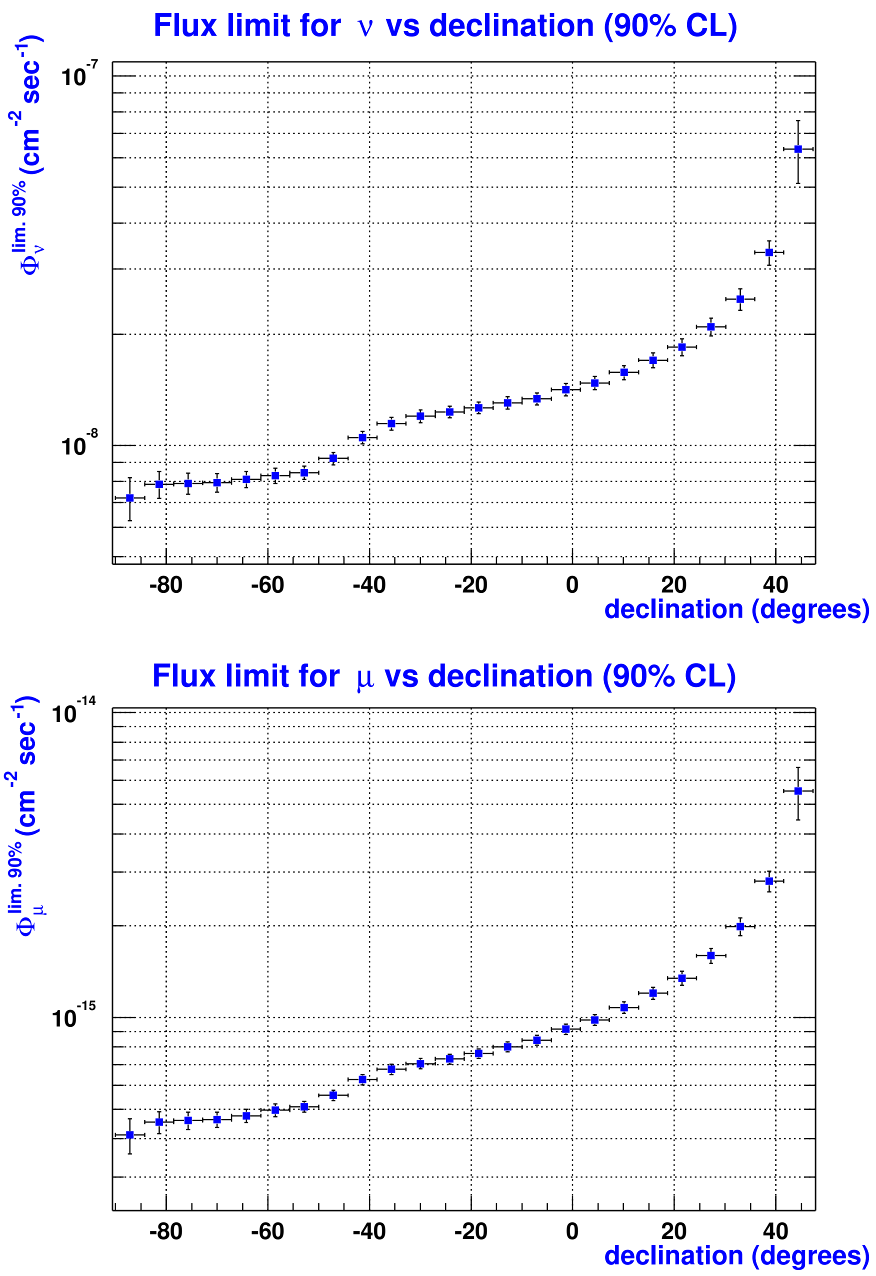

Figure 6.15: All sky flux limits as a function of the declination, assuming a spectral index of 2.0. Upper plot: all sky neutrino flux limit. Lower plot: all sky muon flux limit.

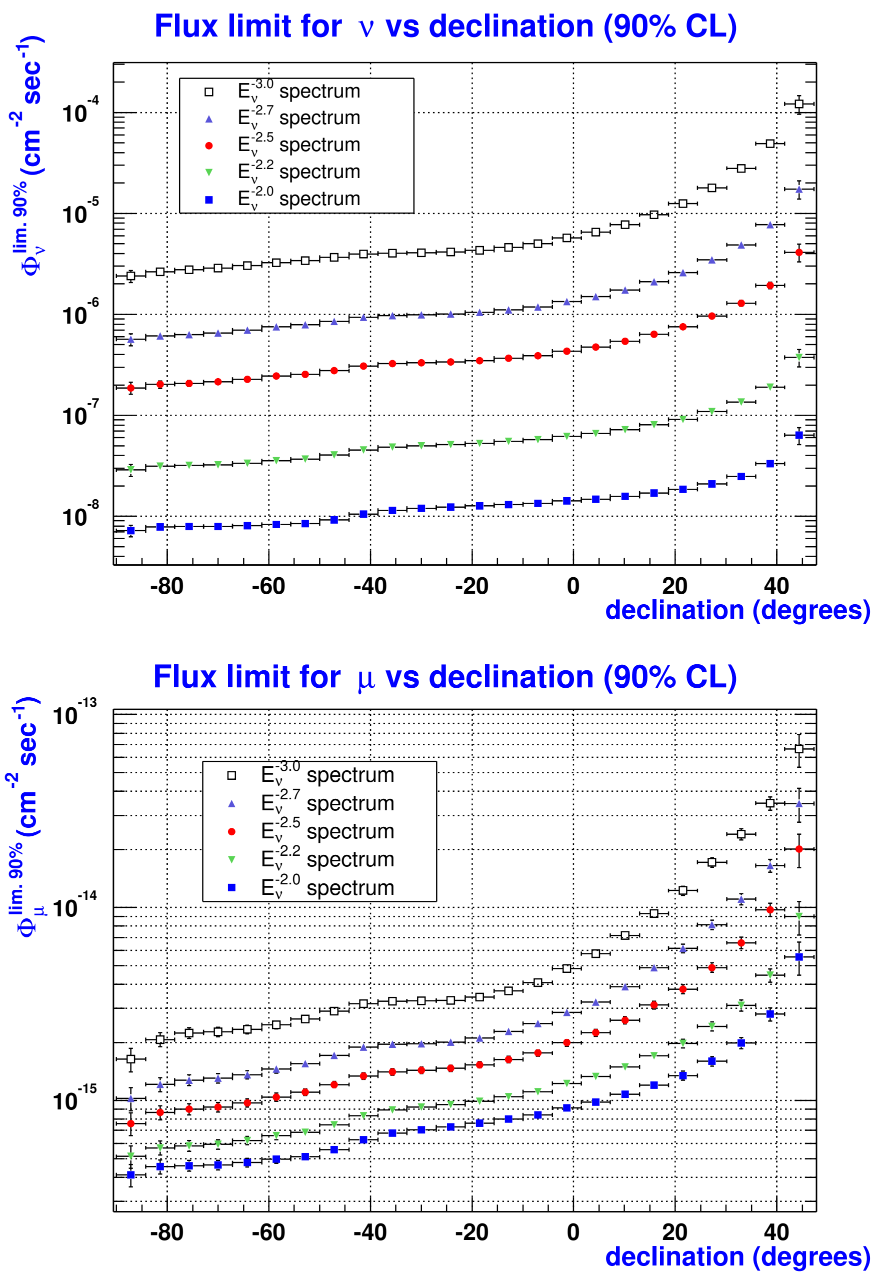

Figure 6.16: All sky flux limits (1 year) as a function of the declination assuming different values of the spectral index between 2.0 and 3.0. Upper plot: all sky neutrino flux limits. Lower plot: all sky muon flux limits.

flux limits after 3 and 5 years of data taking are summarised in figure 6.17.

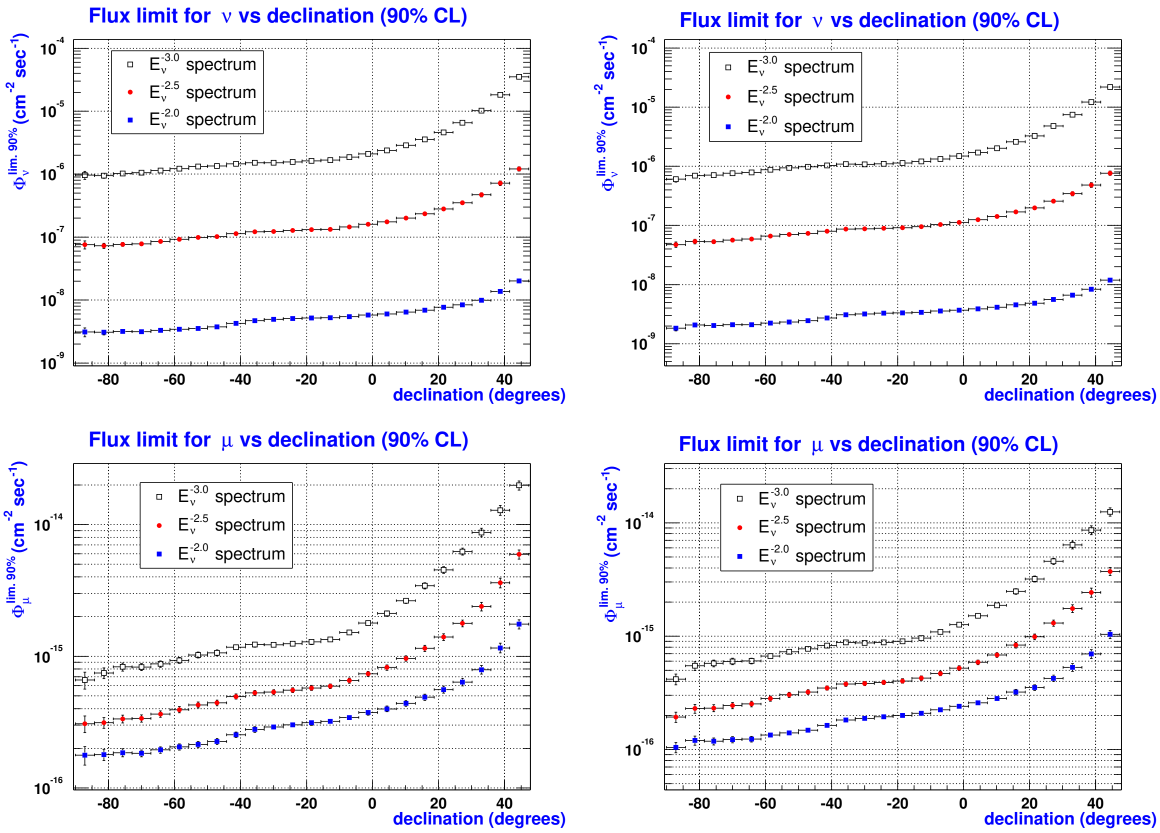

Figure 6.17: Upper plots: neutrino all sky flux limits after 3 (left) and 5 (right) years of data taking. Lower plots: muon all sky flux limits after 3 (left) and 5 (right) years of data taking.

6.4.3 Summary

The previous results show how we can use the grid technique to compute a flux limit for each of the bins in a grid dividing the whole visible sky. They show the average flux limit for each declination. The influence of the spectral index has also been studied. Increasing the value of the spectral index reduces the sensitivity of the flux limits. Finally, the flux limits can be improved by increasing the observation time.

We can compare these results with those obtained by AMANDA [9, 146]. The AMANDA and ANTARES visible skies are complementary, so both experiments can investigate the whole sky with a small region of overlapping for crosscheck. AMANDA uses a similar grid to divide their visible sky and compute a flux limit for each bin. Figure 6.18 shows a comparison of the ANTARES and AMANDA muon flux limits for

$\gamma = 2.0$. The AMANDA-B10 all sky flux limit is represented in the figure with three lines. The line in the middle is the mean flux limit while the other two lines represent the best and worst limits that have been obtained for each declination. A Monte Carlo estimation of the muon flux limit for $\gamma = 2.0$ that can be obtained with the AMANDA II detector after 3 years is also shown in the figure.

The comparison shows that ANTARES all sky flux limits are below AMANDA B-10 average limits at any declination. However, the AMANDA II limits for 3 years are a factor ~ 10 better than the average AMANDA B-10 limit and are similar to the ANTARES limits for 1 year. In fact, in the region where AMANDA and ANTARES overlap, AMANDA II limits can be better than the ANTARES limits. However, ANTARES is able to study a larger range of declinations and its best achievable limit is better than that of AMANDA-II. The latest flux limits obtained with real data (197 days live time) for AMANDA-II are a factor ~ 5 better than the AMANDA B-10 flux limits, which is still better than the expected ANTARES 1 year flux limits in the region where they overlap.

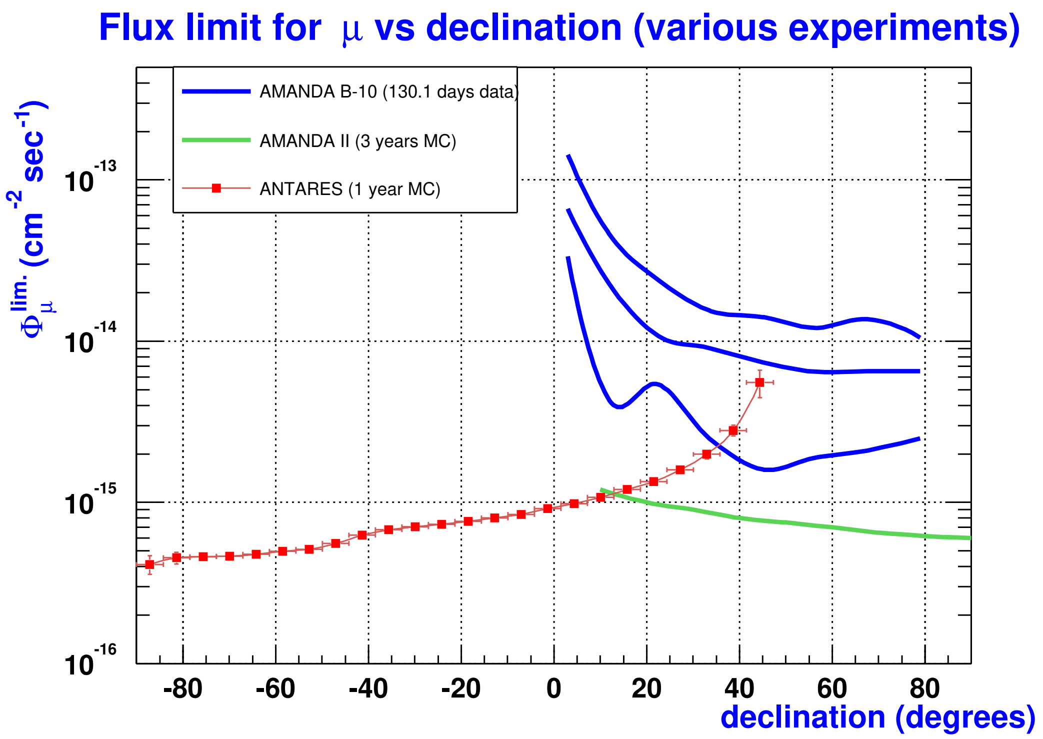

Figure 6.18: All sky flux limit results obtained by the AMANDA B-10 (best, mean and worst limits), and AMANDA II (3 years). Comparison with the Monte Carlo estimate of the ANTARES limits after 1 year. All the results correspond to a spectral index of 2.0.

6.5 Flux limits results for selected sources

The previously computed all sky flux limits apply to the sky region covered by the bin where the flux limit is computed. In this case, we can compute a flux limit to the unknown source or sources that could be located in each bin. Nevertheless, if the position of some luminous neutrino sources were known we could use this information to obtain a better flux limit for that source. The problem is that no observations of high energy astrophysical neutrino sources exist, what makes difficult to select a list of luminous neutrino astrophysical sources. Up to now, the criteria that define the sources with the highest neutrino fluxes are not known, but a great number of theories describe potential astrophysical objects as neutrino sources. For the purpose of this work we have selected the set of candidate sources listed in Appendix B. Most of the sources are known to be high energy gamma emitters and thirteen out of them are known to be TeV gamma rays emitters.

In this section, we present the flux limits results obtained after applying the cluster technique to the proposed neutrino source candidates. Since these results are obtained from Monte Carlo, they must be considered as an estimate of the average result that could be set with the real data obtained by the ANTARES experiment, when they will be available. The results have been obtained using the optimal cone set for a signal with spectral index of 2.0. In this case, the cone set is characterised by a common value of the average background per bin of 0.31, which is equivalent to use an initial cone diameter of 1.2° to build the cones. The optimal cone sets for other spectral indexes are slightly different. However, these differences are so small that they can be neglected (as in the all sky case), and we can use the same cone set for different spectral indexes between 2.0 and 3.0.

For each source candidate, we compute a neutrino flux limit and a muon flux limit. In all cases the limits are computed using the 90% confidence level with the Feldman and Cousins approach.

6.5.1 Results after 1 year of data taking

Figure 6.19 (top) shows the neutrino flux limit obtained for each of the candidate sources assuming three different values of the spectral index (2.0, 2.5 and 3.0). The values obtained correspond to the average flux limit that can be expected after 1 year of data taking for each source. Given a source, the results may change from one particular data sample to another. This is reflected in the figure as the error band that represents one standard deviation of the distribution of flux limits for the source in different data samples.

For each declination, this limit is better than the all sky limit at the same declination. On average, the limits obtained with the cluster technique for a given source with spectral index of 2.0 are a $\sim 22\%$ better than the flux limit obtained with the grid technique for the bin that contains the source. The difference between both techniques increases with the spectral index: the relative improvement of the flux limits obtained with the cluster technique with respect to the grid technique is 27% for $\gamma = 2.5$ and 35% for $\gamma = 3.0$.

In the case of the muon flux limits, the results are shown in figure 6.19 (bottom). The relative improvement with respect to the all sky muon flux limit is the same as in the neutrino case. The average of the distribution of expected flux limits for each source (markers), as well as the standard deviation of the distribution (shadowed area around the points), is shown in the figure for $\gamma = 2.0,\ 2.5$ and 3.0.

6.5.2 Results after several years of data taking

As in the all sky case, the results that can be expected after one year of data taking can be improved if the acquisition time is increased. Figure 6.20 summarises the flux limits for the proposed candidate sources expected for neutrinos and muons after 3 and 5 years of data taking. The improvements with respect to the 1-year results are similar to those in the all sky flux limit case (a factor ~ 2.5 for 3 years and ~ 3.5 for 5 years).

6.5.3 Summary

We have checked that the cluster technique can be applied to the data after a given time period to put a flux limit to certain point-like source candidates. This technique represents a clear improvement ($\sim 22\%$ for $\gamma = 2.0$) with respect to the flux limits that can be established with the grid technique. As a drawback, the limit only applies to a particular candidate source or direction.

We can compare the results obtained with the grid technique after 1 year of data taking with the flux limits established by other experiments. MACRO and Super-Kamiokande are situated at a similar latitude and hence share most of their visible sky with ANTARES. AMANDA, however, is located at the South Pole and there is only a partial overlap of its visible sky with that of ANTARES. Figure 6.21 shows a comparison of the results obtained by MACRO [143], Super-Kamiokande [144] and AMANDA [145, 150] experiments for the muon flux limit of several sources. MACRO data cover the time period from 1989 to September 1999, which represents 6.4 years of data, efficiencies included. Super-Kamiokande data, however, cover a live time of 1138 days. In the case of AMANDA, the live time corresponds to 130 days with the AMANDA B-10 detector. We have included only the flux limits for those 6 sources studied by AMANDA which are also in our list of candidate sources. With AMANDA-II, the live time is 197.0 days.

The flux limits obtained by MACRO exhibit the same behaviour with declination as the ANTARES limits (both sources and all sky). The AMANDA B-10 flux limits for selected sources exhibit the same behaviour as the AMANDA B-10 all sky flux limit. In the case of AMANDA-II the flux limits for selected sources exhibit larger fluctuations. However, the comparison among experiments is not straightforward. Both MACRO and Super-Kamiokande have a lower energy threshold, ~ 1 GeV compared to ~ 10 GeV in ANTARES and AMANDA. Moreover, MACRO flux limits have been computed

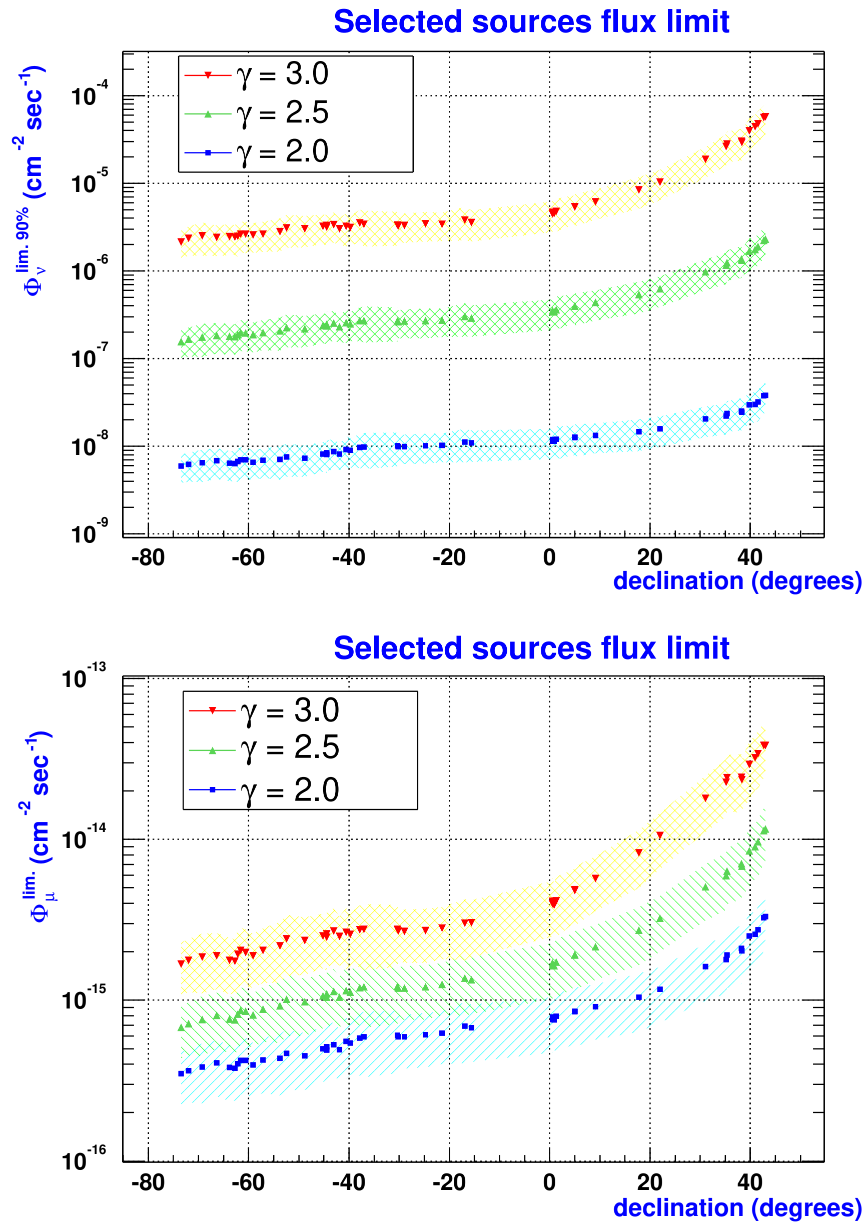

Figure 6.19: Top: Neutrino flux limit (1 year) for each considered candidate neutrino source. Bottom: Muon flux limit (1 year) for each considered candidate neutrino source. In both cases, each marker represents the mean flux limit expected, and the shadowed area represents one standard deviation of the distribution of the flux limits for each candidate.

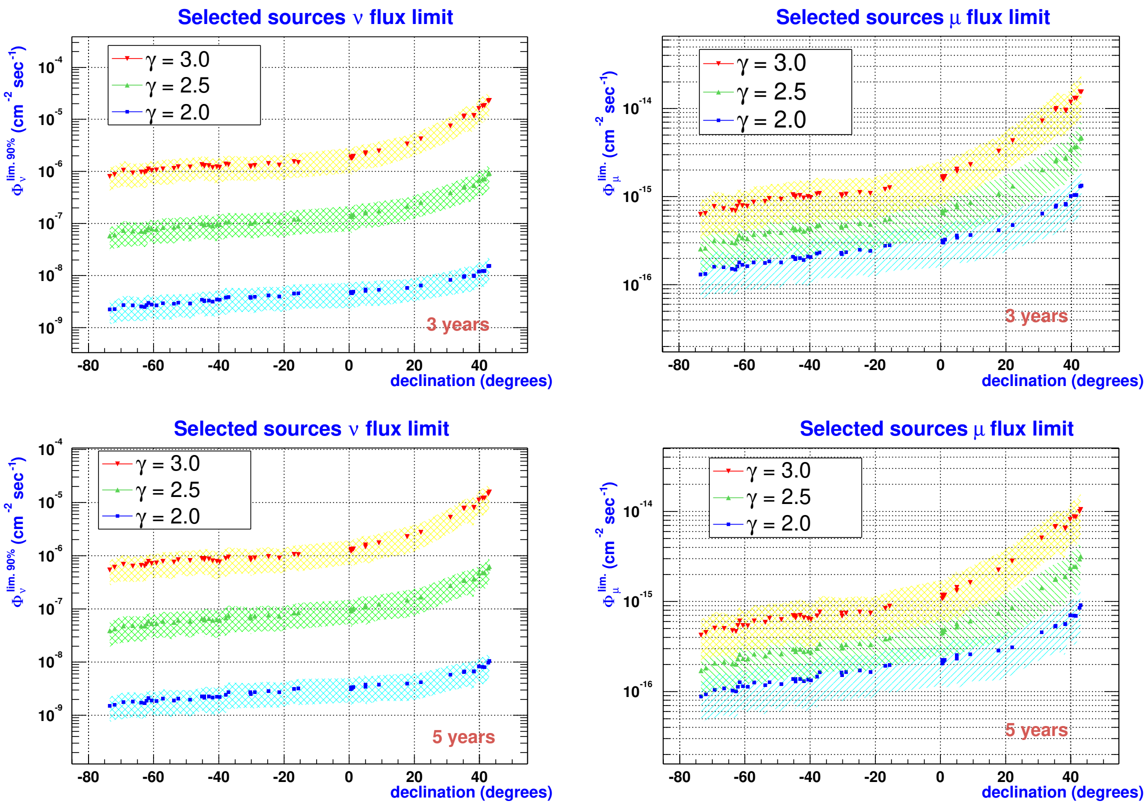

Figure 6.20: Neutrino (left) and muon (right) flux limits for the different neutrino point-like source candidates considered. The results correspond to 3 years (top) and 5 years (bottom) of data taking.

assuming a spectral index of 2.1, whereas in the Super-Kamiokande results the spectral index is not specified. Our results, as well as AMANDA results in figure 6.21, have been computed assuming a spectral index of 2.0. These differences make MACRO results a $\sim$ 10% worse than if they were computed with a threshold of 1 GeV and a spectral index of 2.0. In the case of Super-Kamiokande experiment the difference would be $\sim$ 13% [145]. The estimate of AMANDA and ANTARES limits has been performed using the same parameters, hence their results can be directly compared.

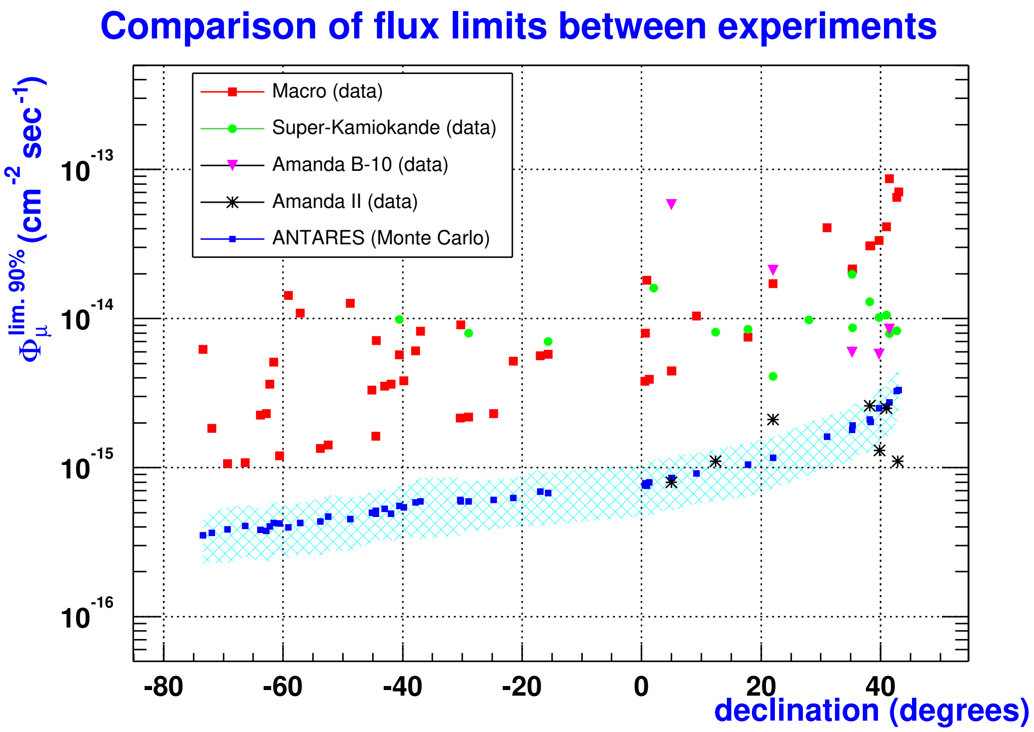

Figure 6.21: Flux limits for various candidate point-like neutrino sources obtained with different experiments. ANTARES, MACRO and Super-Kamiokande cover almost the same sky region. In the case of AMANDA B-10 only 6 of their studied sources, the ones included in our list of candidate sources, are plotted. In the case of AMANDA-II only the 7 sources visible from ANTARES in [150] are plotted.

In figure 6.21 we observe that the limits from ANTARES are the best ones in the range where they can be compared with the other experiments. Even when considering the worst case of the fluctuations expected due to statistics (the shadowed region for ANTARES points represents the one standard deviation of the distribution for each point) the results are better. In the other experiments, these fluctuations produce the vertical spread of the flux limits for sources at the same declination. However, it must be recalled that the data shown in the figure for MACRO, Super-Kamiokande and AMANDA are obtained from real data, whereas in the case of ANTARES they are a

Monte Carlo estimate.

6.6 Point-like discovery flux

Once we have computed the limits that can be set for the flux emitted by point-like sources when no signal is observed, we can consider computing the neutrino/muon flux needed to actually claim the discovery of a point-like neutrino source. This is connected to the results obtained in chapter 5, where we computed the number of events required for a discovery. However, that number was not converted to the corresponding neutrino or muon flux.

The flux limits computed in previous sections represent the maximum signal that can be emitted by a point-like source and be compatible with the observed background. Hence, in the absence of a signal, we can exclude – at 90% confidence level – a flux higher than the limit. In this section, however, we compute the flux that will ensure that a point-like source is discovered. We have some freedom to establish the criteria to claim the discovery. A reasonable requirement is that the background should not produce accidentally a fake source and that real sources should be discovered. To this end, in chapter 5 we used a security threshold of 3σ, i.e. the background has a probability smaller than 1 minus the probability contained in the gaussian distribution between -3σ and $+3\sigma$, for producing the observed number of events, and a discovery probability of 50% i.e. the required number of events guarantees that at least in 50% of the experiments we can discover the point-like source. However, other discovery criteria can be used, provided that they accomplish their goal.

When the limits are properly set, we find three kinds of situations, represented in figure 6.22. Source 1 in the figure, produces a neutrino/muon flux below the computed flux limit in the experiment. In that case, the source is not observable as a point-like neutrino source because the number of detected events (if any) is compatible with the observed background. Source 2, however, emits a neutrino/muon flux that exceeds the flux limit established, but that is not high enough to reach to the discovery flux. This means that the source can be considered as a candidate source but it is not powerful enough to be claimed as a real discovery. Finally, a source that is powerful enough to produce a neutrino/muon flux above the discovery threshold, source 3 in the figure, can be identified as a point-like neutrino source. However, this does not guarantee that a source with a flux above the discovery flux is always discovered, but instead it means that above the discovery flux the source has a probability of being detected which is larger than the criterion we have adopted (typically 50% or 90%) as it was defined in chapter 5.

The search techniques and the flux limit techniques have been individually optimised. This means that, on average, the limits are as low as possible. Besides, the choice of the probability used for flux limits (90%) and the discovery parameters (security threshold and discovery probability) should be made in such a way that the corresponding limits are reasonable. For instance, a discovery flux should not be lower

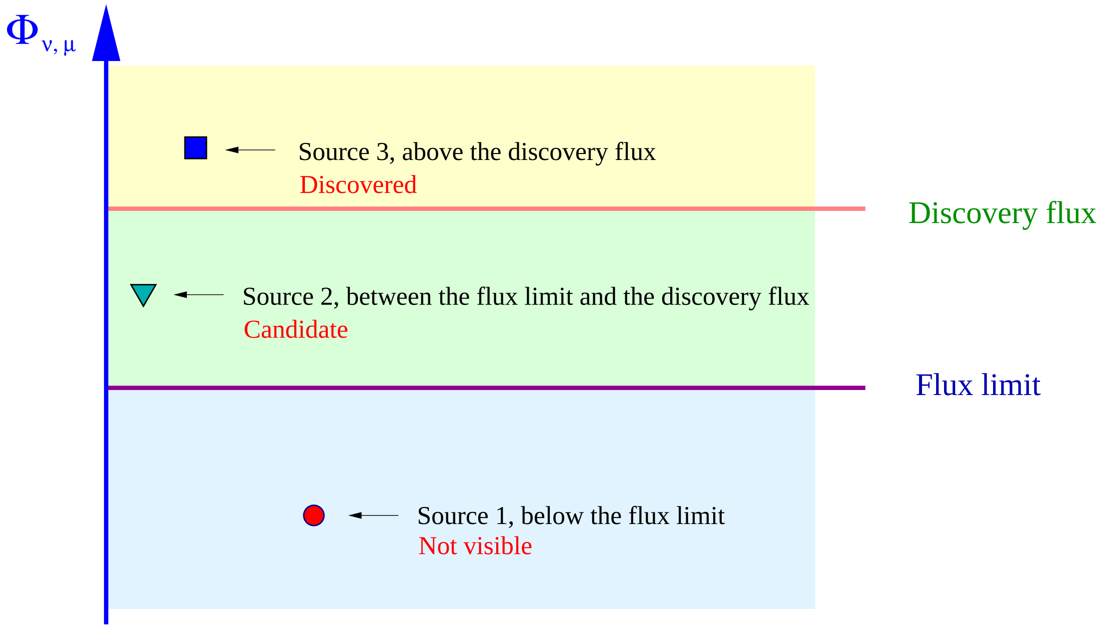

Figure 6.22: A representation of the three possibilities that we can find according to the flux emitted by a neutrino point-like source.

than a flux limit. As we will show in this section, the parameters we have used in this work fulfil this requirement.

We will always find in our data some sources as source 2 in figure 6.22, because the flux limits are computed at 90% confidence level and therefore there will always be a certain fraction of bins or cones above the flux limit, just due to background. If the lower limit (not the upper limit used for previous limits) computed with Feldman and Cousins is different from zero for some of those sources, then this is another slight indication that the source could be a point-like source. However, even this can be produced by background in a certain fraction of cases. Only those sources above the discovery flux can be considered as firm point-like source candidates.

We combine the number of events required for a discovery, computed in the previous chapter, with the averaged effective areas obtained in this chapter to get the discovery neutrino and muon fluxes. This quantity also includes the visibility of the source. Expression 6.3 is used to compute the discovery fluxes for both neutrinos and muons. The only difference is that the upper limit $\mu_s(N_0, N_{bg})$ has been replaced by the number of events needed for discovery.

Figure 6.23 shows the neutrino and muon flux required to find a point-like neutrino source in a data sample covering 1 year of data taking. The upper-left plot corresponds to the results obtained with the grid technique and contains the required neutrino flux in order to ensure a 50% and a 90% probability of finding a bin where the number of events observed is excluded to be a random fluctuation of the background at a level of 3σ and 5σ. In the case of the cluster technique the results are represented in the upper-right plot of figure 6.23. As we showed in chapter 5 the results are very similar for both search techniques. We observe that increasing the probability of success from 50% to 90% with 3σ requires a higher neutrino flux than going from 3σ to 5σ and keeping a probability of success of 50%. In the case of the muon discovery flux, the results are summarised at the bottom of figure 6.23. For neutrino or muon fluxes, the difference between the cluster and grid techniques for discovery is very small.

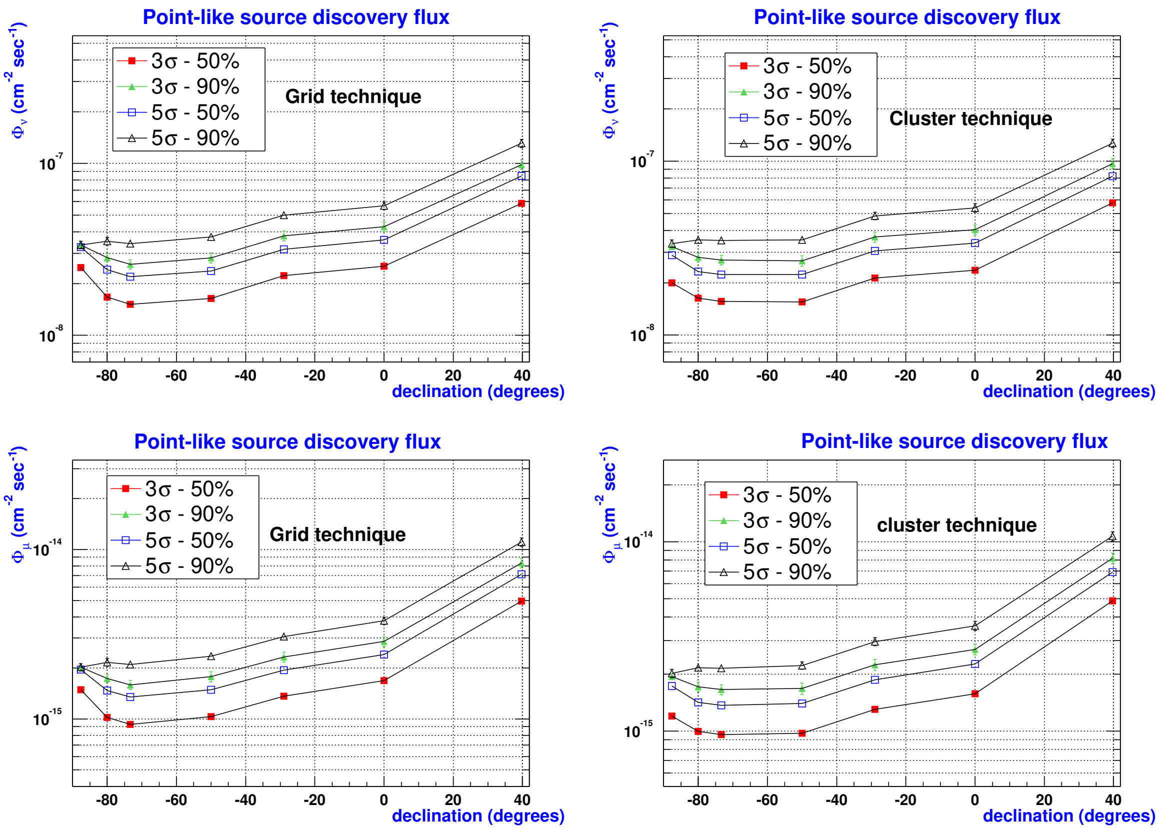

Figure 6.23: Top: Neutrino flux needed to detect a point-like neutrino source with a spectral index of 2 using the grid (left) and cluster (right) techniques. Bottom: Muon flux needed to detect a point-like neutrino source with a spectral index of 2 using the grid (left) and cluster (right) techniques. One year of data taking is assumed.

Increasing the data-taking time improves the results. In this case, the required flux per year needed for a discovery is reduced when the data acquisition time is increased. Figure 6.24 shows the discovery muon flux per year needed to find a point-like source after 3 years and 5 years of data taking.

In both cases (neutrino and muon) and using any of the two search techniques (grid and cluster) the discovery flux exhibits the same behaviour as the previously

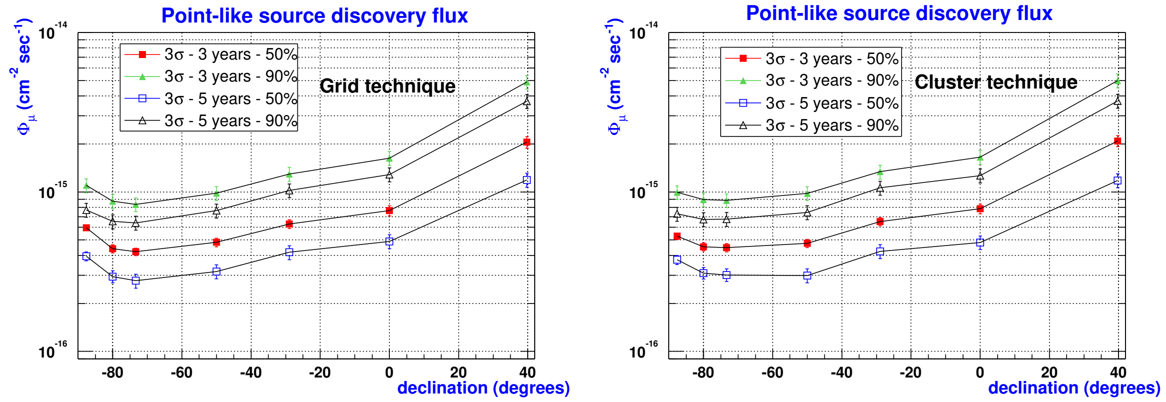

Figure 6.24: Muon flux needed to detect a point-like neutrino source with a spectral index of 2 using the grid and cluster techniques after 3 and 5 years of data taking.

computed flux limits. Moreover the discovery flux is always higher than the flux limit at the same declination, what is consistent with the definition of flux limit and discovery flux. Figure 6.25 shows a comparison between the discovery flux and the flux limits for each technique and for each type of flux.

As can be seen, the flux limits with the grid technique are always a factor ~ 1.8 smaller than the corresponding discovery flux for 3σ (~ 2.5 for 5σ) at the same declination. This result is the same for both neutrino and muon fluxes. For the cluster technique, since the flux limits are better than the grid ones, the specific source flux limits are a factor ~ 2 better than the corresponding discovery flux for 3σ at the same declination and a factor ~ 3 for 5σ. Once more, we observe that the difference between techniques (cluster and grid) is very small for the searches but it is significant when computing flux limits. The flux limit computed with the cluster technique for specific candidate sources is always a **20%** better than the flux limit that can be set with the grid technique at the same declination.

6.7 Diffuse flux limit

In this section we study the diffuse flux limit that can be set with the ANTARES detector. This has been done for comparison with the results obtained for point-like sources. More detailed studies of diffuse flux limits for ANTARES have been performed in [141].

The diffuse flux limit has been computed with the technique used by AMANDA in [151]. The upper limit is set using the number of observed events n_{obs} and the expected background n_{bg}. The flux limit can be computed as:

$$\bar{\Phi}^{\nu}_{lim} = \Phi^{\nu}(E) \times \frac{\mu_s(n_{obs}, n_{bg})}{n_s} \tag{6.5}$$

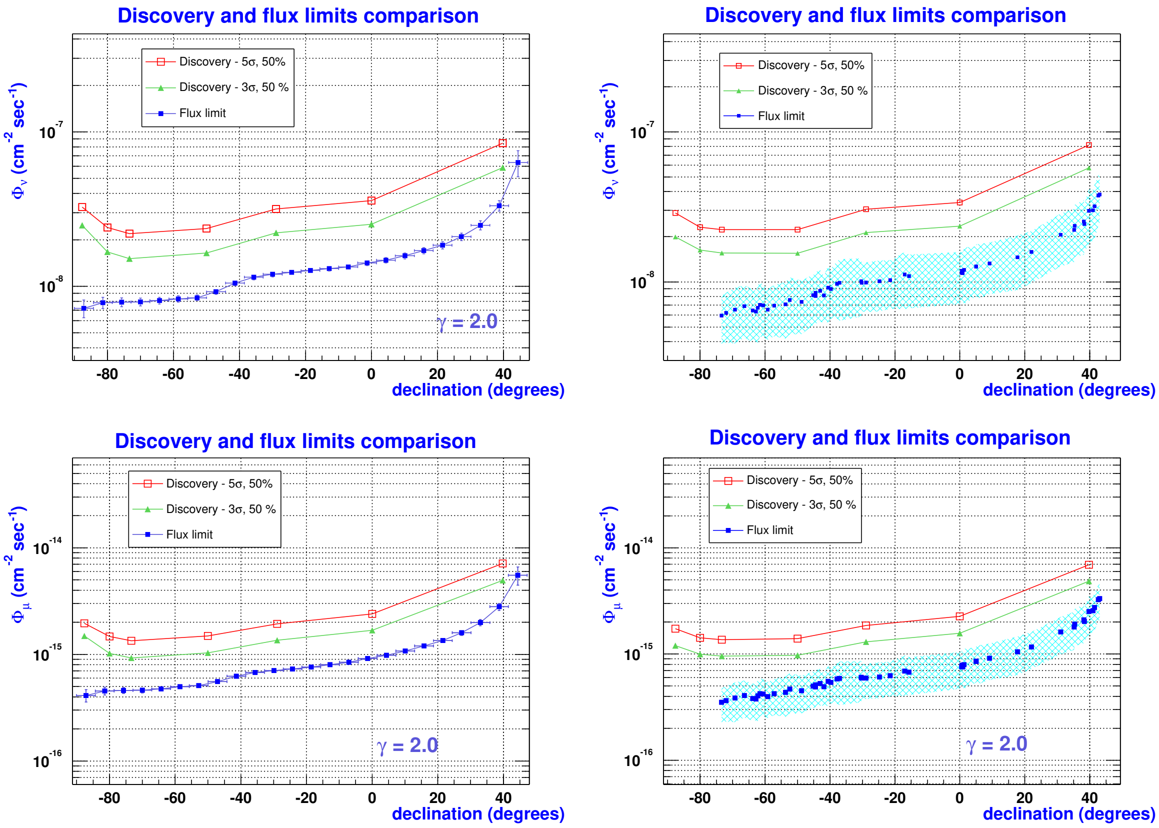

Figure 6.25: Comparison between the discovery limits and the flux limits for 1 year of data taking. Top left: Neutrino limits with the grid technique. Top right: Neutrino limits with the cluster technique. Bottom left: Muon limits with the grid technique. Bottom right: Muon limits with the cluster technique. All limits assume a spectral index of 2.0.

where $\mu_s(n_{obs}, n_{bg})$ is the maximum signal that could be present if the expected background is n_{bg} and n_{obs} the number of observed events. This limit is computed using the upper limit obtained with the Feldman and Cousins unified approach.

The mean expected background is estimated with the Monte Carlo programs using the Bartol model for the atmospheric neutrino flux. The number of signal events (n_s) is also obtained from the Monte Carlo, in this case with a neutrino diffuse flux E^{-2} spectrum. In our case, since no real data are available yet, an *average upper limit* can be computed for an ensemble of experiments. The $\mu_s(n_{obs}, n_{bg})$ for different n_{obs} can be replaced by an average upper limit, where each upper limit is weighted by their probability of occurrence:

$$\bar{\mu}(n_{bg}) = \sum_{n_{obs}=0}^{\infty} \mu_s(n_{obs}, n_{bg}) \cdot \frac{(n_{bg})^{n_{obs}}}{(n_{obs})!} \cdot e^{-n_{bg}} \tag{6.6}$$

which is given by the Poisson distribution with mean n_{bg}. The number of background events, n_{bg}, is computed from the atmospheric neutrino (and anti-neutrino) events simulated with the Bartol model. The confidence intervals have been estimated using Feldman and Cousins.

The atmospheric muon and multi-muon misreconstructed events are not included due to the lack of simulated statistics (we only know the upper limit of the misreconstructed atmospheric events). This makes the upper limit slightly optimistic.

Apart from the selection cuts (described in section 4.2), we have included a new cut on the reconstructed neutrino energy in order to improve the upper limits. When applying this cut, we select only the events with a reconstructed energy above the cut energy. The energy reconstruction algorithm used is the one described in [108, 141]. In figure 6.26 it is shown $E^2\,\bar{\Phi}^{\nu}_{90\%}(E)$ as a function of the cut on the reconstructed neutrino energy.

The optimum flux limit is reached at a cut of 100 TeV on the reconstructed neutrino energy. The flux limit changes smoothly in the range $4.5 \leq log_{10}(E_{\nu}^{rec}) \leq 5.5$. For $log_{10}(E_{\nu}) = 5$ we expect $n_{bg} = 9.2$ giving an average event upper limit ($\bar{\mu}(n_{bg})$) of **6.5** events. The signal (n_s) given by a flux with normalisation $4.5\times10^{-4} cm^{-2}s^{-1}sr^{-1}GeV^{-1}$ (Waxman–Bahcall upper limit) is **3.3** events. This leads to an expected average upper limit:

$$E^2\,\bar{\Phi}^{limit}_{90\%}(E) = 8.8 \times 10^{-8} cm^{-2}s^{-1}sr^{-1}GeV \tag{6.7}$$

This flux limit can be compared with AMANDA B-10 average upper limit of $8.4 \times 10^{-7} cm^{-2}s^{-1}sr^{-1}GeV$ after 130 days of data taking [8]. For AMANDA II data after 197 days of live time, the computed average upper limit is $\sim 2 \times 10^{-7} cm^{-2}s^{-1}sr^{-1}GeV$ [9,10]. ANTARES value is hence notably better but it is an optimistic estimation since neither atmospheric prompt neutrinos nor atmospheric muon background events have been added.

The comparison between the diffuse flux limits and the point-like flux limits shows that for both AMANDA and ANTARES, the diffuse flux limits are roughly a factor

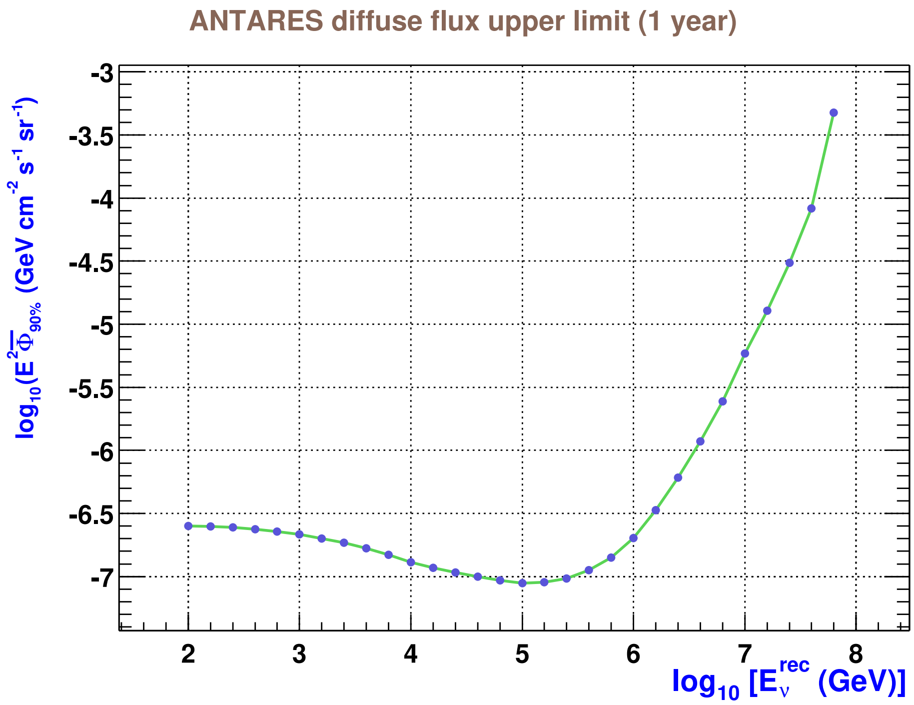

Figure 6.26: Average diffuse upper limit computed for different cuts in the reconstructed energy.

~ 10 worse than the point-like source flux limits. Moreover, the difference in sensitivity between ANTARES and AMANDA flux limits is conserved among the diffuse flux limits and the point-like source flux limits.

Conclusions

After a successful R&D stage, the ANTARES collaboration is currently constructing and deploying a neutrino telescope in the Mediterranean Sea at a depth of 2400 m.

The detector design has been optimised to detect high energy neutrinos from astrophysical sources, but it will also allow the study of neutrino oscillations, annihilation of Dark Matter candidates and the atmospheric neutrino flux. These studies require a high efficiency and precision of the event reconstruction process.

In this work we have studied a new reconstruction strategy to improve the final performances of the detector compared to the standard reconstruction strategy. This strategy has been applied to the search of point-like neutrino sources with the ANTARES detector and the estimate of flux limits in the case where no source is found.

Even though no data will be available until the commissioning and operation of the detector, these studies have been carried out keeping in mind that our primary goal is a straightforward and prompt application to real data of the techniques developed here. In that sense, we have opted for an approach that uses robust techniques whose dependence on the prior, detailed knowledge of the detector performance or additional models or hypotheses is minimised.

New reconstruction strategy

In chapter 3, we presented a new strategy for muon track reconstruction. Whilst the standard technique uses a rather simple estimate of the five muon track parameters, it does not take advantage of the geometrical relation between the muon track, the Cherenkov photons and the hits they produce. On the contrary, the new strategy – called *iterative strategy*– successfully exploits these relations. If the muon direction is known, the remaining track parameters can be extracted from the time information of the produced hits. On this basis, we have developed a technique able to extract by an iterative process all the muon track parameters using the event hits.

Together with the new reconstruction strategy, new selection criteria have been introduced. They are intended to dismiss misreconstructed tracks, and have been chosen to dismiss as much atmospheric muon background (down–going events) as possible, while keeping most of the signal (up–going events). We have checked that our choice of cuts allows the atmospheric muon background to be eliminated and does not bias the results.

The results produced by the *iterative* and the standard reconstruction strategies together with their corresponding selections applied to the Monte Carlo data have been compared. The conclusions are the following:

- The single muon and multi-muon atmospheric background can be reduced using the *iterative strategy* and a set of selection criteria. With the standard reconstruction and standard cuts, however, the atmospheric muon background is so high that it would dominate over the true up–going events. Thus, the standard selection cuts must be tightened.

- The effective areas for muons and neutrinos notably improve when the *iterative* strategy is applied. This effect is especially significant for the highest simulated energies (10^8 GeV). Actually, the increase is higher than **100%** for energies over 100 TeV.

- The angular resolution produced by the *iterative* strategy is also better. While the standard strategy reaches a best value of 0.4° and then worsens as the energy grows over 1 PeV, the new strategy provides an angular resolution that continuously improves as the energy increases, with a best value of 0.15° corresponding to the highest simulated energy.

- When both reconstruction strategies are compared using events from a E^{-2} neutrino flux, the *iterative strategy* provides an increase of **100%** in the number of events. The angular resolution is also improved from 0.49° with the standard strategy to 0.26° with the *iterative strategy.* For the atmospheric neutrino flux, the *iterative strategy* provides an increase of **140%** in the number of events and the angular resolution is improved from 0.64° (standard strategy) to 0.48° (*iterative strategy*).

- The effect of using an incorrect refractive index in the reconstruction has been studied. When the group velocity index is used in the simulation but not in the reconstruction, the effective areas shrink a **30%** for the standard strategy and by a **15%** for the *iterative* one. The angular resolution is more sensitive to this effect. We find that, in any case, the *iterative* strategy is superior, reaching its best angular resolution, namely 0.6°, between 10^3 and 10^4 GeV, against 0.8° for the standard strategy.

- The effect on the performances of diverse light scattering models has also been analysed for the *iterative strategy.* The results show that the more scattering is present, the worse the performances. However, the differences with respect to the reference model are not very important, and even when applied to the worst case, the *iterative* strategy is still superior to the standard strategy with the reference model.

Therefore we conclude that the *iterative* strategy is a valid alternative to the standard reconstruction which allows an improvement of the detector performances and achieves a nearly perfect rejection of the atmospheric background.

Search for point-like neutrino sources

In chapter 5 we investigated the capabilities of the ANTARES detector to search for point-like neutrino sources. We have made use of two binned methods, namely the *grid* and the *cluster* techniques. Both of them have been independently optimised to obtain the grid and the set of cones that produce the best search performances for a source of spectral index 2.

The main results of our analysis, with the optimal grid and cones, are the following:

- The probability of detection of a point-like source at a given confidence level rapidly increases with the number of events emitted by the source. We have determined that the minimum number of events required with these techniques for a discovery (3σ and 50% of success) is between **8.5** ($\delta = -73.4°$) and **5.6** ($\delta = +39.8°$).

- The results for the grid and cluster techniques are very similar. As both of them are optimised, they reach a common limit which does not depend on the technique.

- For a longer period of data-taking the sensitivity improves with both techniques, although the factor of improvement is lower than the increase in time. Increasing the data-taking time from 1 year to 3 years represents a factor **2.3** improvement. For 5 years of data-taking the improvement is a factor **3.3**.

- Besides searching for individual sources, the combined effect of several point-like source candidates has been studied. This analysis shows that a lower number of events is required per source and year, to obtain a significant excess. The total number of events, however, is not smaller. When more candidates are considered, the required number of events per source decreases, but the total required number is higher.

If no point-like neutrino source is observed, the same techniques can be applied to establish a limit for the neutrino or muon fluxes coming from the undetected sources. This analysis yields the following results:

- The optimal bins and cones for limits are larger than those determined for searches. The optimal grid is characterised by an initial bin width of **1.0**° for searches and **2.5**° for flux limits. The optimal cone set is characterised by an initial cone diameter of **0.5**° for searches and **1.2**° for flux limits.

- As the spectral index increases, the reachable limits worsen but the optimal size for the bins and cones remains almost constant. For $\gamma = 2.5$ the S/B ratio is $\sim$**15%** worse and for $\gamma = 3.0$, $\sim$**30%** worse.

- For a given declination, the limit established by the grid technique is always worse than the corresponding limit with the cluster technique.

- In both cases, neutrino and muon flux limits get worse for higher declinations, mainly due to the visibility of the corresponding source from the detector site.

- We have calculated the attainable flux limits for neutrinos and muons with both techniques. We have found that differences among various spectral indexes are more important in the case of neutrinos, and that the limits worsen as the spectral index grows.

- Extending the observation period improves all the reachable limits, but the sensitivity improvement factor is always lower than the increase in time. For 3 years of data-taking the improvement with respect to the results for 1 year is a factor $\sim$**2.5** better. For 5 years of data-taking, the improvement is a factor $\sim$**3.8**.

- From the minimum number of events required to a point-like source to be detected, it is possible to define a discovery flux. The larger the declination, the higher the required flux for a discovery to take place. For a given value of δ, we find that discovery fluxes are always higher, i.e. worse, than the corresponding flux limits.

- Finally, we have also computed a limit on diffuse fluxes. This limit is $E^2\,\bar{\Phi}^{limit}_{90\%}(E) = 8.8 \times 10^{-8} cm^{-2} s^{-1} sr^{-1} GeV$. Such limit has been found to be $\sim$ 10 times higher, i.e. worse, than the corresponding flux limit for specific point-like sources with spectral index 2.

Bibliography

[1] K. S. Hirata et al. Observation of B-8 solar neutrino in the Kamiokande-II detector. *Phys. Rev. Lett.*, 63:16, 1989.

[2] K. S. Hirata et al. *Phys. Rev. Lett.*, 58:1490, 1987.

[3] K. S. Hirata et al. *Phys. Rev.*, D38:448, 1988.

[4] R. M. Bionta et al. *Phys. Rev. Lett.*, 58:1494, 1987.

[5] A. M. Markov. In *Proceedings of the Rochester Conference*, New York, 1960.

[6] E. Waxman and J. Bahcall. High energy neutrinos from astrophysical sources: an upper bound. *Phys. Rev.*, D59:023002, 1999.

[7] G. J. Feldman and R. D. Cousins. Unified approach to the classical statistical analysis of small signal. *Phys. Rev.*, D57:3873, 1998.

[8] J. Ahrens et al. Search for point sources of high energy neutrinos with amanda. *Phys.Rev.Lett.*, 2003.

[9] Paolo Desiati et al. Neutrino astronomy at the south pole: Status of the amanda experiment. In *Proceedings of the Les Rencontres de Physique de la Vallee d'Aoste*, La Thuile (AO), Italy, March 2003.

[10] J. Ahrens et al. Search for extraterrestrial point sources of neutrinos with amanda-ii. *astro-ph/0309585*, 2003.

[11] J. Chadwick. *Nature*, 129:312, 1932.

[12] E. Fermi. *Z. Physik*, 88:161, 1934.

[13] C. L. Cowan et al. *Phys. Rev.*, 90:492, 1953.

[14] C. L. Cowan et al. *Science*, 124:103, 1956.

[15] L. Lederman, M. Schwartz, and J. Steinberger. *Phys. Rev. Lett.*, 9:36, 1962.

[16] K. Kodama et al. Donut Collaboration. *Phys. Lett.*, B504:218, 2001.

[17] K. Hagiwara et al. (Particle Data Group). *Phys. Rev.*, D66:010001, 2002.

[18] The Super-Kamiokande Collaboration. *Nucl. Phys. B (Proc. Suppl.)*, 91:127, 2001.

[19] Y. Fukuda et al. *Phys. Lett.*, B467:185, 1999.

[20] The SNO Collaboration. *Phys. Rev. Lett.*, 87:071301, 2001.

[21] The SNO Collaboration. *Phys. Rev. Lett.*, 89:011301, 2002.

[22] K. Eguchi. *Phys. Rev. Lett.*, 90:021802, 2003.

[23] J. N. Bahcall. *Phys. Rev. Lett.*, 12:300, 1964.

[24] R. Davis. *Phys. Rev. Lett.*, 12:303–305, 1964.

[25] R. Davis, D. S. Harmer, and K.C. Hoffman. Search for neutrinos from the sun. *Phys. Rev. Lett.*, 20:1205–1209, 1968.

[26] B. T. Cleveland et al. *Astrophys. J.*, 496:505, 1998.

[27] Y. Fukuda et al. *Phys. Rev. Lett.*, 81:1562, 1998.

[28] R. J. Wilkes et al. In *Proceedings of teh Int. Symp. UHE Cosmic Ray Interactions*, 1992.

[29] H. Hanada et al. *Nucl. Instrum. Methods A*, 408A:2,3,425, 1998.

[30] K. Greisen. *Phys. Rev. Lett.*, 16:748, 1966.

[31] G. Zatsepin and V. A. Kuzmin. *JETP Lett.*, 4:78, 1966.

[32] V. F. Hess. *Phys. Zeitschr.*, 13:1084, 1913.

[33] P. Bhattacharjee and G. Sigl. Origin and propagation of extremely high-energy cosmic rays. *Phys. Rep.*, 327:109, 2000.

[34] K. H. Kampert et al. Recent results from the kascade air shower experiment. 1998. astro-ph/9902113.

[35] F. Arqueros et al. Energy spectrum and chemical composition of cosmic rays between 0.3-PeV and 10-PeV determined from the Cherenkov-light and charged-particle distributions in air showers. *Astron. Astrophys.*, 359:682, 2000.

[36] K. Boothby et al. *Astrophys. J.*, 491:L35, 1997.

[37] V. L. Ginzburg (ed.), V. A. Dogiel, V. S. Berezinsky, S. V. Bulanov, and V. S. Ptuskin. *Astrophysics of cosmic rays.* North-Holland, Amsterdam, Netherlands, 1990.

[38] T. K. Gaisser. *Cosmic Rays and Particle Physics*. Cambridge University Press, Cambridge, England, 1990.

[39] R. D. Blanford and D. Eichler. *Phys. Rep.*, 154:1, 1987.

[40] C. E. Fichtel and J. I. Trombka. Gamma-ray astrophysics: New insight into the universe. Technical report, 1997. NASA-RP-1386.

[41] R. A. Ong. *Phys. Rep.*, 305:93, 1998.

[42] C. M. Hoffman, C. Sinnis, P. Fleury, and M. Punch. *Rev. Mod. Phys.*, 71:897, 1999.

[43] F. A. Aharonian. *Astropart. Phys.*, 11:225, 1999.

[44] R. C. Hartman et al. *Ap. J.*, 123:79, 1999.

[45] http://lheawww.gsfc.nasa.gov/docs/gamcosray/egret/egret.html.

[46] T. C. Weekes et al. *Ap. J.*, 342:379, 1989.

[47] Trevor C. Weekes. VHE astronomy before the new millenium. Published in "Snowbird 1999, Towards a major atmospheric Cherenkov detector" 3-15.

[48] LV. Volkova. *Sov. J. Nucl. Phys*, 31:784, 1980.

[49] M. Agglietta et al. *Phys. Rev. D*, 58:92005, 1998.

[50] G. Ingelman and M. Thunman. High Energy Neutrino Production by Cosmic Ray Interactions in the Sun. *Phys. Rev.*, D54:4385, 1996.

[51] M. Samorski and W. Stamm. *Ap. J. Lett.*, 268(L17), 1983.

[52] J. Lloyd-Evans et al. *Nature*, 305:784, 1983.

[53] V. S. Berezinsky and O. F. Prilutsky. *Astron. and Astrophys.*, 66:325, 1978.

[54] E. Waxman and A. Loeb. *Phys. Rev. Lett.*, 87:071101, 2001.

[55] T. K. Gassier et al. *Ap. J.*, 492:219, 1998.

[56] T. K. Gassier et al. *Phys. Rep.*, 1990.

[57] T. K. Gaisser, F. Halzen, and T. Stanev. Particle astrophysics with high energy neutrinos. *Phys. Rept. 258*, 258:173, 1995. Erratum-ibid. 271 (1996) 355-356.

[58] F. Halzen and E. Zas. Neutrino fluxes from active galaxies: A model independent estimate. *Astrophys. J.*, 488:669, 1997.

[59] R. Gandhi. *Nucl. Phys. B (Proc. Suppl.)*, 91:453, 2000.

[60] J. G. Learned and K. Manheim. High energy neutrino astrophysics. *Ann. Rev. Nucl. Part. Sci.*, 50:679, 2000.

[61] F. Aharonian (HEGRA Collaboration). *Astron. Astrophys.*, 349:11, 1999.

[62] F. Piron (CAT collaboration). Observations of the gamma-ray emission above 250 gev from the blazars markarian 501 and markarian 421 by the CAT cherenkov atmospheric imaging telescope. In *Proceedings of the XIth rencontres de Blois*, 1999.

[63] J. Holder (CELESTE collaboration). Observations of Mkn 421 with the celeste experiment. *AIP Conf.Proc.*, 558:635, 2001.

[64] P. Meszárós and M. J. Rees. *Ap. J.*, 482:L29, 1997.

[65] E. Waxman and J. Bahcall. *Phys. Rev. Lett.*, 78:2292, 1997.

[66] M. Vietri. *Phys. Rev. Lett.*, 80:3690, 1998.

[67] A. Dar and A. de Rújula. The cannonball model of gamma ray bursts: high-energy neutrinos and γ-rays. astro-ph/0105094.

[68] G. Jungman, M. Kamionkowski, and K. Griest. *Phys. Rept.*, 267:195, 1996.

[69] M. Kamionkowski. *Phys. Rev.*, D44:3021, 1991.

[70] A. Bottino et al. *Astrop. Phys.*, 3:65, 1995.

[71] V. Berezinsky et al. *Astropart. Phys.*, 5:333, 1996.

[72] P. Gondolo and J. Silk. *Nucl. Phys. B Proc. Suppl.*, 87:87, 2000.

[73] J. D. Jackson. *Classical Electrodynamics.* J. Wiley and Sons, New York, third edition, 1998.

[74] I. Frank and I. Tamm. *Dokl. Akad. Nauk.*, SSSR14:109, 1937.

[75] Ch. Spiering. High energy neutrino astronomy: The experimental road. In *Proceedings of the 18th ECRC*, Moscow, 2002. astro-ph/0303068.

[76] The Dumand Collaboration. Proposal to construct a 148000 m^2sr deep ocean lab for the study of high energy neutrino astrophysics and particle physics. Technical report, University of Hawaii, 1988. HCD-2-88.

[77] The Baikal Collaboration. *Nucl. Phys. B (Proc. Suppl.)*, 91:438, 2000.

[78] M. P. Kowalski. Results from the Baikal neutrino telescope. In *Proceedings of the 28th International Cosmic Ray Conference*, volume 3, pages 1353–1356, Tsukuba, Japan, 2003. Universal Academic Press. ISBN 4-946443-80-0.

[79] The AMANDA Collaboration. *Nucl. Phys. B (Proc. Suppl.)*, 91:423, 2000.

[80] M. P. Kowalski and A. Karle et al. AMANDA contributions to the 28th ICRC. In *Proceedings of the 28th International Cosmic Ray Conference*, volume 3, pages 1301–1325, Tsukuba, 2003. Universal Academic Press. ISBN 4-946443-80-0.

[81] The IceCube Collaboration. IceCube: A kilometer scale neutrino observatory. NSF Proposal, 2001. http://pheno.physics.wisc.edu/IceCube/proposal.html.

[82] S. Yoshida. The IceCube high energy neutrino telescope. In *Proceedings of the 28th International Cosmic Ray Conference*, volume 3, pages 1369–1373, Tsukuba, 2003. Universal Academic Press. ISBN 4-946443-80-0.

[83] A. Capone. Site characterisation for a km^3 scale deep underwater astrophysical neutrino observatory in the Mediterranean Sea. In *Proceedings of the 26th International Cosmic Ray Conference.*

[84] The NESTOR Collaboration. *Nucl. Phys. B (Proc. Suppl.)*, 85:153, 2000.

[85] P. K. F. Grieder. Nestor neutrino telescope status report. In *Proceedings of the 28th International Cosmic Ray Conference*, volume 3, page 1377, Tsukuba, Japan, 2003. Universal Academic Press. ISBN 4-946443-80-0.

[86] The ANTARES Collaboration. Background light in potential sites for the ANTARES undersea neutrino telescope. *Astropart. Phys.*, 13:127, 2000.

[87] N. Palanque-Delabrouille. Blue and UV transmission in the ANTARES site (Analysis of Test 3'data). ANTARES Internal Note, 2001. ANTARES-site/2001-002.

[88] P. Amram et al. Sedimentation and fouling of optical surfaces at the ANTARES site. *Astropart. Phys.*, 19:253, 2003.

[89] The ANTARES Collaboration. Technical Design Report. Technical report. http://antares.in2p3.fr.

[90] P. Amram et al. The ANTARES optical module. *Nucl. Instr. and Methods*, A484:369, 2002.

[91] D. Lachartre. ARS1 Analogue Ring Sampler and ARS CONV Users Manual version 1.9. ANTARES Internal Note. ANTARES-Electronics/2000-006.

[92] D. Lachartre. ARS simulation: integration and WF. ANTARES Internal Note. ANTARES-Electronics/2000-008.

[93] J. J. Hernández-Rey. Timing callibration of the antares neutrino telescope. In *Proceedings of the 28th International Cosmic Ray Conference*, volume 3, pages 1537–1540, Tsukuba, Japan, 2003. Universal Academic Press. ISBN 4-946443-80-0.

[94] T. Montaruli. ANTARES Status Report. In *Proceedings of the 28th International Cosmic Ray Conference*, volume 3, pages 1357–1360, Tsukuba, Japan, 2003. Universal Academic Press. ISBN 4-946443-80-0.

[95] F. Cassol. GENDET 1.0: a program to generate detector files. ANTARES Internal Note. ANTARES-Soft/1999-007.

[96] F. Cassol Brunner. GENDET 1.2: Cards and tags. ANTARES Internal Note. ANTARES-Soft/2000-8.

[97] Extension of Genneu v3r0 event generator for high energy neutrino interactions with muon propagation to the detector. ANTARES internal note. ANTARES-Soft/2000-005.

[98] David J.L. Bailey. Genhen v3r1 : Further optimisation for large energy ranges. ANTARES Internal Note. ANTARES-Soft/2000-6.

[99] D. J. L. Bailey. Genhen v5r1: Software documentation. ANTARES internal note. ANTARES-Software/2002-004.

[100] A. Kouchner. GEMINI v0r0 GEnerator of Muons Induced by Neutrino Interactions. ANTARES Internal Note. ANTARES-Soft/2000-4.

[101] E. Scapparone. HEMAS: a Monte Carlo code for hadronic, electromagnetic and TeV muon components in air shower. In *Proceedings of the International Workshop on Simulation and analysis methods for large neutrino detectors, Desy Zeuthen (1998)*, pages 238–246. (physics/9902043).

[102] P. Antonioli, C. Ghetti, E. V. Korolkova, V. A. Kudryavtsev, and G. Sartorelli. A three-dimensional code for muon propagation through the rock: Music. *Astropart. Phys.*, 7:357–368, 1997.

[103] P. Lipari and T. Stanev. Propagation of multi TeV muons. *Phys. Rev.*, D44:3543, 1991.

[104] I.A. Sokalski, E.V. Bugaev, and S.I. Klimushin. MUM: flexible precise Monte Carlo algorithm for muon propagation through thick layers of matter. *Phys. Rev.*, D64:074015, 2001.

[105] D. Bailey. Km3 v2r1 : User guide. ANTARES Internal Note. ANTARES-Soft/2002-006.

[106] J. Brunner. GEASIM: User manual. ANTARES Internal documentation. http://antares.in2p3.fr/internal/software/geasim.html.

[107] S. Navas. A comparison between GEASIM and KM3 generators. ANTARES Internal Note. ANTARES-Soft/1999-002.

[108] A. Romeyer, J. D. Zornoza, and R. Bruijn. In *Proceedings of the 28th International Cosmic Ray Conference*, volume 3, pages 1329–1332, Tsukuba, Japan, 2003. Universal Academic Press. ISBN 4-946443-80-0.

[109] GEANT. Detector description and simulation tool. CERN program library.

[110] R. Brun and F. Rademakers. ROOT - An Object Oriented Data Analysis Framework. *Nucl. Inst. & Meth. in Phys. Res.*, A389:81, 1997. See also http://root.cern.ch/.

[111] F. Cassol. Reconstruction re-organisation: RECO version 2.0. ANTARES internal note. ANTARES-Soft/1999-004.

[112] F. Cassol. RECO version 2.1: code and scripts. ANTARES internal note. ANTARES-Soft/1999-005.

[113] A. Romeyer and Th. Stolarczyk. Reconstruction algorithms: a handbook for developers. ANTARES internal note. ANTARES-Soft/2001-001.

[114] E. Carmona and J. J. Hernández. A new reconstruction technique for ANTARES. ANTARES internal note. ANTARES-Soft/2000-11.

[115] E. Carmona. Update of the new pre-fit for reconstruction. ANTARES internal note. ANTARES-Soft/2001-006.

[116] A. Heijboer. An algorithm for track reconstruction in ANTARES. ANTARES internal note. ANTARES-Phys/2002-002.

[117] V. J. Stenger. Track fitting for the Dumand Octogon. *HDC-1-90*, 1990.

[118] M. Bouwhuis, 2003. Oral Communication.

[119] J. Carr and A. Pohl. Another new trigger for ANTARES. ANTARES internal note. ANTARES-Elec/1999-003.

[120] F. Hubaut. *Optimisation et caractérisation des performances d'un télescope sous-marin a neutrinos pour le projet ANTARES.* PhD thesis, CPPM - Marseille, 1999.

[121] A. Oppelt. *Etude de la résolution angulaire du télescope à neutrino ANTARES.* PhD thesis, Université de la Méditerranée, Marseille, 2001.

[122] C. Carloganu. *Caractérisation des performances à basse énergie du futur télescope sous-marin à neutrinos ANTARES et leur application à l'étude des oscillations des neutrinos atmosphériques.* PhD thesis, CPPM, Marseille, 1999.

[123] F. Bernard. *Caractérisation des performances d'un télescope sous-marin à neutrinos pour la détection de cascades contenues dans le cadre du projet ANTARES.* PhD thesis, Université de la Méditerranée, Aix-Marseille II, Marseille, France, 2000.

[124] A. Kouchner. *Possibilité d'observation, par le télescope ANTARES, de neutrinos de haute énergie associés aux sursauts gamma et validation des techniques de détection à l'aide dun prototype.* PhD thesis, Université de Paris 7, Paris, France, 2001.

[125] A. Okada. *Astrop. Phys.*, 2:393, 1994.

[126] A. Kouchner and L. Moscoso. A generator of muon fluxes: GEM (GEnerator of Muons) v1_0. ANTARES internal note. ANTARES-Soft/1999-001.

[127] A. Kouchner. Up-date of GEM (GEnerator of Muons). ANTARES internal note. ANTARES-Soft/1999-006.

[128] D. J. L. Bailey. *Monte Carlo tools and analysis methods for understanding the ANTARES experiment and predicting its sensitivity to Dark Matter.* PhD thesis, University of Oxford, United Kingdom, 2002.

[129] W. H. Schuster. Water optical properties at the ANTARES site: Absence of degeneracy in the scattering parameters. ANTARES Internal Note. ANTARES-site/2003-002.

[130] W. H. Schuster. *Measurement of the Optical Properties of the Deep Mediterranean -the ANTARES Detector Medium.* PhD thesis, University of Oxford, 2002.

[131] L. A. Kuzmichev. On the velocity of light signals in the deep underwater neutrino experiments. *Nucl. Instrum. Meth.*, A482:304, 2002.

[132] W. H. Schuster. Alternative analysis methods of ANTARES light propagation in the UV (Test 3'). ANTARES Internal Note. ANTARES-site/2001-004.

[133] C. D. Mobley. *Appl. Optics*, 32:7484, 1993.

[134] L. Henyey and J. Greenstein. Diffuse radiation in the galaxy. *Astrophys. J.*, 93:70, 1941.

[135] J. Brunner. Updated tag list for the new antares event format. ANTARES internal note. ANTARES-Soft/1999-003.

[136] S. Navas and L. Thompson. KM3: User guide and reference manual. ANTARES Internal Note, 1999. ANTARES-Software/1999-011.

[137] Vivek Agrawal, T. K. Gaisser, Paolo Lipari, and Todor Stanev. Atmospheric neutrino flux above 1 gev. *Phys. Rev.*, D53:1314, 1996.

[138] A. Kouchner. ANTARES private communication.

[139] C. Hettlage and K. Mannheim. High energy neutrino fluxes from cosmic accelerators. In *Proceedings of the 21st Rencontres de Moriond Workshop on Very High Energy Phenomena in the Universe*, 2001. astro-ph/0103499.

[140] W. Rhode et al. Limits on the flux of very high-energetic neutrinos with the Frejus detector. *Astropart. Phys.*, 4:217, 1996.

[141] A. Romeyer. *Étude de la sensibilité du détecteur ANTARES à un flux diffus de neutrinos cosmiques de haute énergie.* PhD thesis, Université Denis Diderot - Paris VII, 2003.

[142] C. G. S. Costa. *Astropart. Phys.*, 16:193, 2001.

[143] M. Ambrosio et al. Neutrino Astronomy with the MACRO Detector. *Astrophys. J.*, 546:1038, 2001.

[144] The Super-Kamiokande Collaboration. A search for Astronomical Neutrino Sources with the Super-Kamiokande Detector. In *Proceedings of the 27th International Cosmic Ray Conference*, page 1065, 2001.

[145] A. Biron. *Search for Atmospheric Muon–Neutrinos and Extraterrestric Neutrino Point Sources in the 1997 AMANDA-B10 Data.* PhD thesis, University of Berlin, 2002.

[146] J. Ahrens, X. Bai, G. Barouch, and S.W. Barwick et al. Search for point sources of high energy neutrinos with amanda. *Astrophys.J.*, 2003.

[147] D. Bailey. Calculating effective areas for neutrinos. ANTARES Internal Note. ANTARES-Phys/2001-011.

[148] D. Bailey. Calculation of effective muon ranges and application to overall effective areas. ANTARES Internal Note. ANTARES-Phys/2001-007.

[149] S. M. Young. *A Search for Point Sources of High Energy Neutrinos with the AMANDA-B10 Neutrino Telescope.* PhD thesis, University of California, Irvine, 2001.

[150] T. Hauschildt and D. Steele. Search for Extraterrestrial Point Sources of Neutrinos with AMANDA-II. In *Proceedings of the 28th International Cosmic Ray Conference*, volume 3, pages 1305–1308, Tsukuba, 2003. Universal Academic Press. ISBN 4-946443-80-0.

[151] Gary C. Hill and Katherine Rawlins. Unbiased cut selection for optimal upper limits in neutrino detectors: the model rejection potential technique. *Astropart.Phys.*, 19:393–402, 2003.

Appendix A

Parameters used for Monte Carlo and reconstruction

This appendix contains the parameters used in the simulation and the reconstruction programs in most of the results in chapters 4, 5 and 6. The generation-simulation-reconstruction chain used was the following:

- **Generation:** The event generator used to generate the neutrino interactions was GENNEU. The parameters used in the generation are listed in table A.1, the parameters not listed in the table are used with their default values.

- **Simulation:** The event simulator used was KM3 because includes the scattering of the photons, however, in order to add the hadronic cascade to the simulated events, we used KM3 combined with GEASIM. Table A.2 contains the parameters used with the KM3 program and table A.3 the parameters used with GEASIM.

- **Reconstruction:** For reconstruction we use the RECO program and the CarmonaStrategy (in this work *iterative strategy*). The parameters used in reconstruction are listed in table A.4, the *iterative strategy* does not require any additional parameter to work.

The detector used is the 12-strings detector with 900 PMTs as described in the text. However, sometimes, when mentioned, the detector geometry corresponds to the old 10-strings detector with 900 PMTs (30 PMTs per string).

Parameter	**Value**
Version	v5r1
Can radius	260 m
E_{min}	10 GeV
E_{max}	10^8 GeV
cos θ_{min}	0
cos θ_{max}	1
Spectral index	1.4
Events per file	10^{10}

Table A.1: Parameters used for event generation with GENNEU.

Parameter	**Value**
Version	v2r0
^{40}K rate	$0^{(1)}$ Hz
^{40}K window	500 ns
PMT hit merging	1
Water model	partic-0.0075$^{(2)}$
Number of ARS	2
ARS integration time	25 ns
ARS dead time	250 ns
INGRP	2

Table A.2: Parameters used for event simulation with KM3.

(1) 0 Hz when used in combination with GEASIM, 60 kHz otherwise.
(2) Reference scattering model and default choice.

Parameter	**Value**
Version	v4r8
^{40}K rate	60 kHz
^{40}K window	500 ns
PMT hit merging	1
ARS integration time	25 ns
ARS dead time	250 ns
Buffer time termination	60 sec
AUTO	1
DRAY	1
LOSS	1
HADR	1
MUNU	1
CUTS	0.5 0.5 0.05 0.05 0.05 0.5 0.5 0.5 0.5 0.5
SHOT	0.5 0.1
ERAN	10^{-5} 10^{7} 120
DEBU	1 10000 1000
GAIN	2

Table A.3: Parameters used for event simulation with GEASIM.

Parameter	**Value**
Version	v4r3
Strategy	CarmonaStrategy$^{(1)}$
Energy Estimator	J.D. Zornoza
Reco type	only 3D
Min zenith	-1
Max zenith	+1
PE type	1 (hit_raw)
PE Threshold	0.3
Trigger 3D	6 5 2 2 0
maxStrings	100

Table A.4: Parameters used for reconstruction with RECO.

(3) When using the standard strategy: OldRecoStrategy.

Appendix B

Candidate point-like sources

The following table contains a list of astronomical objects, visible from ANTARES, that are known to be gamma emitters and are considered candidates for point-like neutrino sources.

The sources that are known to emit gamma rays above the TeV are marked with $^{(*)}$.

Catalogue name	**RA** (°)	δ (°)	**Description**
SMC X-1	19.27	-73.44	X-ray source
LMC X-2	80.12	-71.96	low–mass X-ray binary
SN1987a	83.87	-69.27	supernova
LMC X-4	83.20	-66.37	high–mass X-ray binary
PSRB1259-63$^{(*)}$	195.70	-63.84	pulsar
GX301-2	186.65	-62.78	variable star
Cen X-5	177.00	-62.21	high–mass X-ray binary
GX304-1	195.32	-61.60	pulsar
Cen X-3$^{(*)}$	170.31	-60.62	high–mass X-ray binary
PSRB1509-58$^{(*)}$	228.48	-59.14	pulsar
Cir X-1	230.17	-57.17	low–mass X-ray binary
2U1637-53	250.23	-53.75	low–mass X-ray binary
MSB1608-52	243.17	-52.42	X-ray source
GX339-4	255.70	-48.79	low–mass X-ray binary
Vela Pulsar$^{(*)}$	128.83	-45.18	pulsar
PSR1706-44$^{(*)}$	257.43	-44.48	pulsar
GX346-7	264.74	-44.45	low–mass X-ray binary

Table B.1: Possible point-like neutrino sources visible from the ANTARES location.

Catalogue name	**RA (°)**	δ (°)	**Description**
ARA X-1	256.56	-43.04	low–mass X-ray binary
SN1006$^{(*)}$	225.59	-41.92	supernova remnant
Vela X-1	135.53	-40.55	high–mass X-ray binary
SNR 347.3$^{(*)}$	258.54	-39.77	supernova remnant
2U1700-37	255.99	-37.84	emission-line star
NGC 6441	267.55	-37.05	globular cluster
SGR X-4	275.92	-30.36	low–mass X-ray binary
PKS2155-304$^{(*)}$	329.72	-30.23	active galaxy nucleus
Gal Center	266.50	-28.93	region in the sky
GX1+4	263.01	-24.75	low–mass X-ray binary
SN1604	262.65	-21.48	supernova remnant
GX9+9	262.93	-16.96	X-ray binary
SCO X-1	244.98	-15.64	low–mass X-ray binary
AQL X-1	287.82	0.58	low–mass X-ray binary
4U0336+01	54.20	0.59	variable of RS CVn type
AE Aqr	310.04	0.87	cataclysmic var. DQ Her type
SNR 034	284.04	1.30	supernova remnant
SS433	287.95	4.98	emission-line star
SER X-1	279.99	5.04	low–mass X-ray binary
2U0613+09	94.28	9.14	low–mass X-ray binary
Geminga	98.47	17.77	pulsar
TAU X-1$^{(*)}$	83.63	22.01	supernova remnant
2U0352+30	58.85	31.05	high–mass X-ray binary
CYG X-1	299.59	35.20	high–mass X-ray binary
Her X-1	254.46	35.34	X-ray binary
MRK421$^{(*)}$	166.11	38.21	active galaxy nucleus
CYG X-2	326.17	38.32	low–mass X-ray binary
MRK501$^{(*)}$	253.47	39.76	blazar
CYG X-3	308.11	40.95	Wolf–Rayet star
Per X-1	49.95	41.51	Seyfert 1 galaxy
3A 1422+425$^{(*)}$	217.13	42.67	BL Lac – type object
3C66A$^{(*)}$	35.66	43.04	active galaxy nucleus

Table B.1: Possible point-like neutrino sources visible from the ANTARES location (cont.).